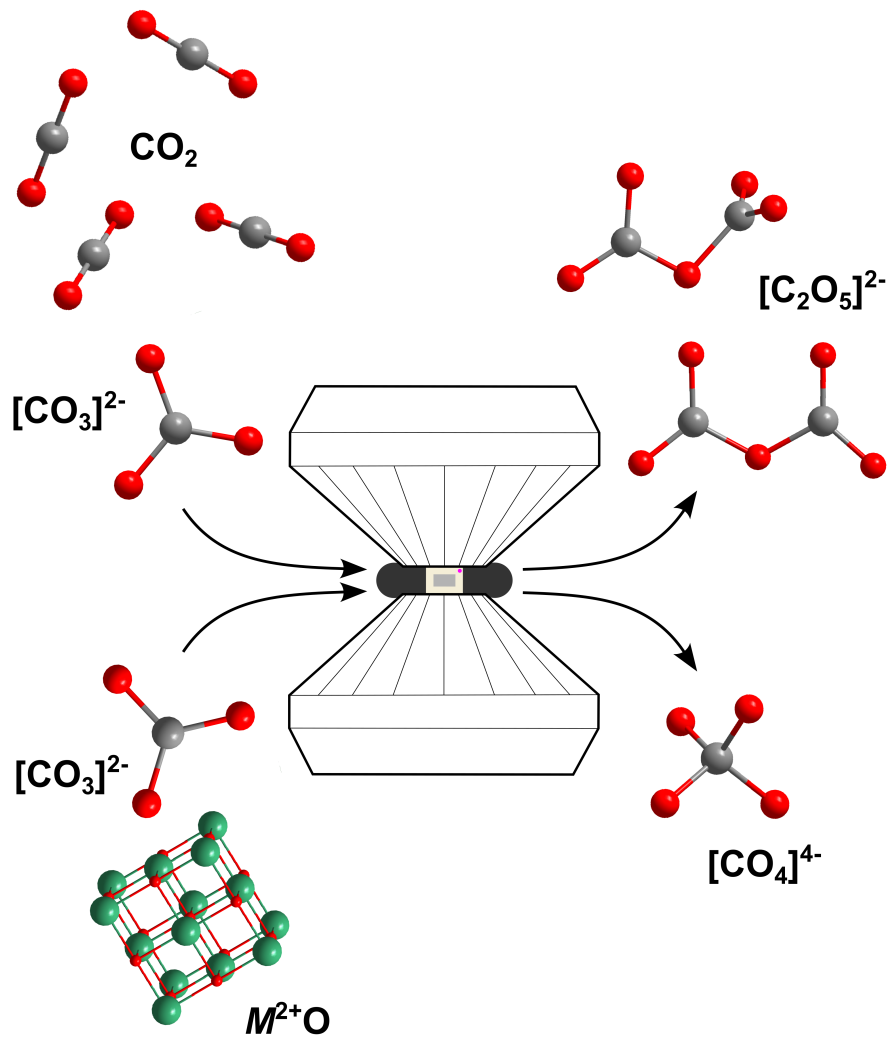


---

# Synthese und Charakterisierung von $sp^2$ -, $sp^3$ - und Pyrocarbonaten

---



von  
Dominik SPAHR



---

# Synthese und Charakterisierung von $sp^2$ -, $sp^3$ - und Pyrocarbonaten

---

Dissertation  
zur Erlangung des Doktorgrades  
der Naturwissenschaften

vorgelegt beim Fachbereich 11, Geowissenschaften/Geographie  
der Johann Wolfgang Goethe-Universität  
in Frankfurt am Main

von  
Dominik SPAHR  
aus Frankfurt am Main, Deutschland

Frankfurt 2023  
(D 30)

Vom Fachbereich 11, Geowissenschaften/Geographie der  
Johann Wolfgang Goethe-Universität als Dissertation angenommen.

Dekan: Prof. Dr. Jürgen RUNGE

Gutachter: Prof. Dr. Björn WINKLER  
PD Dr. Eiken HAUSSÜHL  
Prof. Dr. Lars EHM

Datum der Disputation: 16.11.2023

# Vorwort

Die nachfolgende Dissertation wurde an der Goethe-Universität Frankfurt am Institut für Geowissenschaften (FB 11) in der Arbeitsgruppe Kristallographie und Mineralogie (AG Winkler) verfasst. Die Betreuung der hier durchgeführten Arbeiten erfolgte hauptsächlich durch Prof. B. Winkler in Zusammenarbeit mit Dr. L. Bayarjargal, PD Dr. E. Haussühl und PD Dr. V. Vinograd. Bei dem vorliegenden Manuskript handelt es sich um eine kumulative bzw. publikationsbasierte Dissertation, welche die Forschungsergebnisse verschiedener bereits veröffentlichter wissenschaftlicher Fachartikel zusammenfasst.

Die Arbeit beschreibt verschiedene Synthesen und Untersuchungen an Carbonaten und teilt sich im Wesentlichen in zwei Abschnitte. Zum einen wurden Experimente mit Carbonaten bei Extrembedingungen bzw. unter hohen Drücken und hohen Temperaturen durchgeführt, wie sie auch im Inneren der Erde zu finden sind. Im zweiten Teil wurden Carbonate bei Raumbedingungen synthetisiert und der Einbau von Seltenerdelementen untersucht. Grundsätzlich werden jedoch in beiden Teilen dieser Arbeit die Strukturen und Eigenschaften verschiedener Carbonate und eine mögliche Kationensubstitution bzw. die Synthese isostruktureller Verbindungen erforscht.

Bei dem Titelbild dieser Dissertation handelt es sich um eine schematische Darstellung einer Diamantstempelzelle, wie sie für die hier durchgeführten Hochdruckexperimente verwendet wurde. Zusätzlich sind Ausschnitte verschiedener Kristallstrukturen gezeigt. Im Rahmen unserer Forschung wurden diese zum einen als Startmaterialien verwendet oder nach den Synthesen bei hohen Drücken erhalten: SrO, CO<sub>2</sub> (Trockeneis), Ca[CO<sub>3</sub>], Sr[CO<sub>4</sub>], Sr[C<sub>2</sub>O<sub>5</sub>] und Ba[C<sub>2</sub>O<sub>5</sub>].<sup>[1-6]</sup> Alle Abbildungen in dieser Dissertation sind in englischer Sprache verfasst, um auch nicht deutschsprachigen Leser\*innen deren Verständnis zu ermöglichen. Zusätzlich können die Abbildungen so auch für Publikationen und Vorträge verwendet werden.



# Erklärung

Ich erkläre hiermit, dass ich mich bisher keiner Doktorprüfung im mathematischen bzw. naturwissenschaftlichen Bereich unterzogen habe. Des Weiteren versichere ich, dass ich die vorgelegte Dissertation selbständig angefertigt und mich anderer Hilfsmittel als der in ihr angegebenen nicht bedient habe, insbesondere, dass alle Entlehnungen aus anderen Schriften mit Angabe der betreffenden Schrift gekennzeichnet sind. Ebenfalls versichere ich, die Grundsätze der guten wissenschaftlichen Praxis beachtet, und nicht die Hilfe einer kommerziellen Promotionsvermittlung in Anspruch genommen zu haben.

Die wissenschaftlichen Artikel, welche Teil dieser kumulativen Dissertation sind, wurden bei verschiedenen Fachzeitschriften eingereicht und im Peer-Review-Verfahren begutachtet. Weder die wissenschaftlichen Artikel noch die Dissertation sind Teil einer Dissertation in einem anderen Promotionsfach oder einer anderen Universität.

Frankfurt am Main, den 9. August 2023

*Dominik Spahr*

---

Dominik Spahr



# Inhaltsverzeichnis

<b>Abbildungsverzeichnis</b>	<b>XI</b>
<b>1 Einleitung und Motivation</b>	<b>1</b>
1.1 Kohlenstoff in Carbonaten . . . . .	1
1.2 Carbonate unter Extrembedingungen . . . . .	4
1.3 Einbau von Seltenerdelementen in Carbonaten . . . . .	7
<b>2 Publikationen</b>	<b>11</b>
2.1 Carbonate unter Extrembedingungen . . . . .	13
2.1.1 Tetrahedrally Coordinated $sp^3$ -Hybridized Carbon in $Sr_2CO_4$ Orthocarbonate at Ambient Conditions . . . . .	13
2.1.2 $Sr_3[CO_4]O$ -Antiperovskite with Tetrahedrally Coordinated $sp^3$ -Hybridized Carbon and $OSr_6$ -Octahedra . . . . .	14
2.1.3 $Sr[C_2O_5]$ is an Inorganic Pyrocarbonate Salt with $[C_2O_5]^{2-}$ Complex Anions . . . . .	15
2.1.4 Synthesis and Structure of $Pb[C_2O_5]$ : An Inorganic Pyro- carbonate Salt . . . . .	16
2.2 Einbau von Seltenerdelementen in Carbonaten . . . . .	17
2.2.1 A new $BaCa(CO_3)_2$ polymorph . . . . .	17
2.2.2 Incorporation of Europium into $(Ba,Ca)_2(CO_3)_2$ . . . . .	18
2.2.3 Incorporation of rare earth elements into $(Ba,Ca)_2(CO_3)_2$ . .	19
<b>3 Zusammenfassung und Schlussfolgerung</b>	<b>21</b>
3.1 Carbonate unter Extrembedingungen . . . . .	22
3.2 Einbau von Seltenerdelementen in Carbonaten . . . . .	27
<b>4 Summary and Conclusion</b>	<b>31</b>
<b>Literaturverzeichnis</b>	<b>33</b>
<b>Anhang</b>	<b>45</b>
<b>Danksagung</b>	<b>91</b>



# Abbildungsverzeichnis

1	Kohlenstoffkreislauf der Erde. . . . .	1
2	Carbonatstrukturen in Abhängigkeit des Kationenradius. . . . .	3
3	„Convex hulls“ im System CaO – CO <sub>2</sub> und Struktur von Ca <sub>2</sub> [CO <sub>4</sub> ].	5
4	Querschnitt durch ein Endlager für radioaktives Material. . . . .	7
5	Spaltung von <sup>235</sup> <sub>92</sub> U und Zerfall von <sup>137</sup> <sub>55</sub> Cs. . . . .	8
6	Druck-Tiefe Beziehung innerhalb der Erde. . . . .	21
7	Strukturmodelle von Sr <sub>2</sub> [CO <sub>4</sub> ], Sr <sub>3</sub> [CO <sub>4</sub> ]O und Sr[C <sub>2</sub> O <sub>5</sub> ]. . . . .	22
8	Strukturelle Vielfalt der bekannten sp <sup>3</sup> -Carbonate. . . . .	23
9	Geometrie der [C <sub>2</sub> O <sub>5</sub> ] <sup>2-</sup> -Gruppen in Pyrocarbonaten. . . . .	24
10	Carbonate nach der Reaktion zwischen M <sup>2+</sup> [CO <sub>3</sub> ] und CO <sub>2</sub> . . . . .	26
11	Elementarzellenvolumina von Ca <sub>1-x</sub> Ba <sub>x</sub> [CO <sub>3</sub> ] Mischkristallen. . . . .	27
12	ICP-OES Messungen an (BaCa) <sub>(1-x)</sub> [CO <sub>3</sub> ] <sub>2</sub> + Eu <sub>x</sub> . . . . .	28
13	Ba <sub>0,9</sub> Ca <sub>1,1</sub> [CO <sub>3</sub> ] <sub>2</sub> Pulver mit verschiedenen Seltenerdelementen. . . . .	29



# Kapitel 1

# 1 Einleitung und Motivation

## 1.1 Kohlenstoff in Carbonaten

In der nachfolgenden Dissertation werden die Struktur und die Eigenschaften von Carbonat-Verbindungen bei Raumbedingungen, wie sie an der Erdoberfläche herrschen, genauso wie unter den Extrembedingungen des Erdinneren untersucht. Dabei wird ein besonderes Augenmerk auf die Kationensubstitution bzw. die Synthese isostruktureller Verbindungen mit unterschiedlichen Kationen gelegt. Zunächst sollte daher diskutiert werden, warum Forschung an Carbonaten für uns von Interesse ist.

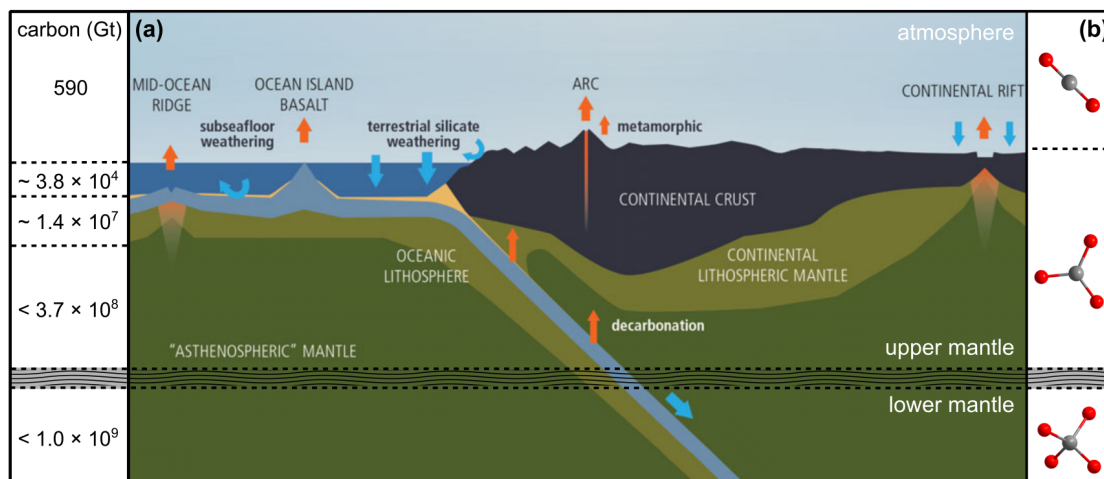


**Abbildung 1:** (a) Kohlenstoffkreislauf der Erde, wobei typische Reservoir-Größen eingetragen sind (modifiziert nach Lee et al.<sup>[7]</sup>). (b) Bekannte Spezies aus Kohlenstoff und Sauerstoff, welche bei den Druck- und Temperaturbedingungen in den verschiedenen Reservoirs der Erde existieren können.<sup>[8]</sup>

Carbonate spielen eine fundamentale Rolle für den Kohlenstoffkreislauf der Erde, da Kohlenstoff sowohl in der Biosphäre, der Hydrosphäre, in Böden als auch in der kontinentalen bzw. der ozeanischen Kruste hauptsächlich in Form von Carbonaten vorkommt.<sup>[9,10]</sup> Vernachlässigt man den Erdkern, befindet sich Kohlenstoff zum aller größten Teil (> 99%) in Kruste und Mantel der Erde.<sup>[7,11]</sup> Abbildung 1 (a) zeigt einen schematischen Ausschnitt des Kohlenstoffkreislaufs

der Erde. Es sind typische Angaben für den Kohlenstoffgehalt einiger Reservoirs eingetragen, wobei zwischen allen Reservoirs ein reger Austausch von Material stattfindet.

In Abbildung 1 (a) ist deutlich zu erkennen, dass der Anteil des Kohlenstoffs in der Erdatmosphäre (590 Gt) gegenüber dem Anteil des oberen ( $< 3.7 \times 10^8$  Gt) bzw. unteren Erdmantels ( $< 1.0 \times 10^9$  Gt) oder auch der Erdkruste verschwindend gering ist.<sup>[7]</sup> Auch der Kohlenstoffanteil in den Ozeanen ( $< 3.8 \times 10^4$  Gt) ist im Verhältnis zur festen Erde klein. Im Gegensatz zu Erdkruste und Erdmantel kommt der Kohlenstoff in der Erdatmosphäre großteilig in Form von gasförmigem, molekularem  $\text{CO}_2$  mit einem ansteigenden Anteil von  $\sim 400$  ppm vor.<sup>[12]</sup>

Typische Spezies aus Kohlenstoff und Sauerstoff, wie sie bei den möglichen Druck- und Temperaturbedingungen in den verschiedenen Reservoirs der Erde auftreten können, sind in Abbildung 1 (b) zu sehen. Im Vergleich zur Erdatmosphäre liegt der Kohlenstoff in der Erdkruste und dem oberen Teil des Erdmantels großteilig in Form so genannter „konventioneller“ Carbonate mit  $M[\text{CO}_3]$  oder  $M_1M_2[\text{CO}_3]_2$  Zusammensetzung vor. Die  $\text{Ca}[\text{CO}_3]$ -Polymorphe (siehe Abbildung 2 a) Calcit ( $R\bar{3}c$ , Nr. 167) und Aragonit ( $Pmcn$ , Nr. 62) machen dabei zusammen mit Dolomit ( $\text{CaMg}[\text{CO}_3]_2$ ) mehr als 90% der Carbonate in der Erdkruste aus.<sup>[13]</sup>

Bei „konventionellen“ Carbonaten handelt es sich chemisch gesehen um die anorganischen Salze der Kohlensäure ( $\text{H}_2\text{CO}_3$ ), welche Metallkationen ( $M^{n+}$ ) verschiedener Größen beherbergen können.<sup>[14]</sup> Im Gegensatz zum molekularen  $\text{CO}_2$  der Erdatmosphäre besitzen diese Carbonate als charakteristische Baueinheit eine trigonal-planar aufgebaute  $[\text{CO}_3]^{2-}$ -Gruppe (Abbildung 1 b) mit  $\text{C-}sp^2$  Hybridorbitalen zwischen dem zentralen Kohlenstoffatom und den drei umgebenden Sauerstoffatomen.<sup>[15]</sup> Aufgrund ihrer Häufigkeit und ihrer geowissenschaftlichen Relevanz sind Carbonate bereits seit vielen Jahrzehnten ein wichtiges Forschungsgebiet. So wurde z. B. die Kristallstruktur von Aragonit vor bereits fast 100 Jahren durch Bragg<sup>[3]</sup> beschrieben.

Betrachtet man die Gruppe der Carbonate mit  $M^{2+}[\text{CO}_3]$  Zusammensetzung, dann ist eine Vielzahl von Verbindungen mit unterschiedlichen divalenten Kationen ( $M^{2+}$ ) bekannt (Abbildung 2 b). In Abhängigkeit des Kationenradius kristallisieren die Carbonate typischerweise in zwei unterschiedlichen Strukturtypen, wobei die Metallkationen entweder durch 6 Sauerstoffatome (Calcit-Struktur) oder 9 Sauerstoffatome (Aragonit-Struktur) koordiniert sind.<sup>[14]</sup> Der Ionenradius von  $\text{Ca}^{2+}$  von  $1.00 \text{ \AA}$  ( $KZ = 6$ ) bzw. von  $1.18 \text{ \AA}$  ( $KZ = 9$ ) kann dabei als

Grenzfall zwischen dem Calcit- und Aragonit-Strukturtyp angesehen werden.<sup>[16]</sup> Carbonate deren Kationen einen Ionenradius  $\leq 1.00 \text{ \AA}$  ( $KZ = 6$ ) wie  $\text{Mg}^{2+}$  oder  $\text{Fe}^{2+}$  besitzen, kristallisieren dabei in Calcit-Struktur, wobei der Einbau größerer Kationen wie  $\text{Sr}^{2+}$  oder  $\text{Ba}^{2+}$  zum Aragonit-Strukturtyp führt.<sup>[17]</sup> Innerhalb der isostrukturellen Carbonate ist Kationensubstitution und auch Mischkristallbildung möglich. In aragonitischem  $\text{Ca}_x\text{Sr}_{1-x}[\text{CO}_3]$  ist z. B. eine vollständige Mischkristallbildung zwischen den beiden Endgliedern ( $x = 0 - 1$ ) möglich.<sup>[18]</sup>

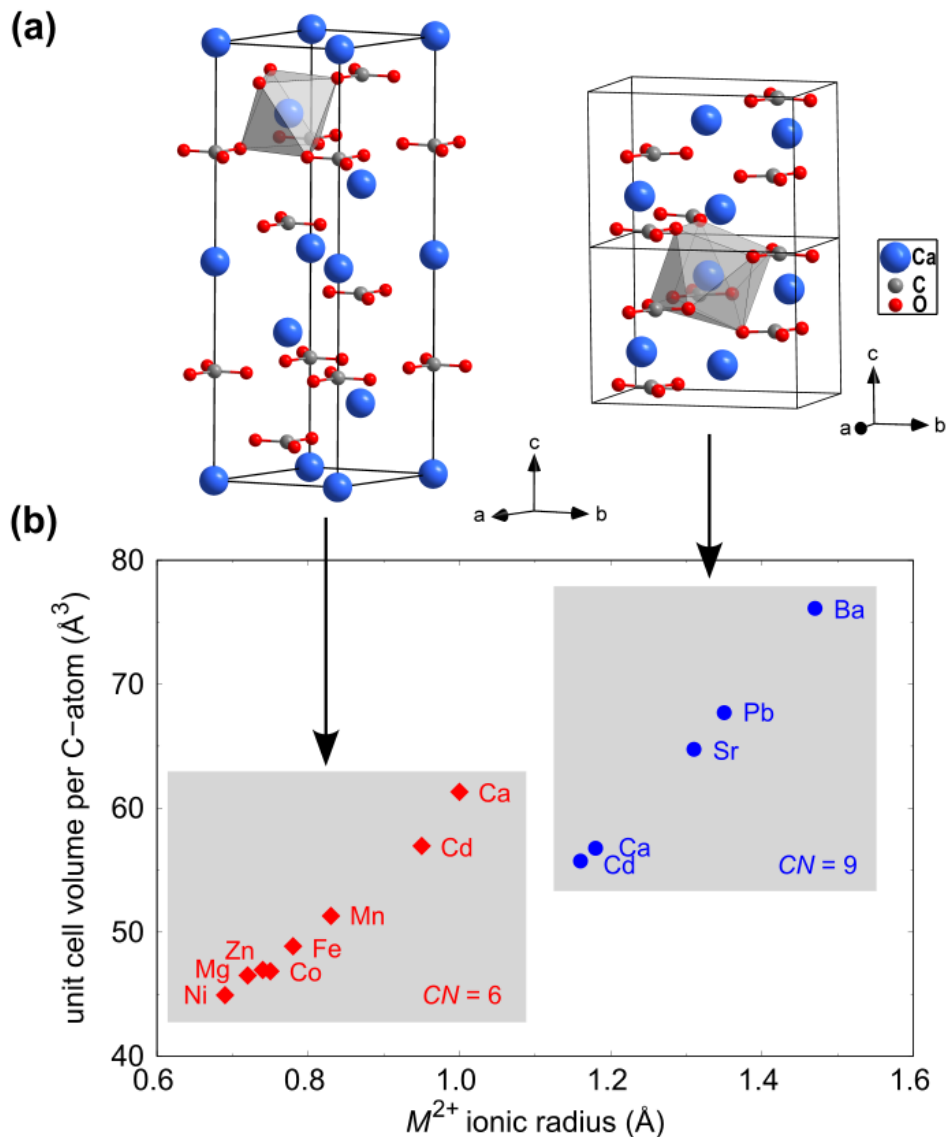


**Abbildung 2:** (a) Kristallstrukturen von Calcit (links,  $KZ = 6$ ) und Aragonit (rechts,  $KZ = 9$ ) bei Raumbedingungen mit Koordinationspolyeder des Ca-Atoms in grau.<sup>[19,20]</sup> (b) Elementarzellvolumen pro Kohlenstoffatom in Abhängigkeit des Kationenradius (nach Shannon<sup>[16]</sup>) für Carbonate mit  $M^{2+}[\text{CO}_3]$  Zusammensetzung in Calcit- ( $R\bar{3}c$ , Nr. 167) oder Aragonit-Strukturtyp ( $Pmcn$ , Nr. 62).<sup>[17,19-21]</sup>

## 1.2 Carbonate unter Extrembedingungen

Die Subduktion von ozeanischer Lithosphäre in den Erdmantel stellt einen wichtigen Teil des globalen Kohlenstoffkreislaufs dar. Dabei gelangen „konventionelle“ Carbonate wie  $\text{Ca}[\text{CO}_3]$  oder  $\text{CaMg}[\text{CO}_3]_2$  und somit auch große Mengen an Kohlenstoff in den Erdmantel.<sup>[22,23]</sup> Aus diesem Grund ist das Verständnis des Verhaltens von Carbonaten unter den extremen Bedingungen innerhalb der Erde relevant für das Verständnis des globalen Kohlenstoffkreislaufs. Der erste Teil dieser Arbeit beschäftigt sich daher mit Carbonaten unter den extremen Druck- und Temperaturbedingungen wie sie innerhalb des Erdmantels herrschen.

In früheren Studien konnte bereits gezeigt werden, dass die  $[\text{CO}_3]^{2-}$ -Gruppen „konventioneller“ Carbonate wie  $\text{Ca}[\text{CO}_3]$ ,  $\text{CaMg}[\text{CO}_3]_2$ ,  $\text{Mg}[\text{CO}_3]$  oder  $\text{Fe}[\text{CO}_3]$  auch über Phasentransformationen hinweg bis hin zu sehr hohen Drücken ( $\sim 70$  GPa) und hohen Temperaturen ( $\sim 2000$  K) stabil sein können und als starre Baueinheit unter diesen Bedingungen erhalten bleiben.<sup>[24–27]</sup> Außer einer beginnenden Dimerisierung in  $\text{Na}_2\text{Ca}_2[\text{CO}_3]_3$  bei hohen Drücken wurde bisher keinerlei Polymerisation von  $[\text{CO}_3]^{2-}$ -Gruppen durch die Verknüpfung über ein geteiltes Sauerstoffatom beobachtet.<sup>[28]</sup> Daher können die Strukturen bekannter  $sp^2$ -Carbonate über einen weiten Druck- und Temperaturbereich im Wesentlichen durch die Stapelung von  $[\text{CO}_3]^{2-}$ -Gruppen beschrieben werden.<sup>[24–27]</sup>

Setzt man „konventionelle“ Carbonate extrem hohen Drücken ( $p \geq 70$  GPa) und hohen Temperaturen ( $T \geq 1500$  K) aus, kann es zur Bildung so genannter  $sp^3$ -Carbonate als Polymorphe dieser Carbonate kommen.<sup>[26,27,29–41]</sup>  $sp^3$ -Carbonate besitzen als zentrale Baueinheit  $[\text{CO}_4]^{4-}$ -Tetraeder (Abbildung 1 b). Dabei bildet das Kohlenstoffatom  $C$ - $sp^3$  Hybridorbitale zu den vier umgebenden Sauerstoffatomen aus. In dieser Familie von Carbonaten wurde eine erhebliche strukturelle Vielfalt beobachtet, da eine Polymerisation der  $[\text{CO}_4]^{4-}$ -Tetraeder über deren Ecken möglich ist. Bisher konnten die Strukturen von  $sp^3$ -Carbonaten mit isolierten  $[\text{CO}_4]^{4-}$ -Tetraedern oder mit Gruppen, Ringen, Ketten bzw. Pyramiden aus  $[\text{CO}_4]^{4-}$ -Tetraedern bestimmt werden.<sup>[26,27,29–41]</sup>

Abgesehen von den experimentell bestimmten  $sp^3$ -Carbonaten bei hohen Drücken und hohen Temperaturen wurden mit Hilfe von Rechnungen, basierend auf Dichtefunktionaltheorie (DFT), theoretische Vorhersagen in Systemen mit verschiedenen chemischen Zusammensetzungen ( $M^{2+}\text{O} - \text{CO}_2$ ) gemacht.<sup>[42–45]</sup> Dabei wurden neue und möglicherweise stabile  $sp^3$ -Carbonate mit  $[\text{CO}_4]^{4-}$ -Tetraedern bei tieferen Drücken ( $p \geq 5$  GPa) und mit  $M_2^{2+}[\text{CO}_4]$  bzw.  $M_3^{2+}[\text{CO}_4]\text{O}$  Zusammensetzung für verschiedene Kationen ( $M^{2+} = \text{Mg}, \text{Ca}, \text{Sr}, \text{Ba}$ ) vorhergesagt. Exemplarisch sind Ergebnisse dieser DFT-Rechnungen im System  $\text{CaO} -$

CO<sub>2</sub> in Abbildung 3 (a) gezeigt. Abgesehen von den Endgliedern des Systems CaO bzw. CO<sub>2</sub> und Aragonit (Ca[CO<sub>3</sub>]), könnten basierend auf den Rechnungen z. B. die beiden *sp*<sup>3</sup>-Carbonate Ca<sub>2</sub>[CO<sub>4</sub>] und Ca<sub>3</sub>[CO<sub>5</sub>]O bei 25 GPa stabil sein.<sup>[43]</sup> Diese DFT-basierten Vorhersagen im System CaO – CO<sub>2</sub> motivierten damit die ersten Experimente unserer Arbeitsgruppe durch J. König und L. Bayarjargal für Reaktionen in einer laser-geheizten Diamantstempelzelle (LH-DAC) in diesem System.<sup>[46]</sup>

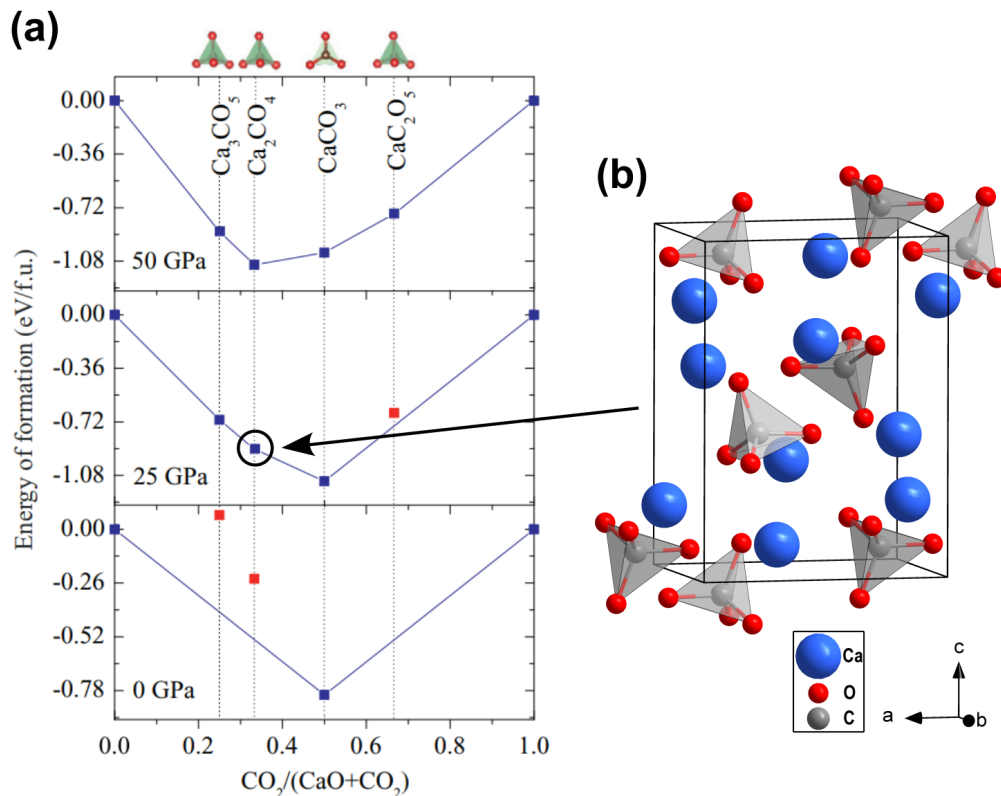


**Abbildung 3:** (a) „Convex hulls“ für das System CaO – CO<sub>2</sub> zwischen 0 GPa und 50 GPa, **blaue Quadrate** zeigen stabile und **rote Quadrate** metastabile Kristallstrukturen.<sup>[43]</sup> (b) Kristallstruktur von Ca<sub>2</sub>[CO<sub>4</sub>] gültig für 20(1) GPa und Raumtemperatur nach der Synthese aus einer CaO/Ca[CO<sub>3</sub>] Mischung bei ~ 20 GPa und ~ 2000 K in einer LH-DAC.<sup>[46]</sup> Koordinationspolyeder der C-Atome sind in grau dargestellt.

Mit ihren Experimenten konnten sie kurze Zeit später zeigen, dass sich das *sp*<sup>3</sup>-Carbonat Ca<sub>2</sub>[CO<sub>4</sub>] bei ~ 20 GPa und ~ 2000 K in einer LH-DAC über eine Reaktion zwischen dem Alkalimetalloxid CaO und einem Ca[CO<sub>3</sub>] Einkristall synthetisieren lässt.<sup>[46]</sup> Abbildung 3 (b) zeigt die Kristallstruktur von Ca<sub>2</sub>[CO<sub>4</sub>] bei 20(1) GPa und Raumtemperatur nach der Synthese in einer LH-DAC. Die Kristallstruktur wurde aus Synchrotroneinkristalldaten verfeinert. Die isolierten [CO<sub>4</sub>]<sup>4-</sup>-Tetraeder sind deutlich zu erkennen.

Die Möglichkeit neue  $sp^3$ -Carbonate bei sehr viel geringeren Drücken ( $\ll 70$  GPa) zu synthetisieren, eröffnete ein neues Feld der Carbonat-Forschung. Niedrigere Drücke (10–50 GPa) sind experimentell mit Hilfe von Diamantstempelzellen viel einfacher zugänglich. Somit legte die Synthese von  $\text{Ca}_2[\text{CO}_4]$  den Grundstein für die im Rahmen dieser Arbeit durchgeführten Hochdruckexperimente an Carbonaten. Die Synthese der zu  $\text{Ca}_2[\text{CO}_4]$  isostrukturellen Verbindung  $\text{Sr}_2[\text{CO}_4]$  bei  $\sim 90$  GPa und  $\sim 2500$  K zeigte, dass Kationensubstitution grundsätzlich auch in  $sp^3$ -Carbonaten möglich ist.<sup>[41]</sup> Daher war eine grundlegende Frage dieser Arbeit: *„Lassen sich Verbindungen wie  $\text{Sr}_2[\text{CO}_4]$  ebenfalls bei vergleichsweise niedrigen Drücken in einer LH-DAC synthetisieren und können experimentell weitere isostrukturelle  $sp^3$ -Carbonate bei vergleichbaren Bedingungen synthetisiert werden?“*

In den Rechnungen im System  $\text{CaO} - \text{CO}_2$  wurden metastabile Kristallstrukturen mit  $\text{Ca}_2[\text{CO}_4]$  und  $\text{Ca}_3[\text{CO}_4]\text{O}$  Zusammensetzung bei Raumdruck gefunden (Abbildung 3 a).<sup>[43]</sup> Hingegen zeigten die experimentellen Daten von  $\text{Ca}_2[\text{CO}_4]$ , dass diese Phase während der Dekompression nur bis  $\sim 4$  GPa beobachtet und nicht zu Raumbedingungen abgeschreckt werden konnte.<sup>[46]</sup> Insgesamt konnte noch kein Carbonat mit  $sp^3$ -hybridisiertem Kohlenstoff zu Raumbedingungen abgeschreckt werden. Falls isostrukturelle Verbindungen mit größeren und gleich koordinierten Kationen wie z. B.  $\text{Sr}^{2+}$  oder  $\text{Ba}^{2+}$  synthetisiert werden können, sollte der Transformationsdruck der jeweiligen Struktur entsprechend der „Druck-Homologen-Regel“ mit steigendem Kationenradius sinken.<sup>[47]</sup> Dieses Verhalten ist auch an den sinkenden Phasentransformationsdrücken mit steigendem Kationenradius für Carbonate mit  $M^{2+}[\text{CO}_3]$  Zusammensetzung zwischen Aragonit- und post-Aragonit-Strukturtyp zu beobachten.<sup>[48]</sup> Somit müsste bei Strukturen mit größeren Kationen die Wahrscheinlichkeit steigen, diese zu Raumbedingungen abschrecken zu können. Die zweite Frage die im Rahmen dieser Arbeit beantwortet werden sollte war: *„Lassen sich Carbonate mit  $sp^3$ -hybridisiertem Kohlenstoff möglicherweise zu Raumbedingungen abschrecken?“*

Durch die Reaktionen zwischen einem „konventionellen“ Carbonat-Kristall und dem zugehörigen Alkalimetalloxid lassen sich jedoch nur Verbindungen synthetisieren, deren chemische Zusammensetzung zwischen  $M^{2+}\text{O}$  und  $M^{2+}[\text{CO}_3]$  im „convex hull“ Diagramm liegen. Jedoch wurden für höhere Drücke ( $> 30$  GPa) auch stabile Carbonate mit höherem  $\text{CO}_2/M^{2+}\text{O}$  Verhältnis, wie  $\text{CaC}_2\text{O}_5$  bei 50 GPa, vorhergesagt (Abbildung 3 a).<sup>[42,43]</sup> Daher sollten im Rahmen dieser Arbeit auch Reaktionen zwischen Carbonaten und  $\text{CO}_2$  in der LH-DAC durchgeführt werden um die Frage zu beantworten: *„Können durch Reaktionen in einer LH-DAC auch neue,  $\text{CO}_2$ -reiche Carbonate synthetisiert werden?“*

## 1.3 Einbau von Seltenerdelementen in Carbonaten

Der zweite Teil dieser Arbeit beschäftigt sich ebenfalls mit Carbonaten, jedoch wird hier der Einbau von Seltenerdelementen in „konventionelle“ Carbonate bei Raumbedingungen untersucht. Da Experimente mit radioaktiven Elementen technisch sehr komplex bzw. gefährlich sind, wurden hier Experimente mit Seltenerdelementen als Stellvertreter für Elemente der Actinoide ( $Z = 89-103$ ) durchgeführt. Als Seltenerdelemente bezeichnet man Sc ( $Z = 21$ ) bzw. Y ( $Z = 39$ ) und die Lanthanoide ( $Z = 57-71$ ).<sup>[49]</sup> Auf der Suche nach einem möglichen Endlager für Atommüll, ist das Verständnis des Verhaltens der radioaktiven Actinoide unabdingbar. Ein schematischer Querschnitt durch ein mögliches Endlager in Tonschichten ist in Abbildung 4 gezeigt.<sup>[50]</sup>

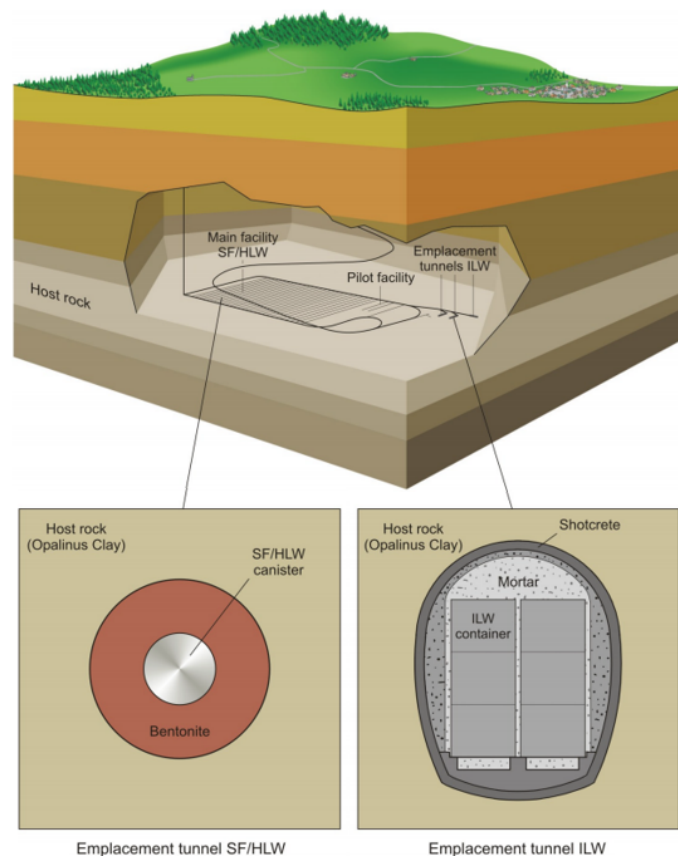


**Abbildung 4:** Schematischer Querschnitt durch ein mögliches Endlager für radioaktives Material in tiefen geologischen Formationen wie der „Opalinus Clay“ (Schweiz).<sup>[50]</sup>

In einem Atommüll-Endlager gibt es verschiedene Möglichkeiten für einen Kontakt zwischen Carbonaten und Elementen der Actinoide. Zum einen bevorzugen verschiedene Länder ein Endlager in tiefen geologischen Formationen wie Tonschichten.<sup>[51]</sup> Manche dieser Formationen wie z. B. die „Boom Clay“

können bis zu 5% Carbonate enthalten.<sup>[52]</sup> Kommt es nun zu einem Austritt von radioaktivem Material aus einem Lagerbehälter, könnte eine Interaktion mit den umgebenden Tonschichten und somit auch den Carbonaten stattfinden. Zum anderen wird in Endlagern Beton bzw. Spritzbeton als Barriere zwischen den Lagerbehältern und dem umgebenden Gestein eingesetzt (Abbildung 4).<sup>[50]</sup> Über geologische Zeit-Skalen hinweg kann sich dieser Beton zersetzen. Durch die Reaktion von gasförmigem oder gelöstem  $\text{CO}_2$  mit dem bereits hydratisiertem Calciumoxid bzw. Branntkalk ( $\text{Ca}(\text{OH})_2$ ) im Beton kommt es zur Bildung von  $\text{Ca}[\text{CO}_3]$  ( $\text{CO}_2 + \text{Ca}(\text{OH})_2 \longleftrightarrow \text{Ca}[\text{CO}_3] + \text{H}_2\text{O}$ ).<sup>[53]</sup> Nach seiner Zersetzung kann der Beton somit ebenfalls eine Quelle für  $\text{Ca}[\text{CO}_3]$  darstellen.

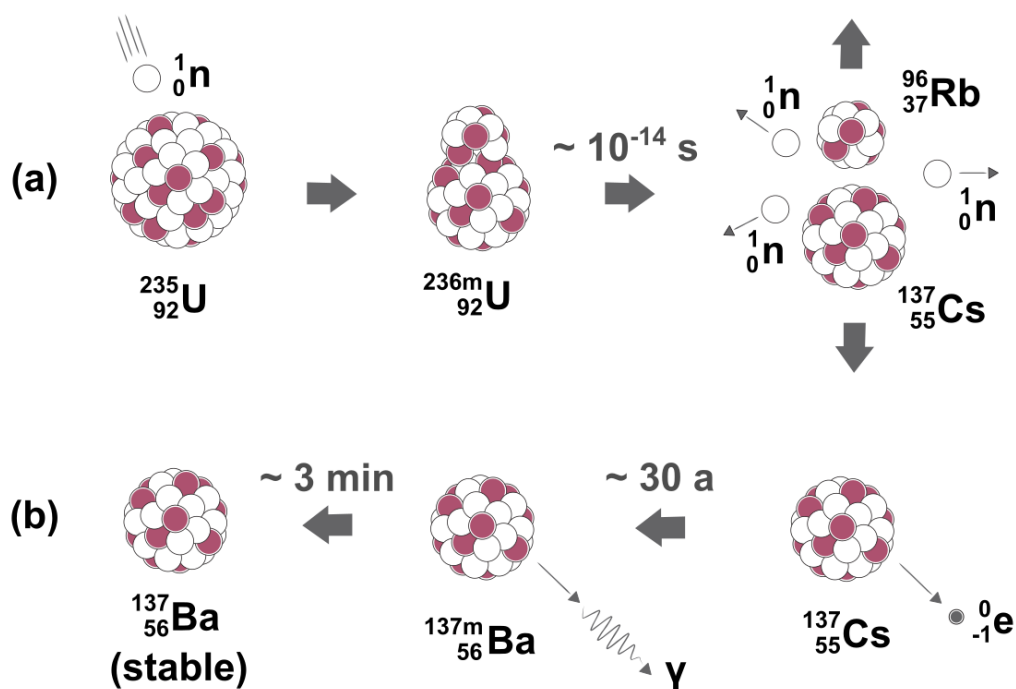


**Abbildung 5:** (a) Neutroneninduzierte Kernspaltung von  ${}^{235}_{92}\text{U}$  zu  ${}^{137}_{55}\text{Cs}$  und  ${}^{96}_{37}\text{Rb}$ . (b)  $\beta^-$ -Zerfall von  ${}^{137}_{55}\text{Cs}$  zu stabilem  ${}^{137}_{56}\text{Ba}$  (modifiziert nach Demtröder<sup>[54]</sup> und Volkmer<sup>[55]</sup>).

Bei den Carbonaten in den geologischen Barrieren und bei jenen welche nach Zersetzung des Betons entstehen, handelt es sich typischerweise um  $\text{Ca}[\text{CO}_3]$ .<sup>[52,53]</sup> Es gibt jedoch radiogene Quellen für das Vorkommen von Barium durch den radioaktiven Abfall in den Endlagern.<sup>[56]</sup> Kernspaltung in Atomkraftwerken führt unter anderem zur neutroneninduzierten Spaltung verschiedener Uran-Isotope. In Abbildung 5 (a) ist eine mögliche Spaltreaktion von  ${}^{235}_{92}\text{U}$  durch ein langsames bzw. thermisches Neutron gezeigt. Durch die Reaktion  ${}^{235}_{92}\text{U} + {}^1_0\text{n} \longrightarrow {}^{236\text{m}}_{92}\text{U} \longrightarrow {}^{137}_{55}\text{Cs} + {}^{96}_{37}\text{Rb} + 3 {}^1_0\text{n}$  kommt es in diesem Beispiel zur Bildung von radioaktivem  ${}^{137}_{55}\text{Cs}$  mit einer Halbwertszeit von  $\sim 30$  Jahren.<sup>[55]</sup>

Im weiteren Verlauf zerfällt dieses dann über  $\beta^-$ -Zerfall und der Abgabe eines Elektrons ( $^{137}_{55}\text{Cs} \longrightarrow ^{137}_{56}\text{Ba} + ^0_{-1}\text{e}$ ) zu dem stabilen Barium-Isotop  $^{137}_{56}\text{Ba}$  unter der Abgabe von  $\gamma$ -Strahlung (Abbildung 5 b). Das radioaktive Isotop  $^{137}_{55}\text{Cs}$  zählt zu den wichtigsten bzw. gesundheitsschädlichsten Spaltprodukten von Uran und wurde unter anderem in enormen Mengen während den Nuklearkatastrophen in den Kernkraftwerken Tschernobyl (85 PBq) oder Fukushima Daiichi (15–20 PBq) freigesetzt.<sup>[57]</sup> Dabei kann  $^{137}_{55}\text{Cs}$  auch über verschiedene Zerfallsreihen wie z. B. über den  $\beta^-$ -Zerfall  $^{137}_{52}\text{Te} \longrightarrow ^{137}_{53}\text{I} + ^0_{-1}\text{e} \longrightarrow ^{137}_{54}\text{Xe} + ^0_{-1}\text{e} \longrightarrow ^{137}_{55}\text{Cs} + ^0_{-1}\text{e}$  gebildet werden.<sup>[55]</sup>

Durch Leckage eines Lagerbehälters in einem Endlager kann somit ein stabiles Barium-Isotop als Zerfallsprodukt in Kontakt mit den Carbonaten des Umgebungsgesteins oder des zersetzten Betons kommen. Dadurch könnten sich aus  $\text{Ca}[\text{CO}_3]$  und Barium möglicherweise Ba/Ca-Carbonate bilden, welche nun auch Elemente der Actinoide einbauen könnten. Im zweiten Teil dieser Arbeit sollte daher die Frage beantwortet werden: „Lassen sich Seltenerdelemente bzw. Lanthanoide als Stellvertreter für Actinoide in Phasen des „konventionellen“ Doppelcarbonats  $\text{BaCa}[\text{CO}_3]_2$  einbauen?“

In vorangegangenen Experimenten im System  $\text{Ba}[\text{CO}_3] - \text{Ca}[\text{CO}_3]$  konnte gezeigt werden, dass Mischkristalle ( $\text{Ca}_{1-x}\text{Ba}_x[\text{CO}_3]$ ) mit unterschiedlichen Kationen-Verhältnissen möglich sind.<sup>[58–61]</sup> Da es trotz der sehr unterschiedlichen Ionenradien von  $\text{Ca}^{2+}$  mit  $r = 1.18 \text{ \AA}$  bzw.  $\text{Ba}^{2+}$  mit  $r = 1.47 \text{ \AA}$  ( $KZ = 9$ ) zu signifikanter Mischkristallbildung kommt, lässt auf eine hohe chemische Variabilität des  $\text{Ba}[\text{CO}_3] - \text{Ca}[\text{CO}_3]$  Systems schließen.<sup>[16]</sup> Dieses Verhalten legt die Vermutung nahe, dass sich dieses System auch für den Einbau unterschiedlich großer Seltenerdelemente bzw. Actinoide eignen könnte, welche in hohen Konzentrationen im Atommüll auftreten. Hier wäre somit Kationensubstitution der Ba/Ca-Atome durch diese Elemente möglich. Im Gegensatz dazu sind die Anteile von Seltenerdelementen in natürlich vorkommenden „konventionellen“ Carbonaten wie z. B. Calcit mit  $\leq 0.1 \text{ mol\%}$  sehr gering.<sup>[62]</sup> Bezogen auf die Immobilisierung des radioaktiven Kohlenstoffisotops  $^{14}\text{C}$  wurde das Doppelcarbonat  $\text{BaCa}[\text{CO}_3]_2$  bereits untersucht.<sup>[63–67]</sup>



## Kapitel 2

# 2 Publikationen

Im nachfolgenden Kapitel sind die Publikationen aufgelistet welche Teil dieser kumulativen Dissertation sind. Insbesondere wird der Eigenanteil des Autors beschrieben, um den Leser\*innen dieser Dissertation einen Einblick in die geleistete Arbeit des Promovenden zu gewähren. Die Publikationen liegen in ihrem publizierten Format im Anhang bei.

### Carbonate unter Extrembedingungen:

1. **D. Spahr**, J. König, L. Bayarjargal, R. Luchitskaia, W. Morgenroth, D. Comboni, V. Milman und B. Winkler. Tetrahedrally Coordinated  $sp^3$ -Hybridized Carbon in  $Sr_2CO_4$  Orthocarbonate at Ambient Conditions. *Inorg. Chem.*, 60:5419–5422, 2021. doi: [10.1021/acs.inorgchem.1c00159](https://doi.org/10.1021/acs.inorgchem.1c00159)‡
2. **D. Spahr**, J. König, L. Bayarjargal, P. N. Gavryushkin, H.-P. Liermann, V. Milman und B. Winkler.  $Sr_3[CO_4]O$ -Antiperovskite with Tetrahedrally Coordinated  $sp^3$ -Hybridized Carbon and  $OSr_6$ -Octahedra. *Inorg. Chem.*, 60:14504–14508, 2021. doi: [10.1021/acs.inorgchem.1c01900](https://doi.org/10.1021/acs.inorgchem.1c01900)†
3. **D. Spahr**, J. König, L. Bayarjargal, V. Milman, A. Perlov, H.-P. Liermann und B. Winkler.  $Sr[C_2O_5]$  is an Inorganic Pyrocarbonate Salt with  $[C_2O_5]^{2-}$  Complex Anions. *J. Am. Chem. Soc.*, 144:2899–2904, 2022. doi: [10.1021/jacs.2c00351](https://doi.org/10.1021/jacs.2c00351)
4. **D. Spahr**, J. König, L. Bayarjargal, R. Luchitskaia, V. Milman, A. Perlov, H.-P. Liermann und B. Winkler. Synthesis and Structure of  $Pb[C_2O_5]$ : An Inorganic Pyrocarbonate Salt. *Inorg. Chem.*, 61:9855–9859, 2022. doi: [10.1021/acs.inorgchem.2c01507](https://doi.org/10.1021/acs.inorgchem.2c01507)

---

‡Featured Article und Editors Choice

†Featured Article

**Einbau von Seltenerdelementen in Carbonate:**

5. **D. Spahr**, L. Bayarjargal, V. Vinograd, R. Luchitskaia, V. Milman und B. Winkler. A new  $\text{BaCa}(\text{CO}_3)_2$  polymorph. *Acta Cryst.*, B75:291–300, **2019**. doi: [10.1107/S2052520619003238](https://doi.org/10.1107/S2052520619003238)
6. **D. Spahr**, L. Bayarjargal, V. Vinograd, M. Etter, J. Raddatz und B. Winkler. Incorporation of Europium into  $(\text{Ba,Ca})_2(\text{CO}_3)_2$ . *J. Solid State Chem.*, 307:122759, **2022**. doi: [10.1016/j.jssc.2021.122759](https://doi.org/10.1016/j.jssc.2021.122759)
7. **D. Spahr**, L. Bayarjargal, V. Vinograd, M. Etter, J. Raddatz und B. Winkler. Incorporation of rare earth elements into  $(\text{Ba,Ca})_2(\text{CO}_3)_2$ . *Solid State Sci.*, 139:107129, **2023**. doi: [10.1016/j.solidstatesciences.2023.107129](https://doi.org/10.1016/j.solidstatesciences.2023.107129)

## 2.1 Carbonate unter Extrembedingungen

### 2.1.1 Tetrahedrally Coordinated $sp^3$ -Hybridized Carbon in $Sr_2CO_4$ Orthocarbonate at Ambient Conditions

#### Autoren

Dominik Spahr, Jannes Binck, Lkhamsuren Bayarjargal, Rita Luchitskaia, Wolfgang Morgenroth, Davide Comboni, Victor Milman und Björn Winkler

#### Abstract

*„We have synthesized the orthocarbonate  $Sr_2[CO_4]$ , in which carbon is tetrahedrally coordinated by four oxygen atoms, at moderately high pressures [20(1) GPa] and high temperatures ( $\sim 3500$  K) in a diamond anvil cell by reacting a  $Sr[CO_3]$  single crystal with SrO powder. We show by synchrotron powder X-ray diffraction, Raman spectroscopy, and density functional theory calculations that this phase, and hence  $sp^3$ -hybridized carbon in a  $[CO_4]^{4-}$ -group, can be recovered at ambient conditions. The C–O bond distances are all of similar lengths [ $\sim 1.41(1)$  Å], and the O–C–O angles deviate from the ideal tetrahedral angle by a few degrees only.“*

#### Eigenanteil

Ich habe die Diamantstempelzellen für diese Experimente vorbereitet und geladen. Anschließend habe ich die Raman-Spektroskopie bei Raumdruck, die druckabhängigen Raman-Messungen und deren Auswertung vorgenommen. Die druckabhängigen Laserheizexperimente wurden zusammen mit L. Bayarjargal durchgeführt. Die Synchrotronmessungen fanden am ESRF in Grenoble durch W. Morgenroth und D. Comboni statt. Im Anschluss habe ich die Auswertung der Diffraktionsdaten, der DFT-Rechnungen durch B. Winkler und die Strukturverfeinerung vorgenommen. Das Manuskript wurde von mir mit Unterstützung von B. Winkler und mit Kommentaren der Co-Autoren geschrieben.

## 2.1.2 Sr<sub>3</sub>[CO<sub>4</sub>]O-Antiperovskite with Tetrahedrally Coordinated sp<sup>3</sup>-Hybridized Carbon and OSr<sub>6</sub>-Octahedra

### Autoren

Dominik Spahr, Jannes König, Lkhamsuren Bayarjargal, Pavel N. Gavryushkin, Victor Milman, Hanns-Peter Liermann und Björn Winkler

### Abstract

*„We have synthesized the orthocarbonate Sr<sub>3</sub>[CO<sub>4</sub>]O in a laserheated diamond anvil cell at 20 and 30 GPa by heating to ~ 3000(300) K. Afterwards, we recovered the orthocarbonate with [CO<sub>4</sub>]<sup>4-</sup> groups at ambient conditions. Single-crystal diffraction shows the presence of [CO<sub>4</sub>]<sup>4-</sup> groups, i.e., sp<sup>3</sup>-hybridized carbon tetrahedrally coordinated by covalently bound oxygen atoms. The [CO<sub>4</sub>]<sup>4-</sup> tetrahedra are located in a cage formed by corner-sharing OSr<sub>6</sub> octahedra, i.e., octahedra with oxygen as a central ion, forming an antiperovskite-type structure. At high pressures, the octahedra are nearly ideal and slightly rotated. The high-pressure phase is tetragonal (I4/mcm). Upon pressure release, there is a phase transition with a symmetry lowering to an orthorhombic phase (Pnma), where the octahedra tilt and deform slightly.“*

### Eigenanteil

Für die Laserheizexperimente habe ich die Diamantstempelzellen vorbereitet und geladen. Die Raman-Spektroskopie bei Raumdruck sowie die druckabhängigen Raman-Messungen wurden von mir durchgeführt und ausgewertet. Anschließend habe ich die Laserheizexperimente in den Diamantstempelzellen durchgeführt. Die Synchrotronmessungen wurden von mir zusammen mit J. König und L. Bayarjargal an Petra III (DESY) in Hamburg durchgeführt. Ich habe die Auswertung der Diffraktionsdaten bzw. die Strukturlösung der neuen Phase, die Strukturverfeinerung, die Auswertung der druckabhängigen Diffraktionsmessungen und der DFT-Rechnungen von B. Winkler vorgenommen. Zuletzt wurde das Manuskript von mir mit Unterstützung von B. Winkler und mit Kommentaren der Co-Autoren geschrieben.

### 2.1.3 Sr[C<sub>2</sub>O<sub>5</sub>] is an Inorganic Pyrocarbonate Salt with [C<sub>2</sub>O<sub>5</sub>]<sup>2-</sup> Complex Anions

#### Autoren

Dominik Spahr, Jannes König, Lkhamsuren Bayarjargal, Victor Milman, Alexander Perlov, Hanns-Peter Liermann und Björn Winkler

#### Abstract

*„The synthesis of a novel type of carbonate, namely of the inorganic pyrocarbonate salt Sr[C<sub>2</sub>O<sub>5</sub>], which contains isolated [C<sub>2</sub>O<sub>5</sub>]<sup>2-</sup>-groups, significantly extends the crystal chemistry of inorganic carbonates beyond the established sp<sup>2</sup>- and sp<sup>3</sup>-carbonates. We synthesized Sr[C<sub>2</sub>O<sub>5</sub>] in a laser-heated diamond anvil cell by reacting Sr[CO<sub>3</sub>] with CO<sub>2</sub>. By single crystal synchrotron diffraction, Raman spectroscopy, and density functional theory (DFT) calculations, we show that it is a pyrocarbonate salt. Sr[C<sub>2</sub>O<sub>5</sub>] is the first member of a novel family of inorganic carbonates. We predict, based on DFT calculations, that further inorganic pyrocarbonates can be obtained and that these will be relevant to geoscience and may provide a better understanding of reactions converting CO<sub>2</sub> into useful inorganic compounds.“*

#### Eigenanteil

Für die Ladungen der Diamantstempelzellen mit CO<sub>2</sub> (Trockeneis) habe ich zusammen mit L. Bayarjargal und der Werkstatt der Arbeitsgruppe ein kryogenes Ladesystem für unsere Bedürfnisse weiterentwickelt. Anschließend habe ich die Diamantstempelzellen vorbereitet, geladen und die druckabhängigen Laserheizexperimente durchgeführt. Zusätzlich habe ich druckabhängig Raman-Spektroskopie gemessen und die Raman-Daten ausgewertet. Nach den Synchrotronmessungen zusammen mit J. König und L. Bayarjargal an Petra III (DESY) habe ich die Struktur der neuen Phase gelöst, diese verfeinert und die experimentellen Daten zusammen mit den DFT-Rechnungen von B. Winkler ausgewertet. Anschließend habe ich das Manuskript mit Unterstützung von B. Winkler und mit Kommentaren der Co-Autoren geschrieben.

## 2.1.4 Synthesis and Structure of $\text{Pb}[\text{C}_2\text{O}_5]$ : An Inorganic Pyrocarbonate Salt

### Autoren

Dominik Spahr, Jannes König, Lkhamsuren Bayarjargal, Rita Luchitskaia, Victor Milman, Alexander Perlov, Hanns-Peter Liermann und Björn Winkler

### Abstract

*„We have synthesized  $\text{Pb}[\text{C}_2\text{O}_5]$ , an inorganic pyrocarbonate salt, in a laser-heated diamond anvil cell (LH-DAC) at 30 GPa by heating a  $\text{Pb}[\text{CO}_3] + \text{CO}_2$  mixture to  $\sim 2000(200)$  K. Inorganic pyrocarbonates contain isolated  $[\text{C}_2\text{O}_5]^{2-}$  groups without functional groups attached. The  $[\text{C}_2\text{O}_5]^{2-}$  groups consist of two oxygen-sharing  $[\text{CO}_3]^{2-}$  groups.  $\text{Pb}[\text{C}_2\text{O}_5]$  was characterized by synchrotron-based single-crystal structure refinement, Raman spectroscopy, and density functional theory calculations.  $\text{Pb}[\text{C}_2\text{O}_5]$  is isostructural to  $\text{Sr}[\text{C}_2\text{O}_5]$  and crystallizes in the monoclinic space group  $P2_1/c$  with  $Z = 4$ . The synthesis of  $\text{Pb}[\text{C}_2\text{O}_5]$  demonstrates that, just like in other carbonates, cation substitution is possible and that therefore inorganic pyrocarbonates are a novel family of carbonates, in addition to the established  $sp^2$ - and  $sp^3$ -carbonates.“*

### Eigenanteil

Das kryogene Ladesystem für die Ladungen der Diamantstempelzellen mit  $\text{CO}_2$  (Trockeneis) wurde von mir und L. Bayarjargal zusammen mit der Werkstatt der Arbeitsgruppe weiter optimiert. Für die Synthese von  $\text{Pb}[\text{C}_2\text{O}_5]$  habe ich die Diamantstempelzellen vorbereitet und geladen. Anschließend habe ich druckabhängige Raman-Spektroskopie und die Laserheizexperimente durchgeführt. Ich habe die experimentellen Daten zusammen mit den DFT-Rechnungen von B. Winkler ausgewertet. Nach den Synchrotronmessungen zusammen mit L. Bayarjargal an Petra III (DESY) habe ich die Hochdruckdiffraktionsdaten ausgewertet und die Struktur verfeinert. Das Manuskript habe ich mit Unterstützung von B. Winkler und mit Kommentaren der Co-Autoren geschrieben.

## 2.2 Einbau von Seltenerdelementen in Carbonaten

### 2.2.1 A new BaCa(CO<sub>3</sub>)<sub>2</sub> polymorph

#### Autoren

**Dominik Spahr**, Lkhamsuren Bayarjargal, Victor Vinograd, Rita Luchitskaia, Victor Milman und Björn Winkler

#### Abstract

*„A new polymorph of the double carbonate BaCa(CO<sub>3</sub>)<sub>2</sub>, a “C2 phase”, has been synthesized. Its structure has been obtained by density-functional-theory-based (DFT-based) model calculations and has been refined by Rietveld analysis of X-ray powder diffraction data. The structure of the new polymorph differs significantly from those of the established polymorphs barytocalcite, paralstonite and alstonite. The unit-cell parameters of the new monoclinic (space group C2) compound are  $a = 6.6775(5)$ ,  $b = 5.0982(4)$ ,  $c = 4.1924(3)$  Å,  $\beta = 109.259(1)^\circ$ . The new compound has been further characterized using Raman spectroscopy. This work shows that earlier studies have misidentified the products of an established synthesis route and that findings based on the incorrect identification of the synthesis product concerning the suitability of barytocalcite as a matrix for the retention of radioactive isotopes will need to be reconsidered.“*

#### Eigenanteil

Die unterschiedlichen Carbonate wurden von mir mit Hilfe verschiedener Synthesewege und mit Unterstützung durch R. Luchitskaia synthetisiert. Anschließend habe ich Raman-Spektroskopie, Röntgenpulverdiffraktion und Rasterelektronenmikroskopie durchgeführt. Danach habe ich die experimentellen Daten und die DFT-Daten von B. Winkler ausgewertet. Die Struktur wurde von mir in Zusammenarbeit mit den DFT-Rechnungen gelöst. Verfasst wurde das Manuskript von mir mit Unterstützung von B. Winkler und den Kommentaren der Co-Autoren.

## 2.2.2 Incorporation of Europium into $(\text{Ba,Ca})_2(\text{CO}_3)_2$

### Autoren

**Dominik Spahr**, Lkhamsuren Bayarjargal, Victor Vinograd, Martin Etter, Jacek Raddatz und Björn Winkler

### Abstract

*„Synchrotron-based powder diffraction measurements in combination with inductively coupled plasma optical emission spectrometry, Raman and fluorescence spectroscopy show that  $(\text{Ba,Ca})_2(\text{CO}_3)_2$  can incorporate significant amounts (up to 6 mol%) of europium. This solid solution is therefore of potential interest for the solidification of nuclear waste streams involving aqueous nitrate solutions of lanthanides. Europium replaces Ba/Ca on lattice sites and is not incorporated as an interstitial defect. Charge compensation is likely due to the presence of OH-groups as we could exclude a coupled substitution involving  $\text{Na}^+$ . The Eu-containing compound is stable to at least 723 K. We show that the one-phase-field of  $(\text{Ba}_x\text{Ca}_{1-x})\text{CO}_3$  solid solutions at ambient conditions is larger ( $0.36 < x < 0.51$ ) than previously thought. The synthesis routes employed here lead to compounds which have similar molar volumes than those of the naturally occurring  $(\text{Ba,Ca})$ -double carbonates, in noted contrast to another synthetic phase, “balcite”.“*

### Eigenanteil

Ich habe die verschiedenen Carbonat-Proben synthetisiert. Diese wurden dann von mir über laborbasierte Röntgenpulverdiffraktion und Rasterelektronenmikroskopie charakterisiert. Ich habe temperaturabhängige Fluoreszenzmessungen und Raman-Spektroskopie durchgeführt. Im Anschluss habe ich die experimentellen Daten ausgewertet. Ich habe die Proben für die optische Emissionsspektrometrie (ICP-OES) vorbereitet und die zugehörigen Messdaten ausgewertet. Die Messungen wurden durch J. Raddatz durchgeführt. Ich habe die Proben für die Synchrotronmessungen präpariert und die Synchrotrondaten ausgewertet, wobei die Messungen von M. Etter durchgeführt wurden. Das Manuskript habe ich mit Unterstützung von B. Winkler und mit Kommentaren der Co-Autoren geschrieben.

### 2.2.3 Incorporation of rare earth elements into $(\text{Ba,Ca})_2(\text{CO}_3)_2$

#### Autoren

**Dominik Spahr**, Lkhamsuren Bayarjargal, Victor Vinograd, Rita Luchitskaia und Björn Winkler

#### Abstract

*„The structural effects of the incorporation of the rare earth elements (REE) La, Ce, Pr, Nd, Eu, Sm, Gd, Er, Tm, Yb and Y into a synthetic Ba–Ca carbonate have been investigated. We precipitated solutions with a composition  $\text{Ba}_{0.9}\text{Ca}_{1.1}(\text{CO}_3)_2$  doped with REE-nitrates. The precipitate, with few exceptions, consisted of a crystalline solid, slightly depleted in Ba with respect to the expected composition, and an amorphous phase. On heating, the whole sample became crystalline and consisted of a Ba-enriched and a Ba-depleted phase. The phases are isostructural. The lattice parameters are strongly influenced by the incorporation of  $\sim 6\%$  REE. There is a linear dependence of the unit cell volume on the radius of the incorporated REE for those elements with a radius  $< 1.0 \text{ \AA}$ , i.e. Yb, Tm, Er, Y, Gd, Sm, Eu, Nd and Pr, while the unit cell volume of a sample doped with La ( $r(\text{La}) = 1.03 \text{ \AA}$ ) and Ce ( $r(\text{Ce}) = 1.01 \text{ \AA}$ ) is not well described by this dependency. Raman spectroscopy shows that the local environment of the  $\text{CO}_3$ -groups does not differ substantially between the Ba-enriched and the Ba-depleted phase, but changes linearly as a function of the ionic radius of the REE. The present study clearly shows that substantial amounts of REE can be incorporated into the Ba–Ca-carbonate studied here, making it potentially useful as a matrix in nuclear waste treatments involving aqueous nitrate solutions of lanthanides and actinides.“*

#### Eigenanteil

Über Ausfällungsexperimente habe ich zusammen mit R. Luchitskaia die Carbonate mit Anteilen von unterschiedlichen Seltenerdelementen synthetisiert. Im Anschluss habe ich Röntgenpulverdiffraktion, Raman-Spektroskopie und Rasterelektronenmikroskopie durchgeführt um die Proben zu charakterisieren. Ich habe die experimentellen Daten ausgewertet und abschließend mit Unterstützung von B. Winkler und mit Kommentaren der Co-Autoren das Manuskript verfasst.



# 3 Zusammenfassung und Schlussfolgerung

Im Rahmen des ersten Teils dieser Doktorarbeit konnten verschiedene neue Carbonat-Phasen in der LH-DAC bei hohen Drücken (20–30 GPa) und hohen Temperaturen (1500–3500 K) synthetisiert werden.<sup>[4,5,68,69]</sup> Im Gegensatz dazu fanden im zweiten Teil dieser Arbeit Synthesen bei Raumbedingungen oder nur leicht erhöhten Drücken und Temperaturen ( $\sim 500$  K und  $\sim 25$  bar) statt.<sup>[70–73]</sup> Um die hier erzeugten Drücke besser einordnen zu können, ist in Abbildung 6 eine schematische Darstellung der Druck-Tiefenbeziehung innerhalb der Erde nach dem „Preliminary Reference Earth Model“ gezeigt.<sup>[74,75]</sup> Dabei steigt der Druck von etwa  $10^{-4}$  GPa an der Erdoberfläche ( $\hat{=}$  1 bar) auf bis zu 360 GPa im Zentrum des festen inneren Erdkerns an. Exemplarisch sind ebenfalls die Synthesedrucke für  $\text{Sr}_2[\text{CO}_4]$  und  $\text{Sr}[\text{C}_2\text{O}_5]$  markiert. Diese würden dabei hypothetischen Tiefen innerhalb der Erde von  $\sim 600$  km und  $\sim 800$  km entsprechen und somit im Grenzbereich zwischen oberem und unterem Erdmantel liegen.

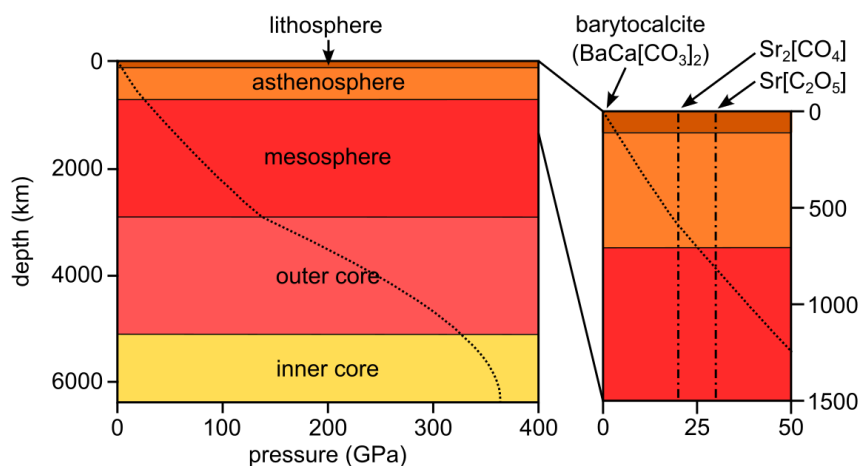


**Abbildung 6:** Schematischer Querschnitt durch die Erde, wobei der Druck in Abhängigkeit der Tiefe innerhalb der Erde nach dem „Preliminary Reference Earth Model“ aufgetragen ist (modifiziert nach Dziewonski und Anderson<sup>[74]</sup> bzw. Zeidler and Crichton<sup>[75]</sup>). In der Vergrößerung (0 km und 1500 km Tiefe) sind die Synthesedrucke von  $\text{Sr}_2[\text{CO}_4]$ ,  $\text{Sr}[\text{C}_2\text{O}_5]$  und Barytocalcit ( $\text{BaCa}[\text{CO}_3]_2$ ) für eine hypothetische Tiefe markiert.<sup>[4,68,71]</sup>

### 3.1 Carbonate unter Extrembedingungen

Zunächst wurden in dieser Arbeit Experimente mit Reaktionen zwischen  $\text{Sr}[\text{CO}_3]$  und  $\text{SrO}$  durchgeführt, um  $\text{Sr}_2[\text{CO}_4]$  in Analogie zu  $\text{Ca}_2[\text{CO}_4]$  bei 20 GPa zu synthetisieren.<sup>[46]</sup> Im Gegensatz zur Synthese von  $\text{Sr}_2[\text{CO}_4]$  bei  $\sim 90$  GPa wurde durch unsere Experimente deutlich, dass sich  $\text{Sr}_2[\text{CO}_4]$  auch bei niedrigen Drücken ( $\sim 20$  GPa) synthetisieren lässt.<sup>[4,41]</sup> Anschließend konnten wir mittels synchrotronbasierter Röntgendiffraktion und Raman-Spektroskopie in Kombination mit DFT-Rechnungen zeigen, dass sich  $\text{Sr}_2[\text{CO}_4]$  zu Raumbedingungen abschrecken lässt. Somit war zum ersten Mal der Beweis erbracht, dass  $sp^3$ -Carbonate mit  $[\text{CO}_4]^{4-}$ -Tetraedern als zentraler Baueinheit abschreckbar sind.<sup>[4]</sup> Abbildung 7 (a) zeigt die verfeinerte Kristallstruktur von  $\text{Sr}_2[\text{CO}_4]$  bei Raumdruck und Raumtemperatur.

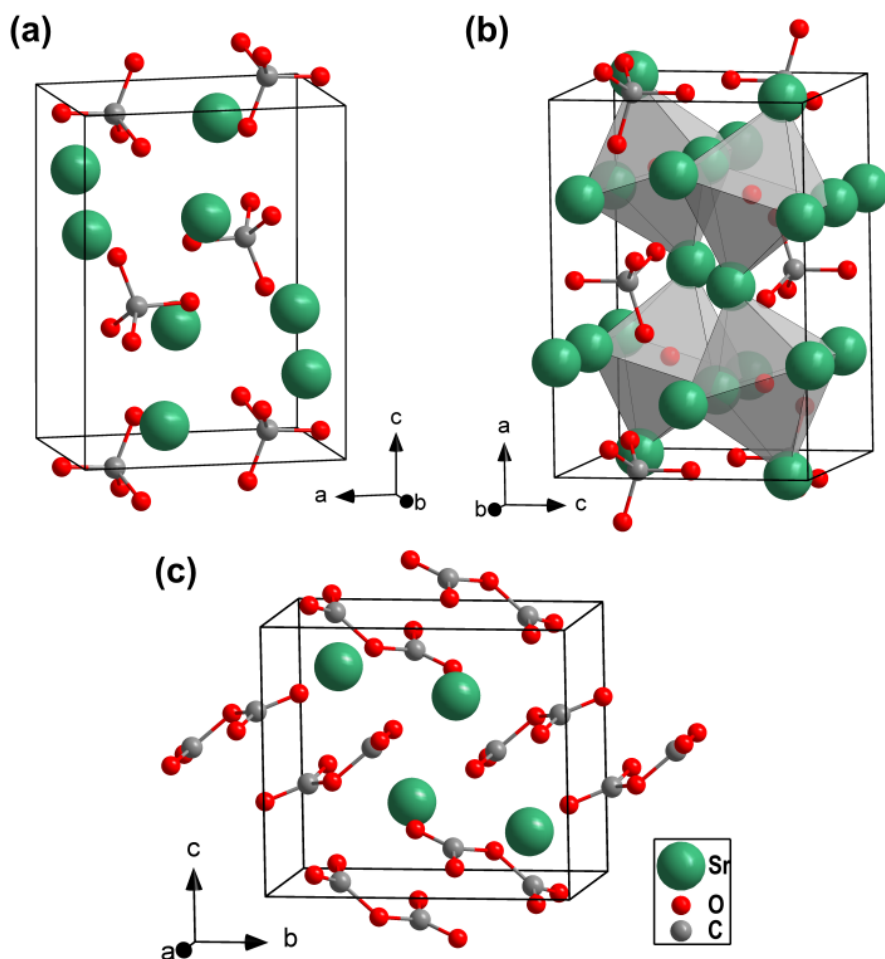


**Abbildung 7:** Strukturmodelle der  $sp^3$ -Carbonate (a)  $\text{Sr}_2[\text{CO}_4]$  und (b)  $\text{Sr}_3[\text{CO}_4]\text{O}$  gültig für Raumbedingungen.<sup>[4,68]</sup>  $\text{SrO}_6$ -Koordinationspolyeder sind in grau gezeigt. (c) Strukturmodell des Pyrocarbonats  $\text{Sr}[\text{C}_2\text{O}_5]$  gültig für 30(2) GPa und Raumtemperatur.<sup>[5]</sup>

In weiteren Versuchen im System  $\text{Sr}[\text{CO}_3] - \text{SrO}$  konnten wir bei vergleichbaren Synthesebedingungen den Antiperowskit  $\text{Sr}_3[\text{CO}_4]\text{O}$  synthetisieren.<sup>[68]</sup> Dessen Hochdruckstruktur deckt sich mit Vorhersagen aus DFT-Rechnungen.<sup>[45]</sup> Im Gegensatz dazu beobachteten wir während der Dekompression der Diamantstempelzelle bei niedrigen Drücken eine Phasentransformation. Mittels Synchrotroneinkristalldiffraktion konnten wir anschließend die Struktur der Tiefdruckphase lösen (Abbildung 7 b) und zusätzlich beweisen, dass auch das  $sp^3$ -Carbonat  $\text{Sr}_3[\text{CO}_4]\text{O}$  zu Raumbedingungen abgeschreckt werden kann.<sup>[68]</sup> Diese Ergebnisse decken sich mit denen unserer Raman-Spektroskopie und den zugehörigen DFT-Rechnungen. Sowohl bei  $\text{Sr}_2[\text{CO}_4]$  als auch bei  $\text{Sr}_3[\text{CO}_4]\text{O}$  handelt es sich um  $sp^3$ -Carbonate mit isolierten  $[\text{CO}_4]^{4-}$ -Tetraedern, welche vor dieser Arbeit noch nie bei Raumbedingungen beobachtet werden konnten. Abbildung 8 zeigt eine Übersicht über die strukturelle Vielfalt der bekannten Carbonate mit  $[\text{CO}_4]^{4-}$ -Tetraedern.

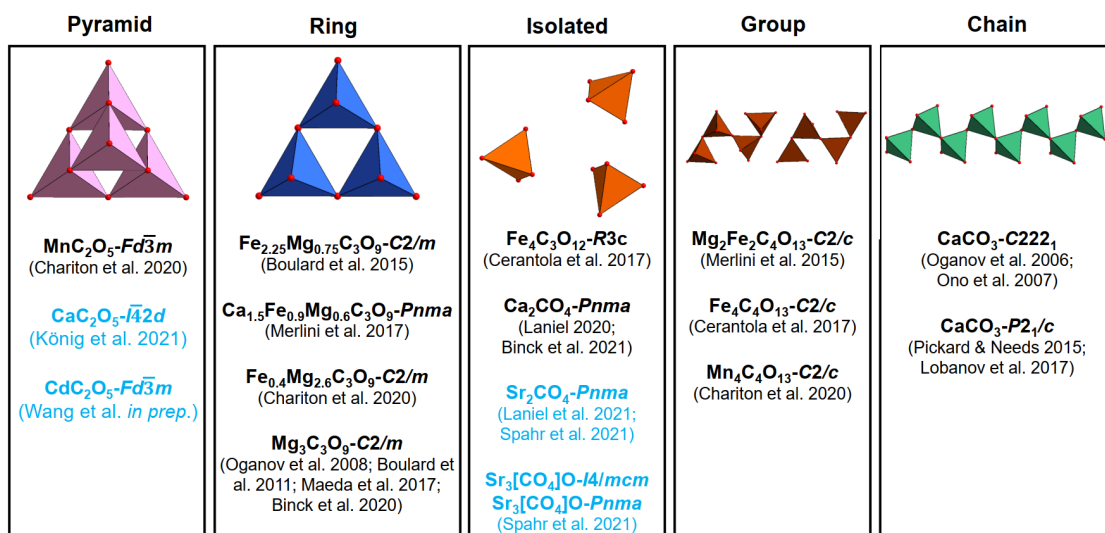


**Abbildung 8:** Strukturelle Vielfalt der bekannten  $sp^3$ -Carbonate (modifiziert nach Spahr et al.<sup>[68]</sup> und König<sup>[76]</sup>). In blau sind neue Carbonat-Phasen dargestellt, an welchen unter anderem im Rahmen dieser Arbeit gearbeitet wurde.

Die ersten Reaktionen zwischen einem Carbonat-Kristall und  $\text{CO}_2$  wurden mit  $\text{Ca}[\text{CO}_3]$  durchgeführt, da in diesem System für Drücke  $> 30$  GPa neue Carbonate mit erhöhten  $\text{CO}_2/M^{2+}\text{O}$  Verhältnis vorhergesagt wurden.<sup>[42,43]</sup> Dabei konnten wir das neue  $sp^3$ -Carbonat  $\text{CaC}_2\text{O}_5$  zwischen 34 GPa und 45 GPa synthetisieren und dessen Struktur bestimmen.<sup>[77]</sup> Hier sind die  $[\text{CO}_4]^{4-}$ -Tetraeder über ihre Ecken verknüpft und bilden im Gegensatz zu  $\text{Sr}_2[\text{CO}_4]$  oder  $\text{Sr}_3[\text{CO}_4]\text{O}$  pyramidenförmige komplexe Anionen (Abbildung 8).

Im Zuge dieser Dissertation wurden Experimente mit  $\text{Sr}[\text{CO}_3]$  in  $\text{CO}_2$  Atmosphäre durchgeführt, um festzustellen, ob auch hier Kationensubstitution möglich ist, so wie auch bei  $\text{Ca}_2[\text{CO}_4]$  und  $\text{Sr}_2[\text{CO}_4]$ .<sup>[46,68]</sup> Jedoch zeigten die Experimente bei  $\sim 30$  GPa, dass zwar eine Reaktion zwischen Carbonat und  $\text{CO}_2$  stattfindet, aber dass kein  $sp^3$ -Carbonat gebildet wird. Mittels Synchrotron-einkristalldiffraktion konnten wir zeigen, dass durch Heizen einer  $\text{Sr}[\text{CO}_3] + \text{CO}_2$  Mischung bei diesem Druck ein so genanntes Pyrocarbonat mit  $\text{Sr}[\text{C}_2\text{O}_5]$  Zusammensetzung entsteht.<sup>[5]</sup> Die Struktur von  $\text{Sr}[\text{C}_2\text{O}_5]$  ist in Abbildung 7 (c) gezeigt. Hier sind zwei  $[\text{CO}_3]^{2-}$ -Gruppen über ein geteiltes Sauerstoffatom zu einer  $[\text{C}_2\text{O}_5]^{2-}$ -Gruppe verknüpft (Abbildung 9). Die Bildung einer solchen Pyro-Gruppe war zwar in Pyrocarbonatestern mit organischen Resten ( $R_1 - [\text{C}_2\text{O}_5] - R_2$ ) bekannt, welche typischerweise in der organischen Synthese oder der Biochemie Anwendung finden, wurden vorher jedoch in anorganischen Carbonaten nicht beobachtet.<sup>[78–82]</sup> Nur zwei schwache Raman-Peaks in einer  $\text{Li}_2[\text{CO}_3] - \text{Na}_2[\text{CO}_3]$  Schmelze und Computersimulationen gaben Hinweise auf die Existenz isolierter  $[\text{C}_2\text{O}_5]^{2-}$ -Gruppen.<sup>[83,84]</sup>

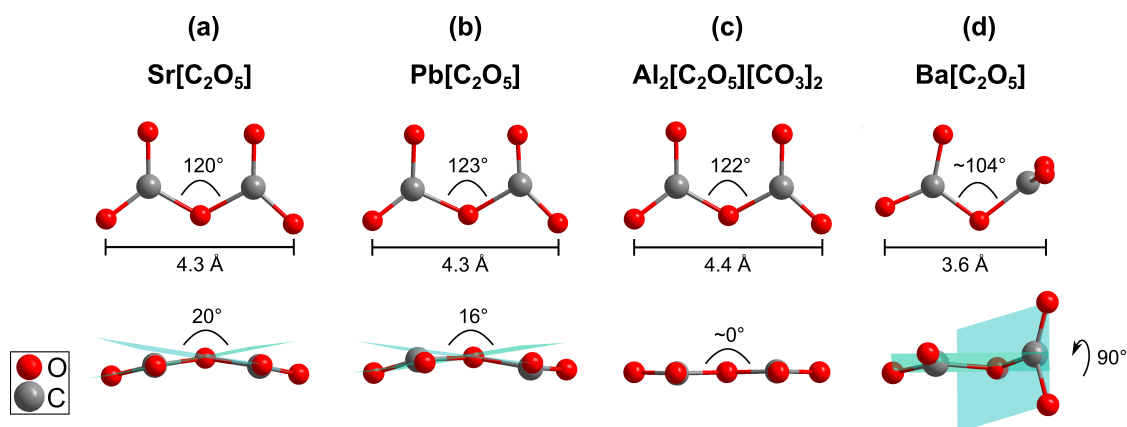


**Abbildung 9:** Geometrie der  $[\text{C}_2\text{O}_5]^{2-}$ -Gruppen in (a)  $\text{Sr}[\text{C}_2\text{O}_5]$ , (b)  $\text{Pb}[\text{C}_2\text{O}_5]$ , (c)  $\text{Al}_2[\text{C}_2\text{O}_5][\text{CO}_3]_2$  und (d)  $\text{Ba}[\text{C}_2\text{O}_5]$ .<sup>[5,6,69,85]</sup>

Die Entdeckung der anorganischen Pyrocarbonate etablierte somit eine neue Familie von Carbonaten, zusätzlich zu den bereits bekannten  $sp^2$ - und  $sp^3$ -Carbonaten. Hier konnte erstmalig die Polymerisation von  $[\text{CO}_3]^{2-}$ -Gruppen beobachtet werden. Des Weiteren konnten wir mit der Synthese von isostrukturellem  $\text{Pb}[\text{C}_2\text{O}_5]$  bei vergleichbaren Synthesebedingungen zeigen, dass auch in dieser neuen Familie von Carbonaten Kationensubstitution möglich ist.<sup>[69]</sup> In Abbildung 9 ist ein Vergleich der Geometrie der  $[\text{C}_2\text{O}_5]^{2-}$ -Gruppen zwischen  $\text{Sr}[\text{C}_2\text{O}_5]$  und  $\text{Pb}[\text{C}_2\text{O}_5]$  gezeigt. Beide entsprechen in erster Näherung der vorhergesagten Gleichgewichtsgeometrie.<sup>[84]</sup> Es ist anzumerken, dass die Ionenradien

von  $\text{Sr}^{2+}$  ( $r = 1.31 \text{ \AA}$ ) und  $\text{Pb}^{2+}$  ( $r = 1.35 \text{ \AA}$ ) für  $KZ = 9$  sehr ähnlich sind.<sup>[16]</sup> Im Gegensatz dazu wurde für das deutlich kleinere  $\text{Ca}^{2+}$  ( $r = 1.18 \text{ \AA}$ ) bis jetzt experimentell kein Pyrocarbonat gefunden.<sup>[77]</sup> Im System  $\text{Cd}[\text{CO}_3] - \text{CO}_2$  wurden erste Experimente durch Y. Wang und L. Bayarjargal durchgeführt, um dieses Verhalten für kleinere Kationen wie  $\text{Cd}^{2+}$  ( $r = 1.16 \text{ \AA}$ ) zu bestätigen.<sup>[86]</sup> Sie konnten zeigen, dass durch Laserheizen einer  $\text{Cd}[\text{CO}_3] + \text{CO}_2$  Mischung bei  $\sim 40 \text{ GPa}$  das  $sp^3$ -Carbonat  $\text{CdC}_2\text{O}_5$  gebildet wird.  $\text{CdC}_2\text{O}_5$  ist vermutlich isostrukturell zu  $\text{MnC}_2\text{O}_5$  bzw. einer nicht verzerrten Struktur von  $\text{CaC}_2\text{O}_5$  (Abbildung 8).<sup>[29,77,86]</sup> Diese Ergebnisse werden auch dadurch gestützt, dass das  $sp^3$ -Carbonat  $\text{MnC}_2\text{O}_5$  mit pyramidenförmigen komplexen Anionen für das noch kleinere  $\text{Mn}^{2+}$  ( $r = 0.83 \text{ \AA}$  für  $KZ = 6$ ), nach der Zersetzung von  $\text{Mn}[\text{CO}_3]$  bei  $66(3) \text{ GPa}$  und  $\sim 2000 \text{ K}$ , gefunden wurde.<sup>[29]</sup>

Unsere Experimente mit  $\text{Ba}[\text{CO}_3]$  und  $\text{CO}_2$  als Startmaterialien zeigen, dass auch hier ein Pyrocarbonat gebildet wird.<sup>[6]</sup> Jedoch führt vermutlich der größere Radius von  $\text{Ba}^{2+}$  ( $r = 1.47 \text{ \AA}$ ) zu einer neuen Geometrie der  $[\text{C}_2\text{O}_5]^{2-}$ -Gruppe (Abbildung 9 d). In  $\text{Ba}[\text{C}_2\text{O}_5]$  sind die beiden  $[\text{CO}_3]^{2-}$ -Gruppen der  $[\text{C}_2\text{O}_5]^{2-}$ -Gruppe gegeneinander um  $\sim 90^\circ$  um das geteilte Sauerstoffatom gedreht. Die Länge des komplexen Anions sinkt von  $\sim 4.3 \text{ \AA}$  in den anderen Pyrocarbonaten auf  $\sim 3.6 \text{ \AA}$  in  $\text{Ba}[\text{C}_2\text{O}_5]$ .<sup>[5,6,69]</sup> Kürzlich konnten wir ein gemischtes Al-Pyrocarbonat synthetisieren und dessen Struktur bestimmen.<sup>[85]</sup> In  $\text{Al}_2[\text{C}_2\text{O}_5][\text{CO}_3]_2$  liegen  $[\text{C}_2\text{O}_5]^{2-}$ -Gruppen neben  $[\text{CO}_3]^{2-}$ -Gruppen vor und die Geometrie der Pyro-Gruppe entspricht in etwa der in  $\text{Sr}[\text{C}_2\text{O}_5]$  bzw.  $\text{Pb}[\text{C}_2\text{O}_5]$  (Abbildung 9). Chemisch gesehen schließen die hier entdeckten anorganischen Pyrocarbonate mit isolierten  $[\text{C}_2\text{O}_5]^{2-}$ -Gruppen die Lücke in der Systematik der Verbindungen mit Pyro-Gruppen ( $[\text{X}_2\text{O}_5]$  mit  $X = \text{B}, \text{C}, \text{N}$ ). Sowohl Pyroborate (z. B.  $\text{Mg}_2[\text{B}_2\text{O}_5]$ ,  $\text{Ca}_2[\text{B}_2\text{O}_5]$ ,  $\text{Sr}_2[\text{B}_2\text{O}_5]$ ) als auch molekulares Pyronitrat ( $\text{N}_2\text{O}_5$ ) sind bereits ausgiebig untersucht worden.<sup>[87–93]</sup>

In Abbildung 10 ist eine Zusammenfassung der durchgeführten Experimente in den verschiedenen  $M^{2+}[\text{CO}_3] - \text{CO}_2$  Systemen zu sehen. Geht man als Startmaterial von dem jeweiligen „konventionellen“ Carbonat mit Aragonit-Strukturtyp ( $KZ = 9$ ) aus, ist deutlich zu erkennen, dass die Carbonate mit kleineren Kationen ( $\text{Cd}, \text{Ca}$ ) zu  $sp^3$ -Carbonaten und solche mit größeren Kationen ( $\text{Sr}, \text{Pb}, \text{Ba}$ ) zu Pyrocarbonaten nach der Reaktion mit  $\text{CO}_2$  führen. Es ist jedoch zu bedenken, dass die stabile Phase der „konventionellen“ Carbonate bei diesen Drücken typischerweise in der post-Aragonit Struktur ( $KZ = 12$ ) vorliegt.<sup>[37,48]</sup> Insgesamt konnten wir zeigen, dass sich Carbonate bei hohen Drücken mit  $\text{CO}_2$  reagieren lassen und somit die Synthese neuer Carbonate möglich ist. Des Weiteren lassen

unsere Synthesen neue Carbonate zu, welche im  $M^{2+}[\text{CO}_3] - \text{CO}_2$  System näher am  $\text{CO}_2$  liegen (siehe Abbildung 3). Mit  $\text{Al}_2[\text{CO}_3]_3$  konnten wir ein neues „konventionelles“ Al-Carbonat aus einer  $\text{Al}_2\text{O}_3 + \text{CO}_2$  Mischung bei  $\sim 20$  GPa und  $\sim 2600$  K synthetisieren und zu Raumbedingungen abschrecken.<sup>[85]</sup> Trotz des kleinen Ionenradius von  $\text{Al}^{3+}$  ( $r = 0.54 \text{ \AA}$ ) passt das Elementarzellvolumen je Kohlenstoffatom von  $\text{Al}_2[\text{CO}_3]_3$  hervorragend in den Trend der bekannten Carbonate mit  $M^{2+}[\text{CO}_3]$  Zusammensetzung bei Raumbedingungen, wie in Abbildung 10 (b) zu sehen.<sup>[16]</sup>

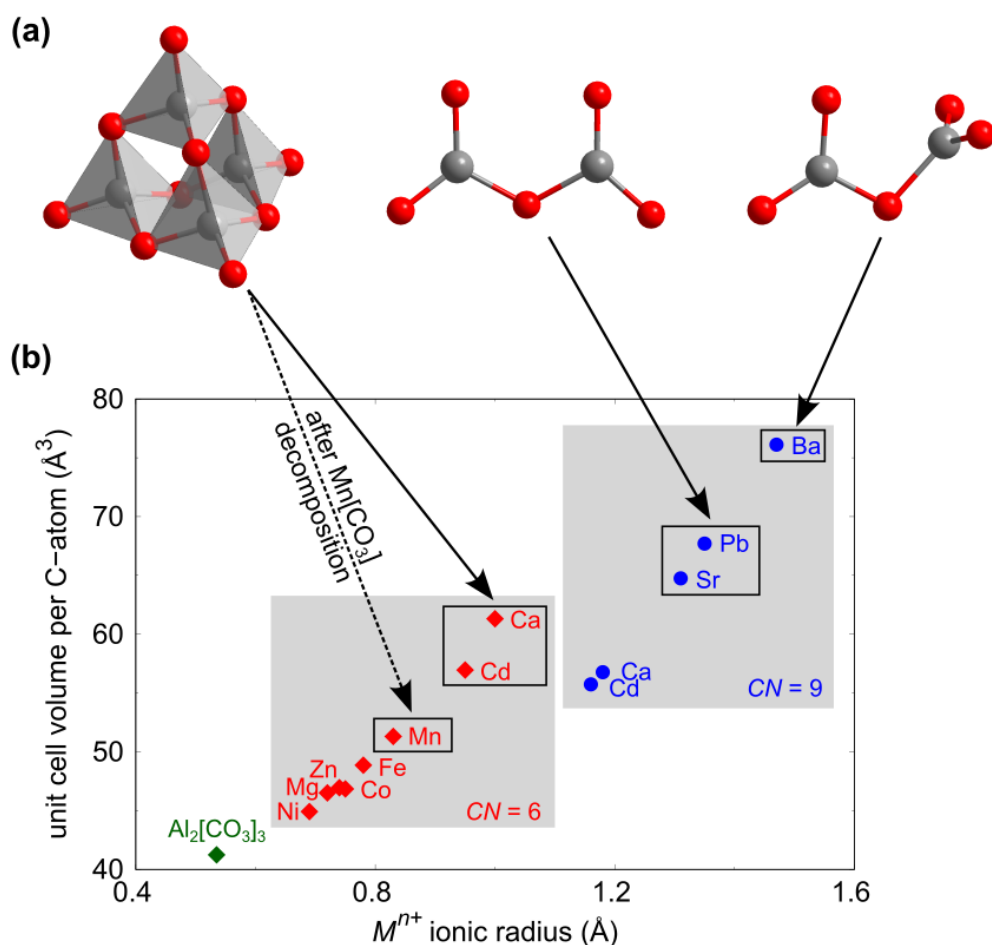


**Abbildung 10:** (a) Komplexe Anionen aus Kohlenstoff und Sauerstoff nach der Reaktion zwischen  $M^{2+}[\text{CO}_3]$  und  $\text{CO}_2$  bei hohen Drücken und hohen Temperaturen:  $[\text{C}_4\text{O}_{10}]$  ( $\text{CaC}_2\text{O}_5$ ,  $\text{CdC}_2\text{O}_5$ ),  $[\text{C}_2\text{O}_5]$  ( $\text{Sr}[\text{C}_2\text{O}_5]$ ,  $\text{Pb}[\text{C}_2\text{O}_5]$ ) und  $[\text{C}_2\text{O}_5]$  ( $\text{Ba}[\text{C}_2\text{O}_5]$ ).<sup>[5,6,77,86]</sup>  $\text{MnC}_2\text{O}_5$  mit  $[\text{C}_4\text{O}_{10}]$ -Pyramiden entstand nach der Zersetzung von  $\text{Mn}[\text{CO}_3]$  in Neon Atmosphäre.<sup>[29]</sup> (b) Elementarzellvolumen pro Kohlenstoffatom in Abhängigkeit des Kationenradius (nach Shannon<sup>[16]</sup>) für Carbonate mit  $M^{2+}[\text{CO}_3]$  Zusammensetzung in Calcit- ( $R\bar{3}c$ , Nr. 167) oder Aragonit-Strukturtyp ( $Pm\bar{c}n$ , Nr. 62).<sup>[17,19–21]</sup> Es wurden „konventionelle“ Carbonate als Startmaterialien für die Reaktionen in der LH-DAC verwendet.  $\text{Al}_2[\text{CO}_3]_3$  wurde aus einer  $\text{Al}_2\text{O}_3 + \text{CO}_2$  Mischung bei  $\sim 20$  GPa und  $\sim 2600$  K synthetisiert und dann zu Raumbedingungen abgeschreckt.<sup>[85]</sup>

### 3.2 Einbau von Seltenerdelementen in Carbonaten

Im zweiten Teil dieser Arbeit konnten wir zunächst einmal zeigen, dass das natürlich vorkommende  $\text{BaCa}[\text{CO}_3]_2$  Polymorph Barytocalcit hydrothermal synthetisiert werden kann.<sup>[71,94]</sup> Die Synthesebedingungen entsprechen dabei den Druck- und Temperatur-Bedingungen ( $\sim 500$  K und  $\sim 25$  bar) wie sie im obersten Bereich der Lithosphäre herrschen würden (Abbildung 6).<sup>[70,74]</sup> Des Weiteren konnten wir („C2-Phase“), genauso wie Whittaker und Joester<sup>[95]</sup> („Balcit“), einen neuen Polymorph synthetisieren. Zusätzlich zur Synthese über Ausfällung konnte wir auch dessen Bildung über Hochtemperatursynthese nach mechanochemischer Aktivierung der Endglieder ( $\text{Ba}[\text{CO}_3]$  und  $\text{Ca}[\text{CO}_3]$ ) in einer Kugelmühle oder direkt über Mechanosynthese zeigen.<sup>[71]</sup> Auf den ersten Blick sehen die Strukturen beider Phasen zwar identisch aus, jedoch zeigt „Balcit“ ein deutlich größeres Volumen pro  $[\text{CO}_3]^{2-}$ -Gruppe ( $V_{\text{CO}_3} = 72.88 \text{ \AA}^3$ ) im Vergleich zur „C2-Phase“ ( $68.20(1) \text{ \AA}^3$ ) bei gleichem Ba/Ca Verhältnis, wie in Abbildung 11 zu sehen.<sup>[72,95]</sup>

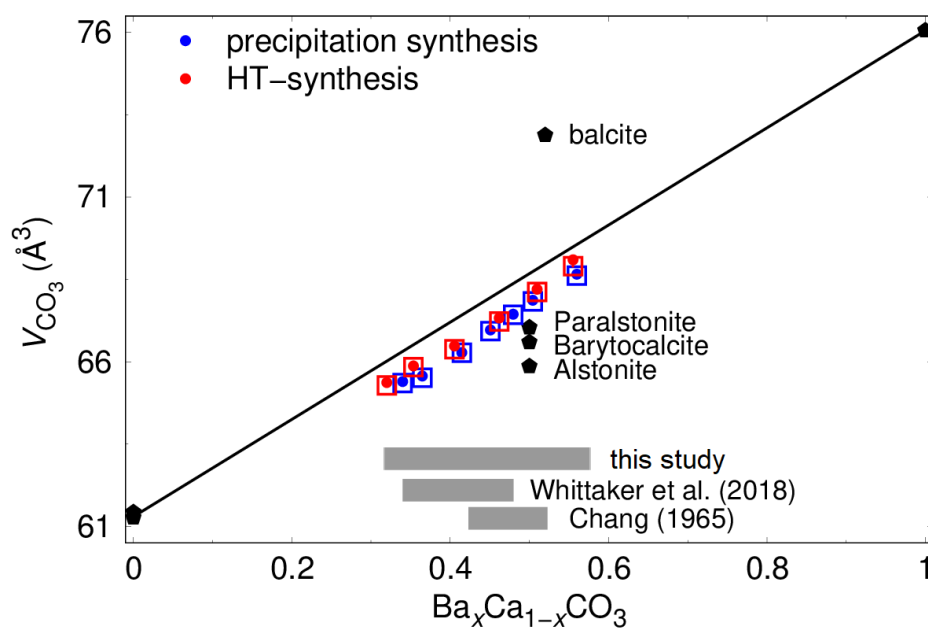


**Abbildung 11:** Elementarzellvolumen je  $[\text{CO}_3]^{2-}$ -Gruppe in  $\text{Ca}_{1-x}\text{Ba}_x[\text{CO}_3]$  nach Ausfällung bzw. Hochtemperatursynthese in Abhängigkeit der chemischen Zusammensetzung aus Synchrotron- (●) und Laborpulverdiffraktion (□).<sup>[72]</sup> Zum Vergleich sind die natürlich vorkommenden Polymorphe Barytocalcit, Paralstonit und Alstonit bzw. das synthetische Polymorph „Balcit“ eingetragen.<sup>[94–97]</sup> Es sind die Endglieder Calcit ( $\text{Ca}[\text{CO}_3]$ ) und Witherit ( $\text{Ba}[\text{CO}_3]$ ) gezeigt.<sup>[19,20]</sup> Die einphasigen Bereiche der bis jetzt untersuchten Mischkristallreihen sind ebenfalls aufgetragen.<sup>[58,61]</sup> Die Fehlerbalken sind kleiner als die Symbolgröße.

Weiterhin konnten wir zeigen, dass die hier über Ausfällung bzw. Hochtemperatursynthese erhaltenen  $\text{Ca}_{1-x}\text{Ba}_x[\text{CO}_3]$  Mischkristalle eine deutlich größere chemische Zusammensetzung abdecken und somit in einem größeren Bereich einphasig synthetisiert werden können als bisher angenommen.<sup>[58,61]</sup> Dabei liegt das Volumen nur knapp unterhalb des erwarteten Volumens für eine ideale Mischung zwischen  $\text{Ba}[\text{CO}_3]$  und  $\text{Ca}[\text{CO}_3]$ .<sup>[19,20]</sup> Es lässt sich sowohl in unseren Ausfällungsexperimenten als auch bei Whittaker et al.<sup>[61]</sup> ein leicht erniedrigtes Ba/Ca-Verhältnis im ausgefällten Carbonat im Vergleich zur initialen Lösung beobachten.<sup>[72]</sup> Im Gegensatz dazu führt die Hochtemperatursynthese nicht zu einer Abweichung zwischen eingewogenen Edukten und gemessener Zusammensetzung der Mischkristalle.

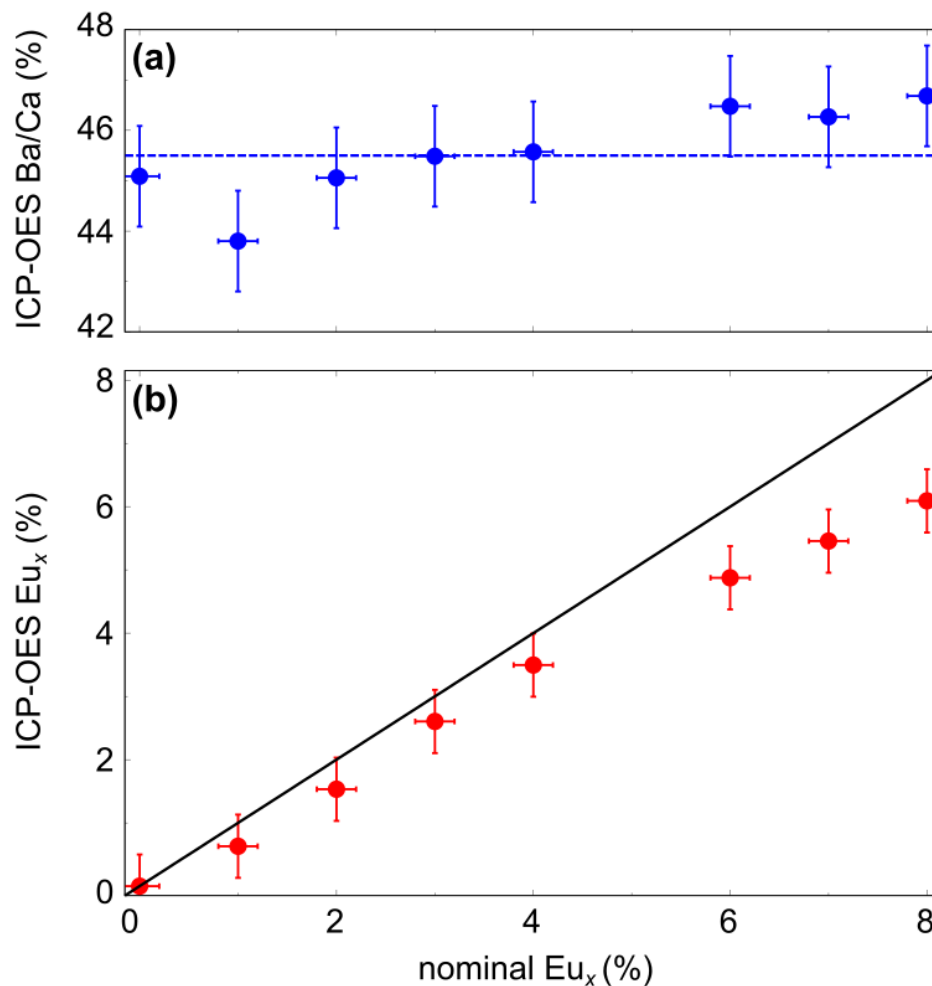


**Abbildung 12:** (a) ICP-OES Messungen des Ba/Ca-Verhältnisses und (b) Messungen der Europium-Konzentration in  $(\text{BaCa})_{(1-x)}[\text{CO}_3]_2 + \text{Eu}_x$  in Abhängigkeit der Europium-Konzentration der initialen Lösung vor der Ausfällung.<sup>[72]</sup> Die **blaue Strichlinie** markiert den Mittelwert der Messungen, die schwarze Linie ist eine Hilfslinie.

Durch die Zugabe von Europiumnitrat während der Ausfällungssynthese konnten wir demonstrieren, dass größere Mengen eines Seltenerdelements in das „konventionelle“ Ba/Ca-Doppelcarbonat eingebaut und somit Carbonate mit  $(\text{BaCa})_{(1-x)}[\text{CO}_3]_2 + \text{Eu}_x$  Zusammensetzung synthetisiert werden können.<sup>[72]</sup> Durch ICP-OES Messungen konnten wir zeigen, dass bei einer äquimolaren Ba/Ca-Konzentration in der Ausgangslösung ein Carbonat mit  $\text{Ba}_{0,9}\text{Ca}_{1,1}[\text{CO}_3]_2$  Zusammensetzung entsteht. Das Ba/Ca-Verhältnis ändert sich mit steigender Europium-Konzentration nicht signifikant (Abbildung 12 a). Mit steigender Europium-Konzentration in der Ausgangslösung kommt es auch zum verstärkten Einbau von Europium in  $\text{Ba}_{0,9}\text{Ca}_{1,1}[\text{CO}_3]_2$ . In Abbildung 12 (b) ist deutlich zu sehen, dass bis zu 6 mol% Europium in  $\text{Ba}_{0,9}\text{Ca}_{1,1}[\text{CO}_3]_2$  eingebaut werden konnten. Unsere Fluoreszenzmessungen mit einer Lebenszeit von 1 ms für die getesteten Übergänge in den verschiedenen Proben legen nahe, dass Europium überall auf den gleichen Gitterpositionen eingebaut wird. Des Weiteren würde diese Lebenszeit etwa einer  $\text{OH}^-$ -Gruppe in der Umgebung des  $\text{Eu}^{3+}$  entsprechen, ähnlich wie auch in  $\text{Ca}[\text{CO}_3]$ .<sup>[98-100]</sup> Das Vorhandensein von etwa einer  $\text{OH}^-$ -Gruppe pro  $\text{Eu}^{3+}$ -Ion würde zudem auch einen Ladungsausgleich bereitstellen.

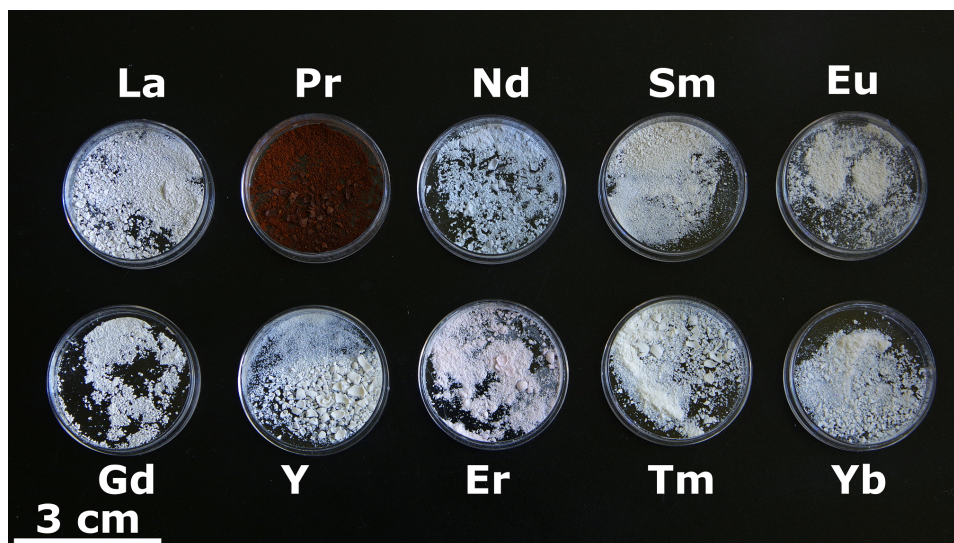


Abbildung 13:  $\text{Ba}_{0,9}\text{Ca}_{1,1}[\text{CO}_3]_2$  Pulver mit verschiedenen Seltenerdelementen nach der Ausfällungssynthese und anschließendem Erhitzen auf 723(1) K.<sup>[73]</sup>

Der Einbau von 6 mol% Europium in  $\text{Ba}_{0,9}\text{Ca}_{1,1}[\text{CO}_3]_2$  liegt deutlich oberhalb der Spurenelement-Konzentrationen in anderen Carbonaten. Sowohl in natürlich vorkommendem  $\text{Ca}[\text{CO}_3]$  als auch in  $\text{Mg}[\text{CO}_3]$  liegen die höchsten Konzentrationen für leichte Seltenerdelemente bei  $\leq 0.2\%$ .<sup>[101-103]</sup> Des Weiteren sind die Konzentrationen von Europium sowohl in synthetischem als auch

natürlich vorkommendem  $\text{Ca}[\text{CO}_3]$  erheblich geringer ( $\leq 0.1\%$ ).<sup>[62]</sup> Es ist hier anzumerken, dass Seltenerdcarbonate wie  $\text{Na}_3\text{Eu}[\text{CO}_3]_3$  durch hydrothermale Synthese erhalten werden können.<sup>[104]</sup> In weiteren Experimenten konnten wir zeigen, dass sich über Ausfällungssynthese auch eine Vielzahl weiterer Seltenerdelemente in  $\text{Ba}_{0.9}\text{Ca}_{1.1}[\text{CO}_3]_2$  einbauen lassen und somit Kationensubstitution der Ba/Ca-Atome durch viele verschiedene Elemente möglich ist.<sup>[73]</sup> Die geheizten Präzipitate dieser Synthesen sind in Abbildung 13 gezeigt. Je nach zugegebenem Seltenerdelement ist hier auch ein deutlicher Farbunterschied zu erkennen.

Der signifikante Einbau von Seltenerdelementen in  $\text{Ba}_{0.9}\text{Ca}_{1.1}[\text{CO}_3]_2$  während der Ausfällung legt die Vermutung nahe, dass sich dieses Doppelcarbonat auch bei der Ausfällung mit Actinoiden in der Ausgangslösung bilden kann. Somit würde sich bei Leckage eines Lagerbehälters in einem Endlager möglicherweise Ba/Ca-Carbonat mit eingebauten Actinoiden durch Reaktion mit dem vorhandenen Carbonat bilden. Da die Ausfällung hier aus Nitratlösungen vorgenommen wurde und die Carbonate bis zu höheren Temperaturen ( $\sim 723\text{ K}$ ) stabil sind, könnten diese möglicherweise auch zur Kristallisation von Lanthanoid- bzw. Actinoid-reichen Phasen aus der Aufbereitung von Kernbrennstoff verwendet werden. Als Ergebnis von Verfahren wie dem so genannten „Actinide Lanthanide Separation Process“ (ALSEP) entstehen unter anderem Lanthanoid- bzw. Actinoid-haltige Nitratlösungen, welche einer Ausfällung bedürfen.<sup>[105,106]</sup> Diese könnten dann über die Synthese von  $\text{Ba}_{0.9}\text{Ca}_{1.1}[\text{CO}_3]_2$  kristallisiert werden.

# 4 Summary and Conclusion

In the first part of this thesis we have synthesized several new carbonates at high pressures (20–30 GPa) and high temperatures (1500–3500 K) and investigated their structures. First, we obtained the  $sp^3$ -carbonate  $\text{Sr}_2[\text{CO}_4]$  at significantly lower pressures ( $\sim 20$  GPa) than reported earlier by a reaction of a  $\text{Sr}[\text{CO}_3]$  crystal with SrO powder in a laser-heated diamond anvil cell (LH-DAC).<sup>[4,41]</sup> Afterwards, we demonstrated that this carbonate with isolated  $[\text{CO}_4]^{4-}$ -tetrahedra can be recovered at ambient conditions using synchrotron powder X-ray diffraction, Raman spectroscopy and density functional theory (DFT) calculations. This was the first time that a carbonate with  $sp^3$ -hybridized carbon, in which carbon is tetrahedrally coordinated by four oxygen atoms, had been recovered at ambient conditions. With the synthesis and characterization of the antiperovskite  $\text{Sr}_3[\text{CO}_4]\text{O}$  we found a second  $sp^3$ -carbonate with isolated  $[\text{CO}_4]^{4-}$ -tetrahedra which can be recovered at ambient conditions.<sup>[68]</sup> This phase was synthesized in a similar manner as  $\text{Sr}_2[\text{CO}_4]$ . In addition, we observed a pressure-induced phase transition from tetragonal to orthorhombic space group symmetry upon pressure release in  $\text{Sr}_3[\text{CO}_4]\text{O}$ . The orthorhombic crystal structure at ambient pressure was solved by synchrotron-based X-ray single-crystal diffraction confirming the presence of isolated  $[\text{CO}_4]^{4-}$ -tetrahedra. These results are in good agreement with our Raman spectroscopy measurements and DFT-based calculations.

By the reaction of a  $\text{Sr}[\text{CO}_3]$  crystal with  $\text{CO}_2$  in a LH-DAC at  $\sim 30$  GPa we obtained the novel carbonate  $\text{Sr}[\text{C}_2\text{O}_5]$ .<sup>[5]</sup> With the synthesis of  $\text{Sr}[\text{C}_2\text{O}_5]$  we discovered a new family of carbonates called „inorganic pyrocarbonates“ beyond the well-known  $sp^2$ - and  $sp^3$ -carbonates. We solved the structure of  $\text{Sr}[\text{C}_2\text{O}_5]$  by synchrotron single crystal X-ray diffraction and characterized it by Raman spectroscopy and DFT-based calculations. In this compound, we observed for the first time the polymerization of two  $[\text{CO}_3]^{2-}$ -groups by sharing a central oxygen atom and the resulting formation of isolated  $[\text{C}_2\text{O}_5]^{2-}$ -groups. The discovery of the pyrocarbonate anion closes the gap in the periodic table between molecular  $\text{N}_2\text{O}_5$  and the pyroborates containing isolated  $[\text{B}_2\text{O}_5]^{4-}$ -groups (e. g.  $\text{Ca}_2[\text{B}_2\text{O}_5]$ ,  $\text{Sr}_2[\text{B}_2\text{O}_5]$ ).<sup>[87-93]</sup> In further experiments we synthesized

and characterized  $\text{Pb}[\text{C}_2\text{O}_5]$ , a second member of the inorganic pyrocarbonates, with isolated  $[\text{C}_2\text{O}_5]^{2-}$ -groups.<sup>[69]</sup>  $\text{Pb}[\text{C}_2\text{O}_5]$  was synthesized in a similar manner. The synthesis of isostructural  $\text{Pb}[\text{C}_2\text{O}_5]$  established the inorganic pyrocarbonates as a novel family of carbonates and demonstrated that cation substitution is possible in this group, similar to the family of  $sp^2$ - or  $sp^3$ -carbonates.

In the second part of this work we investigated Ba/Ca double carbonates. We found that the naturally occurring  $\text{BaCa}[\text{CO}_3]_2$  polymorph barytocalcite can be obtained by hydrothermal synthesis.<sup>[71,94]</sup> In addition, we and Whittaker and Joester<sup>[95]</sup> independently described a new  $\text{BaCa}[\text{CO}_3]_2$  polymorph. In contrast to Whittaker and Joester<sup>[95]</sup>, in our experiments the synthetic Ba/Ca-carbonate polymorph can be obtained by heating a mechanochemical-activated precursor, directly by mechanosynthesis from the end-member carbonates ( $\text{CaCO}_3$ ,  $\text{BaCO}_3$ ) in stoichiometric proportions or by slow precipitation synthesis at ambient conditions.<sup>[71]</sup> By synchrotron powder diffraction in combination with inductively coupled plasma optical emission spectrometry, Raman and fluorescence spectroscopy we demonstrated that this new Ba/Ca carbonate phase can incorporate significant amounts of europium (up to 6 mol%).<sup>[72]</sup> We assume that  $\text{Eu}^{3+}$  is incorporated on a lattice site after the precipitation synthesis and we expect a charge compensation due to the presence of approximately one  $\text{OH}^-$ -group per europium. Using equimolar Ba/Ca concentrations during the synthesis results in samples with  $\text{Ba}_{0.9}\text{Ca}_{1.1}[\text{CO}_3]_2 + \text{Eu}_x$  composition, independent from the Eu-concentration in the feed-solution. In further experiments we extended the incorporation of rare earth elements into  $\text{Ba}_{0.9}\text{Ca}_{1.1}[\text{CO}_3]_2$ .<sup>[73]</sup> We observed that incorporation of various rare earth elements in Ba/Ca double carbonate is possible. It seems most likely that radioactive actinides can be incorporated in this type of carbonate in case of a container failure in a nuclear waste disposal. Furthermore, this phase may be suitable for the solidification of actinide and lanthanide rich aqueous nitrate solution received from Actinide Lanthanide Separation (ALSEP) like processes, employed in the recycling procedures of spent nuclear fuel.<sup>[105,106]</sup>

# Literaturverzeichnis

- [1] W. Primak, H. Kaufman und R. Ward. X-Ray Diffraction Studies of Systems Involved in the Preparation of Alkaline Earth Sulfide and Selenide Phosphors. *J. Am. Chem. Soc.*, 70:2043–2046, **1948**. doi: 10.1021/ja01186a018.
- [2] A. Simon und K. Peters. Single-Crystal Refinement of the Structure of Carbon Dioxide. *Acta Cryst.*, B36:2750–2751, **1980**. doi: 10.1107/S0567740880009879.
- [3] W. L. Bragg. The structure of aragonite. *Proc. R. Soc. Lond.*, A105:16–39, **1924**. doi: 10.1098/rspa.1924.0002.
- [4] D. Spahr, J. König, L. Bayarjargal, R. Luchitskaia, W. Morgenroth, D. Comboni, V. Milman und B. Winkler. Tetrahedrally Coordinated  $sp^3$ -Hybridized Carbon in  $Sr_2CO_4$  Orthocarbonate at Ambient Conditions. *Inorg. Chem.*, 60: 5419–5422, **2021**. doi: 10.1021/acs.inorgchem.1c00159.
- [5] D. Spahr, J. König, L. Bayarjargal, V. Milman, A. Perlov, H.-P. Liermann und B. Winkler.  $Sr[C_2O_5]$  is an Inorganic Pyrocarbonate Salt with  $[C_2O_5]^{2-}$  Complex Anions. *J. Am. Chem. Soc.*, 144:2899–2904, **2022**. doi: 10.1021/jacs.2c00351.
- [6] D. Spahr, L. Bayarjargal, E. Haussühl, R. Luchitskaia, A. Friedrich, V. Milman, T. Fedotenko und B. Winkler. Twisted  $[C_2O_5]^{2-}$ -groups in  $Ba[C_2O_5]$  pyrocarbonate. *Chem. Commun.*, **under review**.
- [7] C.-T. A. Lee, H. Jiang, R. Dasgupta und M. Torres. *A Framework for Understanding Whole-Earth Carbon Cycling*, pages 313–357. Cambridge University Press, **2019**. doi: 10.1017/9781108677950.
- [8] V. Stagno, V. Cerantola, S. Aulbach, S. Lobanov, C. A. McCammon und M. Merlini. *Carbon-Bearing Phases throughout Earth's Interior*, pages 66–88. Cambridge University Press, **2019**. doi: 10.1017/9781108677950.

- [9] N. R. McKenzie, B. K. Horton, S. E. Loomis, D. F. Stockli, N. J. Planavsky und C.-T. A. Lee. Continental arc volcanism as the principal driver of icehouse-greenhouse variability. *Science*, 352:444–447, **2016**. doi: 10.1126/science.aad5787.
- [10] M. M. Hirschmann. Comparative deep Earth volatile cycles: The case for C recycling from exosphere/mantle fractionation of major (H<sub>2</sub>O, C, N) volatiles and from H<sub>2</sub>O/Ce, CO<sub>2</sub>/Ba, and CO<sub>2</sub>/Nb exosphere ratios. *EPSL*, 502:262–273, **2018**. doi: 10.1016/j.epsl.2018.08.023.
- [11] N. H. Sleep. Stagnant lid convection and carbonate metasomatism of the deep continental lithosphere. *Geochem Geophys*, 10:Q11010, **2009**. doi: 10.1029/2009GC002702.
- [12] C. Werner, T. P. Fischer, A. Aiuppa, M. Edmonds, C. Cardellini, S. Carn, G. Chiodini, E. Cottrell, M. Burton, H. Shinohara und P. Allard. *Carbon Dioxide Emissions from Subaerial Volcanic Regions*, pages 188–236. Cambridge University Press, **2019**. doi: 10.1017/9781108677950.
- [13] R. J. Reeder, editor. *Carbonates: Mineralogy and Chemistry*. De Gruyter, Berlin, Boston, **1983**. doi: 10.1515/9781501508134.
- [14] M. Okrusch und H. Frimmel. *Mineralogy: An Introduction to Minerals, Rocks, and Mineral Deposits*. Springer-Verlag, Berlin, **2020**. doi: 10.1007/978-3-662-57316-7.
- [15] B. Winkler, J. Zemmann und V. Milman. Aplanarity of CO<sub>3</sub> groups: A theoretical investigation. *Acta Cryst.*, B56:648–653, **2000**. doi: 10.1107/S0108768100003621.
- [16] R. D. Shannon. Revised effective ionic radii and systematic studies of interatomic distances in halides and chalcogenides. *Acta Cryst.*, A32:751–767, **1976**. doi: 10.1107/S0567739476001551.
- [17] L.-G. Liu und C.-C. Lin. A calcite → aragonite-type phase transition in CdCO<sub>3</sub>. *Am. Mineral.*, 82:643–646, **1997**. doi: 10.2138/am-1997-5-625.
- [18] D. Spahr, J. König, L. Bayarjargal, V. Milman, M. P. Persson und B. Winkler. Structural, Physical, and Thermodynamic Properties of Aragonitic Ca<sub>x</sub>Sr<sub>1-x</sub>CO<sub>3</sub> Solid Solutions. *J. Phys. Chem. C*, 125:17474–17481, **2021**. doi: 10.1021/acs.jpcc.1c04703.

- [19] H. Effenberger, K. Mereiter und J. Zemann. Crystal structure refinements of magnesite, calcite, rhodochrosite, siderite, smithonite, and dolomite, with discussion of some aspects of the stereochemistry of calcite type carbonates. *Z. Kristallogr.*, 156:233–243, **1981**. doi: 10.1524/zkri.1981.156.14.233.
- [20] S. M. Antao und I. Hassan. The orthorhombic structure of  $\text{CaCO}_3$ ,  $\text{SrCO}_3$ ,  $\text{PbCO}_3$  and  $\text{BaCO}_3$ : Linear structural trends. *Can. Mineral.*, 47:1245–1255, **2009**. doi: 10.3749/canmin.47.5.1245.
- [21] D. L. Graf. Crystallographic tables for the rhombohedral carbonates. *Am. Mineral.*, 46:1283–1316, **1961**.
- [22] R. Dasgupta und M. M. Hirschmann. The deep carbon cycle and melting in Earth's interior. *EPSL*, 298:1–13, **2010**. doi: 10.1016/j.epsl.2010.06.039.
- [23] P. B. Kelemen und C. E. Manning. Reevaluating carbon fluxes in subduction zones, what goes down, mostly comes up. *PNAS*, 11:E3997–E4006, **2015**. doi: 10.1073/pnas.1507889112.
- [24] L. Bayarjargal, C.-J. Fruhner, N. Schrodte und B. Winkler.  $\text{CaCO}_3$  phase diagram studied with Raman spectroscopy at pressures up to 50 GPa and high temperatures and DFT modeling. *Phys. Earth Planet. Inter.*, 281:31–45, **2018**. doi: 10.1016/j.pepi.2018.05.002.
- [25] J. Binck, S. Chariton, M. Stekiel, L. Bayarjargal, W. Morgenroth, V. Milman, L. Dubrovinsky und B. Winkler. High-pressure, high-temperature phase stability of iron-poor dolomite and the structures of dolomite-IIIc and dolomite-V. *Phys. Earth Planet. Inter.*, 299:106403, **2020**. doi: 10.1016/j.pepi.2019.106403.
- [26] J. Binck, L. Bayarjargal, S. S. Lobanov, W. Morgenroth, R. Luchitskaia, C. J. Pickard, V. Milman, K. Refson, D. B. Jochym, P. Byrne und B. Winkler. Phase stabilities of  $\text{MgCO}_3$  and  $\text{MgCO}_3$ -II studied by Raman spectroscopy, X-ray diffraction, and density functional theory calculations. *Phys. Rev. Mater.*, 4:055001, **2020**. doi: 10.1103/PhysRevMaterials.4.055001.
- [27] V. Cerantola, E. Bykova, I. Kuppenko, M. Merlini, L. Ismailova, C. McCammon, M. Bykov, A. I. Chumakov, S. Petitgirard, I. Kantor, V. Svitlyk, J. Jacobs, M. Hanfland, M. Mezouar, C. Prescher, R. Rüffer, V. B. Prakapenka und L. Dubrovinsky. Stability of iron-bearing carbonates in the deep Earth's interior. *Nat. Commun.*, 8:15960, **2017**. doi: 10.1038/ncomms15960.

- [28] C. Vennari, C. Beavers und Q. Williams. High-Pressure/Temperature Behavior of the Alkali/Calcium Carbonate Shortite ( $\text{Na}_2\text{Ca}_2(\text{CO}_3)_3$ ): Implications for Carbon Sequestration in Earth's Transition Zone. *J. Geophys. Res. Solid Earth*, 123:6574–6591, **2018**. doi: 10.1029/2018JB015846.
- [29] S. Chariton. *The elastic properties and the crystal chemistry of carbonates in the deep Earth*. PhD thesis, University of Bayreuth, **2020**.
- [30] E. Boulard, D. Pan, G. Galli, Z. Liu und W. L. Mao. Tetrahedrally coordinated carbonates in Earth's lower mantle. *Nat. Commun.*, 6:6311, **2015**. doi: 10.1038/ncomms7311.
- [31] M. Merlini, V. Cerantola, G. D. Gatta, M. Gemmi, M. Hanfland, I. Kupenko, P. Lotti, H. Müller und L. Zhang. Dolomite-IV: Candidate structure for a carbonate in the Earth's lower mantle. *Am. Mineral.*, 102:1763–1766, **2017**. doi: 10.2138/am-2017-6161.
- [32] A. R. Oganov, S. Ono, Y. Ma, C. W. Glass und A. Garcia. Novel high-pressure structures of  $\text{MgCO}_3$ ,  $\text{CaCO}_3$  and  $\text{CO}_2$  and their role in Earth's lower mantle. *EPSL*, 273:38–47, **2008**. doi: 10.1016/j.epsl.2008.06.005.
- [33] E. Boulard, A. Gloter, A. Corgne, D. Antonangeli, A.-L. Auzende, J.-P. Perrillat, F. Guyot und G. Fiquet. New host for carbon in the deep Earth. *PNAS*, 108:5184–5187, **2011**. doi: 10.1073/pnas.1016934108.
- [34] F. Maeda, E. Ohtani, S. Kamada, T. Sakamaki, N. Hirao und Y. Ohishi. Diamond formation in the deep lower mantle: A high-pressure reaction of  $\text{MgCO}_3$  and  $\text{SiO}_2$ . *Sci. Rep.*, 7:40602, **2017**. doi: 10.1038/srep40602.
- [35] M. Merlini, M. Hanfland, A. Salamat, S. Petitgirard und H. Müller. The crystal structures of  $\text{Mg}_2\text{Fe}_2\text{C}_4\text{O}_{13}$ , with tetrahedrally coordinated carbon, and  $\text{Fe}_{13}\text{O}_{19}$ , synthesized at deep mantle conditions. *Am. Mineral.*, 100: 2001–2004, **2015**. doi: 10.2138/am-2015-5369.
- [36] A. R. Oganov, C. W. Glass und S. Ono. High-pressure phases of  $\text{CaCO}_3$ : Crystal structure prediction and experiment. *EPSL*, 241:95–103, **2006**. doi: 10.1016/j.epsl.2005.10.014.
- [37] S. Ono, T. Kikegawa und Y. Ohishi. High-pressure transition of  $\text{CaCO}_3$ . *Am. Mineral.*, 92:1246–1249, **2007**. doi: 10.2138/am.2007.2649.

- [38] C. J. Pickard und R. J. Needs. Structures and stability of calcium and magnesium carbonates at mantle pressures. *Phys. Rev. B*, 91:104101, **2015**. doi: 10.1103/PhysRevB.91.104101.
- [39] S. S. Lobanov, X. Dong, N. S. Martirosyan, A. I. Samtsevich, V. Stevanovic, P. N. Gavryushkin, K. D. Litasov, E. Greenberg, V. B. Prakapenka, A. R. Oganov und A. F. Goncharov. Raman spectroscopy and X-ray diffraction of  $sp^3$ -CaCO<sub>3</sub> at lower mantle pressures. *Phys. Rev. B*, 96:104101, **2017**. doi: 10.1103/PhysRevB.96.104101.
- [40] D. Laniel. CCDC 2026976: Experimental Crystal Structure Determination. *CCDC, FIZ Karlsruhe*, **2020**. doi: 10.5517/ccdc.csd.cc2617bv.
- [41] D. Laniel, J. Binck, B. Winkler, S. Vogel, T. Fedotenko, S. Chariton, V. Prakapenka, V. Milman, W. Schnick, L. Dubrovinsky und N. Dubrovinskaja. Synthesis, crystal structure and structure-property relations of strontium orthocarbonate, Sr<sub>2</sub>CO<sub>4</sub>. *Acta Cryst.*, B77:131–137, **2021**. doi: 10.1107/S2052520620016650.
- [42] X. Yao, C. Xie, X. Dong, A. R. Oganov und Q. Zeng. Novel high-pressure calcium carbonates. *Phys. Rev. B*, 98:014108, **2018**. doi: 10.1103/PhysRevB.98.014108.
- [43] D. Sagatova, A. Shatskiy, N. Sagatova, P. N. Gavryushkin und K. D. Litasov. Calcium orthocarbonate, Ca<sub>2</sub>CO<sub>4</sub>-*Pnma*: A potential host for subducting carbon in the transition zone and lower mantle. *Lithos*, 370–371:105637, **2020**. doi: 10.1016/j.lithos.2020.105637.
- [44] P. N. Gavryushkin, D. Sagatova, N. Sagatova und K. D. Litasov. Formation of Mg-Orthocarbonate through the Reaction MgCO<sub>3</sub> + MgO = Mg<sub>2</sub>CO<sub>4</sub> at Earth's Lower Mantle *P – T* Conditions. *Cryst. Growth Des.*, 21:2986–2992, **2021**. doi: 10.1021/acs.cgd.1c00140.
- [45] P. N. Gavryushkin, D. N. Sagatova, N. Sagatov und K. D. Litasov. Orthocarbonates of Ca, Sr, and Ba — the appearance of  $sp^3$ -hybridized carbon at a pressure of 5 GPa and dynamic stability at ambient pressure. *Earth. Space. Chem.*, 5:1948–1957, **2021**. doi: 10.1021/acsearthspacechem.1c00084.

- [46] J. Binck, D. Laniel, L. Bayarjargal, S. Khandarkhaeva, T. Fedotenko, A. Aslandukov, K. Glazyrin, V. Milman, S. Chariton, V. B. Prakapenka, N. Dubrovinskaia, L. Dubrovinsky und B. Winkler. Synthesis of calcium ortho-carbonate,  $\text{Ca}_2\text{CO}_4$ -*Pnma* at *p, T*-conditions of Earth's transition zone and lowermantle. *Am. Mineral.*, 107:336–342, **2021**. doi: 10.2138/am-2021-7872.
- [47] A. Neuhaus. Synthese, Strukturverhalten und Valenzzustände der anorganischen Materie im Bereich hoher und höchster Drücke. *Chimia*, 18:93–103, **1964**.
- [48] N. Biedermann, S. Speziale, B. Winkler, H. J. Reichmann, M. Koch-Müller und G. Heide. High-pressure phase behavior of  $\text{SrCO}_3$ : An experimental and computational Raman scattering study. *Phys. Chem. Minerals*, 44: 335–343, **2017**. doi: 10.1007/s00269-016-0861-2.
- [49] H. P. Latscha und M. Mutz. *Chemie der Elemente: Chemie-Basiswissen IV*. Springer-Verlag, Berlin, Heidelberg, **2011**. doi: 10.1007/978-3-642-16915-1.
- [50] P. Delage und A.-M. Tang. Clays in radioactive waste disposal. *J. Rock Mech. Geotech. Eng.*, 2:111–123, **2010**. doi: 10.3724/SP.J.1235.2010.00111.
- [51] S. Norris. Radioactive waste confinement: clays in natural and engineered barriers — introduction. *Geol. Soc. Spec. Publ.*, 443:1–8, **2014**. doi: 10.1144/SP443.26.
- [52] M. De Craen, M. Van Geet, L. Wang und M. Put. High sulphate concentrations in squeezed Boom Clay porewater: evidence of oxidation of clay cores. *Phys. Chem. Earth*, 29:91–103, **2004**. doi: j.pce.2003.11.002.
- [53] M. Jedidi und O. Benjeddou. Chemical Causes of Concrete Degradation. *MOJ Civil. Eng.*, 4:00095, **2018**. doi: 10.15406/mojce.2018.04.00095.
- [54] W. Demtröder. *Experimentalphysik 4: Kern-, Teilchen- und Astrophysik*. Springer-Verlag, Berlin, Heidelberg, **2014**. doi: 10.1007/978-3-642-21476-9.
- [55] M. Volkmer. *Kernenergie Basiswissen*. Deutsches Atomforum e.V., Berlin, **2013**.
- [56] M.-M. Bé, V. Chisté, C. Dulieu, E. Browne, C. Baglin, V. Chechev, N. Kuzmenko, R. L. Helmer, F. Kondev und T. D. Macmahon. Table of radionuclides (Vol. 3: A = 3 to 244). *BIPM*, 3:cea-02476243, **2006**.

- [57] Y. Cao, L. Zhou, H. Ren und H. Zou. Determination, Separation and Application of  $^{137}\text{Cs}$ : A Review. *Int. J. Environ. Res. Public Health*, 19:10183, **2022**. doi: 10.3390/ijerph191610183.
- [58] L. L. Y. Chang. Subsolidus Phase Relations in the Systems  $\text{BaCO}_3\text{-SrCO}_3$ ,  $\text{SrCO}_3\text{-CaCO}_3$ , and  $\text{BaCO}_3\text{-CaCO}_3$ . *J. Geol.*, 73:346–368, **1965**. doi: 10.1086/627065.
- [59] L. L. Y. Chang. Subsolidus Phase Relations in the Aragonite-Type Carbonates: I.  $\text{CaCO}_3\text{-SrCO}_3\text{-BaCO}_3$ . *Am. Mineral.*, 56:1660–1673, **1971**.
- [60] W. R. Brice und L. L. Y. Chang. Subsolidus Phase Relations in Aragonite-type Carbonates. III. The System  $\text{MgCO}_3\text{-CaCO}_3\text{-BaCO}_3$ ,  $\text{MgCO}_3\text{-CaCO}_3\text{-SrCO}_3$  and  $\text{MgCO}_3\text{-SrCO}_3\text{-BaCO}_3$ . *Am. Mineral.*, 58:979–985, **1973**.
- [61] M. L. Whittaker, W. Sun, K. A. DeRocher, S. Jayaraman, G. Ceder und D. Joester. Structural Basis for Metastability in Amorphous Calcium Barium Carbonate (ACBC). *Adv. Funct. Mater.*, 28:1704202, **2018**. doi: 10.1002/adfm.201704202.
- [62] S. L. S. Stipp, J. T. Christensen, L. Z. Lakshtanov, J. A. Baker und T. E. Waight. Rare Earth element (REE) incorporation in natural calcite: Upper limits for actinide uptake in a secondary phase. *Radiochim. Acta*, 94:523–528, **2006**. doi: 10.1524/ract.2006.94.9.523.
- [63] A. Grandjean und G. Leturcq. Natural sintering of carbonate powder for use as a carbon-14 immobilization matrix. *J. Nucl. Mater.*, 345:11–18, **2005**. doi: 10.1016/j.jnucmat.2005.04.062.
- [64] N. Massoni, J. Rosen, M. Chartier und T. Cozzika. Study of barytocalcite as a conditioning matrix for carbon 14: Comparison of several synthesis routes. *J. Nuc. Mater.*, 441:152–158, **2013**. doi: 10.1016/j.jnucmat.2013.06.003.
- [65] N. Massoni, C. Marcou, J. Rosen, M. Chartier und P. Jollivet. The use of barytocalcite for carbon 14 immobilization: One-year leaching behavior. *J. Nuc. Mater.*, 454:230–237, **2014**. doi: 10.1016/j.jnucmat.2014.07.077.
- [66] N. Massoni, S. Le Gallet, S. Hoffmann, Launeau. P., Y. Grin und F. Bernard. Sintering of synthetic barytocalcite  $\text{BaCa}(\text{CO}_3)_2$ , kutnahorite  $\text{CaMn}(\text{CO}_3)_2$  and rhodochrosite  $\text{MnCO}_3$  for carbon-14 sequestration. *J. Eur. Ceram. Soc.*, 35:297–308, **2015**. doi: 10.1016/j.jeurceramsoc.2014.08.002.

- [67] N. Massoni und S. Le Gallet. Investigation of the sintering of barytocalcite with  $\text{BaCO}_3$  as a secondary phase for immobilizing carbon-14. *J. Nuc. Mater.*, 476:13–19, **2016**. doi: 10.1016/j.jnucmat.2016.04.031.
- [68] D. Spahr, J. König, L. Bayarjargal, P. N. Gavryushkin, H.-P. Liermann, V. Milman und B. Winkler.  $\text{Sr}_3[\text{CO}_4]\text{O}$ -antiperovskite with tetrahedrally-coordinated  $sp^3$ -hybridized carbon and  $\text{OSr}_6$ -octahedra. *Inorg. Chem.*, 60: 14504–14508, **2021**. doi: 10.1021/acs.inorgchem.1c01900.
- [69] D. Spahr, J. König, L. Bayarjargal, R. Luchitskaia, V. Milman, A. Perlov, H.-P. Liermann und B. Winkler. Synthesis and Structure of  $\text{Pb}[\text{C}_2\text{O}_5]$ : An Inorganic Pyrocarbonate Salt. *Inorg. Chem.*, 61:9855–9859, **2022**. doi: 10.1021/acs.inorgchem.2c01507.
- [70] P. J. Linstrom und W. G. Mallard. The NIST Chemistry WebBook: A Chemical Data Resource on the Internet. *J. Chem. Eng. Data*, 46:1059–1063, **2001**. doi: 10.1021/je000236i. (*Thermophysical properties of fluids*).
- [71] D. Spahr, L. Bayarjargal, V. Vinograd, R. Luchitskaia, V. Milman und B. Winkler. A new  $\text{BaCa}(\text{CO}_3)_2$  polymorph. *Acta Cryst.*, B75:291–300, **2019**. doi: 10.1107/S2052520619003238.
- [72] D. Spahr, L. Bayarjargal, V. Vinograd, M. Etter, J. Raddatz und B. Winkler. Incorporation of Europium into  $(\text{Ba,Ca})_2(\text{CO}_3)_2$ . *J. Solid State Chem.*, 307: 122759, **2022**. doi: 10.1016/j.jssc.2021.122759.
- [73] D. Spahr, L. Bayarjargal, V. Vinograd, R. Luchitskaia und B. Winkler. Incorporation of rare earth elements into  $(\text{Ba,Ca})_2(\text{CO}_3)_2$ . *Solid State Sci.*, 139: 107129, **2023**. doi: 10.1016/j.solidstatesciences.2023.107129.
- [74] A. M. Dziewonski und D. L. Anderson. Preliminary reference Earth model. *Phys. Earth Planet. Inter.*, 25:297–356, **1981**. doi: 10.1016/0031-9201(81)90046-7.
- [75] A. Zeidler und W. A. Crichton. Materials under pressure. *MRS Bull.*, 42: 710–713, **2001**. doi: 10.1557/mrs.2017.208.
- [76] J. König. *Phasenstabilität und Strukturen von Karbonaten bei den Druck-Temperatur-Bedingungen des Erdmantels*. PhD thesis, Johann Wolfgang Goethe-Universität, **2021**.

- [77] J. König, D. Spahr, L. Bayarjargal, P. N. Gavryushkin, V. Milman, H.-P. Liermann und B. Winkler. Novel calcium  $sp^3$ -carbonate  $\text{CaC}_2\text{O}_5$ - $I\bar{4}2d$  may be a carbon host in Earth's lower mantle. *Earth. Space. Chem.*, 6:73–80, **2022**. doi: 10.1021/acsearthspacechem.1c00284.
- [78] T. Bohem und D. Mehta. Ester der Pyrokohlensäure. *Chem. Ber.*, 71: 1797–1802, **1938**. doi: 10.1002/cber.19380710904.
- [79] F. Solymosy, I. Fedorcsák, A. Gulyás, G. Farkas und L. Ehrenberg. A new method based on the use of diethyl pyrocarbonate as a nuclease inhibitor for the extraction of undegraded nucleic acid from plant tissues. *Eur. J. Biochem.*, 5:520–527, **1968**. doi: 10.1111/J.1432-1033.1968.TB00401.X.
- [80] W. C. Summers. A simple method for extraction of RNA from *E. coli* utilizing diethyl pyrocarbonate. *Anal. Biochem.*, 33:459–463, **1970**. doi: 10.1016/0003-2697(70)90316-7.
- [81] R. Dalpozzo, G. Bartoli, M. Bosco, P. Melchiorre und L. Sambri. Recent Development about the Use of Pyrocarbonates as Activator in Organic Synthesis: A Review. *Curr. Org. Synth.*, 336:79–101, **2009**. doi: 10.2174/157017909787314867.
- [82] B. An, Y. Meng, Z. Li, Y. Hong, T. Wang, S. Wang, J. Lin, C. Wang, S. Wan, Y. Wang und W. Lin. A pyrocarbonate intermediate for  $\text{CO}_2$  activation and selective conversion in bifunctional metal-organic frameworks. *J. Catal.*, 373:37–47, **2019**. doi: 10.1016/j.jcat.2019.03.008.
- [83] L. Zhang, X. Huang, C. Qin, K. Brinkman, Y. Gong, S. Wang und K. Huang. First Spectroscopic Identification of Pyrocarbonate for High  $\text{CO}_2$  Flux Membranes Containing Highly Interconnected Three Dimensional Ionic Channels. *Phys. Chem. Chem. Phys.*, 15:13147–13152, **2013**. doi: 10.1039/c3cp52362d.
- [84] D. Corradini, F.-X. Coudert und R. Vuilleumier. Carbon dioxide transport in molten calcium carbonate occurs through an oxo-Grotthuss mechanism via a pyrocarbonate anion. *Nat. Chem.*, 8:454–460, **2016**. doi: 10.1038/nchem.2450.
- [85] L. Bayarjargal, D. Spahr, V. Milman, J. Marquardt, N. Giordano und B. Winkler. Anhydrous aluminium carbonates and isostructural compounds. *Inorg. Chem.*, **accepted**.

- [86] Y. Wang, L. Bayarjargal, D. Spahr, R. Luchitskaia, V. Milman und B. Winkler. Synthesis of  $\text{CdC}_2\text{O}_5$ . **in preparation**.
- [87] Y. Takéuchi. The crystal structure of magnesium pyroborate. *Acta. Cryst.*, 5:574–581, **1952**. doi: 10.1107/S0365110X52001623.
- [88] W.-S. Lin, W.-D. Cheng, J.-T. Chen und J.-S. Huang. Calcium pyroborate,  $\text{Ca}_2\text{B}_2\text{O}_5$ . *Acta. Cryst.*, C55:4–6, **1999**. doi: 10.1107/S0108270198010439.
- [89] S. Volkov, M. Dušek, R. Bubnova, M. Krzhizhanovskaya, V. Ugolkov, E. Obózova und S. Filatov. Orientational order-disorder  $\gamma \leftrightarrow \beta \leftrightarrow \alpha' \leftrightarrow \alpha$  phase transitions in  $\text{Sr}_2\text{B}_2\text{O}_5$  pyroborate and crystal structures of  $\beta$  and  $\alpha$  phases. *Acta. Cryst.*, B73:1056–1067, **2017**. doi: 10.1107/S2052520617012689.
- [90] I. C. Hisatsune, J. P. Devlin und Y. Wada. Vibrational spectrum and structure of  $\text{N}_2\text{O}_5$ . *Spectrochim. Acta*, 18:1641–1653, **1962**. doi: 10.1016/0371-1951(62)80028-9.
- [91] A. M. Shams El Din und A. A. El hosary. Pyronitrate: a new anion of pentavalent nitrogen. *J. inorg. nucl. Chem.*, 28:3043–3045, **1966**. doi: 10.1016/0022-1902(66)80032-5.
- [92] B. W. McClelland, L. Hedberg, K. Hedberg und K. Hagen. Molecular Structure of  $\text{N}_2\text{O}_5$  in the Gas Phase. Large Amplitude Motion in a System of Coupled Rotors. *J. Am. Chem. Soc.*, 105:3789–3793, **1983**. doi: 10.1021/ja00350a006.
- [93] B. M. McClelland, A. D. Richardson und K. Hedberg. A Reinvestigation of the Structure and Torsional Potential of  $\text{N}_2\text{O}_5$  by GasPhase Electron Diffraction Augmented by *AbInitio* Theoretical Calculations. *Helv. Chim. Acta*, 84:1612–1624, **2001**. doi: 10.1002/1522-2675(20010613)84:63.0.CO;2-K.
- [94] B. Dickens und J. S. Bowen. The Crystal Structure of  $\text{BaCa}(\text{CO}_3)_2$  (barytocalcite). *J. Res. Nat. Bur. Stand.*, 75A:197–203, **1971**. doi: 10.6028/jres.075A.020.
- [95] M. L. Whittaker und D. Joester. ACBC to Balcite: Bioinspired Synthesis of a Highly Substituted High-Temperature Phase from an Amorphous Precursor. *Adv. Mater.*, 29:1606730, **2017**. doi: 10.1002/adma.201606730.
- [96] H. Effenberger. The crystal structure of the mineral paralstonite,  $\text{BaCa}(\text{CO}_3)_2$ . *N. Jb. Miner. Mh.*, pages 353–363, **1980**.
- [97] F. Sartori. New data on alstonit. *Lithos*, 8:199–207, **1975**.

- [98] W. D. Horrocks und D. R. Sudnick. Lanthanide ion probes of structure in biology — Laser-Induced Luminescence decay constants provide a direct measure of the number of metal-coordinated water-molecules. *J. Am. Chem. Soc.*, 101:334–340, **1979**. doi: 10.1021/ja00496a010.
- [99] M. Marques Fernandes, M. Schmidt, C. Walther, D. Bosbach und R. Klenze. Site-selective time-resolved laser fluorescence spectroscopy of  $\text{Eu}^{3+}$  in calcite. *J. Colloid. Interface. Sci.*, 321:323–331, **2008**. doi: j.jcis.2008.01.017.
- [100] S. E. Hellebrandt, S. Hofmann, N. Jordan, A. Barkleit und M. Schmidt. Incorporation of Eu(III) into Calcite under Recrystallization conditions. *Sci. Rep.*, 6:33137, **2016**. doi: 10.1038/srep33137.
- [101] I. M. Kjarsgaard. Rare Earth Elements in Sovietic Carbonatites and their Mineral Phase. *J. Petrol.*, 39:2105–2121, **2007**. doi: 10.1093/petroj/39.11-12.2105.
- [102] A. R. Chakhmouradian, C. O. Böhm, A. Demény, E. P. Reguir, E. Hegner, R. A. Creaser, N. M. Halden und P. Yang. „Kimberlite“ from Wekusko Lake, Manitoba: actually a diamond-indicator-bearing dolomite carbonatite. *Lithos*, 112:347–357, **2009**. doi: 10.1016/j.lithos.2009.03.039.
- [103] A. R. Chakhmouradian, E. P. Reguir, C. Couëslan und P. Yang. Calcite and dolomite in intrusive carbonatites. II. Trace-element variations. *Miner. Petrol.*, 110:361–377, **2016**. doi: 10.1007/s00710-015-0392-4.
- [104] N. Mercier, M. Leblanc, E. Antic-Fidancev und M. Lemaitre-Blaise. Structural and Optical Investigations of Sodium Europium Carbonate  $\text{Na}_3\text{Eu}(\text{CO}_3)_3$ . *J. Solid State Chem.*, 132:33–40, **1997**. doi: 10.1006/jssc.1997.7400.
- [105] A. V. Gelis, P. Kozak, A. T. Breshears, M. A. Brown, C. Launier, E. L. Campbell, G. B. Hall, V. E. Levitskaia, T. G. and Holfeltz und G. J. Lumetta. Closing the Nuclear Fuel Cycle with a Simplified Minor Actinide Lanthanide Separation Process (ALSEP) and Additive Manufacturing. *Sci. Rep.*, 9: 12842, **2019**. doi: 10.1038/s41598-019-48619-x.
- [106] A. Wilden, F. Kreft, D. Schneider, Z. Pappas, G. Modolo, G. J. Lumetta, A. V. Gelis, J. D. Law und A. Geist. Countercurrent Actinide Lanthanide Separation Process (ALSEP) Demonstration Test with a Simulated PUREX Raffinate in Centrifugal Contactors on the Laboratory Scale. *Appl. Sci.*, 10: 7217, **2020**. doi: 10.3390/app10207217.



# Anhang

Im nachfolgenden Anhang sind die veröffentlichten Manuskripte aufgeführt, welche Teil dieser kumulativen Dissertation sind. Sie sind unverändert im Stil der jeweiligen Fachzeitschrift eingefügt:

Seiten	Manuskript
46–49	Tetrahedrally Coordinated $sp^3$ -Hybridized Carbon in $Sr_2CO_4$ Orthocarbonate at Ambient Conditions
50–54	$Sr_3[CO_4]O$ -Antiperovskite with Tetrahedrally Coordinated $sp^3$ -Hybridized Carbon and $OSr_6$ -Octahedra
55–60	$Sr[C_2O_5]$ is an Inorganic Pyrocarbonate Salt with $[C_2O_5]^{2-}$ Complex Anions
61–65	Synthesis and Structure of $Pb[C_2O_5]$ : An Inorganic Pyrocarbonate Salt
66–75	A new $BaCa(CO_3)_2$ polymorph
76–83	Incorporation of Europium into $(Ba,Ca)_2(CO_3)_2$
84–89	Incorporation of rare earth elements into $(Ba,Ca)_2(CO_3)_2$



## Tetrahedrally Coordinated $sp^3$ -Hybridized Carbon in $Sr_2CO_4$ Orthocarbonate at Ambient Conditions

Dominik Spahr,\* Jannes Binck, Lkhamsuren Bayarjargal, Rita Luchitskaia, Wolfgang Morgenroth, Davide Comboni, Victor Milman, and Björn Winkler

Cite This: *Inorg. Chem.* 2021, 60, 5419–5422

Read Online

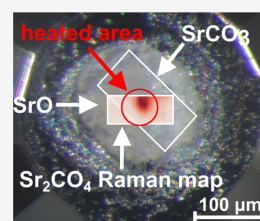
ACCESS |

Metrics & More

Article Recommendations

Supporting Information

**ABSTRACT:** We have synthesized the orthocarbonate  $Sr_2CO_4$ , in which carbon is tetrahedrally coordinated by four oxygen atoms, at moderately high pressures [20(1) GPa] and high temperatures ( $\approx 3500$  K) in a diamond anvil cell by reacting a  $SrCO_3$  single crystal with SrO powder. We show by synchrotron powder X-ray diffraction, Raman spectroscopy, and density functional theory calculations that this phase, and hence  $sp^3$ -hybridized carbon in a  $CO_4^{4-}$  group, can be recovered at ambient conditions. The C–O bond distances are all of similar lengths [ $\approx 1.41(1)$  Å], and the O–C–O angles deviate from the ideal tetrahedral angle by a few degrees only.



Carbonates play a fundamental role in the global carbon cycle and have therefore been extensively studied.<sup>1,2</sup> In nature, trigonal calcite ( $CaCO_3$ ), one of its high-pressure polymorphs, orthorhombic aragonite, and the “double carbonate” dolomite [ $CaMg(CO_3)_2$ ], dominate. They also are employed in numerous technological applications, such as in the deacidification and ion exchange of groundwater or its remineralization following reverse osmosis processes. Because of the flexibility of the structure, the divalent cations can be replaced, and numerous end members and solid solutions are known, where, as a general rule, replacement of  $Ca^{2+}$  by a cation with an ionic radius of  $\leq 1.0$  Å (e.g.,  $Mg^{2+}$ ,  $Co^{2+}$ , and  $Zn^{2+}$ ) will lead to a compound isostructural to calcite, while carbonates with larger divalent cations (e.g.,  $Sr^{2+}$ ,  $Ba^{2+}$ , and  $Pb^{2+}$ ) typically crystallize in the aragonite structure type.<sup>3</sup> Phase diagrams may be very rich for these carbonates because, for example, there are at least 12 high-pressure, high-temperature phases for  $CaCO_3$ .<sup>4</sup> The structure–property relationships of alkali carbonates, such as  $M_2CO_3$  with  $M = Li^+$ ,  $Na^+$ , and  $K^+$ , and of numerous other carbonates with more complex composition and structures, such as  $NaEu(CO_3)_2$  or  $UO_2CO_3$ , are also well established. Carbonates may also contain hydroxyl groups (such as in azurite), or molecular water.<sup>5,6</sup> In summary, carbonates display a remarkable crystal chemical and structural variability.

Until quite recently, it was thought that the common feature of all of these structurally and chemically distinct carbonates was the presence of isolated  $CO_3^{2-}$  groups. These  $CO_3^{2-}$  groups are generally considered to be fairly rigid structural units because they typically show only minor deviations from the average C–O bond length of 1.30 Å and an ideal O–C–O angle of  $120^\circ$ . This is thought to be due to the formation of strongly covalent bonds involving  $sp^2$ -hybridized orbitals of the

central carbon atom because the observed C–O bond length is between the 1.43 Å expected for a single bond and the 1.23 Å for a double bond. Notably, these  $CO_3^{2-}$  groups maintain their shape up to at least 70 GPa and 2000 K, and no polymerization of the  $CO_3^{2-}$  groups has been observed.

It was therefore an important discovery that under extreme pressure ( $p > 70$  GPa) and temperature conditions a fundamental change in bonding may occur, and in a sequence of papers, carbonates with  $sp^3$ -hybridized carbon in tetrahedral coordination were found. The first reports of such novel carbonates were based on synchrotron powder X-ray diffraction and in situ IR spectroscopy using either magnesite ( $MgCO_3$ ) or ferromagnesite ( $Mg_{0.25}Fe_{0.75}CO_3$ ) as starting compositions.<sup>7,8</sup> Further experimental confirmations were based on single-crystal X-ray diffraction studies, where the structures of  $Mg_2Fe_2^{III}C_4O_{13}$ - $C2/c$ ,<sup>9</sup>  $CaMg_{0.6}Fe_{0.4}C_2O_6$ - $Pnma$ ,<sup>10</sup>  $Mg_{2.53}Fe_{0.47}C_3O_9$ - $C2/m$ ,<sup>11</sup>  $Fe_4^{III}C_3O_{12}$ - $R3c$ ,<sup>12</sup>  $Fe_2^{II}Fe_2^{III}C_4O_{13}$ - $C2/c$ ,<sup>12</sup>  $Mn_2O_5$ - $Fd\bar{3}m$ ,<sup>11</sup> and  $Mn_4C_4O_{13}$ - $C2/c$ <sup>11</sup> were solved. It was found that, in analogy to  $SiO_4^{4-}$  groups,  $CO_4^{4-}$  groups may polymerize by corner-sharing an oxygen atom, forming rings, chains, or pyramids (e.g.,  $FeCO_3$  at  $\approx 70$  GPa,  $MgCO_3$  at  $\approx 85$  GPa, and  $CaCO_3$  at  $\approx 110$  GPa).<sup>12–14</sup> Very recently, strontium orthocarbonate,  $Sr_2CO_4$ , with space group  $Pnma$  was serendipitously synthesized at 92 GPa and 2500 K and its structure solved by single-crystal X-ray

Received: January 18, 2021

Published: April 4, 2021



diffraction but without further measurements during decompression.<sup>15</sup>

However, the extreme conditions ( $p > 70$  GPa in laser-heated diamond anvil cells, LH-DACs) required for the formation of  $sp^3$ -hybridized carbon and the experimental challenges involved in structure determination, in conjunction with the observation that these phases are only stable at very high pressures and cannot be quenched to ambient conditions, impeded the effort to explore the crystal chemistry and determine the structure–property relationships of carbonates containing  $sp^3$ -hybridized carbon.

More recently, theoretical studies have reported the formation of stable carbonates with  $CO_4^{4-}$  units in the system  $CaO-CO_2$  at much lower pressures, and it was proposed that  $Ca_3CO_3-Cmcm$  may become stable at pressures  $>11$  GPa, while  $Ca_2CO_4-Pnma$  was predicted to be stable at  $>13$  GPa.<sup>16,17</sup> We then synthesized calcium orthocarbonate ( $Ca_2CO_4-Pnma$ ) at 20 GPa by laser heating to  $>1800$  K and noted that, upon cold decompression, the phase was still present as long as the pressure was  $>4$  GPa.<sup>18</sup> This prompted us to attempt a synthesis of  $Sr_2CO_4$  at moderate pressures and to attempt a recovery to ambient conditions. The successful outcome of this experiment is described here.

In this study, we report the synthesis of  $Sr_2CO_4$  with space group  $Pnma$  in a LH-DAC using a strontianite ( $SrCO_3$ ) crystal and strontium oxide (SrO) powder as starting materials and the subsequent recovery at ambient conditions. The individual stages of the experiment are shown in Figure 1.

After a transparent  $SrCO_3$  crystal (edge length  $\approx 120$   $\mu m$ ) and white SrO powder were loaded and before the cell was closed, Raman spectroscopy showed the expected Raman spectrum of  $SrCO_3$  (Figure 2a). SrO crystallizes in the cubic space group  $Fm\bar{3}m$  ( $a = 5.160$  Å). It is isostructural to NaCl and, hence, does not show a first-order Raman signal.<sup>19</sup> As expected, the agreement between the experimental data and theoretical Raman spectra from density functional theory (DFT)-based calculations for  $SrCO_3$  at ambient conditions is very satisfactory, and no unexpected Raman modes can be observed in the experimental data. The  $SrCO_3 + SrO$  mixture was cold-compressed to 20(1) GPa (Figure 2b). Up to this pressure,  $SrCO_3$  is not undergoing any phase transition because the phase transition of  $SrCO_3$  to a polymorph with a post-aragonite structure (space group  $Pmnm$ ) is expected above 23 GPa.<sup>20</sup>

At a pressure of 20(1) GPa, the  $SrCO_3 + SrO$  mixture was laser-heated from both sides up to a maximum temperature of  $\approx 3500$  (500) K for several minutes in an area with  $\approx 50$   $\mu m$  diameter in the center of the DAC. During laser heating, the  $SrCO_3$  crystal and SrO powder melted completely and the crystal could not be identified anymore. After laser heating, the Raman spectrum at 20(1) GPa (Figure 2c) strongly differed from that of the cold-compressed  $SrCO_3 + SrO$  mixture at the same pressure. The characteristic  $CO_3$  stretching ( $\nu_1$ ) mode, which is expected at around  $\approx 1120$   $cm^{-1}$  at 20 GPa, disappeared, and instead a new mode occurred at  $\approx 920$   $cm^{-1}$ . This Raman mode indicates the presence of  $CO_4^{4-}$  groups. It is in good agreement with the Raman data obtained for the related carbonate  $Ca_2CO_4$ , for which this Raman mode occurs at  $\approx 936$   $cm^{-1}$ .<sup>18</sup> Furthermore, the experimental data at 20 GPa match the theoretical Raman spectra predicted by DFT-based calculations for  $Sr_2CO_4$  very well.<sup>15</sup>

After the synthesis of  $Sr_2CO_4$  at elevated pressure and temperature, we measured the Raman spectra during cold

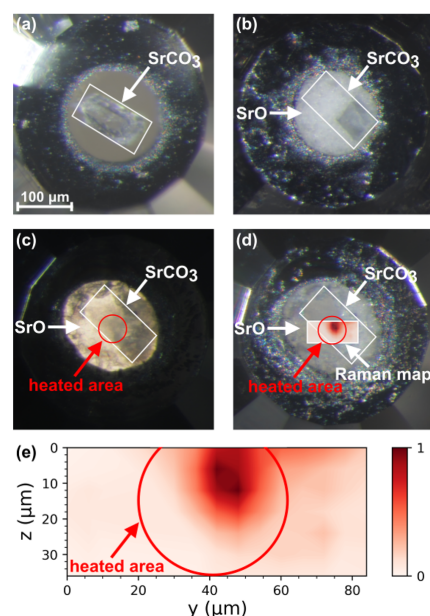


**Figure 1.** (a) Transparent  $SrCO_3$  single crystal placed on the culet. (b) SrO powder added, with neon loaded as a pressure-transmitting medium. (c) View through the LH-DAC, with transmitted light only. (d) View through the DAC, with transmitted and reflected light. A map showing the spatial distribution of the normalized intensity at  $885$   $cm^{-1}$  is superimposed on the area heated by the laser shown by a circle. The presence of  $CO_4^{4-}$  groups can be inferred from a characteristic band at this Raman shift. (e) Enlargement of the map from part d.

decompression (Figure 2d,e). We observed that  $Sr_2CO_4$  neither amorphises nor undergoes a structural phase transition upon decompression to ambient conditions (Figure 2e). This is in contrast to  $Ca_2CO_4$ , which seems to amorphise when the pressure is lowered to less than  $\approx 4$  GPa.<sup>18</sup>

At ambient conditions, we used Raman spectroscopy to map the laser-heated region and to determine where the  $Sr_2CO_4$  phase was formed during the heating process. Figure 1d,e show the intensity of the characteristic  $CO_4$  mode at  $885$   $cm^{-1}$ . The clear and strong maximum in this map at the center of the DAC shows that  $Sr_2CO_4$  was synthesized in the heated volume. These spectra were therefore the first demonstration of a carbonate with  $CO_4^{4-}$  units at ambient conditions.

To confirm these findings, we employed synchrotron powder X-ray diffraction. The diffraction pattern was recorded in the region where we had located  $Sr_2CO_4$  by Raman spectroscopy in an opened DAC after decompression. As starting values for the Rietveld refinement of the powder X-ray diffraction data (Figure 3), we employed structural parameters from DFT calculations, which, in turn, were derived by replacing Ca by Sr in the structure of  $Ca_2CO_4$ .<sup>15,18</sup> The successful refinement unequivocally confirms the conclusions drawn from the Raman measurements, namely, that we obtained the orthocarbonate  $Sr_2CO_4$  with space group  $Pnma$  and that this phase can be quenched to ambient conditions.

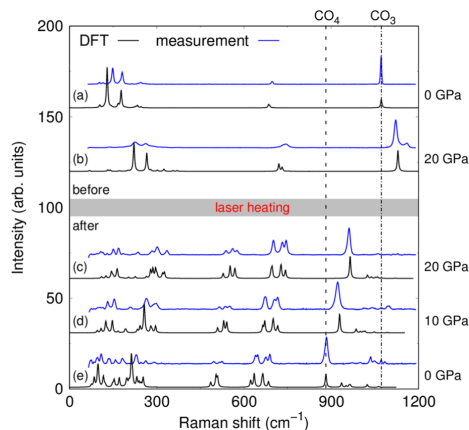


**Figure 2.** Experimentally determined Raman spectra for  $\text{Sr}_2\text{CO}_4$  synthesized at  $T_{\text{max}} \approx 3500(500)$  K and 20(1) GPa in a DAC in comparison to DFT-based calculations. Measurements were performed at ambient pressure and 20 GPa before the laser-heating process (a and b) and after heating (c–e) while the pressure was decreased to ambient conditions. The positions of the  $\text{CO}_3$  and  $\text{CO}_4$  stretching modes at ambient conditions are marked with dashed and dashed-dotted lines, respectively.

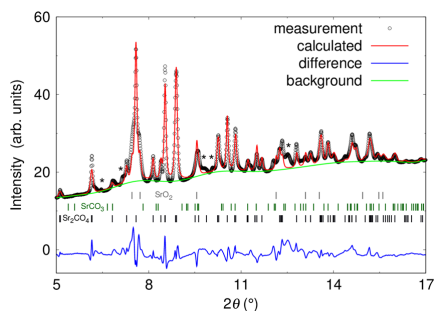


**Figure 3.** Rietveld refinement using the powder X-ray diffraction data of  $\text{Sr}_2\text{CO}_4$  obtained from the high-pressure and -temperature synthesis in a DAC at ambient conditions. The refinement was carried out in space group  $Pnma$  using  $\lambda = 0.4106$  Å. Reflection positions are indicated by tick marks, and the residuals between the measurement and refinement are shown by the blue line. Unidentified reflections are marked by an asterisk (\*).

The refined structural model of  $\text{Sr}_2\text{CO}_4$  is shown in Figure 4. We find that at ambient conditions  $\text{Sr}_2\text{CO}_4$  has the lattice parameters  $a = 6.9110(6)$  Å,  $b = 5.2942(6)$  Å, and  $c = 9.214(1)$  Å, in good agreement with the values predicted from DFT calculations  $a_{\text{DFT}} = 6.9398$  Å,  $b_{\text{DFT}} = 5.3254$  Å, and  $c_{\text{DFT}} = 9.3315$  Å (Table S1).  $\text{Sr}_2\text{CO}_4$  is isostructural to  $\text{Ca}_2\text{CO}_4$ . The experimentally determined C–O bond lengths [ $d_{\text{C-O,exp}} \approx 1.41(1)$  Å] are in very good agreement with the range calculated from DFT ( $d_{\text{C-O,DFT}} = 1.39$ – $1.43$  Å), where a Mulliken population analysis shows that all bonds are equally strongly covalent with a bond population of  $\approx 0.66 e^- \text{Å}^{-1}$ . The tetrahedral angles are very close to the ideal tetrahedral angle in the structure obtained from the Rietveld refinement, while in the DFT structure, they deviate by less than  $2^\circ$  from  $109.5^\circ$ .

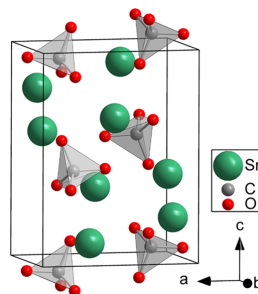


**Figure 4.** Crystal structure of  $\text{Sr}_2\text{CO}_4$  at ambient conditions obtained from Rietveld refinement of synchrotron powder X-ray diffraction with space group symmetry  $Pnma$ ,  $Z = 4$ ,  $a = 6.9110(6)$  Å,  $b = 5.2942(6)$  Å, and  $c = 9.214(1)$  Å.

In addition to  $\text{Sr}_2\text{CO}_4$ , we can identify unreacted  $\text{SrCO}_3$  or rather unlikely  $\text{SrO}_2$  in the diffraction pattern. Furthermore, a few tiny peaks cannot be associated with either  $\text{Sr}_2\text{CO}_4$ ,  $\text{SrCO}_3$ , or  $\text{SrO}_2$ . They are marked by an asterisk (\*) and may be due to reactions of the starting material with the diamonds or the formation of hydroxides or other new phases, which cannot be identified based on the small amount of weak reflections.

In conclusion, we synthesized  $\text{Sr}_2\text{CO}_4$  at 20(1) GPa and  $\approx 3500$  K in a LH-DAC by rapid cooling from a melt under high-pressure conditions. We demonstrated by Raman spectroscopy and synchrotron powder X-ray diffraction that this phase is quenchable to ambient conditions. DFT calculations show that  $\text{Sr}_2\text{CO}_4$  is metastable at ambient conditions because it is less stable by  $\approx 70$  kJ mol $^{-1}$  than the mixture of the starting materials. For hypothetical  $\text{Ba}_2\text{CO}_4$ , the enthalpy differences are similar, and thus it seems plausible that the approach described here can be used to introduce  $\text{Ba}^{2+}$  or  $\text{Pb}^{2+}$  into this structure. In conjunction with the earlier synthesis of isostructural  $\text{Ca}_2\text{CO}_4$ , where the cation is somewhat smaller, it now seems likely that it is possible to obtain numerous novel carbonates by isomorphous substitution, going far beyond the restricted chemistry of the 13 known novel carbonates, which contain one or two elements from the set {Mn, Fe, Mg, Ca, Sr}. The present study implies that at least some novel carbonates can be synthesized in milligram quantities in large volume presses. This is a major advancement because this will allow the use of a much broader range of analytical approaches (e.g., NMR, EELS) for characterization of their structure–property relationships.

## ASSOCIATED CONTENT

### Supporting Information

The Supporting Information is available free of charge at <https://pubs.acs.org/doi/10.1021/acs.inorgchem.1c00159>.

Synthesis process of  $\text{SrCO}_3$ , experimental and computational details of the experiments, and results of the Rietveld refinement (PDF)

### Accession Codes

CCDC 2056962 and 2056963 contain the supplementary crystallographic data for this paper. These data can be obtained free of charge via [www.ccdc.cam.ac.uk/data\\_request/cif](http://www.ccdc.cam.ac.uk/data_request/cif), or by emailing [data\\_request@ccdc.cam.ac.uk](mailto:data_request@ccdc.cam.ac.uk), or by contacting The

Cambridge Crystallographic Data Centre, 12 Union Road, Cambridge CB2 1EZ, UK; fax: +44 1223 336033.

## AUTHOR INFORMATION

### Corresponding Author

**Dominik Spahr** – Institute of Geosciences, Goethe University—Frankfurt, 60438 Frankfurt, Germany; [orcid.org/0000-0003-0489-5270](https://orcid.org/0000-0003-0489-5270); Email: [d.spahr@kristall.uni-frankfurt.de](mailto:d.spahr@kristall.uni-frankfurt.de)

### Authors

**Jannes Binck** – Institute of Geosciences, Goethe University—Frankfurt, 60438 Frankfurt, Germany

**Lkhamsuren Bayarjargal** – Institute of Geosciences, Goethe University—Frankfurt, 60438 Frankfurt, Germany

**Rita Luchitskaia** – Institute of Geosciences, Goethe University—Frankfurt, 60438 Frankfurt, Germany

**Wolfgang Morgenroth** – Institute of Geosciences, University of Potsdam, 14469 Potsdam, Germany

**Davide Comboni** – ESRF European Synchrotron, 38043 Grenoble 9, France

**Victor Milman** – Dassault Systèmes BIOVIA, CB4 0WN Cambridge, United Kingdom; [orcid.org/0000-0003-2258-1347](https://orcid.org/0000-0003-2258-1347)

**Björn Winkler** – Institute of Geosciences, Goethe University—Frankfurt, 60438 Frankfurt, Germany; [orcid.org/0000-0001-8029-478X](https://orcid.org/0000-0001-8029-478X)

Complete contact information is available at: <https://pubs.acs.org/10.1021/acs.inorgchem.1c00159>

### Notes

The authors declare no competing financial interest.

## ACKNOWLEDGMENTS

We thank Michael Hanfland (ESRF) for the provision of beam time at beamline ID15B. We gratefully acknowledge funding from the DFG (Projects Wi1232 and Ba4020), the DFG-Research Unit FOR2125/CarboPaT, and the BMBF (Project 05K19IP2). B.W. is grateful for support by the BIOVIA Science Ambassador program.

## REFERENCES

- Reeder, R. J., Ed. *Carbonates: Mineralogy and Chemistry*; De Gruyter: Berlin, 1983; DOI: [10.1515/9781501508134](https://doi.org/10.1515/9781501508134).
- Hazen, R. M.; Jones, A. P.; Baross, J. A., Eds. *Carbon in Earth*; De Gruyter: Berlin, 2013; DOI: [10.1515/9781501508318](https://doi.org/10.1515/9781501508318).
- Liu, L.-G.; Lin, C.-C. A calcite → aragonite-type phase transition in CdCO<sub>3</sub>. *Am. Mineral.* **1997**, *82*, 643–646.
- Bayarjargal, L.; Fruhner, C.-J.; Schrod, N.; Winkler, B. CaCO<sub>3</sub> phase diagram studied with Raman spectroscopy at pressures up to 50 GPa and high temperatures and DFT modeling. *Phys. Earth Planet. Inter.* **2018**, *281*, 31–45.
- Marschner, H. Hydrocalcite (CaCO<sub>3</sub> · H<sub>2</sub>O) and Nesquehonite (MgCO<sub>3</sub> · 3H<sub>2</sub>O) in Carbonate Scales. *Science* **1969**, *165*, 1119–1121.
- Rule, K. C.; Reehuis, M.; Gibson, M. C. R.; Ouladdiaf, B.; Gutmann, M. J.; Hoffmann, J.-U.; Gerischer, S.; Tennant, D. A.; Süllow, S.; Lang, M. Magnetic and crystal structure of azurite Cu<sub>3</sub>(CO<sub>3</sub>)<sub>2</sub>(OH)<sub>2</sub> as determined by neutron diffraction. *Phys. Rev. B: Condens. Matter Mater. Phys.* **2011**, *83*, 104401.
- Boulard, E.; Gloter, A.; Corgne, A.; Antonangeli, D.; Auzende, A.-L.; Perrillat, J.-P.; Guyot, F.; Fiquet, G. New host for carbon in the deep Earth. *Proc. Natl. Acad. Sci. U. S. A.* **2011**, *108*, 5184–5187.
- Boulard, E.; Pan, D.; Galli, G.; Liu, Z.; Mao, W. L. Tetrahedrally coordinated carbonates in Earth's lower mantle. *Nat. Commun.* **2015**, *6*, 6311; DOI: [10.1038/ncomms7311](https://doi.org/10.1038/ncomms7311).
- Merlini, M.; Hanfland, M.; Salamat, A.; Petitgirard, S.; Müller, H. The crystal structures of Mg<sub>2</sub>Fe<sub>2</sub>C<sub>4</sub>O<sub>13</sub> with tetrahedrally coordinated carbon, and Fe<sub>13</sub>O<sub>19</sub>, synthesized at deep mantle conditions. *Am. Mineral.* **2015**, *100*, 2001–2004.
- Merlini, M.; Cerantola, V.; Gatta, G. D.; Gemmi, M.; Hanfland, M.; Kupenko, I.; Lotti, P.; Müller, H.; Zhang, L. Dolomite-IV: Candidate structure for a carbonate in the Earth's lower mantle. *Am. Mineral.* **2017**, *102*, 1763–1766.
- Chariton, S. The elastic properties and the crystal chemistry of carbonates in the deep Earth. Ph.D. Thesis, University of Bayreuth, Bayreuth, Germany, 2020.
- Cerantola, V.; et al. Stability of iron-bearing carbonates in the deep Earth's interior. *Nat. Commun.* **2017**, *8*, 15960.
- Binck, J.; Bayarjargal, L.; Lobanov, S. S.; Morgenroth, W.; Luchitskaia, R.; Pickard, C. J.; Milman, V.; Refson, K.; Jochym, D. B.; Byrne, P.; Winkler, B. Phase stabilities of MgCO<sub>3</sub> and MgCO<sub>3</sub>-II studied by Raman spectroscopy, X-ray diffraction, and density functional theory calculations. *Phys. Rev. Mater.* **2020**, *4*, 055001.
- Lobanov, S. S.; Dong, X.; Martirosyan, N. S.; Samtsevich, A. I.; Stevanovic, V.; Gavryushkin, P. N.; Litasov, K. D.; Greenberg, E.; Prakupenka, V. B.; Oganov, A. R.; et al. Raman spectroscopy and x-ray diffraction of sp<sup>3</sup> CaCO<sub>3</sub> at lower mantle pressures. *Phys. Rev. B: Condens. Matter Mater. Phys.* **2017**, *96*, 104101.
- Laniel, D.; Binck, J.; Winkler, B.; Vogel, S.; Fedotenko, T.; Chariton, S.; Prakupenka, V.; Milman, V.; Schnick, W.; Dubrovinsky, L.; Dubrovinskaia, N. Synthesis, crystal structure and structure-property relations of strontium orthocarbonate, Sr<sub>2</sub>CO<sub>4</sub>. *Acta Crystallogr., Sect. B* **2021**, *77*, 131–137.
- Yao, X.; Xie, C.; Dong, X.; Oganov, A. R.; Zeng, Q. Novel high-pressure calcium carbonates. *Phys. Rev. B: Condens. Matter Mater. Phys.* **2018**, *98*, 014108.
- Sagatova, D.; Shatskiy, A.; Sagatov, N.; Gavryushkin, P. N.; Litasov, K. D. Calcium orthocarbonate, Ca<sub>2</sub>CO<sub>4</sub>-Pnma: A potential host for subducting carbon in the transition zone and lower mantle. *Lithos* **2020**, *370–371*, 105637.
- Binck, J.; Laniel, D.; Bayarjargal, L.; Khandarkhaeva, S.; Fedotenko, T.; Aslandukov, A.; Glazyrin, K.; Milman, V.; Chariton, S.; Prakupenka, V. B.; Dubrovinskaia, N.; Dubrovinsky, L.; Winkler, B. Synthesis of calcium orthocarbonate, Ca<sub>2</sub>CO<sub>4</sub>-Pnma at P,T-conditions of Earth's transition zone and lowermantle. *Am. Mineral.* **2020** DOI: [10.2138/am-2021-7872](https://doi.org/10.2138/am-2021-7872).
- Liu, L.-G.; Bassett, A. A. Changes of the crystal structure and the lattice parameter of SrO at high pressure. *J. Geophys. Res.* **1973**, *78*, 8470–8473.
- Biedermann, N.; Speziale, S.; Winkler, B.; Reichmann, H. J.; Koch-Müller, M.; Heide, G. High-pressure phase behavior of SrCO<sub>3</sub>: an experimental and computational Raman scattering study. *Phys. Chem. Miner.* **2017**, *44*, 335–343.

# Inorganic Chemistry

pubs.acs.org/IC

Featured Article

## Sr<sub>3</sub>[CO<sub>4</sub>]O Antiperovskite with Tetrahedrally Coordinated sp<sup>3</sup>-Hybridized Carbon and OSr<sub>6</sub> Octahedra

Dominik Spahr,\* Jannes König, Lkhamsuren Bayarjargal, Pavel N. Gavryushkin, Victor Milman, Hanns-Peter Liermann, and Björn Winkler

Cite This: *Inorg. Chem.* 2021, 60, 14504–14508

Read Online

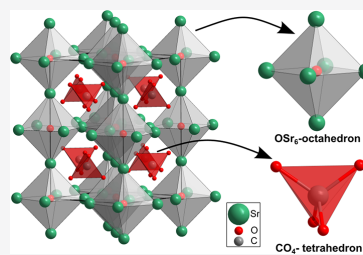
ACCESS |

Metrics &amp; More

Article Recommendations

Supporting Information

**ABSTRACT:** We have synthesized the orthocarbonate Sr<sub>3</sub>[CO<sub>4</sub>]O in a laser-heated diamond anvil cell at 20 and 30 GPa by heating to ≈3000 (300) K. Afterward, we recovered the orthocarbonate with [CO<sub>4</sub>]<sup>4−</sup> groups at ambient conditions. Single-crystal diffraction shows the presence of [CO<sub>4</sub>]<sup>4−</sup> groups, i.e., sp<sup>3</sup>-hybridized carbon tetrahedrally coordinated by covalently bound oxygen atoms. The [CO<sub>4</sub>]<sup>4−</sup> tetrahedra are located in a cage formed by corner-sharing OSr<sub>6</sub> octahedra, i.e., octahedra with oxygen as a central ion, forming an antiperovskite-type structure. At high pressures, the octahedra are nearly ideal and slightly rotated. The high-pressure phase is tetragonal (*I4/mcm*). Upon pressure release, there is a phase transition with a symmetry lowering to an orthorhombic phase (*Pnma*), where the octahedra tilt and deform slightly.



Carbonates are ubiquitous in nature and are employed in numerous technological applications. The defining structural feature of conventional carbonates is nearly trigonal-planar [CO<sub>3</sub>]<sup>2−</sup> groups, where a central carbon atom is coordinated by three oxygen atoms, forming C-sp<sup>2</sup> hybrid orbitals.<sup>1</sup> The [CO<sub>3</sub>]<sup>2−</sup> groups can be considered to be rigid units and persist to very high pressures (≈70 GPa). They generally do not polymerize by sharing an oxygen (an exception is, e.g., Na<sub>2</sub>Ca<sub>2</sub>[CO<sub>3</sub>]<sub>3</sub>, where an onset of dimerization is observed at 15 GPa),<sup>2</sup> so all conventional carbonate structures can be described in terms of the stacking of [CO<sub>3</sub>]<sup>2−</sup> groups.<sup>3–6</sup>

The synthesis of carbonates with tetrahedrally coordinated carbon was therefore a substantial extension of the carbonate crystal chemistry. Tetrahedral coordination implies the presence of C-sp<sup>3</sup> hybrid orbitals. Initially, such sp<sup>3</sup> carbonates were obtained as high-pressure polymorphs of conventional carbonates at very high pressures (*p* > 70 GPa) and high temperatures (a few thousand Kelvin) and were thought to exist only at these extreme conditions.<sup>5–17</sup> This situation changed when, instead of transforming carbonates by pressure, novel sp<sup>3</sup> carbonates were formed by reactions.<sup>18–21</sup> Guided by density functional theory (DFT)-based predictions,<sup>22–25</sup> alkaline-earth oxides were reacted with the corresponding carbonates at high temperatures and Sr<sub>2</sub>[CO<sub>4</sub>]-*Pnma* and isostructural Ca<sub>2</sub>[CO<sub>4</sub>]-*Pnma* were formed in a laser-heated diamond anvil cell (LH-DAC) at ≈20 GPa.<sup>19–21</sup>

Another interesting feature of novel carbonates with sp<sup>3</sup>-hybridized carbon is that the [CO<sub>4</sub>]<sup>4−</sup> groups may polymerize by corner-sharing. As a result, carbonates with isolated [CO<sub>4</sub>]<sup>4−</sup> tetrahedra or carbonates with groups, rings, chains, or pyramids can be formed (Figure 1). This structural variety is

reminiscent of the structural variability of silicates.<sup>26</sup> In addition to the [SiO<sub>4</sub>]<sup>4−</sup> tetrahedra of silicates, further orthoanions such as [PO<sub>4</sub>]<sup>3−</sup> (phosphates), [BO<sub>4</sub>]<sup>3−</sup> (borates), or [SO<sub>4</sub>]<sup>2−</sup> (sulfates) are key components in basic chemistry and well-known building blocks of various minerals.<sup>27</sup> The family of orthoanions was enlarged in the past by, e.g., determination of the structure of the orthonitrate Na<sub>3</sub>[NO<sub>4</sub>].<sup>28</sup>

In addition to the established orthoanions, it was recently predicted and experimentally shown that carbonates with [CO<sub>4</sub>]<sup>4−</sup> groups may even be recovered at ambient conditions.<sup>21,25</sup> Further, stable structures with stoichiometries M<sub>2</sub>[CO<sub>4</sub>] and M<sub>3</sub>[CO<sub>4</sub>]O (M = Mg, Ca, Sr, and Ba) have been predicted by DFT-based calculations.<sup>22–25</sup> Here, we report the successful outcome of the synthesis of one of these structures using M = Sr. In contrast to earlier syntheses, we obtained a carbonate with an antiperovskite structure, where the oxygen anion is coordinated by six Sr cations. With this finding, we are enlarging the crystal chemistry of compounds containing orthoanions, of carbonates, and also of the family of compounds with an antiperovskite structure.<sup>29</sup> Sr<sub>3</sub>[CO<sub>4</sub>]O was synthesized in a LH-DAC using a Sr[CO<sub>3</sub>] single crystal and SrO powder as starting materials and afterward recovered at ambient conditions.

Received: June 25, 2021

Published: September 14, 2021



ACS Publications

© 2021 American Chemical Society

14504

<https://doi.org/10.1021/acs.inorgchem.1c01900>  
*Inorg. Chem.* 2021, 60, 14504–14508

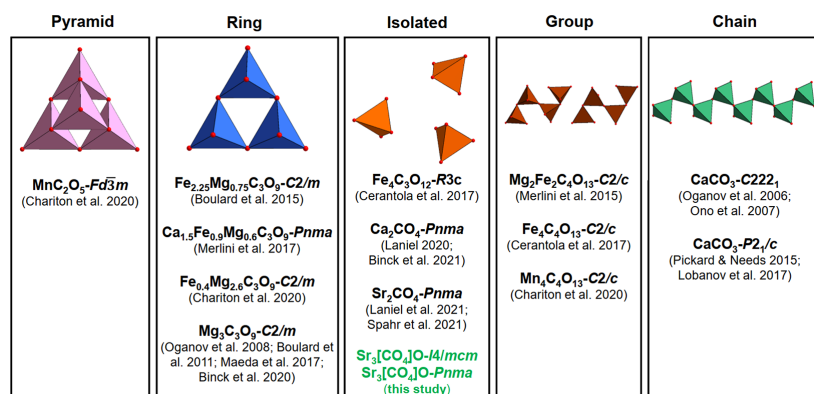


**Figure 1.** Structural variety of carbonates containing  $[\text{CO}_4]^{4-}$  groups. In addition to orthocarbonates with isolated  $[\text{CO}_4]^{4-}$  groups, the  $[\text{CO}_4]^{4-}$  tetrahedra can polymerize by corner-sharing to form carbonates with groups of  $[\text{CO}_4]^{4-}$  tetrahedra, chains, rings, or pyramidal groups.<sup>5–21</sup>

Figure 2a shows a  $\text{Sr}[\text{CO}_3]$  crystal at ambient conditions in a DAC. We used Raman spectroscopy to confirm the phase purity of our  $\text{Sr}[\text{CO}_3]$  crystals. Figure 3a shows a Raman

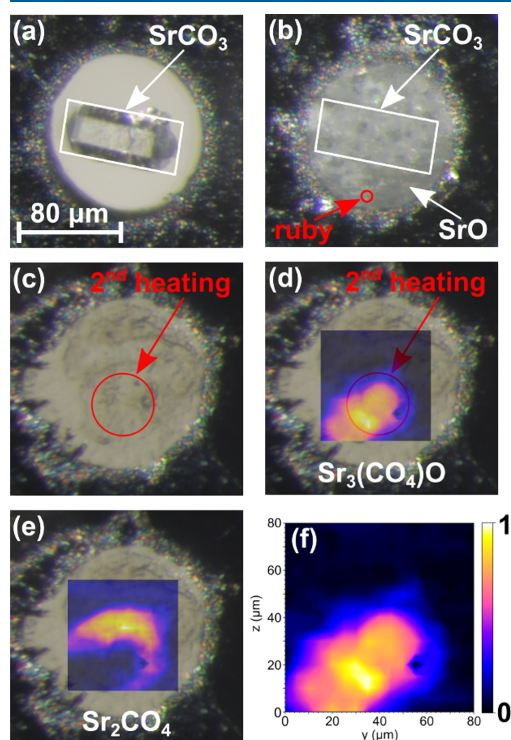


**Figure 2.** (a)  $\text{Sr}[\text{CO}_3]$  crystal placed in the culet's center. (b) SrO powder added and compressed in the gasket hole. A ruby is added. (c) Laser-heated sample. Raman maps for (d)  $\text{Sr}_3[\text{CO}_4]\text{O}$  and (e)  $\text{Sr}_2[\text{CO}_4]$ . (f) Enlargement of part d showing the presence of  $\text{Sr}_3[\text{CO}_4]\text{O}$  in the center of the area that had been laser-heated.

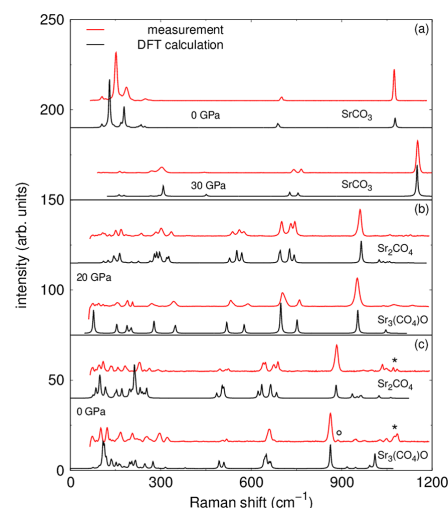


**Figure 3.** (a) Raman spectra for the  $\text{Sr}[\text{CO}_3] + \text{SrO}$  mixture in a DAC at 0 GPa ( $\text{Sr}[\text{CO}_3]$ ,  $Pm\bar{c}n$ ) and at 30(2) GPa ( $\text{Sr}[\text{CO}_3]$ ,  $Pm\bar{m}n$ ) in comparison to DFT-based calculations. Raman spectra for  $\text{Sr}_3[\text{CO}_4]\text{O}$  and  $\text{Sr}_2[\text{CO}_4]$  synthesized at 20(1) GPa in a DAC in comparison to DFT-based calculations at 20(1) GPa (b) and ambient conditions (c). The frequencies of the calculated Raman spectra were rescaled by 3%. The position of the  $[\text{CO}_3]$  stretching mode is marked by an asterisk, and the position of the characteristic  $[\text{CO}_4]$  mode in  $\text{Sr}_2[\text{CO}_4]$  is marked by a circle at ambient conditions.

spectrum of a  $\text{Sr}[\text{CO}_3]$  crystal in a DAC covered with SrO powder at ambient conditions. Because SrO crystallizes in the cubic space group  $Fm\bar{3}m$ , there are no Raman active modes and only Raman modes due to  $\text{Sr}[\text{CO}_3]$  can be observed.<sup>30</sup> The agreement between the experimental Raman spectra and the data from DFT-based calculations for  $\text{Sr}[\text{CO}_3]$  is convincing. We cold-compressed the  $\text{Sr}[\text{CO}_3] + \text{SrO}$  mixtures up to a pressure of 30(2) GPa (Figure 2b). At  $\approx 25$  GPa,  $\text{Sr}[\text{CO}_3]$  undergoes a pressure-induced phase transition from the aragonite structure type ( $Pm\bar{c}n$ ) to a postaragonite

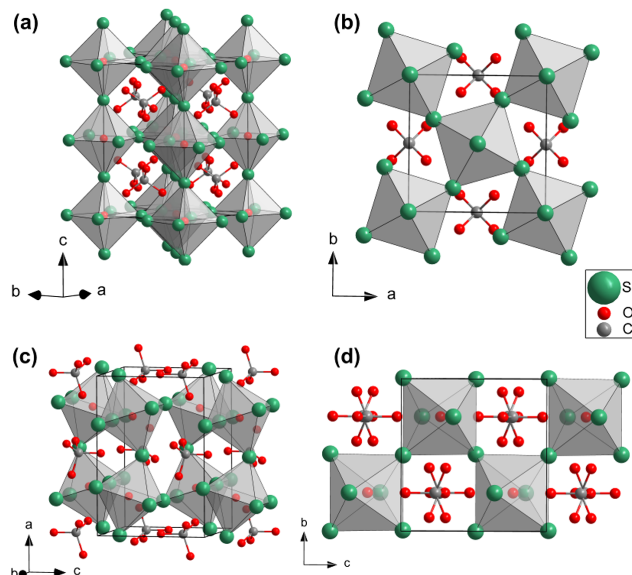


**Figure 4.** Tetragonal structure ( $I4/mcm$ ) of  $Sr_3[CO_4]O$  at 20 GPa (a and b) and orthorhombic structure ( $Pnma$ ) at ambient conditions (c and d).

structure ( $Pnmm$ ).<sup>31,32</sup> The experimental Raman spectrum at 30(2) GPa is accurately reproduced by the spectrum from DFT-based calculations for  $Sr[CO_3]$  with a postaragonite structure (Figure 3a). Although the pressure conditions in the cell are very likely nonhydrostatic, there was no significant broadening of the Raman bands.

After cold-compressing of the  $Sr[CO_3] + SrO$  mixture, several parts of the crystal were laser-heated to a maximum temperature of  $\approx 2500$  (250) K for 20 min. Subsequently, a central area on the crystal was heated to significantly higher temperatures [ $\approx 3000$  (300) K]. During laser heating, the  $Sr[CO_3]$  crystal as well as the  $SrO$  powder melted completely (Figure 2c). The Raman spectra after laser heating do not substantially differ as a function of the pressure [either 20(1) or 30(2) GPa], but they are very different from those of the cold-compressed  $Sr[CO_3] + SrO$  mixture. The characteristic Raman mode for conventional carbonates is the  $[CO_3]$  stretching mode ( $\nu_1$ ), expected to have a Raman shift of  $\approx 1120$   $cm^{-1}$  at 20 GPa and of  $\approx 1150$   $cm^{-1}$  at 30 GPa. In our experiments, the  $[CO_3]$  stretching mode disappears in the laser-heated regions at both pressures and two intense new modes appear between 900 and 1000  $cm^{-1}$  (Figure 3b). Both new modes are characteristic  $[CO_4]$  modes. They belong to two different  $sp^3$  carbonates because we can assign the Raman mode at higher wavenumbers [ $\approx 990$   $cm^{-1}$  at 30(2) GPa and  $\approx 960$   $cm^{-1}$  at 20(1) GPa] to the  $[CO_4]^{4-}$  group of orthorhombic orthocarbonate  $Sr_2[CO_4]$  ( $Pnma$ ) with tetrahedrally coordinated  $sp^3$ -hybridized carbon. The Raman spectrum of this phase is in complete agreement with the results of earlier investigations.<sup>20,21</sup> The high-frequency Raman mode at slightly lower wavenumbers [ $\approx 970$   $cm^{-1}$  at 30 GPa and  $\approx 950$   $cm^{-1}$  at 20(1) GPa] belongs to a new strontium orthocarbonate phase. Mapping the intensities of the two new stretching modes allows one to locate a region in the DAC where only one phase is present (Figure 2d–f).

We employed synchrotron powder X-ray diffraction to characterize the temperature-quenched samples. We analyzed the powder X-ray diffraction data recorded at 20(1) GPa and found that the diffraction data could be well fitted with tetragonal  $Sr_3[CO_4]O$ , which had recently been predicted and is thought to be isostructural to other predicted carbonates,  $Ca_3[CO_4]O$  and  $Ba_3[CO_4]O$ .<sup>22,25</sup> The Rietveld refinement (Figure S2) of  $Sr_3[CO_4]O$  was carried out in the tetragonal space group  $I4/mcm$  with  $Z = 4$  ( $wR = 3.9\%$ ). At 20(1) GPa, we obtained the lattice parameters of  $a = 6.562(1)$  Å and  $c = 9.751(3)$  Å, which are in good agreement with the values obtained by DFT calculations (Table S1). The anisotropic displacement parameters of the symmetrically independent strontium as well as of the oxygen atoms were constrained to be identical. Furthermore, we applied restraints to ensure that the C–O bond distances are  $\approx 1.4$  Å and the O–C–O angles are  $\approx 109.5^\circ$ . We included  $SrO$  ( $Fm\bar{3}m$ ) in the refinement, and in addition to  $Sr_3[CO_4]O$  and the precursor  $SrO$ , we can identify a few tiny peaks of  $Sr_2[CO_4]$ . According to Gibbs free energy calculations,  $Sr_3[CO_4]O$  is formed by the reaction  $2Sr_2[CO_4] \rightarrow Sr_3[CO_4]O + Sr[CO_3]$  at high temperatures.<sup>25</sup> We suggest that this reaction occurs in our experiments during the second stage of heating.

During decompression, we observed that  $Sr_3[CO_4]O$  undergoes a phase transition from a tetragonal to an orthorhombic structure below  $\approx 7$  GPa. After pressure release, we opened the DAC and collected single-crystal X-ray diffraction data. These data allowed us to determine the crystal structure of  $Sr_3[CO_4]O$  at ambient conditions. From the single-crystal data, we found that at ambient conditions  $Sr_3[CO_4]O$  is orthorhombic ( $Pnma$ ) with  $Z = 4$  and  $a = 9.892(1)$  Å,  $b = 7.131(2)$  Å, and  $c = 6.806(1)$  Å ( $wR = 6.5\%$ ). This is in good agreement with our DFT calculations (Table S1). Our diffraction data and the Raman spectra are inconsistent with the predicted metastable low-pressure

structures of  $\text{Ca}_3[\text{CO}_4]\text{O}$  and  $\text{Sr}_3[\text{CO}_4]\text{O}$  with space group symmetry  $\text{Cmcm}$ .<sup>22,25</sup>

The results of the structure refinements are shown in Figure 4 and Tables S1 and S2. The structure is best described as a framework antiperovskite structure, where the  $\text{OSr}_6$  octahedra are linked by corner-sharing  $\text{Sr}^{2+}$ , and the  $[\text{CO}_4]^{4-}$  group replaces the A cation in a prototypical  $\text{ABX}_3$  perovskite.<sup>29</sup> The  $\text{OSr}_6$  octahedra in the high-pressure phase are nearly undistorted; i.e., the O–Sr contacts in (001) are  $\approx 2\%$  shorter than those along [001], while the octahedra angles are constrained by symmetry to be  $90^\circ$ . The cooperative rotation of the octahedra is  $\approx 30^\circ$  purely around [001] and essentially independent of the pressure. The structure of  $\text{Sr}_3[\text{CO}_4]\text{O}$  is slightly distinct from the structure of the related antiperovskite  $\text{Sr}_3(\text{SiO}_4)\text{O}$  ( $P4/nmc$ ).<sup>33</sup> In the low-pressure polymorph, the octahedra are tilted; i.e., the –Sr–O–Sr– chains, which are linear in the tetragonal phase, are slightly kinked in the orthorhombic phase. The O–Sr contacts show a slightly larger variation (from 2.5–2.7 Å), but, nevertheless, the characteristic perovskite structure is still clearly present.

Hence, the new phase extends the family of framework antiperovskite compounds, which can generally be described as having a composition  $\text{M}_3(\text{TO}_4)\text{X}$ .<sup>29,34,35</sup> Up to now, compounds with  $\text{M} = \text{Na}, \text{K}, \text{Ca}, \text{Pb}, \text{Cs}, \text{Cd}, \text{Sr}, \text{or Ba}$ ,  $\text{T} = \text{Si}, \text{Ge}, \text{S}, \text{Co}, \text{Cr}, \text{Fe}, \text{or P}$ , and  $\text{X} = \text{O}, \text{F}, \text{or Cl}$  have been synthesized.<sup>29,34,35</sup> Here, we have found that  $\text{M}_3(\text{TO}_4)\text{X}$  antiperovskite with  $\text{T} = \text{C}$  can be formed at moderate  $p$  and  $T$  conditions and be recovered. A Mulliken population analysis of the self-consistent electron densities shows some charge accumulation of  $\approx 0.14 e^- \text{Å}^{-3}$  along the Sr–O contacts; i.e., these are weakly covalent bonds. This is consistent with the electronegativity difference between Sr ( $n_{\text{Pauling}}^{\text{Sr}} = 0.95$ ) and O ( $n_{\text{Pauling}}^{\text{O}} = 3.44$ ), which is  $\Delta n = 2.49$ , which implies an  $\approx 80\%$  ionic character of this bond. Therefore, directional bonding does not seem to be important, and in conjunction with the chemical diversity and structural flexibility mentioned above, we therefore expect that other antiperovskite framework compounds  $\text{M}_3[\text{CO}_4]\text{X}$  and their solid solutions can be obtained at high pressures.

We used the powder X-ray diffraction data obtained between 30 GPa and ambient conditions measured during the decompression to obtain the unit cell parameters of  $\text{Sr}_3[\text{CO}_4]\text{O}$  and  $\text{Sr}_2[\text{CO}_4]$  (Figure S3). These data sets were used to compute the values of the bulk modulus  $K$  for both phases.

We fitted a second and third-order Birch–Murnaghan equation of state (EOS) to unit cell volume between 30 GPa and ambient conditions for  $\text{Sr}_2[\text{CO}_4]$ . For the tetragonal high-pressure phase of  $\text{Sr}_3[\text{CO}_4]\text{O}$ , only the pressure points between  $\approx 7$  and 30 GPa were considered. The bulk moduli obtained by a second-order EOS of the high-pressure phase of  $\text{Sr}_3[\text{CO}_4]\text{O}$  [ $K_{\text{Sr}_3[\text{CO}_4]\text{O}} = 94(7)$  GPa] and of  $\text{Sr}_2[\text{CO}_4]$  [ $K_{\text{Sr}_2[\text{CO}_4]} = 127(3)$  GPa] differ by  $\approx 25\%$ . The experimentally obtained bulk modulus for  $\text{Sr}_2[\text{CO}_4]$  is in reasonable agreement with the value obtained by DFT-based calculations [ $K_{\text{Sr}_2[\text{CO}_4]}^{\text{DFT}} = 110(5)$  GPa].<sup>20</sup> The bulk moduli determined using a third-order EOS do not substantially differ from those using a second-order EOS within the experimental uncertainties (see the Supporting Information).

In summary, we have synthesized  $\text{Sr}_3[\text{CO}_4]\text{O}$ , a novel carbonate with  $\text{sp}^3$ -hybridized carbon and isolated  $[\text{CO}_4]^{4-}$  tetrahedra in a LH-DAC at moderate  $p$  and  $T$  conditions. In

contrast to  $\text{Sr}_2[\text{CO}_4]$ , this new compound is characterized by an antiperovskite structure with corner-sharing  $\text{OSr}_6$  octahedra, and the  $[\text{CO}_4]^{4-}$  tetrahedra are located in cages between the  $\text{OSr}_6$  octahedra. This compound undergoes a structural phase transition between a tetragonal high-pressure polymorph and an orthorhombic low-pressure polymorph. The synthesis conditions required for the synthesis of  $\text{Sr}_3[\text{CO}_4]\text{O}$  can be achieved in large volume presses, and because the orthorhombic polymorph can be recovered at ambient conditions, it is now possible to recover milligram quantities of  $\text{Sr}_3[\text{CO}_4]\text{O}$ . This increased amount of sample material will allow the use of a much broader range of analytical approaches to investigate the chemical and physical properties, such as heat capacity, water solubility, or thermal/chemical stability, of this compound.

## ■ ASSOCIATED CONTENT

### SI Supporting Information

The Supporting Information is available free of charge at <https://pubs.acs.org/doi/10.1021/acs.inorgchem.1c01900>.

Experimental and computational details of the experiments and results of the Rietveld refinement and single-crystal structure solution (PDF)

### Accession Codes

CCDC 2089820–2089823 contain the supplementary crystallographic data for this paper. These data can be obtained free of charge via [www.ccdc.cam.ac.uk/data\\_request/cif](http://www.ccdc.cam.ac.uk/data_request/cif), or by emailing [data\\_request@ccdc.cam.ac.uk](mailto:data_request@ccdc.cam.ac.uk), or by contacting The Cambridge Crystallographic Data Centre, 12 Union Road, Cambridge CB2 1EZ, UK; fax: +44 1223 336033.

## ■ AUTHOR INFORMATION

### Corresponding Author

Dominik Spahr – Institute of Geosciences, Goethe University Frankfurt, Frankfurt 60438, Germany; [orcid.org/0000-0003-0489-5270](https://orcid.org/0000-0003-0489-5270); Email: [d.spahr@kristall.uni-frankfurt.de](mailto:d.spahr@kristall.uni-frankfurt.de)

### Authors

Jannes König – Institute of Geosciences, Goethe University Frankfurt, Frankfurt 60438, Germany; [orcid.org/0000-0003-2960-7714](https://orcid.org/0000-0003-2960-7714)

Lkhamsuren Bayarjargal – Institute of Geosciences, Goethe University Frankfurt, Frankfurt 60438, Germany

Pavel N. Gavryushkin – Novosibirsk State University, Novosibirsk 630090, Russian Federation; Sobolev Institute of Geology and Mineralogy (IGM), Siberian Branch of Russian Academy of Sciences (SB RAS), Novosibirsk 630090, Russian Federation

Victor Milman – Dassault Systèmes BIOVIA, Cambridge CB4 0WN, United Kingdom; [orcid.org/0000-0003-2258-1347](https://orcid.org/0000-0003-2258-1347)

Hanns-Peter Liermann – DESY, Hamburg 22607, Germany

Björn Winkler – Institute of Geosciences, Goethe University Frankfurt, Frankfurt 60438, Germany; [orcid.org/0000-0001-8029-478X](https://orcid.org/0000-0001-8029-478X)

Complete contact information is available at: <https://pubs.acs.org/doi/10.1021/acs.inorgchem.1c01900>

### Notes

The authors declare no competing financial interest.

## ■ ACKNOWLEDGMENTS

We gratefully acknowledge funding from the DFG (Projects WI1232 and BA4020) and the DFG-Research Unit FOR2125/CarboPaT. B.W. is grateful for support by the BIOVIA Science Ambassador program. P.N.G. was supported by RFBR (Project 20-03-00774) and by the state assignment project of IGM SB RAS. We acknowledge DESY (Hamburg, Germany), a member of the Helmholtz Association HGF, for the provision of experimental facilities. Parts of this research were carried out at PETRA III on beamline P02.2.

## ■ REFERENCES

- Reeder, R. J., Ed. *Carbonates: Mineralogy and Chemistry*; De Gruyter: Berlin, 1983; DOI: 10.1515/9781501508134.
- Vennari, C.; Beavers, C.; Williams, Q. High-Pressure/Temperature Behavior of the Alkali/Calcium Carbonate Shortite ( $\text{Na}_2\text{Ca}_2(\text{CO}_3)_3$ ): Implications for Carbon Sequestration in Earth's Transition Zone. *J. Geophys. Res.: Solid Earth* **2018**, *123*, 6574–6591.
- Bayarjargal, L.; Fruhner, C.-J.; Schrodt, N.; Winkler, B.  $\text{CaCO}_3$  phase diagram studied with Raman spectroscopy at pressures up to 50 GPa and high temperatures and DFT modeling. *Phys. Earth Planet. Inter.* **2018**, *281*, 31–45.
- Binck, J.; Chariton, S.; Stekiel, M.; Bayarjargal, L.; Morgenroth, W.; Milman, V.; Dubrovinsky, L.; Winkler, B. High-pressure, high-temperature phase stability of iron-poor dolomite and the structures of dolomite-IIIc and dolomite-V. *Phys. Earth Planet. Inter.* **2020**, *299*, 106403.
- Cerantola, V.; et al. Stability of iron-bearing carbonates in the deep Earth's interior. *Nat. Commun.* **2017**, *8*, 15960.
- Binck, J.; Bayarjargal, L.; Lobanov, S. S.; Morgenroth, W.; Luchitskaia, R.; Pickard, C. J.; Milman, V.; Refson, K.; Jochym, D. B.; Byrne, P.; Winkler, B. Phase stabilities of  $\text{MgCO}_3$  and  $\text{MgCO}_3$ -II studied by Raman spectroscopy, X-ray diffraction, and density functional theory calculations. *Phys. Rev. Mater.* **2020**, *4*, 055001.
- Chariton, S. The elastic properties and the crystal chemistry of carbonates in the deep Earth. Ph.D. Thesis, University of Bayreuth, Bayreuth, Germany, 2020.
- Boulard, E.; Pan, D.; Galli, G.; Liu, Z.; Mao, W. L. Tetrahedrally coordinated carbonates in Earth's lower mantle. *Nat. Commun.* **2015**, *6*, 6311.
- Merlini, M.; Cerantola, V.; Gatta, G. D.; Gemmi, M.; Hanfland, M.; Kuznetsov, I.; Lotti, P.; Müller, H.; Zhang, L. Dolomite-IV: Candidate structure for a carbonate in the Earth's lower mantle. *Am. Mineral.* **2017**, *102*, 1763–1766.
- Oganov, A. R.; Ono, S.; Ma, Y.; Glass, C. W.; Garcia, A. Novel high-pressure structures of  $\text{MgCO}_3$ ,  $\text{CaCO}_3$  and  $\text{CO}_2$  and their role in Earth's lower mantle. *Earth Planet. Sci. Lett.* **2008**, *273*, 38–47.
- Boulard, E.; Gloter, A.; Corgne, A.; Antonangeli, D.; Auzende, A.-L.; Perrillat, J.-P.; Guyot, F.; Fiquet, G. New host for carbon in the deep Earth. *Proc. Natl. Acad. Sci. U. S. A.* **2011**, *108*, 5184–5187.
- Maeda, F.; Ohtani, E.; Kamada, S.; Sakamaki, T.; Hirao, N.; Ohishi, Y. Diamond formation in the deep lower mantle: A high-pressure reaction of  $\text{MgCO}_3$  and  $\text{SiO}_2$ . *Sci. Rep.* **2017**, *7*, 40602.
- Merlini, M.; Hanfland, M.; Salamat, A.; Petitgirard, S.; Müller, H. The crystal structures of  $\text{Mg}_2\text{Fe}_2\text{C}_4\text{O}_{13}$  with tetrahedrally coordinated carbon, and  $\text{Fe}_{13}\text{O}_{19}$  synthesized at deep mantle conditions. *Am. Mineral.* **2015**, *100*, 2001–2004.
- Oganov, A. R.; Glass, C. W.; Ono, S. High-pressure phases of  $\text{CaCO}_3$ : Crystal structure prediction and experiment. *Earth Planet. Sci. Lett.* **2006**, *241*, 95–103.
- Ono, S.; Kikegawa, T.; Ohishi, Y. High-pressure transition of  $\text{CaCO}_3$ . *Am. Mineral.* **2007**, *92*, 1246–1249.
- Pickard, C. J.; Needs, R. J. Structures and stability of calcium and magnesium carbonates at mantle pressures. *Phys. Rev. B: Condens. Matter Mater. Phys.* **2015**, *91*, 104101.
- Lobanov, S. S.; Dong, X.; Martirosyan, N. S.; Samtsevich, A. I.; Stevanovic, V.; Gavryushkin, P. N.; Litasov, K. D.; Greenberg, E.; Prapakpenka, V. B.; Oganov, A. R.; Goncharov, A. F. Raman spectroscopy and X-ray diffraction of  $sp^3$ - $\text{CaCO}_3$  at lower mantle pressures. *Phys. Rev. B: Condens. Matter Mater. Phys.* **2017**, *96*, 104101.
- Laniel, D. CCDC 2026976: *Experimental Crystal Structure Determination*; FIZ Karlsruhe: Eggenstein-Leopoldshafen, Germany, 2020; DOI: 10.5517/ccdc.csd.cc2617bv.
- Binck, J.; Laniel, D.; Bayarjargal, L.; Khandarkhaeva, S.; Fedotenko, T.; Aslandukov, A.; Glazyrin, K.; Milman, V.; Chariton, S.; Prapakpenka, V. B.; Dubrovinskaia, N.; Dubrovinsky, L.; Winkler, B. Synthesis of calcium orthocarbonate,  $\text{Ca}_2\text{CO}_4$ -*Pnma* at *p*, *T*-conditions of Earth's transition zone and lower mantle. *Am. Mineral.* **2021**, DOI: 10.2138/am-2021-7872.
- Laniel, D.; Binck, J.; Winkler, B.; Vogel, S.; Fedotenko, T.; Chariton, S.; Prapakpenka, V.; Milman, V.; Schnick, W.; Dubrovinsky, L.; Dubrovinskaia, N. Synthesis, crystal structure and structure-property relations of strontium orthocarbonate,  $\text{Sr}_2\text{CO}_4$ . *Acta Crystallogr., Sect. B: Struct. Sci., Cryst. Eng. Mater.* **2021**, *B77*, 131–137.
- Spahr, D.; Binck, J.; Bayarjargal, L.; Luchitskaia, R.; Morgenroth, W.; Comboni, D.; Milman, V.; Winkler, B. Tetrahedrally Coordinated  $sp^3$ -Hybridized Carbon in  $\text{Sr}_2\text{CO}_4$  Orthocarbonate at Ambient Conditions. *Inorg. Chem.* **2021**, *60*, 5419–5422.
- Yao, X.; Xie, C.; Dong, X.; Oganov, A. R.; Zeng, Q. Novel high-pressure calcium carbonates. *Phys. Rev. B: Condens. Matter Mater. Phys.* **2018**, *98*, 014108.
- Sagatova, D.; Shatskiy, A.; Sagatov, N.; Gavryushkin, P. N.; Litasov, K. D. Calcium orthocarbonate,  $\text{Ca}_2\text{CO}_4$ -*Pnma*: A potential host for subducting carbon in the transition zone and lower mantle. *Lithos* **2020**, *370–371*, 105637.
- Gavryushkin, P. N.; Sagatova, D.; Sagatov, N.; Litasov, K. D. Formation of Mg-Orthocarbonate through the Reaction  $\text{MgCO}_3 + \text{MgO} = \text{Mg}_2\text{CO}_4$  at Earth's Lower Mantle *P–T* Conditions. *Cryst. Growth Des.* **2021**, *21*, 2986–2992.
- Gavryushkin, P. N.; Sagatova, D. N.; Sagatov, N.; Litasov, K. D. Orthocarbonates of Ca, Sr, and Ba – the appearance of  $sp^3$ -hybridized carbon at a pressure of 5 GPa and dynamic stability at ambient pressure. *Earth. Space. Chem.* **2021**, *5*, 1948.
- Liebau, F. *Structural Chemistry of Silicates*; Springer-Verlag: Berlin, 1985; DOI: 10.1007/978-3-642-50076-3.
- Okrusch, M.; Frimmel, H., Eds. *Mineralogy: An Introduction to Minerals, Rocks, and Mineral Deposits*; Springer-Verlag: Berlin, 2020; DOI: 10.1007/978-3-662-57316-7.
- Jansen, M. Crystal Structure of  $\text{Na}_3\text{NO}_4$ . *Angew. Chem., Int. Ed. Engl.* **1979**, *18*, 698–699.
- Krivovichev, S. V. Minerals with antiperovskite structure: A review. *Z. Kristallogr. - Cryst. Mater.* **2008**, *223*, 109–113.
- Liu, L.-G.; Bassett, A. A. Changes of the crystal structure and the lattice parameter of SrO at high pressure. *J. Geophys. Res.* **1973**, *78*, 8470–8473.
- Biedermann, N.; Speziale, S.; Winkler, B.; Reichmann, H. J.; Koch-Müller, M.; Heide, G. High-pressure phase behavior of  $\text{SrCO}_3$ : an experimental and computational Raman scattering study. *Phys. Chem. Miner.* **2017**, *44*, 335–343.
- Biedermann, N.; Bykova, E.; Morgenroth, W.; Efthimiopoulos, I.; Mueller, J.; Spiekermann, G.; Glazyrin, K.; Pakhomova, A.; Appel, K.; Wilke, M. Equation of state and high-pressure phase behaviour of  $\text{SrCO}_3$ . *Eur. J. Mineral.* **2020**, *32*, 575–586.
- Glasser, L. S. D.; Glasser, F. P. Silicates  $\text{Mg}_3\text{SiO}_5$ , I.  $\text{Sr}_3\text{SiO}_5$ . *Acta Crystallogr.* **1965**, *18*, 453–454.
- Mansmann, M. Die Kristallstruktur von Tribariumpentaoxometallaten(IV) und isotypen Verbindungen. *Z. Anorg. Allg. Chem.* **1965**, *339*, 52–56.
- Skakle, J. M. S.; Fletcher, J. G.; West, A. R. Polymorphism, structures and phase transformation of  $\text{K}_3[\text{SO}_4]\cdot\text{F}$ . *J. Chem. Soc., Dalton Trans.* **1996**, 2497–2501.

## Sr[C<sub>2</sub>O<sub>5</sub>] is an Inorganic Pyrocarbonate Salt with [C<sub>2</sub>O<sub>5</sub>]<sup>2-</sup> Complex Anions

Dominik Spahr,\* Jannes König, Lkhamsuren Bayarjargal, Victor Milman, Alexander Perlov, Hanns-Peter Liermann, and Björn Winkler

Cite This: *J. Am. Chem. Soc.* 2022, 144, 2899–2904

Read Online

ACCESS |

Metrics & More

Article Recommendations

Supporting Information

**ABSTRACT:** The synthesis of a novel type of carbonate, namely of the inorganic pyrocarbonate salt Sr[C<sub>2</sub>O<sub>5</sub>], which contains isolated [C<sub>2</sub>O<sub>5</sub>]<sup>2-</sup>-groups, significantly extends the crystal chemistry of inorganic carbonates beyond the established *sp*<sup>2</sup>- and *sp*<sup>3</sup>-carbonates. We synthesized Sr[C<sub>2</sub>O<sub>5</sub>] in a laser-heated diamond anvil cell by reacting Sr[CO<sub>3</sub>] with CO<sub>2</sub>. By single crystal synchrotron diffraction, Raman spectroscopy, and density functional theory (DFT) calculations, we show that it is a pyrocarbonate salt. Sr[C<sub>2</sub>O<sub>5</sub>] is the first member of a novel family of inorganic carbonates. We predict, based on DFT calculations, that further inorganic pyrocarbonates can be obtained and that these will be relevant to geoscience and may provide a better understanding of reactions converting CO<sub>2</sub> into useful inorganic compounds.

Carbonates are ubiquitous in nature, as they are the major reservoir of carbon in the biosphere, hydrosphere, in soils, and in the Earth's crust.<sup>1,2</sup> Conventional carbonates, such as calcite (CaCO<sub>3</sub>), aragonite (CaCO<sub>3</sub>), or dolomite [CaMg(CO<sub>3</sub>)<sub>2</sub>], are a structurally and chemically very diverse group of compounds. They are characterized by nearly planar trigonal [CO<sub>3</sub>]<sup>2-</sup>-groups where C-*sp*<sup>2</sup> hybrid orbitals are formed between a central carbon atom and each of the three surrounding oxygen atoms.<sup>3,4</sup> The crystal structure of most carbonates has been investigated in great detail, where, for example, the structure of aragonite (CaCO<sub>3</sub>) has been well established for nearly 100 years.<sup>5</sup> The [CO<sub>3</sub>]<sup>2-</sup>-groups can be considered as rigid units, and hence, the conventional *sp*<sup>2</sup>-carbonates can be described in terms of stacking of [CO<sub>3</sub>]<sup>2-</sup>-groups.<sup>6–9</sup> These *sp*<sup>2</sup>-carbonate groups may persist up to very high pressures (*p* > 70 GPa) and high temperatures. Up to now, it is generally thought that [CO<sub>3</sub>]<sup>2-</sup>-groups do not polymerize by sharing oxygen. Only in a few compounds such as Na<sub>2</sub>Ca<sub>2</sub>[CO<sub>3</sub>]<sub>3</sub>, an onset of a near-dimerization is observed at high pressures.<sup>10</sup>

The family of carbonates was extended by the discovery of carbonates with tetrahedrally coordinated carbon, where a central carbon atom forms C-*sp*<sup>3</sup> hybrid orbitals to four surrounding oxygen atoms. These novel carbonates were obtained either at very high pressures and temperatures<sup>8,9,11–21</sup> or synthesized by reactions of carbonates with alkaline earth oxides<sup>22–25</sup> or CO<sub>2</sub><sup>26</sup> at moderate pressures. The characteristic feature of *sp*<sup>3</sup>-carbonates includes [CO<sub>4</sub>]<sup>4-</sup>-groups, which may polymerize by corner-sharing. Recently, it was found that some of them can be recovered to ambient conditions.<sup>24,25</sup>

A third group of carbonates includes pyrocarbonates, which are characterized by the presence of [C<sub>2</sub>O<sub>5</sub>]<sup>2-</sup>-groups, in which two *sp*<sup>2</sup>-hybridized carbons share one oxygen. Since their discovery by Bohem and Mehta<sup>27</sup> in 1938, pyrocarbonate esters (R<sub>1</sub>–[C<sub>2</sub>O<sub>5</sub>]<sup>2-</sup>–R<sub>2</sub>) have found extensive use in organic syntheses and biochemistry.<sup>28–31</sup> In contrast, pyrocarbonate

salts with [C<sub>2</sub>O<sub>5</sub>]<sup>2-</sup> complex anions have not been reported yet. The formation of [C<sub>2</sub>O<sub>5</sub>]<sup>2-</sup>-groups in melts, aqueous carbonate solutions, or in the gas-phase has been proposed earlier.<sup>32–38</sup> These pyrocarbonate groups were suggested to be formed by the reaction of CO<sub>2</sub> with the [CO<sub>3</sub>]<sup>2-</sup>-anion. However, the evidence for the existence of isolated [C<sub>2</sub>O<sub>5</sub>]<sup>2-</sup>-groups is circumstantial, as their presence was either inferred from two weak Raman peaks in the spectrum of an eutectic Li<sub>2</sub>[CO<sub>3</sub>]-Na<sub>2</sub>[CO<sub>3</sub>] melt<sup>37</sup> or from computer simulations<sup>38</sup> without experimental benchmarks.

The synthesis of inorganic pyrocarbonates with isolated [C<sub>2</sub>O<sub>5</sub>]<sup>2-</sup> complex anions would therefore constitute a new family of carbonates. It would also allow a gap to be filled in crystal chemical systematics for compounds with pyro-groups [X<sub>2</sub>O<sub>5</sub>], where X = B, C, N. Pyroborates, containing isolated [B<sub>2</sub>O<sub>5</sub>]<sup>4-</sup>-groups (e.g., (Co,Ni,Zn)<sub>2</sub>[B<sub>2</sub>O<sub>5</sub>], Mg<sub>2</sub>[B<sub>2</sub>O<sub>5</sub>], Ca<sub>2</sub>[B<sub>2</sub>O<sub>5</sub>], Sr<sub>2</sub>[B<sub>2</sub>O<sub>5</sub>], or BaMn[B<sub>2</sub>O<sub>5</sub>]) are well established.<sup>39–43</sup> Molecular N<sub>2</sub>O<sub>5</sub> has also been studied extensively.<sup>44–47</sup>

The pyrocarbonate Sr[C<sub>2</sub>O<sub>5</sub>] contains isolated [C<sub>2</sub>O<sub>5</sub>]<sup>2-</sup>-groups and forms after the reaction between Sr[CO<sub>3</sub>] and CO<sub>2</sub> at 30(2) GPa and temperatures of ~2000(200) K. We have performed the synthesis in a laser-heated diamond anvil cell (LH-DAC) following the procedure shown in Figure 1.

First, a Sr[CO<sub>3</sub>] crystal and a ruby for pressure determination were placed in the gasket hole (Figure 1a). Then the DAC was cooled down to ~100 K and CO<sub>2</sub>-I (dry ice) was directly condensed into the hole from a CO<sub>2</sub> gas jet

Received: January 11, 2022

Published: February 8, 2022



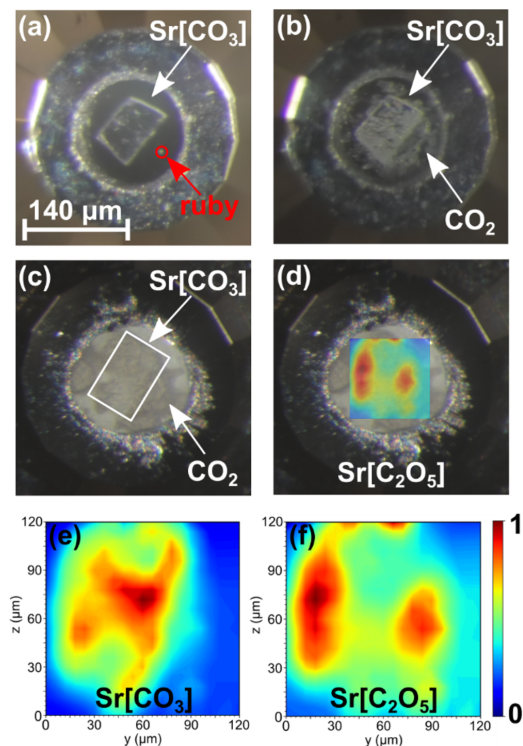


**Figure 1.** (a) Sr[CO<sub>3</sub>] crystal placed in the culet's center; a ruby is added for pressure determination. (b) DAC is cooled down to ~100 K, and CO<sub>2</sub>-I (dry ice) is condensed into the gasket hole. (c) Sr[CO<sub>3</sub>] + CO<sub>2</sub> mixture after laser heating at 30(2) GPa up to temperatures of ~2000(200) K. (d) Raman map for Sr[C<sub>2</sub>O<sub>5</sub>] as an overlay over the photograph of the gasket hole. (e) Raman map of residual Sr[CO<sub>3</sub>] after laser heating. (f) Enlargement of panel d, showing the presence of Sr[C<sub>2</sub>O<sub>5</sub>] at the boundaries of the laser-heated Sr[CO<sub>3</sub>] crystal.

(Figure 1b). Afterwards, the Sr[CO<sub>3</sub>] crystal was completely surrounded by CO<sub>2</sub>. We compressed the Sr[CO<sub>3</sub>] + CO<sub>2</sub> mixture up to a pressure of 30(2) GPa. Upon pressure increase, CO<sub>2</sub>-I (*Pa3*) undergoes a phase transition to CO<sub>2</sub>-III (*Cmca*) at ~11 GPa.<sup>48</sup> In addition, Sr[CO<sub>3</sub>]-I undergoes a pressure-induced phase transition from aragonite structure type (*Pmnc*) to Sr[CO<sub>3</sub>]-II in the postaragonite structure (*Pmmm*) at ~25 GPa.<sup>49</sup> These phase transitions and the high-temperature reaction can conveniently be followed via Raman spectroscopy (Figure 2).

The experimental Raman spectra of CO<sub>2</sub>-III and Sr[CO<sub>3</sub>]-II measured at 30(2) GPa at different positions on the sample before laser heating are accurately reproduced by the Raman spectra from DFT-based calculations (Figure 2a,b). No significant broadening of Sr[CO<sub>3</sub>]-II Raman bands was observed. After reaching the target pressure, different parts of the Sr[CO<sub>3</sub>] crystal were heated to a maximum temperature of ~2000(200) K for 30 min in the CO<sub>2</sub> environment. During the heating, CO<sub>2</sub>-III transformed to CO<sub>2</sub>-V (*I42d*)<sup>50</sup> and the Sr[CO<sub>3</sub>] crystal could not visually be identified anymore (Figure 1c). The Raman spectra of the heated sample differ

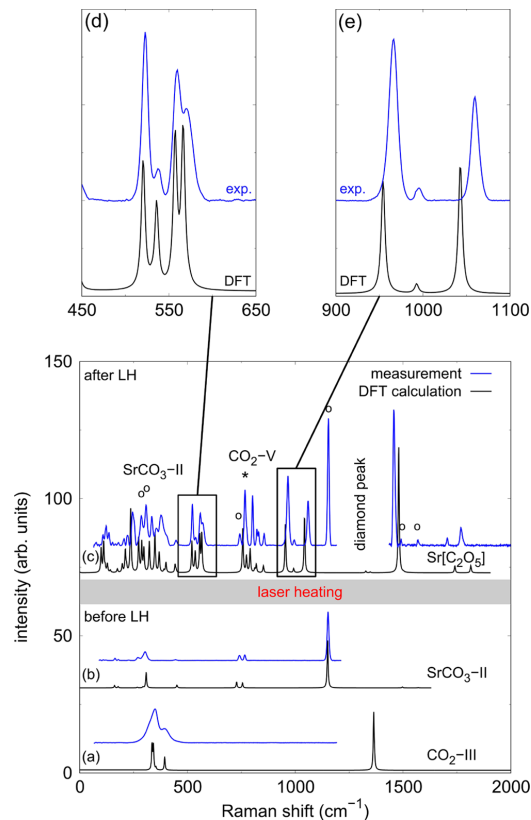


**Figure 2.** (a) Experimental Raman spectra for CO<sub>2</sub>-III and for (b) Sr[CO<sub>3</sub>]-II at 30(2) GPa before laser heating (blue) compared to DFT-based calculations (black). (c) Raman spectrum of Sr[C<sub>2</sub>O<sub>5</sub>] after laser heating the Sr[CO<sub>3</sub>] + CO<sub>2</sub> mixture in comparison to DFT-based calculations. Peaks of Sr[CO<sub>3</sub>]-II are marked by a circle (deg) and CO<sub>2</sub>-V are marked by an asterisk (\*). (d) Close-up of the region between 450–550 cm<sup>-1</sup>, (e) between 900–1100 cm<sup>-1</sup>. The shifts of the calculated Raman spectra were rescaled by 4%.

significantly in several regions from the starting material (Figure 2c). At 30(2) GPa, the characteristic CO<sub>3</sub> stretching mode of Sr[CO<sub>3</sub>]-II has a Raman shift of ~1150 cm<sup>-1</sup>, while CO<sub>2</sub>-V shows a very strong Raman mode at ~760 cm<sup>-1</sup>.<sup>49,51</sup> Both phases can be observed after laser heating, but several new Raman modes occur up to 1800 cm<sup>-1</sup>. We mapped the intensities of the Raman modes of the new and yet unknown phase to precisely determine the parts of the sample that completely converted to Sr[C<sub>2</sub>O<sub>5</sub>]. Two main areas, located toward the edges of the Sr[CO<sub>3</sub>] crystal (Figure 1d–f), showed the highest intensities and thus the most complete transformation.

We determined the crystal structure (Figure 3) of the new phase by synchrotron-based single crystal diffraction (Figure S1, Tables S1 and S2). We found that the unknown phase is a novel pyrocarbonate with Sr[C<sub>2</sub>O<sub>5</sub>] composition.

At 30(2) GPa, Sr[C<sub>2</sub>O<sub>5</sub>] crystallizes in the monoclinic space group *P2<sub>1</sub>/c* with *Z* = 4 and *a* = 4.736(2) Å, *b* = 8.175(2) Å, *c* = 7.140(1) Å, and *β* = 91.34(3)° (*V* = 276.3(2) Å<sup>3</sup>). The *wR*-

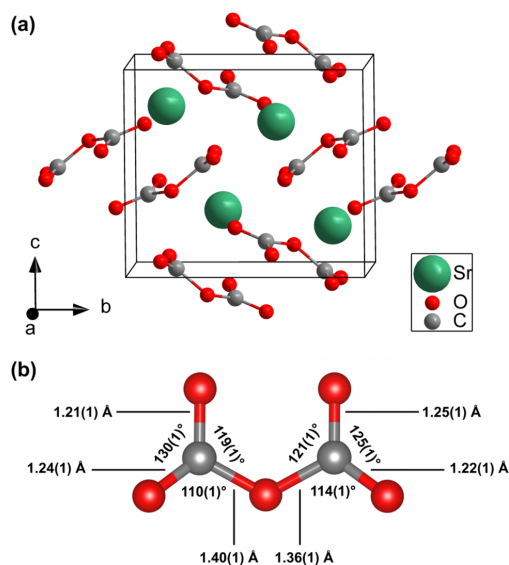


**Figure 3.** (a) Monoclinic structure ( $P2_1/c$ ,  $Z = 4$ ) of  $\text{Sr}[\text{C}_2\text{O}_5]$  at 30(2) GPa obtained from single crystal structure solution. (b) Enlargement of the  $[\text{C}_2\text{O}_5]^{2-}$ -group with C–O bond distances and O–C–O angles.

factor obtained from the structure refinement was  $wR = 4.9\%$ , thus demonstrating the high quality of the experimental data, which are in very good agreement with our DFT-based calculations (see Tables S1 and S2). Furthermore, the theoretical Raman spectrum nicely reproduces the experimental data (Figure 2c–e), including phonons with high Raman shifts of  $\sim 1700\text{ cm}^{-1}$ , confirming that the structural model is appropriate.

The  $[\text{C}_2\text{O}_5]^{2-}$ -groups are formed by the polymerization of two  $[\text{CO}_3]^{2-}$ -groups, where these groups share one oxygen atom (Figure 3b). The C–O bonds to the shared oxygen atom are slightly longer (1.36(1)–1.40(1) Å) than the C–O bonds between the C atoms and the terminal oxygen atoms (1.21(1)–1.25(1) Å). The O–C–O angles differ by no more than  $10^\circ$  from the ideal O–C–O angle of  $120^\circ$ . Our experimental and calculated data (Figure S2) are in very good agreement with the calculated equilibrium geometry of the  $[\text{C}_2\text{O}_5]^{2-}$ -group proposed earlier.<sup>37,38</sup> A comparison of the bond lengths and bond populations (Table S3 and associated discussion) shows that the pyrocarbonate bridges the gap between the pyroborate  $\text{Sr}_2[\text{B}_2\text{O}_5]$  and  $\text{N}_2\text{O}_5$ , that is, that  $[\text{X}_2\text{O}_5]^{2-}$ -groups, with  $X = \text{B}, \text{C}, \text{N}$  are crystal chemically closely related.

After establishing that the DFT calculations accurately reproduce the experimental findings with respect to the structure and Raman spectrum at 30 GPa, we employed the DFT calculations to further investigate structure–property relations. The single crystal structure refinement showed that the bonds between the carbon atoms and the shared and terminal oxygen atoms are quite different. The density functional perturbation theory (DFPT) results allowed us to compute eigenvectors of the atomic displacements. They show that phonons that are predominantly stretching vibrations of the bonds between C and terminal atoms are at Raman shifts

of  $\sim 1700\text{ cm}^{-1}$ , while those for the bonds between C atoms and the shared oxygen atoms are at much lower shifts of  $\sim 900\text{ cm}^{-1}$  (Figure S3). Consistent with this finding are the magnitudes of the Mulliken bond populations, which provide a measure for the charge accumulation between atoms due to the formation of covalent bonds.<sup>52,53</sup> The Mulliken bond populations are  $\sim 1.0\text{ e}^- \text{ \AA}^{-3}$  for the stiffer, shorter bonds to the terminal oxygen atoms and thus significantly larger than the Mulliken bond populations of the C–O bonds involving the shared oxygen atoms ( $\sim 0.6\text{ e}^- \text{ \AA}^{-3}$ ).

Harmonic lattice dynamic calculations show the structure to be dynamically stable in the investigated pressure regime in the athermal limit. We have employed stress–strain calculation to obtain elastic stiffness coefficients at several pressures. We find that the Born criteria<sup>54</sup> are always fulfilled. The components for the stiffness tensor at 0 GPa are given in Table S4. The bulk modulus of  $\text{Sr}[\text{C}_2\text{O}_5]$  ( $K_0 = 30.8(3)\text{ GPa}$ ) is smaller than that of  $\text{Sr}[\text{CO}_3]$  ( $K_0 = 63(3)\text{ GPa}$ ).<sup>55</sup> At 30 GPa, the new compound is stable by  $12\text{ kJ mol}^{-1}$  in the athermal limit with respect to a mixture of  $\text{SrCO}_3$ –II and  $\text{CO}_2$ –V. At ambient pressure,  $\text{Sr}[\text{C}_2\text{O}_5]$  is unstable by  $57\text{ kJ mol}^{-1}$  with respect to  $\text{Sr}[\text{CO}_3]$ –I and  $\text{CO}_2$ –I. The new compound is more stable up to at least 60 GPa than a hypothetical  $sp^3$ -carbonate polymorph with a  $\text{Ca}[\text{C}_2\text{O}_5]$ –I42d structure, in which the  $[\text{CO}_4]^{4-}$ -tetrahedra polymerize to form  $[\text{C}_4\text{O}_{10}]^{4-}$ -groups.<sup>26</sup>

We measured Raman spectra on pressure decrease. The Raman spectra unambiguously show that at 5 GPa  $\text{Sr}[\text{C}_2\text{O}_5]$  is still present with no anomalous changes other than bands shift due to pressure release (Figure S5). After opening the DAC, we performed post-mortem Raman analysis on the sample, but the signal proved to be weak and it was difficult to measure good quality spectra. On the basis of comparatively weak Raman modes (Figure S5) associated with a hindered rotation mode of the  $[\text{C}_2\text{O}_5]^{2-}$ -group, we currently assume that  $\text{Sr}[\text{C}_2\text{O}_5]$  may be recovered to ambient conditions. An unambiguous demonstration by a combination of diffraction and Raman spectroscopy is still outstanding.

In pyroborates, the cation can be replaced, and numerous earth alkali and transition metal pyroborates have been discovered and synthesized (e.g.,  $\text{Mg}_2[\text{B}_2\text{O}_5]$ ,  $\text{Ca}[\text{B}_2\text{O}_5]$  and  $\text{Sr}[\text{B}_2\text{O}_5]$ ).<sup>40–42</sup> We have therefore carried out preliminary DFPT-based lattice dynamical calculations, including calculations of complete phonon dispersion curves for  $\text{Mg}[\text{C}_2\text{O}_5]$ ,  $\text{Ca}[\text{C}_2\text{O}_5]$ ,  $\text{Ba}[\text{C}_2\text{O}_5]$ , and  $\text{Pb}[\text{C}_2\text{O}_5]$ , and found that these structures are dynamically stable. Typical Raman spectra and phonon densities of states are given in Figures S4 and S6, which will facilitate the identification of the compounds without the use of synchrotron radiation. All these results indicate that these compounds are experimentally accessible.

Compounds with C/Sr ratios of 1 ( $\text{Sr}[\text{CO}_3]$ ), 1/2 ( $\text{Sr}_2[\text{CO}_4]$ ), and 1/3 ( $\text{Sr}_3[\text{CO}_4]\text{O}$ ) have been obtained earlier in the binary system  $\text{CO}_2$ – $\text{SrO}$ .<sup>24,25</sup> Here, we have extended the family of compounds by the synthesis of a  $\text{CO}_2$ -rich phase with a C/Sr ratio of 2 ( $\text{Sr}[\text{C}_2\text{O}_5]$ ). We are confident that a possible cationic substitution as in pyroborates is also straightforward in pyrocarbonates, and we therefore expect that pyrocarbonate salts will show a rich chemical and structural diversity. Specifically, based on the DFT calculations, we expect that a similar  $\text{CO}_2$ -rich Ca-containing compound exists. This would be of substantial geological relevance, as in oceanic crust that is subducting into Earth's mantle, one would expect both  $\text{Ca}[\text{CO}_3]$  and  $\text{CO}_2$ -containing fluids to be present<sup>22,56–58</sup> and hence the formation of a Ca-pyrocar-

bonate. Also, we have directly converted CO<sub>2</sub> into a more (from an environmental point of view) benign compound. While here rather high pressures and temperatures have been employed, it is conceivable that other yet to be synthesized pyrocarbonates may open a new avenue to obtain compounds that either can serve to store CO<sub>2</sub> or can be used as intermediate products on the route to convert CO<sub>2</sub> into useful chemicals, which is currently a very attractive goal in “green chemistry”.<sup>59–62</sup>

## ■ ASSOCIATED CONTENT

### Supporting Information

The Supporting Information is available free of charge at <https://pubs.acs.org/doi/10.1021/jacs.2c00351>.

Experimental and computational details of experiments; results of single crystal structure solution and DFT-based calculations (PDF)

CASTEP input files for Sr[C<sub>2</sub>O<sub>3</sub>] at 0 GPa (ZIP)

### Accession Codes

CCDC 2108016–2108017 contain the supplementary crystallographic data for this paper. These data can be obtained free of charge via [www.ccdc.cam.ac.uk/data\\_request/cif](http://www.ccdc.cam.ac.uk/data_request/cif), or by emailing [data\\_request@ccdc.cam.ac.uk](mailto:data_request@ccdc.cam.ac.uk), or by contacting The Cambridge Crystallographic Data Centre, 12 Union Road, Cambridge CB2 1EZ, UK; fax: +44 1223 336033.

## ■ AUTHOR INFORMATION

### Corresponding Author

DominiK Spahr – Institute of Geosciences, Goethe University Frankfurt, 60438 Frankfurt, Germany; [orcid.org/0000-0003-0489-5270](https://orcid.org/0000-0003-0489-5270); Email: [d.spahr@kristall.uni-frankfurt.de](mailto:d.spahr@kristall.uni-frankfurt.de)

### Authors

Jannes König – Institute of Geosciences, Goethe University Frankfurt, 60438 Frankfurt, Germany; [orcid.org/0000-0003-2960-7714](https://orcid.org/0000-0003-2960-7714)

Lkhamsuren Bayarjargal – Institute of Geosciences, Goethe University Frankfurt, 60438 Frankfurt, Germany

Victor Milman – Dassault Systèmes BIOVIA, Cambridge CB4 0WN, United Kingdom; [orcid.org/0000-0003-2258-1347](https://orcid.org/0000-0003-2258-1347)

Alexander Perlov – Dassault Systèmes BIOVIA, Cambridge CB4 0WN, United Kingdom

Hanns-Peter Liermann – DESY, 22607 Hamburg, Germany

Björn Winkler – Institute of Geosciences, Goethe University Frankfurt, 60438 Frankfurt, Germany; [orcid.org/0000-0001-8029-478X](https://orcid.org/0000-0001-8029-478X)

Complete contact information is available at: <https://pubs.acs.org/doi/10.1021/jacs.2c00351>

### Notes

The authors declare no competing financial interest.

## ■ ACKNOWLEDGMENTS

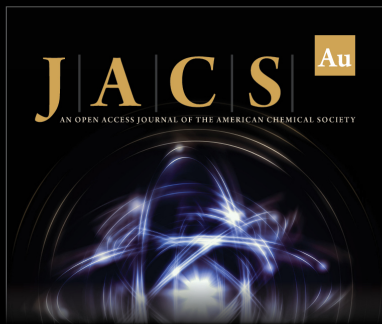
We gratefully acknowledge funding from the DFG (WI1232, BA4020, and FOR2125/CarboPaT) and appreciate the support from Rita Luchitskaia. B.W. is grateful for support by the BIOVIA Science Ambassador program. We acknowledge DESY (Hamburg, Germany), a member of the Helmholtz Association HGF, for the provision of experimental facilities. Parts of this research were carried out at PETRA III, beamline P02.2.

## ■ REFERENCES

- (1) McKenzie, N. R.; Horton, B. K.; Loomis, S. E.; Stockli, D. F.; Planavsky, N. J.; Lee, C.-T. A. Continental arc volcanism as the principal driver of icehouse-greenhouse variability. *Science* **2016**, *352*, 444–447.
- (2) Hirschmann, M. M. Comparative deep Earth volatile cycles: The case for C recycling from exosphere/mantle fractionation of major (H<sub>2</sub>O, C, N) volatiles and from H<sub>2</sub>O/Ce, CO<sub>2</sub>/Ba, and CO<sub>2</sub>/Nb exosphere ratios. *EPSL* **2018**, *502*, 262–273.
- (3) *Carbonates: Mineralogy and Chemistry*; Reeder, R. J., Ed.; De Gruyter: Berlin, 1983.
- (4) Winkler, B.; Zemann, J.; Milman, V. Aplanarity of CO<sub>3</sub> groups: A theoretical investigation. *Acta Cryst. B* **2000**, *56*, 648–653.
- (5) Bragg, W. L. The structure of aragonite. *Proc. R. Soc. London* **1924**, *A105*, 16–39.
- (6) Bayarjargal, L.; Fruhner, C.-J.; Schrodtr, N.; Winkler, B. CaCO<sub>3</sub> phase diagram studied with Raman spectroscopy at pressures up to 50 GPa and high temperatures and DFT modeling. *Phys. Earth Planet. Inter.* **2018**, *281*, 31–45.
- (7) Binck, J.; Chariton, S.; Stekiel, M.; Bayarjargal, L.; Morgenroth, W.; Milman, V.; Dubrovinsky, L.; Winkler, B. High-pressure, high-temperature phase stability of iron-poor dolomite and the structures of dolomite-IIIc and dolomite-V. *Phys. Earth Planet. Inter.* **2020**, *299*, 106403.
- (8) Cerantola, V.; et al. Stability of iron-bearing carbonates in the deep Earth's interior. *Nat. Commun.* **2017**, *8*, 15960.
- (9) Binck, J.; Bayarjargal, L.; Lobanov, S. S.; Morgenroth, W.; Luchitskaia, R.; Pickard, C. J.; Milman, V.; Refson, K.; Jochym, D. B.; Byrne, P.; Winkler, B. Phase stabilities of MgCO<sub>3</sub> and MgCO<sub>3</sub>-II studied by Raman spectroscopy, X-ray diffraction, and density functional theory calculations. *Phys. Rev. Mater.* **2020**, *4*, 055001.
- (10) Vennari, C.; Beavers, C.; Williams, Q. High-Pressure/Temperature Behavior of the Alkali/Calcium Carbonate Shortite (Na<sub>2</sub>Ca<sub>2</sub>(CO<sub>3</sub>)<sub>3</sub>): Implications for Carbon Sequestration in Earth's Transition Zone. *J. Geophys. Res. Solid Earth* **2018**, *123*, 6574–6591.
- (11) Chariton, S. *The elastic properties and the crystal chemistry of carbonates in the deep Earth*, Ph.D. Thesis, University of Bayreuth, 2020.
- (12) Boulard, E.; Pan, D.; Galli, G.; Liu, Z.; Mao, W. L. Tetrahedrally coordinated carbonates in Earth's lower mantle. *Nat. Commun.* **2015**, *6*, 6311.
- (13) Merlini, M.; Cerantola, V.; Gatta, G. D.; Gemmi, M.; Hanfland, M.; Kuznetsov, I.; Lotti, P.; Müller, H.; Zhang, L. Dolomite-IV: Candidate structure for a carbonate in the Earth's lower mantle. *Am. Mineral.* **2017**, *102*, 1763–1766.
- (14) Oganov, A. R.; Ono, S.; Ma, Y.; Glass, C. W.; Garcia, A. Novel high-pressure structures of MgCO<sub>3</sub>, CaCO<sub>3</sub> and CO<sub>2</sub> and their role in Earth's lower mantle. *EPSL* **2008**, *273*, 38–47.
- (15) Boulard, E.; Gloter, A.; Corgne, A.; Antonangeli, D.; Auzende, A.-L.; Perrillat, J.-P.; Guyot, F.; Fiquet, G. New host for carbon in the deep Earth. *Proc. Natl. Acad. Sci. U.S.A.* **2011**, *108*, 5184–5187.
- (16) Maeda, F.; Ohtani, E.; Kamada, S.; Sakamaki, T.; Hirao, N.; Ohishi, Y. Diamond formation in the deep lower mantle: A high-pressure reaction of MgCO<sub>3</sub> and SiO<sub>2</sub>. *Sci. Rep.* **2017**, *7*, 40602.
- (17) Merlini, M.; Hanfland, M.; Salamat, A.; Petitgirard, S.; Müller, H. The crystal structures of Mg<sub>2</sub>Fe<sub>2</sub>C<sub>4</sub>O<sub>13</sub>, with tetrahedrally coordinated carbon, and Fe<sub>13</sub>O<sub>19</sub>, synthesized at deep mantle conditions. *Am. Mineral.* **2015**, *100*, 2001–2004.
- (18) Oganov, A. R.; Glass, C. W.; Ono, S. High-pressure phases of CaCO<sub>3</sub>: Crystal structure prediction and experiment. *EPSL* **2006**, *241*, 95–103.
- (19) Ono, S.; Kikegawa, T.; Ohishi, Y. High-pressure transition of CaCO<sub>3</sub>. *Am. Mineral.* **2007**, *92*, 1246–1249.
- (20) Pickard, C. J.; Needs, R. J. Structures and stability of calcium and magnesium carbonates at mantle pressures. *Phys. Rev. B* **2015**, *91*, 104101.
- (21) Lobanov, S. S.; Dong, X.; Martirosyan, N. S.; Samtsevich, A. I.; Stevanovic, V.; Gavryushkin, P. N.; Litasov, K. D.; Greenberg, E.; Prakapenka, V. B.; Oganov, A. R.; Goncharov, A. F. Raman

- spectroscopy and X-ray diffraction of  $sp^3$ -CaCO<sub>3</sub> at lower mantle pressures. *Phys. Rev. B* **2017**, *96*, 104101.
- (22) Binck, J.; Laniel, D.; Bayarjargal, L.; Khandarkhaeva, S.; Fedotenko, T.; Aslandukov, A.; Glazyrin, K.; Milman, V.; Chariton, S.; Prakupenka, V. B.; Dubrovinskaja, N.; Dubrovinsky, L.; Winkler, B. Synthesis of calcium orthocarbonate, Ca<sub>2</sub>CO<sub>4</sub>-Pnma at *p,T*-conditions of Earth's transition zone and lower mantle. *Am. Mineral.* **2021**, DOI: 10.2138/am-2021-7872.
- (23) Laniel, D.; Binck, J.; Winkler, B.; Vogel, S.; Fedotenko, T.; Chariton, S.; Prakupenka, V.; Milman, V.; Schnick, W.; Dubrovinsky, L.; Dubrovinskaja, N. Synthesis, crystal structure and structure-property relations of strontium orthocarbonate, Sr<sub>2</sub>CO<sub>4</sub>. *Acta Crystallogr.* **2021**, *B77*, 131–137.
- (24) Spahr, D.; König, J.; Bayarjargal, L.; Luchitskaia, R.; Morgenroth, W.; Comboni, D.; Milman, V.; Winkler, B. Tetrahedrally Coordinated  $sp^3$ -Hybridized Carbon in Sr<sub>2</sub>CO<sub>4</sub> Orthocarbonate at Ambient Conditions. *Inorg. Chem.* **2021**, *60*, 5419–5422.
- (25) Spahr, D.; König, J.; Bayarjargal, L.; Gavryushkin, P. N.; Liermann, H.-P.; Milman, V.; Winkler, B. Sr<sub>3</sub>[CO<sub>4</sub>]O-antiperovskite with tetrahedrally-coordinated  $sp^3$ -hybridized carbon and OSr<sub>6</sub>-octahedra. *Inorg. Chem.* **2021**, *60*, 14504–14508.
- (26) König, J.; Spahr, D.; Bayarjargal, L.; Gavryushkin, P. N.; Milman, V.; Liermann, H.-P.; Winkler, B. Novel calcium  $sp^3$ -carbonate CaC<sub>2</sub>O<sub>5</sub>-I42d may be a carbon host in Earth's lower mantle. *Earth. Space. Chem.* **2022**, *6*, 73–80.
- (27) Boehm, T.; Mehta, D. Ester der Pyrokohlensäure. *Chem. Ber.* **1938**, *71*, 1797–1802.
- (28) Solymosy, F.; Fedorcsák, I.; Gulyás, A.; Farkas, L.; Ehrenberg, G. A new method based on the use of diethyl pyrocarbonate as a nuclease inhibitor for the extraction of undegraded nucleic acid from plant tissues. *Eur. J. Biochem.* **1968**, *5*, 520–527.
- (29) Summers, W. C. A simple method for extraction of RNA from *E. coli* utilizing diethyl pyrocarbonate. *Anal. Biochem.* **1970**, *33*, 459–463.
- (30) Dalpozzo, R.; Bartoli, G.; Bosco, M.; Melchiorre, P.; Sambri, L. Recent Development about the Use of Pyrocarbonates as Activator in Organic Synthesis: A Review. *Curr. Org. Synth.* **2009**, *336*, 79–101.
- (31) An, B.; Meng, Y.; Li, Z.; Hong, Y.; Wang, T.; Wang, S.; Lin, J.; Wang, C.; Wan, S.; Wang, Y.; Lin, W. A pyrocarbonate intermediate for CO<sub>2</sub> activation and selective conversion in bifunctional metal-organic frameworks. *J. Catal.* **2019**, *373*, 37–47.
- (32) Claes, P.; Moyaux, D.; Peeters, D. Solubility and solvation of carbon dioxide in the molten Li<sub>2</sub>CO<sub>3</sub>/Na<sub>2</sub>CO<sub>3</sub>/K<sub>2</sub>CO<sub>3</sub> (43.5:31.5:25.0 mol-%) eutectic mixture at 973K. I. Experimental part. *Eur. J. Inorg. Chem.* **1999**, *1999*, 583–588.
- (33) Peeters, D.; Moyaux, D.; Claes, P. Solubility and solvation of carbon dioxide in the molten Li<sub>2</sub>CO<sub>3</sub>/Na<sub>2</sub>CO<sub>3</sub>/K<sub>2</sub>CO<sub>3</sub> (43.5:31.5:25.0 mol-%) eutectic mixture at 973K. I. Theoretical part. *Eur. J. Inorg. Chem.* **1999**, *1999*, 589–592.
- (34) Frapper, G.; Saillard, J.-Y. Search for new allotropic forms of carbon dioxide and carbon disulfide: a density functional study of CX<sub>2</sub>-based oligomers (X = O, S). *J. Am. Chem. Soc.* **2000**, *122*, 5367–5370.
- (35) Zeller, K.-P.; Schuler, P.; Haiss, P. The hidden equilibrium in aqueous sodium carbonate solutions-evidence for the formation of the dicarbonate anion. *Eur. J. Inorg. Chem.* **2005**, *2005*, 168–172.
- (36) Bruna, P. J.; Grein, F.; Passmore, J. Density functional theory (DFT) calculations on the structures and stabilities of [C<sub>n</sub>O<sub>2n+1</sub>]<sup>2-</sup> and [C<sub>n</sub>O<sub>2n+1</sub>]<sub>X</sub> polycarbonates containing chainlike (CO<sub>2</sub>)<sub>n</sub> units (*n* = 2–6; X = H or Li). *Can. J. Chem.* **2011**, *89*, 671–687.
- (37) Zhang, L.; Huang, X.; Qin, C.; Brinkman, K.; Gong, Y.; Wang, S.; Huang, K. First Spectroscopic Identification of Pyrocarbonate for High CO<sub>2</sub> Flux Membranes Containing Highly Interconnected Three Dimensional Ionic Channels. *Phys. Chem. Chem. Phys.* **2013**, *15*, 13147–13152.
- (38) Corradini, D.; Coudert, F.-X.; Vuilleumier, R. Carbon dioxide transport in molten calcium carbonate occurs through an oxo-Grothuss mechanism via a pyrocarbonate anion. *Nat. Chem.* **2016**, *8*, 454–460.
- (39) Busche, S.; Bluhm, K. Synthese und Kristallstruktur der ersten zinkhaltigen Pyroborat Ni<sub>1.5</sub>Zn<sub>0.5</sub>(B<sub>2</sub>O<sub>5</sub>) und Co<sub>1.5</sub>Zn<sub>0.5</sub>(B<sub>2</sub>O<sub>5</sub>). *Z. Naturforsch.* **1995**, *50b*, 1445–1449.
- (40) Takéuchi, Y. The crystal structure of magnesium pyroborate. *Acta Crystallogr.* **1952**, *5*, 574–581.
- (41) Lin, W.-S.; Cheng, W.-D.; Chen, J.-T.; Huang, J.-S. Calcium pyroborate, Ca<sub>3</sub>B<sub>2</sub>O<sub>5</sub>. *Acta Crystallogr.* **1999**, *C55*, 4–6.
- (42) Volkov, S.; Dušek, M.; Bubnova, R.; Krzhizhanovskaya, M.; Ugolkov, V.; Obozova, E.; Filatov, S. Orientational order-disorder  $\gamma \leftrightarrow \beta \leftrightarrow \alpha'$  phase transitions in Sr<sub>2</sub>B<sub>2</sub>O<sub>5</sub> pyroborate and crystal structures of  $\beta$  and  $\alpha'$  phases. *Acta Crystallogr.* **2017**, *B73*, 1056–1067.
- (43) Maschmeyer, E. M.; Sanjeewa, L. D.; Ranmohotti, K. G. S. Crystal structure of BaMnB<sub>2</sub>O<sub>5</sub> containing structurally isolated manganese oxide sheets. *Acta Crystallogr.* **2016**, *E72*, 1315–1320.
- (44) Hisatsune, I. C.; Devlin, J. P.; Wada, Y. Vibrational spectrum and structure of N<sub>2</sub>O<sub>5</sub>. *Spectrochim. Acta* **1962**, *18*, 1641–1653.
- (45) El Din, A. M. S.; El Hosary, A. A. Pyronitrate: a new anion of pentavalent nitrogen. *J. Inorg. Nucl. Chem.* **1966**, *28*, 3043.
- (46) McClelland, B. W.; Hedberg, L.; Hedberg, K.; Hagen, K. Molecular Structure of N<sub>2</sub>O<sub>5</sub> in the Gas Phase. Large Amplitude Motion in a System of Coupled Rotors. *J. Am. Chem. Soc.* **1983**, *105*, 3789–3793.
- (47) McClelland, B. M.; Richardson, A. D.; Hedberg, K. A Reinvestigation of the Structure and Torsional Potential of N<sub>2</sub>O<sub>5</sub> by Gas Phase Electron Diffraction Augmented by *Ab Initio* Theoretical Calculations. *Helv. Chim. Acta* **2001**, *84*, 1612–1624.
- (48) Yoo, C.-S.; Iota, V.; Cynn, H. Nonlinear Carbon Dioxide at High Pressures and Temperatures. *Phys. Rev. Lett.* **2001**, *86*, 444–447.
- (49) Biedermann, N.; Speziale, S.; Winkler, B.; Reichmann, H. J.; Koch-Müller, M.; Heide, G. High-pressure phase behavior of SrCO<sub>3</sub>: an experimental and computational Raman scattering study. *Phys. Chem. Minerals* **2017**, *44*, 335–343.
- (50) Datchi, F.; Mallick, B.; Salamat, A.; Ninet, S. Structure of Polymeric Carbon Dioxide CO<sub>2</sub>-V. *Phys. Rev. Lett.* **2012**, *108*, 125701.
- (51) Dziubek, K. F.; Ende, M.; Scelta, D.; Bini, R.; Mezouar, M.; Garbarino, G.; Miletich, R. Crystalline polymeric carbon dioxide stable at megabar pressures. *Nat. Commun.* **2018**, *9*, 3148.
- (52) Segall, M. D.; Pickard, C. J.; Shah, R.; Payne, M. C. Population analysis in plane wave electronic structure calculations. *Mol. Phys.* **1996**, *89*, 571–577.
- (53) Segall, M. D.; Shah, R.; Pickard, C. J.; Payne, M. C. Population analysis of plane-wave electronic structure calculations of bulk materials. *Phys. Rev. B* **1996**, *54*, 16317–16320.
- (54) Mouhat, F.; Coudert, F.-X. Necessary and sufficient elastic stability conditions in various crystal systems. *Phys. Rev. B* **2014**, *90*, 224104.
- (55) Nguyen-Thanh, T.; Bosak, A.; Bauer, J. D.; Luchitskaia, R.; Refson, K.; Milman, V.; Winkler, B. Lattice dynamics and elasticity of SrCO<sub>3</sub>. *J. Appl. Crystallogr.* **2016**, *49*, 1982–1990.
- (56) Dasgupta, R.; Hirschmann, M. M. The deep carbon cycle and melting in Earth's interior. *EPSL* **2010**, *298*, 1–13.
- (57) Kelemen, P. B.; Manning, C. E. Reevaluating carbon fluxes in subduction zones, what goes down, mostly comes up. *Proc. Natl. Acad. Sci. U.S.A.* **2015**, *111*, E3997–E4006.
- (58) Li, X.; Zhang, Z.; Lin, J.-F.; Ni, H.; Prakupenka, V. B.; Mao, Z. New high-pressure phase of CaCO<sub>3</sub> at the topmost lower mantle: Implication for the deep-mantle carbon transportation. *Geophys. Res. Lett.* **2018**, *45*, 1355–1360.
- (59) Aresta, M.; Dibenedetto, A. Utilisation of CO<sub>2</sub> as a chemical feedstock: opportunities and challenges. *Dalton Trans.* **2007**, *28*, 2975–2992.
- (60) Sakakura, T.; Choi, J.-C.; Yasuda, H. Transformation of carbon dioxide. *Chem. Rev.* **2007**, *107*, 2365–2387.
- (61) Cokoja, M.; Bruckmeier, C.; Rieger, B.; Herrmann, W. A.; Kühn, F. E. Transformation of Carbon Dioxide with Homogeneous Transition-Metal Catalysts: A Molecular Solution to a Global Challenge? *Angew. Chem., Int. Ed.* **2011**, *50*, 8510–8537.

(62) Tamura, M.; Ito, K.; Honda, M.; Nakagawa, Y.; Sugimoto, H.; Tomishige, K. Direct Copolymerization of CO<sub>2</sub> and Diols. *Sci. Rep.* **2016**, *6*, 24038.



**JACS** Au  
AN OPEN ACCESS JOURNAL OF THE AMERICAN CHEMICAL SOCIETY



Editor-in-Chief  
**Prof. Christopher W. Jones**  
Georgia Institute of Technology, USA

**Open for Submissions** 

pubs.acs.org/jacsau  ACS Publications  
Most Trusted. Most Cited. Most Read.

## Synthesis and Structure of Pb[C<sub>2</sub>O<sub>5</sub>]: An Inorganic Pyrocarbonate Salt

Dominik Spahr,\* Jannes König, Lkhamsuren Bayarjargal, Rita Luchitskaia, Victor Milman, Alexander Perlov, Hanns-Peter Liermann, and Björn Winkler

Cite This: *Inorg. Chem.* 2022, 61, 9855–9859

Read Online

ACCESS |

Metrics & More

Article Recommendations

Supporting Information

**ABSTRACT:** We have synthesized Pb[C<sub>2</sub>O<sub>5</sub>], an inorganic pyrocarbonate salt, in a laser-heated diamond anvil cell (LH-DAC) at 30 GPa by heating a Pb[CO<sub>3</sub>] + CO<sub>2</sub> mixture to ≈2000(200) K. Inorganic pyrocarbonates contain isolated [C<sub>2</sub>O<sub>5</sub>]<sup>2-</sup> groups without functional groups attached. The [C<sub>2</sub>O<sub>5</sub>]<sup>2-</sup> groups consist of two oxygen-sharing [CO<sub>3</sub>]<sup>3-</sup> groups. Pb[C<sub>2</sub>O<sub>5</sub>] was characterized by synchrotron-based single-crystal structure refinement, Raman spectroscopy, and density functional theory calculations. Pb[C<sub>2</sub>O<sub>5</sub>] is isostructural to Sr[C<sub>2</sub>O<sub>5</sub>] and crystallizes in the monoclinic space group *P*2<sub>1</sub>/*c* with *Z* = 4. The synthesis of Pb[C<sub>2</sub>O<sub>5</sub>] demonstrates that, just like in other carbonates, cation substitution is possible and that therefore inorganic pyrocarbonates are a novel family of carbonates, in addition to the established sp<sup>2</sup> and sp<sup>3</sup> carbonates.

The so-called “conventional” carbonates with M[CO<sub>3</sub>] composition are characterized by nearly trigonal-planar [CO<sub>3</sub>]<sup>2-</sup> groups in which the carbon atom is forming C sp<sup>2</sup> hybrid orbitals with the three surrounding oxygen atoms.<sup>1,2</sup> In these carbonates, cation substitution is well-known, and depending on the size of the cation (M<sup>2+</sup>), different structures can be found.<sup>2,3</sup> Carbonates containing smaller cations such as magnesite (Mg[CO<sub>3</sub>]), siderite (Fe[CO<sub>3</sub>]), or otavite (Cd[CO<sub>3</sub>]) generally crystallize at ambient conditions with a calcite-type crystal structure and *R*3̄*c* space group symmetry. In contrast, larger cations lead to the formation of an aragonite-type structure and space group symmetry *Pm**cn* as observed, e.g., in strontianite (Sr[CO<sub>3</sub>]), witherite (Ba[CO<sub>3</sub>]), or cerussite (Pb[CO<sub>3</sub>]).<sup>4</sup> High-pressure polymorphs of “conventional” carbonates such as Mg[CO<sub>3</sub>], Ca[CO<sub>3</sub>], or Fe[CO<sub>3</sub>] can persist up to pressures of ≈70 GPa, while the [CO<sub>3</sub>]<sup>2-</sup> groups behave as rigid units.<sup>5–7</sup>

Other types of carbonates are sp<sup>3</sup> carbonates. Here, a central carbon atom is tetrahedrally coordinated by four covalently bound oxygen atoms, forming [CO<sub>4</sub>]<sup>4-</sup> tetrahedra. They are structurally diverse because the [CO<sub>4</sub>]<sup>4-</sup> tetrahedra may polymerize by corner-sharing.<sup>6–23</sup> Hence, carbonates with isolated [CO<sub>4</sub>]<sup>4-</sup> tetrahedra or with groups, rings, chains, or pyramids of [CO<sub>4</sub>]<sup>4-</sup> tetrahedra can be obtained (see the summary in Spahr et al.<sup>22</sup>). Cation substitution is also possible in sp<sup>3</sup> carbonates, where, e.g., isostructural Ca<sub>2</sub>[CO<sub>4</sub>] and Sr<sub>2</sub>[CO<sub>4</sub>] have been found.<sup>19,20</sup> Ba<sub>3</sub>[CO<sub>4</sub>]O was predicted to be isostructural to the recently synthesized sp<sup>3</sup> carbonate Sr<sub>3</sub>[CO<sub>4</sub>]O.<sup>22,24</sup> Alkali-metal sp<sup>3</sup> carbonates such as Li<sub>4</sub>[CO<sub>4</sub>] and Na<sub>4</sub>[CO<sub>4</sub>] have been predicted but have not yet been synthesized.<sup>25,26</sup>

Recently, a further novel carbonate type has been synthesized. Sr[C<sub>2</sub>O<sub>5</sub>] is the first inorganic pyrocarbonate salt.<sup>27</sup> It is characterized by [C<sub>2</sub>O<sub>5</sub>]<sup>2-</sup> complex anions in which two [CO<sub>3</sub>]<sup>2-</sup> groups are linked by sharing one oxygen atom. It was obtained by the synthesis from Sr[CO<sub>3</sub>] and CO<sub>2</sub> at 30

GPa in a laser-heated diamond anvil cell (LH-DAC). Until the discovery of Sr[C<sub>2</sub>O<sub>5</sub>], the experimental demonstration of the existence of isolated [C<sub>2</sub>O<sub>5</sub>]<sup>2-</sup> groups was tenuous. Their formation had earlier been proposed in melts, in aqueous carbonate solutions, and in the gas phase and had been inferred from two weak Raman peaks in the spectrum of a eutectic Li<sub>2</sub>[CO<sub>3</sub>]-Na<sub>2</sub>[CO<sub>3</sub>] melt.<sup>28–34</sup> This is in contrast to pyrocarbonate esters (R<sub>1</sub>-[C<sub>2</sub>O<sub>5</sub>]-R<sub>2</sub>), which do not contain isolated [C<sub>2</sub>O<sub>5</sub>]<sup>2-</sup> groups but are well-known, e.g., from organic syntheses and biochemistry.<sup>35–38</sup>

Our density functional theory (DFT)-based calculations have indicated that further pyrocarbonates may be obtained.<sup>27</sup> In order to establish pyrocarbonates as a novel carbonate group, we describe the successful approach to obtaining a further inorganic pyrocarbonate salt in this study. The ionic radii of Sr<sup>2+</sup> (*r* = 1.31 Å) and Pb<sup>2+</sup> (*r* = 1.35 Å) only differ by ≈3% for a 9-fold coordination.<sup>39</sup> Furthermore, at ambient conditions, the carbonates Sr[CO<sub>3</sub>] (*V* = 259.00 Å<sup>3</sup>) and Pb[CO<sub>3</sub>] (*V* = 270.82 Å<sup>3</sup>) both have an aragonite-type structure, and the unit cell volume of Pb[CO<sub>3</sub>] is just ≈4% larger than that of Sr[CO<sub>3</sub>].<sup>40</sup> It therefore seems likely that if a cation substitution is possible in pyrocarbonates, Pb[C<sub>2</sub>O<sub>5</sub>] can be obtained in a manner similar to that of Sr[C<sub>2</sub>O<sub>5</sub>].

In the present study, we synthesized Pb[C<sub>2</sub>O<sub>5</sub>] in analogy to the successful synthesis of Sr[C<sub>2</sub>O<sub>5</sub>] in a LH-DAC using a Pb[CO<sub>3</sub>] single crystal and CO<sub>2</sub>-I (dry ice) as starting materials. In a first step, a Pb[CO<sub>3</sub>] crystal and a ruby chip for pressure determination were placed on the diamond's culet.

Received: May 4, 2022

Published: June 22, 2022



Afterward, CO<sub>2</sub> was directly condensed from a gas jet into the gasket hole, and the DAC was closed tightly (Figure 1a). The

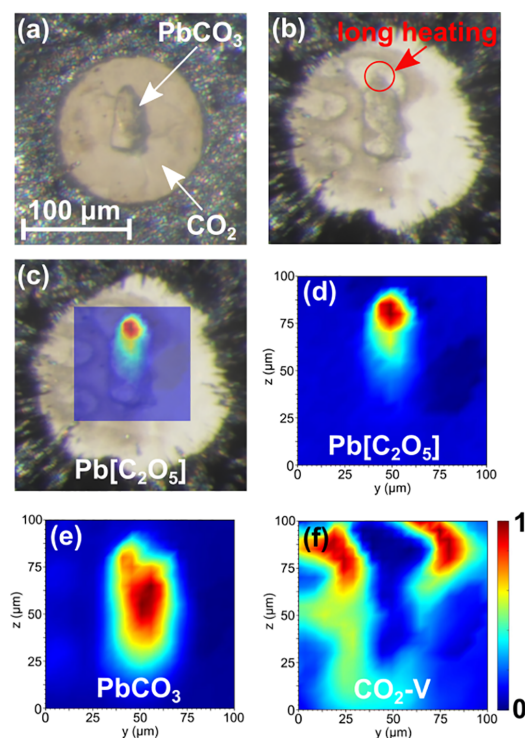


**Figure 1.** (a) Pb[CO<sub>3</sub>] and CO<sub>2</sub>-I (dry ice) in the gasket hole after cryogenic loading at 5.0(3) GPa. (b) Pb[CO<sub>3</sub>] + CO<sub>2</sub> mixture after laser heating at 30(2) GPa. (c) Raman map of Pb[C<sub>2</sub>O<sub>5</sub>] overlaying a picture of the gasket hole. Raman maps of Pb[C<sub>2</sub>O<sub>5</sub>] (d), Pb[CO<sub>3</sub>] (e), and CO<sub>2</sub>-V (f) after heating.

Pb[CO<sub>3</sub>] and CO<sub>2</sub> mixture was compressed without heating to target pressures of approximately 10, 20, and 30 GPa. A reaction could only be induced by laser-heating at 30(2) GPa.

It was described earlier that upon compression Pb[CO<sub>3</sub>] undergoes two-phase transitions up to 20 GPa, but these do not result in noticeable changes in our Raman spectra (Figure S2).<sup>41–45</sup> CO<sub>2</sub>-I (dry ice) undergoes a phase transition to CO<sub>2</sub>-III at ≈12 GPa, and the transition may take place in a broad pressure interval.<sup>46–48</sup> In contrast to earlier studies, our Raman spectra (Figure S2) show the transition at slightly higher pressures (15–20 GPa). This may be due to a pressure gradient in the gasket hole between the position of the ruby and the spot where the Raman data were acquired. The pressure conditions in the DAC are very likely nonhydrostatic because CO<sub>2</sub>-III may sustain large pressure gradients (e.g., 0.2 GPa μm<sup>-1</sup> at high pressures).<sup>49</sup> In general, we observed no significant broadening of the Raman bands of Pb[CO<sub>3</sub>] and CO<sub>2</sub> but slightly shifted peak positions of the Raman bands depending on the location of the laser spot in the DAC caused by the pressure gradients.

After reaching the target pressure, the Pb[CO<sub>3</sub>]-III + CO<sub>2</sub>-III mixture was laser-heated at an edge of the Pb[CO<sub>3</sub>] crystal

from both sides (Figure 1b). An initial heating caused a small pressure drop, and the pressure was therefore readjusted. Afterward, the crystal was heated to a maximum temperature of ≈2000(200) K for 30 min. During heating, CO<sub>2</sub>-III underwent a phase transition to CO<sub>2</sub>-V in the heated regions, causing the occurrence of an intense new Raman mode at ≈750 cm<sup>-1</sup>.<sup>50</sup> In addition to the characteristic CO<sub>3</sub> stretching mode of Pb[CO<sub>3</sub>] at ≈1120 cm<sup>-1</sup>, several new Raman modes appear in the regions at 500–600 and 900–1100 cm<sup>-1</sup> in the heated area (Figure 2). These Raman modes are characteristic for the vibrations of the [C<sub>2</sub>O<sub>5</sub>] group.<sup>27</sup>

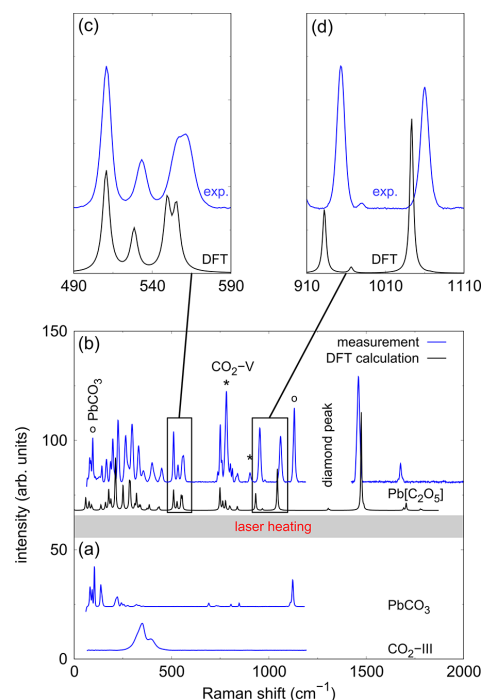


**Figure 2.** (a) Raman spectra for Pb[CO<sub>3</sub>] and CO<sub>2</sub> before laser heating in a DAC. (b) Experimental Raman spectra for Pb[C<sub>2</sub>O<sub>5</sub>] at 30(2) GPa after heating in comparison to DFT-based calculations. The peaks of Pb[CO<sub>3</sub>] are marked by a circle (O), and those of CO<sub>2</sub>-V are marked by an asterisk (\*). Enlargement of the regions at (c) 490–590 and (d) 910–1110 cm<sup>-1</sup>, which are characteristic for the pyrocarbonate eigenmodes. The calculated Raman shifts were rescaled by 3%.

Mapping the intensity distribution of the Raman modes (Pb[C<sub>2</sub>O<sub>5</sub>], 953 cm<sup>-1</sup>; CO<sub>2</sub>, 782 cm<sup>-1</sup>; Pb[CO<sub>3</sub>], 1130 cm<sup>-1</sup>) allowed us to locate a region in the DAC where the pyrocarbonate was formed (Figure 1c,d). This region coincides with the heated area of the Pb[CO<sub>3</sub>] crystal. We used the monoclinic structural model determined for Sr[C<sub>2</sub>O<sub>5</sub>] (P2<sub>1</sub>/c; Z = 4) to calculate the theoretical Raman spectrum of Pb[C<sub>2</sub>O<sub>5</sub>].<sup>27</sup> The agreement between the experimental data and DFT calculations is very satisfactory over the full accessible energy range, including Raman peaks with wavenumbers of >1400 cm<sup>-1</sup> (Raman measurements are not possible in the diamond window, ≈1300–1400 cm<sup>-1</sup>).

Specifically, the Raman modes in the regions of 500–600 and 900–1100  $\text{cm}^{-1}$  were accurately reproduced by the calculations (Figure 2c,d), confirming the presence of the pyrocarbonate group. We also mapped the intensity of the  $\text{CO}_3$  stretching mode of unreacted  $\text{Pb}[\text{CO}_3]$  in the DAC (Figure 1e). The Raman map accurately reproduces the shape of the crystal (Figure 1b). In addition, the intense Raman mode of  $\text{CO}_2\text{-V}$  can be observed around the heated area at the top of the  $\text{Pb}[\text{CO}_3]$  crystal (Figure 1f). Upon the release of pressure, the characteristic Raman modes of the pyrocarbonate group are present until pressures reach  $\approx 5$  GPa. However, they cannot be observed any more after the DAC is opened, implying that  $\text{Pb}[\text{C}_2\text{O}_5]$  is only stable at elevated pressures.

We employed synchrotron-based single-crystal X-ray diffraction in the area where  $\text{Pb}[\text{C}_2\text{O}_5]$  has unambiguously been identified by Raman spectroscopy (Figure 1c,d) to confirm the structural model employed in the DFT-based calculations. The refined structural model of the temperature-quenched sample at 30(2) GPa is shown in Figure 3a, and the results of the structure refinement are listed in Tables S1 and S2.

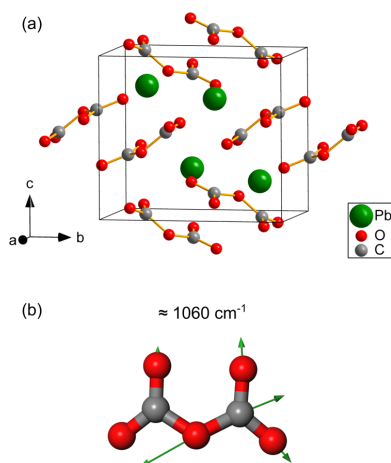


**Figure 3.** (a) Structural model of  $\text{Pb}[\text{C}_2\text{O}_5]$  obtained at 30(2) GPa by synchrotron-based single-crystal structure refinement in the monoclinic space group  $P2_1/c$  with  $Z = 4$ . (b) Eigenvector of the atomic displacements in the  $[\text{C}_2\text{O}_5]^{2-}$  group for a characteristic Raman mode at  $\approx 1060 \text{ cm}^{-1}$ .

By single-crystal structure refinement, we confirmed that  $\text{Pb}[\text{C}_2\text{O}_5]$  crystallizes at ambient temperature and 30(2) GPa in the monoclinic space group  $P2_1/c$  with  $Z = 4$ . The experimentally determined lattice parameters  $a = 4.771(1) \text{ \AA}$ ,  $b = 8.079(4) \text{ \AA}$ ,  $c = 7.070(7) \text{ \AA}$ , and  $\beta = 91.32(5)^\circ$  [ $V = 272.4(3) \text{ \AA}^3$ ] are in good agreement with our DFT-based calculations (Table S1). The relatively low  $wR$  value ( $wR = 6.7\%$ ) and an appropriate reflection to the parameter ratio ( $\approx 12:1$ ) strongly support the reliability of our analysis of the experimental data. In order to reduce the amount of free parameters, the isotropic displacement parameters of the symmetrically independent carbon atoms as well as of the oxygen atoms were constrained to be identical. The differences between the structural models of  $\text{Pb}[\text{C}_2\text{O}_5]$  and  $\text{Sr}[\text{C}_2\text{O}_5]$  are very small (Table S1). At 30 GPa, we observed only a  $\approx 1\%$  difference in the unit cell volume between the structures. This

is consistent with the very similar cation radii of  $\text{Pb}^{2+}$  and  $\text{Sr}^{2+}$ .<sup>27,39</sup> The geometry of the  $[\text{C}_2\text{O}_5]^{2-}$  group in  $\text{Pb}[\text{C}_2\text{O}_5]$  is similar to that in  $\text{Sr}[\text{C}_2\text{O}_5]$  and in very good agreement with the calculated and proposed equilibrium geometry of the  $[\text{C}_2\text{O}_5]^{2-}$  group.<sup>27,33,34</sup> The C–O bonds to the shared oxygen atom are slightly longer [1.42(3)  $\text{\AA}$ ] than the C–O bonds between the carbon atoms and the terminal oxygen atoms [1.15(3)–1.25(3)  $\text{\AA}$ ], which is also observed in  $\text{Sr}[\text{C}_2\text{O}_5]$ . The deviation from the ideal O–C–O angle of  $120^\circ$  is larger in  $\text{Pb}[\text{C}_2\text{O}_5]$  than that in  $\text{Sr}[\text{C}_2\text{O}_5]$ . The diffraction data were dominated by the contribution of the heavy lead atoms, and the access to the reciprocal space is limited in the DAC. While this leads to an increase in the uncertainties on the atomic positions of carbon and oxygen atoms relative to the error on the positional parameters of lead, the structural model is robust.

We used the structural model of  $\text{Pb}[\text{C}_2\text{O}_5]$  for density functional perturbation theory calculations and calculated selected eigenvectors of the atomic displacements in the  $[\text{C}_2\text{O}_5]^{2-}$  group. An example of the displacements in the  $[\text{C}_2\text{O}_5]^{2-}$  group for the characteristic Raman mode at  $\approx 1060 \text{ cm}^{-1}$  at 30 GPa is shown in Figure 3b. Equation-of-state fits to the theoretical data (Figure S4) yield  $K_0^{\text{Pb}[\text{C}_2\text{O}_5]} = 36(3)$  GPa and  $K_0^{\text{Sr}[\text{C}_2\text{O}_5]} = 40(3)$  GPa. The chemically related strontium orthocarbonate has a bulk modulus of  $K_0^{\text{Sr}[\text{CO}_3]} = 110(5)$  GPa, while strontianite has  $K_0^{\text{Sr}[\text{CO}_3]} = 63(3)$  GPa.<sup>19,51</sup>

The presence of  $\text{Pb}^{2+}$  raises the question of whether a stereochemically active lone electron pair is present. Stereochemically active lone electron pairs on large, polarizable ions such as lead or bismuth may persist up to very high pressures.<sup>52–54</sup> It is straightforward to identify them in DFT electron density difference maps, i.e., in isosurfaces depicting the difference between the self-consistent electron density distribution and an electron density distribution obtained by overlapping atomic electron density distributions. In such isosurfaces, stereochemically active localized electron pairs appear as umbrella-shaped maxima at difference densities of  $\approx 0.03\text{--}0.04 \text{ e}^-/\text{\AA}^3$  at about 0.5  $\text{\AA}$  away for the ion position.<sup>52–54</sup> For  $\text{Pb}[\text{C}_2\text{O}_5]$ , no such localized stereochemically active lone electron pairs were found at any pressure between 0 and 50 GPa.

In conclusion, we have synthesized  $\text{Pb}[\text{C}_2\text{O}_5]$ , a new inorganic pyrocarbonate salt with isolated  $[\text{C}_2\text{O}_5]^{2-}$  groups in a LH-DAC at moderate pressure and temperature conditions and characterized it by synchrotron-based single-crystal X-ray diffraction, Raman spectroscopy, and DFT-based calculations. The synthesis of  $\text{Pb}[\text{C}_2\text{O}_5]$  establishes pyrocarbonates as a novel group of carbonates. Inorganic pyrocarbonates close the gap of compounds with pyro-groups between the well-established pyroborates ( $[\text{B}_2\text{O}_5]^{4-}$ ) and molecular pyronitrate ( $\text{N}_2\text{O}_5$ ).<sup>55–63</sup> We demonstrated that cation substitution is possible in this new family of carbonates ( $\text{M}[\text{C}_2\text{O}_5]$  with  $\text{M}^{2+} = \text{Sr}, \text{Pb}, \text{etc.}$ ), providing a roadmap for the discovery of new compounds containing  $[\text{C}_2\text{O}_5]^{2-}$  groups.

## ■ ASSOCIATED CONTENT

### SI Supporting Information

The Supporting Information is available free of charge at <https://pubs.acs.org/doi/10.1021/acs.inorgchem.2c01507>.

Experimental and computational details of the experiments and the results of single-crystal structure refinement (PDF)

### Accession Codes

CCDC 2151951 and 2151952 contain the supplementary crystallographic data for this paper. These data can be obtained free of charge via [www.ccdc.cam.ac.uk/data\\_request/cif](http://www.ccdc.cam.ac.uk/data_request/cif), or by emailing [data\\_request@ccdc.cam.ac.uk](mailto:data_request@ccdc.cam.ac.uk), or by contacting The Cambridge Crystallographic Data Centre, 12 Union Road, Cambridge CB2 1EZ, UK; fax: +44 1223 336033.

### AUTHOR INFORMATION

#### Corresponding Author

**Dominik Spahr** – Institute of Geosciences, Goethe University Frankfurt, Frankfurt 60438, Germany; [orcid.org/0000-0003-0489-5270](https://orcid.org/0000-0003-0489-5270); Email: [d.spahr@kristall.uni-frankfurt.de](mailto:d.spahr@kristall.uni-frankfurt.de)

#### Authors

**Jannes König** – Institute of Geosciences, Goethe University Frankfurt, Frankfurt 60438, Germany; [orcid.org/0000-0003-2960-7714](https://orcid.org/0000-0003-2960-7714)

**Lkhamsuren Bayarjargal** – Institute of Geosciences, Goethe University Frankfurt, Frankfurt 60438, Germany

**Rita Luchitskaia** – Institute of Geosciences, Goethe University Frankfurt, Frankfurt 60438, Germany

**Victor Milman** – Dassault Systèmes BIOVIA, Cambridge CB4 0WN, United Kingdom; [orcid.org/0000-0003-2258-1347](https://orcid.org/0000-0003-2258-1347)

**Alexander Perlov** – Dassault Systèmes BIOVIA, Cambridge CB4 0WN, United Kingdom

**Hanns-Peter Liermann** – Deutsches Elektronen-Synchrotron DESY, Hamburg 22607, Germany

**Björn Winkler** – Institute of Geosciences, Goethe University Frankfurt, Frankfurt 60438, Germany; [orcid.org/0000-0001-8029-478X](https://orcid.org/0000-0001-8029-478X)

Complete contact information is available at: <https://pubs.acs.org/10.1021/acs.inorgchem.2c01507>

#### Notes

The authors declare no competing financial interest.

### ACKNOWLEDGMENTS

We gratefully acknowledge funding from the DFG (Projects WI1232 and BA4020) and the DFG-Research Unit FOR2125/CarboPaT. B.W. is grateful for support by the BIOVIA Science Ambassador program. We acknowledge DESY (Hamburg, Germany), a member of the Helmholtz Association HGF, for the provision of experimental facilities. Parts of this research were carried out at PETRA III, beamline P02.2.

### REFERENCES

- Winkler, B.; Zemann, J.; Milman, V. Aplanarity of CO<sub>3</sub> groups: A theoretical investigation. *Acta Cryst. B* **2000**, *56*, 648–653.
- Reeder, R. J., Ed. *Carbonates: Mineralogy and Chemistry*; De Gruyter: Berlin, 1983; DOI: [10.1515/9781501508134](https://doi.org/10.1515/9781501508134).
- Okrusch, M.; Frimmel, H., Eds. *Mineralogy: An Introduction to Minerals, Rocks, and Mineral Deposits*; Springer-Verlag: Berlin, 2020; DOI: [10.1007/978-3-662-57316-7](https://doi.org/10.1007/978-3-662-57316-7).
- Liu, L.-G.; Lin, C.-C. A calcite → aragonite-type phase transition in CdCO<sub>3</sub>. *Am. Mineral.* **1997**, *82*, 643–646.
- Bayarjargal, L.; Fruhner, C.-J.; Schrodt, N.; Winkler, B. CaCO<sub>3</sub> phase diagram studied with Raman spectroscopy at pressures up to 50 GPa and high temperatures and DFT modeling. *Phys. Earth Planet. Inter.* **2018**, *281*, 31–45.
- Cerantola, V.; et al. Stability of iron-bearing carbonates in the deep Earth's interior. *Nat. Commun.* **2017**, *8*, 15960.
- Binck, J.; Bayarjargal, L.; Lobanov, S. S.; Morgenroth, W.; Luchitskaia, R.; Pickard, C. J.; Milman, V.; Refson, K.; Jochym, D. B.; Byrne, P.; Winkler, B. Phase stabilities of MgCO<sub>3</sub> and MgCO<sub>3</sub>-II studied by Raman spectroscopy, X-ray diffraction, and density functional theory calculations. *Phys. Rev. Mater.* **2020**, *4*, 055001.
- Chariton, S. The elastic properties and the crystal chemistry of carbonates in the deep Earth. Ph.D. Thesis, University of Bayreuth, Bayreuth, Germany, 2020.
- Boulard, E.; Pan, D.; Galli, G.; Liu, Z.; Mao, W. L. Tetrahedrally coordinated carbonates in Earth's lower mantle. *Nat. Commun.* **2015**, *6*, 8111; DOI: [10.1038/ncomms7311](https://doi.org/10.1038/ncomms7311).
- Merlini, M.; Cerantola, V.; Gatta, G. D.; Gemmi, M.; Hanfland, M.; Kuznetsov, I.; Lotti, P.; Müller, H.; Zhang, L. Dolomite-IV: Candidate structure for a carbonate in the Earth's lower mantle. *Am. Mineral.* **2017**, *102*, 1763–1766.
- Oganov, A. R.; Ono, S.; Ma, Y.; Glass, C. W.; Garcia, A. Novel high-pressure structures of MgCO<sub>3</sub>, CaCO<sub>3</sub> and CO<sub>2</sub> and their role in Earth's lower mantle. *EPSL* **2008**, *273*, 38–47.
- Boulard, E.; Gloter, A.; Cogné, A.; Antonangeli, D.; Auzende, A.-L.; Perrillat, J.-P.; Guyot, F.; Fiquet, G. New host for carbon in the deep Earth. *Proc. Natl. Acad. Sci. U.S.A.* **2011**, *108*, 5184–5187.
- Maeda, F.; Ohtani, E.; Kamada, S.; Sakamaki, T.; Hirao, N.; Ohishi, Y. Diamond formation in the deep lower mantle: A high-pressure reaction of MgCO<sub>3</sub> and SiO<sub>2</sub>. *Sci. Rep.* **2017**, *7*, 40602.
- Merlini, M.; Hanfland, M.; Salamat, A.; Petitgirard, S.; Müller, H. The crystal structures of Mg<sub>2</sub>Fe<sub>2</sub>C<sub>4</sub>O<sub>13</sub>, with tetrahedrally coordinated carbon, and Fe<sub>13</sub>O<sub>19</sub>, synthesized at deep mantle conditions. *Am. Mineral.* **2015**, *100*, 2001–2004.
- Oganov, A. R.; Glass, C. W.; Ono, S. High-pressure phases of CaCO<sub>3</sub>: Crystal structure prediction and experiment. *EPSL* **2006**, *241*, 95–103.
- Ono, S.; Kikegawa, T.; Ohishi, Y. High-pressure transition of CaCO<sub>3</sub>. *Am. Mineral.* **2007**, *92*, 1246–1249.
- Pickard, C. J.; Needs, R. J. Structures and stability of calcium and magnesium carbonates at mantle pressures. *Phys. Rev. B* **2015**, *91*, 104101.
- Lobanov, S. S.; Dong, X.; Martirosyan, N. S.; Samtsevich, A. I.; Stevanovic, V.; Gavryushkin, P. N.; Litasov, K. D.; Greenberg, E.; Prakapenka, V. B.; Oganov, A. R.; Goncharov, A. F. Raman spectroscopy and X-ray diffraction of sp<sup>3</sup>-CaCO<sub>3</sub> at lower mantle pressures. *Phys. Rev. B* **2017**, *96*, 104101.
- Laniel, D.; Binck, J.; Winkler, B.; Vogel, S.; Fedotenko, T.; Chariton, S.; Prakapenka, V.; Milman, V.; Schnick, W.; Dubrovinsky, L.; Dubrovinskaia, N. Synthesis, crystal structure and structure-property relations of strontium orthocarbonate, Sr<sub>2</sub>CO<sub>4</sub>. *Acta Crystallogr.* **2021**, *B77*, 131–137.
- Binck, J.; Laniel, D.; Bayarjargal, L.; Khandarkhaeva, S.; Fedotenko, T.; Aslandukov, A.; Glazyrin, K.; Milman, V.; Chariton, S.; Prakapenka, V. B.; Dubrovinskaia, N.; Dubrovinsky, L.; Winkler, B. Synthesis of calcium orthocarbonate, Ca<sub>2</sub>CO<sub>4</sub>-Pnma in *p*, *T*-conditions of Earth's transition zone and lowermantle. *Am. Mineral.* **2021**; DOI: [10.2138/am-2021-7872](https://doi.org/10.2138/am-2021-7872).
- Spahr, D.; Binck, J.; Bayarjargal, L.; Luchitskaia, R.; Morgenroth, W.; Comboni, D.; Milman, V.; Winkler, B. Tetrahedrally Coordinated sp<sup>3</sup>-Hybridized Carbon in Sr<sub>2</sub>CO<sub>4</sub> Orthocarbonate at Ambient Conditions. *Inorg. Chem.* **2021**, *60*, 5419–5422.
- Spahr, D.; König, J.; Bayarjargal, L.; Gavryushkin, P. N.; Liermann, H.-P.; Milman, V.; Winkler, B. Sr<sub>3</sub>[CO<sub>4</sub>]O-antiperovskite with tetrahedrally-coordinated sp<sup>3</sup>-hybridized carbon and OSr<sub>6</sub>-octahedra. *Inorg. Chem.* **2021**, *60*, 14504–14508.
- König, J.; Spahr, D.; Bayarjargal, L.; Gavryushkin, P. N.; Milman, V.; Liermann, H.-P.; Winkler, B.; Sagatova, D.; Sagatov, N. Novel calcium sp<sup>3</sup>-carbonate CaC<sub>2</sub>O<sub>4</sub>-I42d may be a carbon host in Earth's lower mantle. *Earth. Space. Chem.* **2022**, *6*, 73–80.
- Gavryushkin, P. N.; Sagatova, D. N.; Sagatov, N.; Litasov, K. D. Orthocarbonates of Ca, Sr, and Ba — the appearance of sp<sup>3</sup>-hybridized carbon at a pressure of 5 GPa and dynamic stability at ambient pressure. *Earth. Space. Chem.* **2021**, *5*, 1948–1957.

- (25) Čančarević, Z. P.; Schön, J. C.; Jansen, M. Possible Existence of Alkali Metal Orthocarbonates at High Pressure. *Chem. Eur. J.* **2007**, *13*, 7330–7348.
- (26) Sagatova, N. E.; Sagatov, D. N.; Gavryushkin, P. N.; Banaev, M. V.; Litasov, K. D. Alkali Metal (Li, Na, and K) Orthocarbonates: Stabilization of  $sp^3$ -Bonded Carbon at Pressures above 20 GPa. *Cryst. Growth Des.* **2021**, *21*, 6744–6751.
- (27) Spahr, D.; König, J.; Bayarjargal, L.; Milman, V.; Perlov, A.; Liermann, H.-P.; Winkler, B.  $Sr[C_2O_3]$  is an Inorganic Pyrocarbonate Salt with  $[C_2O_3]^{2-}$  Complex Anions. *J. Am. Chem. Soc.* **2022**, *144*, 2899–2904.
- (28) Claes, P.; Moyaux, D.; Peeters, D. Solubility and solvation of carbon dioxide in the molten  $Li_2CO_3/Na_2CO_3/K_2CO_3$  (43.5:31.5:25.0 mol-%) eutectic mixture at 973K. I. Experimental part. *Eur. J. Inorg. Chem.* **1999**, *1999*, 583–588.
- (29) Peeters, D.; Moyaux, D.; Claes, P. Solubility and solvation of carbon dioxide in the molten  $Li_2CO_3/Na_2CO_3/K_2CO_3$  (43.5:31.5:25.0 mol-%) eutectic mixture at 973K. I. Theoretical part. *Eur. J. Inorg. Chem.* **1999**, *1999*, 589–592.
- (30) Frapper, G.; Saillard, J.-Y. Search for new allotropic forms of carbon dioxide and carbon disulfide: a density functional study of  $CX_2$ -based oligomers ( $X = O, S$ ). *J. Am. Chem. Soc.* **2000**, *122*, 5367–5370.
- (31) Zeller, K.-P.; Schuler, P.; Haiss, P. The hidden equilibrium in aqueous sodium carbonate solutions—evidence for the formation of the dicarbonate anion. *Eur. J. Inorg. Chem.* **2005**, *2005*, 168–172.
- (32) Bruna, P. J.; Grein, F.; Passmore, J. Density functional theory (DFT) calculations on the structures and stabilities of  $[CnO_{2n+1}]^{2-}$  and  $[C_nO_{2n+1}]X_2$  polycarbonates containing chainlike  $(CO_2)_n$  units ( $n = 2 - 6$ ;  $X = H$  or  $Li$ ). *Can. J. Chem.* **2011**, *89*, 671–687.
- (33) Zhang, L.; Huang, X.; Qin, C.; Brinkman, K.; Gong, Y.; Wang, S.; Huang, K. First Spectroscopic Identification of Pyrocarbonate for High  $CO_2$  Flux Membranes Containing Highly Interconnected Three Dimensional Ionic Channels. *Phys. Chem. Chem. Phys.* **2013**, *15*, 13147–13152.
- (34) Corradini, D.; Coudert, F.-X.; Vuilleumier, R. Carbon dioxide transport in molten calcium carbonate occurs through an oxo-grothuss mechanism via a pyrocarbonate anion. *Nat. Chem.* **2016**, *8*, 454–460.
- (35) Solymosy, F.; Fedorcsák, I.; Gulyás, A.; Farkas, L. G.; Ehrenberg. A new method based on the use of diethyl pyrocarbonate as a nuclease inhibitor for the extraction of undegraded nucleic acid from plant tissues. *Eur. J. Biochem.* **1968**, *5*, 520–527.
- (36) Summers, W. C. A simple method for extraction of RNA from *E. coli* utilizing diethyl pyrocarbonate. *Anal. Biochem.* **1970**, *33*, 460–463.
- (37) Dalpozzo, R.; Bartoli, G.; Bosco, M.; Melchiorre, P.; Sambri, L. Recent Development about the Use of Pyrocarbonates as Activator in Organic Synthesis: A Review. *Curr. Org. Synth.* **2009**, *6*, 79–101.
- (38) An, B.; Meng, Y.; Li, Z.; Hong, Y.; Wang, T.; Wang, S.; Lin, J.; Wang, C.; Wan, S.; Wang, Y.; Lin, W. A pyrocarbonate intermediate for  $CO_2$  activation and selective conversion in bifunctional metal-organic frameworks. *J. Catal.* **2019**, *373*, 37–47.
- (39) Shannon, R. D. Revised effective ionic radii and systematic studies of interatomic distances in halides and chalcogenides. *Acta Crystallogr.* **1976**, *A32*, 751–767.
- (40) Antao, S. M.; Hassan, I. The orthorhombic structure of  $CaCO_3$ ,  $SrCO_3$ ,  $PbCO_3$  and  $BaCO_3$ : Linear structural trends. *Can. Mineral.* **2009**, *47*, 1245–1255.
- (41) Lin, C.-C.; Liu, L.-G. Post-aragonite phase transitions in strontianite and cerussite — a high pressure Raman spectroscopic study. *J. Phys. Chem. Solids* **1997**, *58*, 977–987.
- (42) Catalli, K.; Santillán, J.; Williams, Q. A high pressure infrared spectroscopic study of  $PbCO_3$ —cerussite: constraints on the structure of the post-aragonite phase. *Phys. Chem. Minerals* **2005**, *32*, 412–417.
- (43) Minch, R.; Dubrovinsky, L.; Kurnosov, A.; Ehm, L.; Knorr, K.; Depmeier, W. Raman spectroscopic study of  $PbCO_3$  at high pressures and temperatures. *Phys. Chem. Minerals* **2010**, *37*, 45–56.
- (44) Zhang, Y.-F.; Liu, J.; Qin, Z.-X.; Lin, C.-L.; Xiong, L.; Li, R.; Bai, L.-G. A high-pressure study of  $PbCO_3$  by XRD and Raman spectroscopy. *Chin. Phys. C* **2013**, *37*, 038001.
- (45) Gao, J.; Wu, X.; Qin, S.; Li, Y.-C. Pressure-induced phase transformations of  $PbCO_3$  by X-ray diffraction and Raman spectroscopy. *High Press. Res.* **2016**, *36*, 1–15.
- (46) Aoki, K.; Yamawaki, H.; Sakashita, M.; Gotoh, Y.; Takemura, K. Crystal Structure of the High-Pressure Phase of Solid  $CO_2$ . *Science* **1994**, *263*, 356–358.
- (47) Olijnyk, H.; Jephcoat, A. P. Vibrational studies on  $CO_2$  up to 40 GPa by Raman spectroscopy at room temperature. *Phys. Rev. B* **1998**, *57*, 879–888.
- (48) Scelta, D.; Dziubek, K. F.; Ende, M.; Miletich, R.; Mezouar, M.; Garbarino, G.; Bini, R. Extending the Stability Field of Polymeric Carbon Dioxide Phase V beyond the Earth's Geotherm. *Phys. Rev. Lett.* **2021**, *126*, 065701.
- (49) Yoo, C. S.; Cynn, H.; Gygi, F.; Galli, G.; Iota, V.; Nicol, M.; Carlson, S.; Hausermann, D.; Mailhot, C. Crystal Structure of Carbon Dioxide at High Pressure: “Superhard” Polymeric Carbon Dioxide. *Phys. Rev. Lett.* **1999**, *83*, 5527–5530.
- (50) Datchi, F.; Mallick, B.; Salamat, A.; Ninet, S. Structure of Polymeric Carbon Dioxide  $CO_2$ -V. *Phys. Rev. Lett.* **2012**, *108*, 125701.
- (51) Nguyen-Thanh, T.; Bosak, A.; Bauer, J. D.; Luchitskaia, R.; Refson, K.; Milman, V.; Winkler, B. Lattice dynamics and elasticity of  $SrCO_3$ . *J. Appl. Crystallogr.* **2016**, *49*, 1982–1990.
- (52) Friedrich, A.; Juarez-Arellano, E. A.; Haussühl, E.; Boehler, R.; Winkler, B.; Wiehl, L.; Morgenroth, W.; Burianek, W.; Mühlberg, M. Persistence of the stereochemical activity of the  $Bi^{3+}$  lone electron pair in  $Bi_2Ga_4O_9$  up to 50 GPa and crystal structure of the high-pressure phase. *Acta Crystallogr.* **2019**, *B66*, 323–337.
- (53) Girard, A.; Stekiel, M.; Morgenroth, W.; Taniguchi, H.; Milman, V.; Bosak, A.; Winkler, B. High-pressure compressibility and electronic properties of bismuth silicate  $Bi_2SiO_5$  from synchrotron experiments and first-principles calculations. *Phys. Rev. B* **2019**, *99*, 064116.
- (54) Spahr, D.; Stekiel, M.; Zimmer, D.; Bayarjargal, L.; Bunk, K.; Morgenroth, W.; Milman, V.; Refson, K.; Jochym, D.; Byrnee, P. J. P.; Winkler, B. Pressure-induced Pb–Pb bonding and phase transition in  $Pb_3SnO_8$ . *Acta Crystallogr.* **2020**, *B76*, 979–991.
- (55) Busche, S.; Bluhm, K. Synthese und Kristallstruktur der ersten zinkhaltigen Pyroborat  $Ni_{1.5}Zn_{0.5}(B_2O_5)$  und  $Co_{1.5}Zn_{0.5}(B_2O_5)$ . *Z. Naturforsch.* **1995**, *50b*, 1445–1449.
- (56) Takéuchi, Y. The crystal structure of magnesium pyroborate. *Acta Crystallogr.* **1952**, *5*, 574–581.
- (57) Lin, W.-S.; Cheng, W.-D.; Chen, J.-T.; Huang, J.-S. Calcium pyroborate,  $Ca_2B_2O_5$ . *Acta Crystallogr.* **1999**, *C55*, 4–6.
- (58) Volkov, S.; Dušek, M.; Bubnova, R.; Krzhizhanovskaya, M.; Ugolkov, V.; Obozova, E.; Filatov, S. Orientational order-disorder  $\gamma \leftrightarrow \beta \leftrightarrow \alpha' \leftrightarrow \alpha$  phase transitions in  $Sr_2B_2O_5$  pyroborate and crystal structures of  $\beta$  and  $\alpha$  phases. *Acta Crystallogr.* **2017**, *B73*, 1056–1067.
- (59) Maschmeyer, E. M.; Sanjeeva, L. D.; Ranmohotti, K. G. S. Crystal structure of  $BaMnB_2O_5$  containing structurally isolated manganese oxide sheets. *Acta Crystallogr.* **2016**, *E72*, 1315–1320.
- (60) Hisatsune, I. C.; Devlin, J. P.; Wada, Y. Vibrational spectrum and structure of  $N_2O_5$ . *Spectrochim. Acta* **1962**, *18*, 1641–1653.
- (61) El Din, A. M. S.; El hosary, A. A. Pyronitrate: a new anion of pentavalent nitrogen. *J. inorg. nucl. Chem.* **1966**, *28*, 3043.
- (62) McClelland, B. W.; Hedberg, L.; Hedberg, K.; Hagen, K. Molecular Structure of  $N_2O_5$  in the Gas Phase. Large Amplitude Motion in a System of Coupled Rotors. *J. Am. Chem. Soc.* **1983**, *105*, 3789–3793.
- (63) McClelland, B. M.; Richardson, A. D.; Hedberg, K. A Reinvestigation of the Structure and Torsional Potential of  $N_2O_5$  by GasPhase Electron Diffraction Augmented by *AbInitio* Theoretical Calculations. *Helv. Chim. Acta* **2001**, *84*, 1612–1624.



STRUCTURAL SCIENCE  
CRYSTAL ENGINEERING  
MATERIALS

ISSN 2052-5206

research paper



## A new $\text{BaCa}(\text{CO}_3)_2$ polymorph

Dominik Spahr,<sup>a\*</sup> Lkhamsuren Bayarjargal,<sup>a</sup> Victor Vinograd,<sup>b</sup> Rita Luchitskaia,<sup>a</sup> Victor Milman<sup>c</sup> and Björn Winkler<sup>a</sup>

<sup>a</sup>Institute of Geosciences, Crystallography, Frankfurt, Germany, <sup>b</sup>Institute of Energy and Climate Research (IEK-6), Nuclear Waste Management and Reactor Safety, Forschungszentrum Jülich, Jülich, Germany, and <sup>c</sup>Dassault Systèmes BIOVIA, Cambridge, United Kingdom. \*Correspondence e-mail: d.spahr@kristall.uni-frankfurt.de

Received 9 November 2018

Accepted 6 March 2019

Edited by R. Černý, University of Geneva, Switzerland

**Keywords:**  $\text{BaCa}(\text{CO}_3)_2$ ; barytocalcite; density functional theory; X-ray powder diffraction; Rietveld refinement; Raman spectroscopy.

**Supporting information:** this article has supporting information at journals.iucr.org/b

A new polymorph of the double carbonate  $\text{BaCa}(\text{CO}_3)_2$ , ‘a C2 phase’, has been synthesized. Its structure has been obtained by density-functional-theory-based (DFT-based) model calculations and has been refined by Rietveld analysis of X-ray powder diffraction data. The structure of the new polymorph differs significantly from those of the established polymorphs barytocalcite, paralstonite and alstonite. The unit-cell parameters of the new monoclinic (space group C2) compound are  $a = 6.6775$  (5),  $b = 5.0982$  (4),  $c = 4.1924$  (3) Å,  $\beta = 109.259$  (1)°. The new compound has been further characterized using Raman spectroscopy. This work shows that earlier studies have misidentified the products of an established synthesis route and that findings based on the incorrect identification of the synthesis product concerning the suitability of barytocalcite as a matrix for the retention of radioactive isotopes will need to be reconsidered.

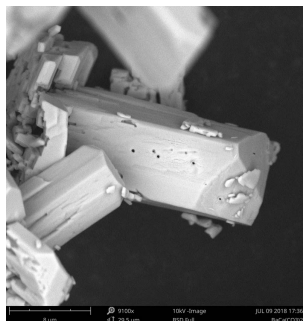
### 1. Introduction

Double carbonates with the composition  $M1M2(\text{CO}_3)_2$  ( $M = \text{Ca, Mg, Mn, Zn, Ba, Sr}$ ) are an interesting group of materials, where, for example, dolomite [ $\text{CaMg}(\text{CO}_3)_2$ ] has attracted attention as it is a geologically relevant model system in which to study cation order–disorder processes (Vinograd *et al.*, 2009; Burton & Van de Walle, 2003). The double carbonate  $\text{BaCa}(\text{CO}_3)_2$  has recently been investigated with respect to its suitability for the immobilisation of radioactive isotopes (Grandjean & Leturcq, 2005; Massoni *et al.*, 2013, 2014, 2015; Massoni & Le Gallet, 2016), where the incorporation of  $^{14}\text{C}$  was explored as an alternative to the incorporation of  $^{14}\text{C}$  in  $\text{CaCO}_3$  (Brooks *et al.*, 1974; Croff, 1976).

Up to now, three polymorphs of  $\text{BaCa}(\text{CO}_3)_2$ , namely barytocalcite, paralstonite and alstonite have been identified. The crystal structure of barytocalcite is monoclinic (see Fig. 1). The structure was first described in the space group  $P2_1$  (Cossner *et al.*, 1930; Alm, 1960), which was later revised to  $P2_1/m$  based on single-crystal diffraction data from natural samples (Dickens & Bowen, 1971).

The crystal structure of paralstonite is also well established as there is a single-crystal diffraction study on natural samples by Effenberger (1980). Paralstonite crystallizes in the trigonal space group  $P321$  with  $Z = 3$ ; its structure is shown in Fig. 2.

A third (pseudo-hexagonal) polymorph is alstonite. However, for alstonite the available crystallographic information is much less reliable and no structure refinement has been published to date. The structure is probably related to that of witherite ( $\text{BaCO}_3$ ), which in turn is isostructural to aragonite ( $\text{CaCO}_3$ ). In contrast to aragonite, alstonite has a supercell due to the ordering of Ba and Ca atoms within the



© 2019 International Union of Crystallography

## research papers

layers and the structure is built up by the stacking of these layers (Sartori, 1975; Roberts, 1978). The crystal structure data of these three polymorphs are listed in Table 1.

Terada (1952, 1953) described rhombohedral crystals in the Ba–Ca double carbonate system and a change of the X-ray powder patterns of carbonates in the  $\text{BaCO}_3$ – $\text{CaCO}_3$  system depending on the composition. Later, the subsolidus phase relations in the  $\text{BaCO}_3$ – $\text{CaCO}_3$  system have been studied as a function of composition, temperature and pressure (Chang, 1965, 1971; Brice & Chang, 1973), but no detailed crystallographic analyses have been carried out.

Grandjean & Leturcq (2005) and Massoni *et al.* (2013) described the synthesis of barytocalcite powder by precipitation and by mechanosynthesis. Their aim was to study the suitability of barytocalcite as a conditioning matrix for  $^{14}\text{C}$  (Grandjean & Leturcq, 2005). The interpretation of their diffraction data relied on indexing their powder X-ray diffraction (XRD) data using the ICDD database entry

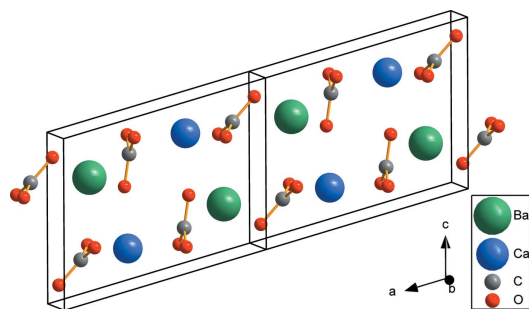


Figure 1  
Crystal structure of barytocalcite with space group  $P2_1/m$  and  $Z = 2$  (Dickens & Bowen, 1971). Two unit cells viewed along the  $b$  axis are shown.

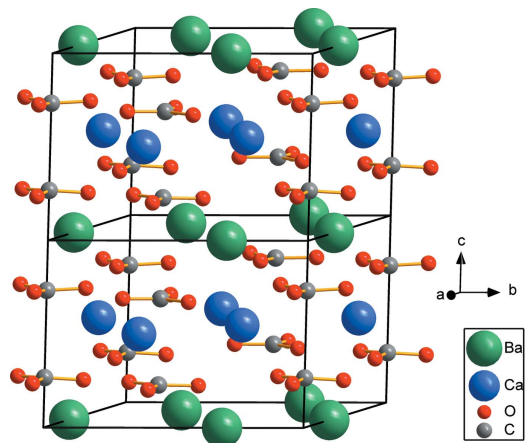


Figure 2  
Crystal structure of paralstonite with space group  $P321$  and  $Z = 3$  (Effenberger, 1980). Two unit cells viewed along the  $a$  axis are shown.

Table 1  
Crystal structure data for  $\text{BaCa}(\text{CO}_3)_2$  polymorphs.

	Barytocalcite†	Paralstonite‡	Alstonite§
Crystal system	Monoclinic	Trigonal	Triclinic
Space group	$P2_1/m$	$P321$	$C1$ or $C\bar{1}$
$a$ (Å)	8.092 (1)	8.692 (3)	30.14
$b$ (Å)	5.2344 (6)	8.692 (3)	17.40
$c$ (Å)	6.544 (1)	6.148 (4)	6.12
$\alpha$ (°)	90	90	90
$\beta$ (°)	106.05 (1)	90	90
$\gamma$ (°)	90	120	90
$Z$	2	3	24
$V$ (Å <sup>3</sup> )	266.4	402.26	3161.59
$\rho$ (g cm <sup>-3</sup> )	3.71	3.68	3.69

† Dickens & Bowen (1971). ‡ Effenberger (1980). § Sartori (1975).

PDF #001-0770 (Kabekkodu, 2010) which has been marked as deleted (Massoni *et al.*, 2013, 2015).

In the framework of a project aimed to understand the potential role of barytocalcite in the deep geological storage of nuclear waste, we carried out similar syntheses to those reported earlier, and complemented them by using additional synthesis routes. We characterized our samples by X-ray diffraction and Raman spectroscopy and confirmed our findings by comparing the experimental results to results obtained from density-functional-theory-based model calculations. Our results unambiguously show that Grandjean & Leturcq (2005) and Massoni *et al.* (2013) did not obtain barytocalcite, but rather a new phase, which crystallizes in a structure type that differs from those of the established three polymorphs.

## 2. Experimental

### 2.1. Sample synthesis

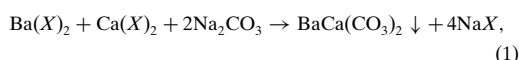
**2.1.1. Precursor materials.** All chemicals were analytical grade reagents used as purchased: barium nitrate  $\text{Ba}(\text{NO}_3)_2$  (99.95% purity, chemPUR, Karlsruhe, Germany), calcium nitrate  $\text{Ca}(\text{NO}_3)_2$  (99.9% purity, chemPUR, Karlsruhe, Germany), barium chloride  $\text{BaCl}_2$  (99% purity, Merck KGaA, Darmstadt, Germany), calcium chloride  $\text{CaCl}_2$  (96% purity, Merck KGaA, Darmstadt, Germany), sodium carbonate  $\text{Na}_2\text{CO}_3$  (99.9% purity, Merck KGaA, Darmstadt, Germany), barium carbonate  $\text{BaCO}_3$  (99.95% purity, Alfa Aesar, Karlsruhe, Germany) and calcium carbonate  $\text{CaCO}_3$  (99.95% purity, Merck KGaA, Darmstadt, Germany).

**2.1.2. High-temperature synthesis.** A precursor material for the high-temperature synthesis was obtained by mechanical activation (*e.g.* Massoni *et al.*, 2013) of a stoichiometric mixture of  $\text{BaCO}_3$  and  $\text{CaCO}_3$ . We used a Fritch PULVERISETTE 7 premium-line planetary micro mill equipped with agate crucibles and 10 mm-sized agate balls. The starting materials were ground dry for 120 min using a 10:1 ball to sample mass ratio with 500 rpm.

The resulting powder was pressed into 5 mm-sized pellets with an Across International Desktop pellet press employing a pressure of 6 kbar. The pellets were mounted into quartz glass ampoules, which were evacuated before they were transferred

into a Nabertherm L08/14 muffle furnace and heated to between 623 (1) and 823 (1) K (e.g. Massoni *et al.*, 2013) for 48 h.

**2.1.3. Precipitation synthesis.** For the precipitation synthesis we chose a chloride and a nitrate route following the work by Grandjean & Leturcq (2005) and Massoni *et al.* (2013). The reaction can be described by the following equation,



where  $X = \text{Cl}^-$  or  $\text{NO}_3^-$ .

Syntheses based on the nitrate and chloride route were carried out according to reaction (1). Barium and calcium precursors were dissolved together in double-distilled water (100 ml) to obtain 5 mmol solutions. The salt solution was added dropwise to a precipitant solution of sodium carbonate (50 ml, 10 mmol) while magnetically stirring at ambient temperature. The precipitate was filtered under vacuum, washed with distilled water repeatedly and dried at 333 (1) K in an oven.

**2.1.4. Hydrothermal synthesis.** The suspension from the precipitation synthesis, reaction (1), was transferred into 60 ml Teflon cups which were filled to 80% of their volume and then placed in stainless steel autoclaves. After keeping the suspensions at 503 (1) K for 24 h, the autoclaves were slowly cooled down [from 503 (1) to 453 (1) K in 48 h, then from 453 (1) to 298 (1) K in 24 h]. The solid obtained from this process was treated similarly to the product of the precipitation synthesis. Micrometre-sized crystals were obtained by using this slow cooling rate. For the synthesis of powder samples, the autoclaves were cooled more rapidly.

**2.1.5. Mechanosynthesis.** An attempt to completely amorphize the starting materials led to the formation of pure crystalline  $\text{BaCa}(\text{CO}_3)_2$  after grinding for a prolonged time (15 h, 10:1 ball to sample mass ratio, 500 rpm, agate crucibles and 10 mm-sized balls).

### 3. Computational details

First-principles calculations were carried out within the framework of DFT (Hohenberg & Kohn, 1964), employing the Perdew–Burke–Ernzerhof (PBE) exchange–correlation function (Perdew *et al.*, 1996) and the pseudopotential method using the *CASTEP* (Clark *et al.*, 2005) simulation package. On-the-fly norm-conserving or ultrasoft pseudopotentials from the *CASTEP* database were employed in conjunction with plane waves up to a kinetic energy cut-off of 990 eV or 630 eV, respectively. A Monkhorst–Pack (Monkhorst & Pack, 1976) grid was used for Brillouin-zone integrations with a distance  $<0.023 \text{ \AA}^{-1}$  between grid points. Convergence criteria included an energy change of  $<5 \times 10^{-6}$  eV per atom for self-consistent field, a maximal force of  $<0.008 \text{ eV \AA}^{-1}$  and a maximal component of the stress tensor  $<0.02$  GPa. Phonon frequencies were obtained from density functional perturbation theory (DFPT) calculations. Calculations employing the

‘virtual crystal approximation’ (VCA) follow the description given by Winkler *et al.* (2002).

Based on the experimental data, it became evident during the study that the new compound obtained was a disordered structure in which Ba and Ca occupy the same Wyckoff site *2b*. Atomistic modelling of structures, in which different atoms can randomly substitute each other on a specific Wyckoff position, may be carried out by averaging computed properties of a large number of supercell structures with randomly generated atomic configurations. The problem is that the properties of each individual structure (e.g. its enthalpy) may deviate quite strongly from the ensemble average.

The computation of specific properties of disordered compounds is greatly simplified by the use of so-called quasi-random structures, QRSs (Zunger *et al.*, 1990). QRSs are characterized by a minimal deviation of the frequencies of occurrence of various groupings of atoms (clusters) from the corresponding theoretical probabilities in a perfectly random solid solution. The advantage is that the enthalpy of a structure with a perfectly random occupation of a Wyckoff position can be accurately estimated using a few supercell structures of a small size which are characterized by quasi-random distributions.

As the enthalpy of a solid solution can typically be well mapped onto a limited set of pairwise interactions, the most important characteristic of a QRS is the sum of the squared deviations of probabilities of atomic pairs from their theoretical values,  $(Z_n/2)X_A X_B$ , where  $Z_n$  is the number of neighbours at distance  $n$ .

The present approach to finding a QRS consisted of an analysis of a large set of random structures within the  $2 \times 3 \times 3$  supercell of the new phase ( $a = 14.32$ ,  $b = 15.80$ ,  $c = 13.32 \text{ \AA}$  and  $\beta = 111.70^\circ$ ), in which the frequencies of Ba–Ca pairs at all cation–cation distances deviated as little as possible from the product  $(Z_n/2)X_A X_B$ . The test structures were created by random swaps of Ba and Ca within the  $2 \times 3 \times 3$  supercell. The frequencies of Ba–Ca pairs were monitored at eight distances in the range of 4.44–10.34 Å. As the strength of pairwise interactions generally decreases with increasing distance, the squared deviation for each cation–cation pair was weighted by a factor proportional to the inverse of the squared distance between the cations. This procedure allowed us to find a QRS which was optimized to resemble truly random structures.

### 4. Sample characterization

#### 4.1. X-ray powder diffraction

The sample material was characterized by XRD using a PANalytical X’Pert Pro with Bragg–Brentano geometry and a PANalytical PIXcel3D detector. The diffractometer was equipped with a Johansson monochromator. The measurements were performed with  $\text{Cu K}\alpha_1$  radiation and fixed divergence slits. Instrument parameters were obtained by measuring an Si standard of 99.999% purity.

## research papers

Before the analysis, all samples were ground in an agate mortar and powders were mounted on an oriented Si single-crystal sample holder. Samples were measured in the range  $10^\circ < 2\theta < 100^\circ$  with a scan speed of  $0.036^\circ \text{ min}^{-1}$ . *EXPO2014* (Altomare *et al.*, 2013) and *DICVOL06* (Boultif & Louer, 2004) were employed for powder pattern indexing and used for space group determination. Crystal structure refinement was performed using Rietveld refinement (Rietveld, 1969) with the software package *GSAS* (Larson & Von Dreele, 2004) and the graphical user interface *EXPGUI* (Toby, 2001).

### 4.2. Further characterization

For Raman spectroscopy we used an OXXIUS S.A. LaserBoxx LMX532 laser with a wavelength of 532.14 nm and a Princeton Instruments ACTON SpectraPro 2300i spectro-

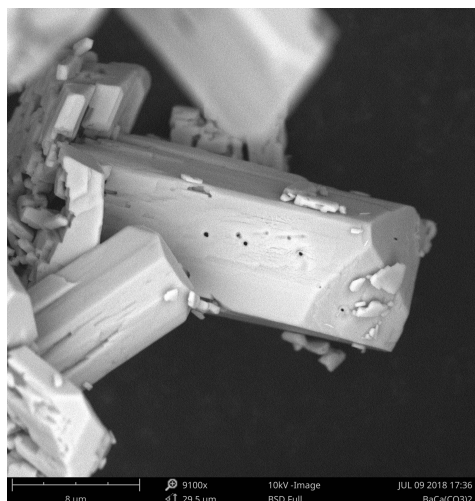


Figure 3  
SEM image of a barytocalcite crystal obtained by hydrothermal synthesis.

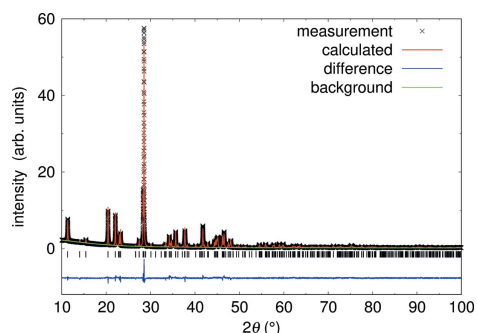


Figure 4  
Rietveld refinement of barytocalcite obtained by hydrothermal synthesis. Peak positions are indicated by tickmarks and the residuals between measurement and refinement are shown by the blue line.

Table 2

Crystallographic data of barytocalcite, with the monoclinic space group  $P2_1/m$  and  $Z = 2$ , obtained by Rietveld refinement and DFT calculations.

	Hydrothermal synthesis	DFT calculations
Crystal data		
$a$ (Å)	8.1205 (3)	8.2674
$b$ (Å)	5.2386 (2)	5.3033
$c$ (Å)	6.5562 (3)	6.6372
$\beta$ (°)	106.106 (1)	105.911
$V$ (Å <sup>3</sup> )	267.96 (3)	279.86
$\rho$ (g cm <sup>-3</sup> )	3.69	3.53
Refinement		
$R_p$ (%)	7.0	–
$R_{wp}$ (%)	9.4	–
$\chi^2$	6.6	–
No. of reflections	317	–
No. of parameters	43	–
No. of restraints	6	–

graph with a Pixis256E CCD camera. The setup is described in more detail by Bayarjargal *et al.* (2018). Raman spectra were background-corrected and analysed using the software *Fityk* (Wojdyr, 2010). Second-harmonic generation (SHG) experiments were carried out using the experimental setup described by Bayarjargal *et al.* (2009). In our study, we used quartz and corundum as reference minerals to compare the resulting SHG signal from the sample. We used a Phenom World ProX desktop SEM for the acquisition of electron-backscatter images. Furthermore, energy-dispersive X-ray spectroscopy (EDX) experiments for a semi-quantitative characterization of the composition were carried out.

## 5. Results

### 5.1. Barytocalcite

We synthesized monoclinic barytocalcite by hydrothermal synthesis, using either nitrates or chlorides for the starting material. When using a slow cooling rate, micrometre-sized crystals were obtained. Most crystals form aggregates, but some crystals show an idiomorphic crystal habit (Fig. 3).

The results of the EDX analysis are in good agreement with the expected chemical composition for barytocalcite [nominal *versus* EDX in at.%, Ba: 10/14 (1) and Ca: 10/14 (2), C: 20/17 (2), O: 60/55 (5)].

The barytocalcite sample is a single phase within an experimental uncertainty of  $\sim 3\%$ , as no secondary phase was detected by XRD. A Rietveld refinement provided a very satisfactory fit of the established structural model to the diffraction data (Fig. 4). The crystallographic parameters obtained here from the Rietveld refinement are in good agreement with DFT calculations and structural data presented by Dickens & Bowen (1971) (Table 2).

In summary, we have confirmed the established structure of barytocalcite and the powder diffractogram can now be used as a reference to distinguish other phases from barytocalcite. Also, with these results we have established a synthesis route for barytocalcite.

## research papers

## 5.2. New polymorph

From the precipitation and high-temperature syntheses, we obtained a different phase which we refer to as the ‘C2 phase’. Fig. 5 shows that the powder diffractogram of the new phase is rather distinct from that of barytocalcite.

For barytocalcite, the reflections (100) at  $11.33^\circ$ , (001)  $14.05^\circ$  and  $(10\bar{1})$   $15.42^\circ$  at low diffraction angles are characteristic as well as the presence of numerous reflections between  $30$  and  $40^\circ 2\theta$  for Cu  $K\alpha_1$  radiation. The simulation of the lattice spacing corresponding to the deleted ICDD entry No. 001-0770 and the new C2 phase is evident. They perfectly fit the strongest reflections of the C2 phase. The positions of the reflections are in good agreement with those published by Massoni *et al.* (2013), while a powder diffractogram of barytocalcite has many more reflections.

Fig. 6 implies that independent of the synthesis route (nitrate or chloride precipitation, high-temperature or mechanosynthesis), a single-phase sample of the C2 phase can be obtained. This was later confirmed by Rietveld refinement (Fig. 8).

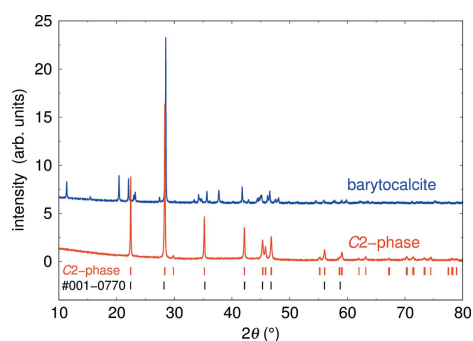


Figure 5  
X-ray powder diffractograms of barytocalcite from the hydrothermal synthesis and of the new C2 phase from the precipitation synthesis. Peak positions indicated by red tick marks correspond to the new C2 phase and the black tick marks to those of the deleted ICDD entry No. 001-0770.

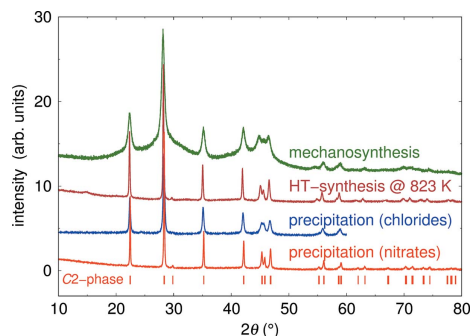


Figure 6  
X-ray powder diffractograms of the new C2 phase from precipitation, HT synthesis and mechanosynthesis. Peak positions indicated by red tick marks correspond to the new C2 phase.

The sample obtained by mechanosynthesis is poorly crystalline, as can be deduced from the obvious peak broadening. The precipitation route with nitrates as starting materials has proven to yield the best sample with respect to phase purity and crystallinity, hence we used samples from this synthesis route for all further investigations. The powder obtained by the precipitation route does not reveal any distinct growth morphology (Fig. 7) and we were careful not to introduce any texture into the sample preparation for the powder diffraction measurements. The high-temperature (HT) synthesis was also successful; however, the high temperatures used during the synthesis may cause some ordering in the structure which results in a small and broad reflection at low diffraction angles violating the C-centering.

Starting with *EXPO/DICVOL* using the 15 strongest reflections, we obtained five potential unit cells. Using the constraint that there has to be at least one formula per unit cell, we concluded that the most probable unit cell we found by *EXPO/DICVOL* had a volume of  $\sim 135 \text{ \AA}^3$ . Based on the observed systematic absence of reflections in the diffraction pattern, we found that the monoclinic noncentrosymmetric space group *C2* with  $Z = 1$  gave a good description of the experimental data. The experimentally obtained space group and lattice parameters were then used to investigate probable trial structures by DFT calculations. The results from the DFT geometry optimization were then used as a starting model for the Rietveld refinements of the experimental data. The systematic absence of reflections at low diffraction angles imply that there is no violation of the C-centering. This implies a random distribution of the Ba and Ca atoms on the  $2b$  Wyckoff position at  $(0, y, \frac{1}{2})$  with  $y \approx 0.15$ . The centrosymmetric space group *C2/m* can be excluded as there is no physically reasonable and small unit cell containing only one formula unit of  $\text{BaCa}(\text{CO}_3)_2$  with *C2/m* symmetry. Unfortu-

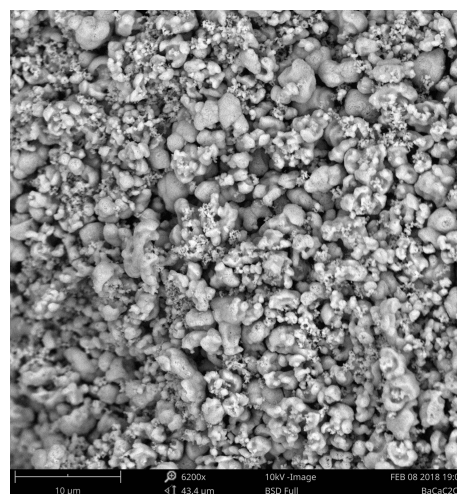
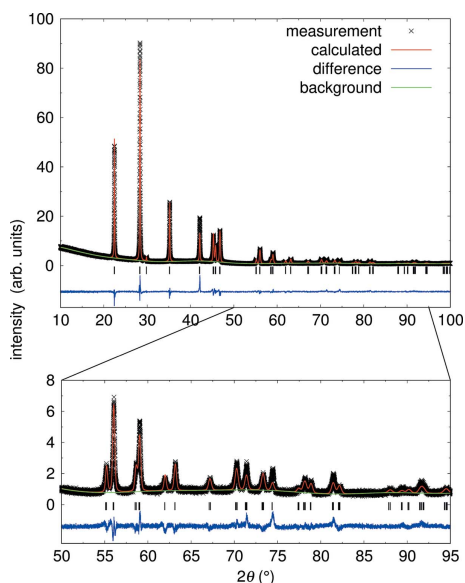


Figure 7  
SEM image of the C2 phase powder obtained by precipitation synthesis.

## research papers

nately, the SHG experiments were not able to unambiguously show the absence of a centre of symmetry in the new polymorph and support the exclusion of the space group  $C2/m$ . Fig. 8 shows the result of the Rietveld refinement of the  $C2$  phase and the refined structure is shown in Fig. 9.



**Figure 8**  
Rietveld refinement of the new  $C2$  phase from the precipitation synthesis. The high-angle reflections from 50 to 95° are enlarged for closer examination. Peak positions are indicated by tickmarks and the residuals between measurement and refinement are shown by the blue line.

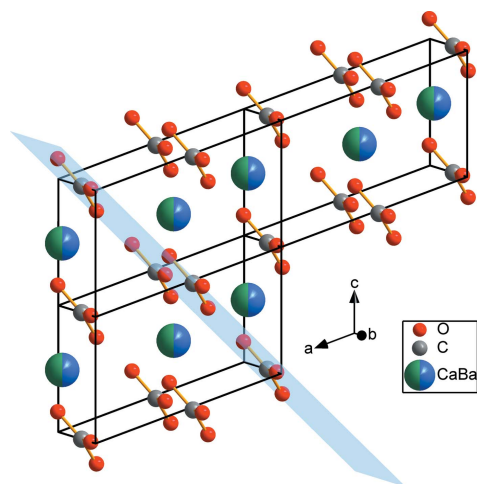


**Figure 9**  
Crystal structure of the new  $C2$  phase with space group  $C2$  and  $Z = 1$ . Three unit cells are shown viewed along the  $b$  axis; the  $(201)$  lattice plane is shown in light blue.

**Table 3**

Crystallographic data of the new  $C2$  phase from  $BaCa(CO_3)_2$  obtained by Rietveld refinement and DFT calculations with the monoclinic space group  $C2$  and  $Z = 1$ .

	HT synthesis	Precipitation synthesis	DFT (QRS)
<b>Crystal data</b>			
$a$ (Å)	6.7064 (5)	6.6775 (5)	6.8355
$b$ (Å)	5.1186 (4)	5.0982 (4)	5.1588
$c$ (Å)	4.2067 (3)	4.1924 (3)	4.3364
$\beta$ (°)	109.284 (1)	109.259 (1)	109.57
$V$ (Å <sup>3</sup> )	136.30 (3)	134.73 (3)	144.02
$\rho$ (g cm <sup>-3</sup> )	3.63	3.67	3.43
<b>Refinement</b>			
$R_p$ (%)	6.86	6.02	—
$R_{wp}$ (%)	8.79	8.43	—
$\chi^2$	3.30	2.96	—
No. of reflections	112	112	—
No. of parameters	42	40	—
No. of restraints	7	7	—

**Table 4**

Atomic coordinates and isotropic displacement parameters of the new  $C2$  phase from Rietveld refinement.

The  $U_{iso}$  of the symmetrically independent oxygen atoms were constrained to be identical.

Atom	Site	$x$	$y$	$z$	$U_{iso}$ (Å <sup>2</sup> )
Ba, Ca	$2b$	0.0	0.103 (1)	0.5	0.0456 (3)
C	$2a$	0.0	0.6259 (3)	1.0	0.058 (2)
O1	$4c$	-0.1043 (6)	0.5037 (2)	0.7367 (5)	0.078 (2)
O2	$2a$	0.5	0.3722 (2)	1.0	0.078 (2)

Clearly, the refinement gives an excellent description of the diffraction pattern. However, as the structure factors are dominated by the atomic form factors of Ba and Ca, the unconstrained refinement of the oxygen positions led to unexpected distortions of the  $CO_3$  groups. Therefore, restraints for the C—O bond length  $1.3 \pm 0.1$  Å and the O—O bond length  $2.2 \pm 0.1$  Å were introduced, which are the expected distances in related carbonates (*e.g.* Dickens & Bowen, 1971; Effenberger, 1980). We constrained the isotropic displacement parameters of the O1 and the O2 atoms to be identical. An analogous constraint was applied to the isotropic displacement parameters of the Ba and Ca atoms, which were also constrained to occupy the same position. A refinement of the site occupancy factors of Ba and Ca is problematic, as the site occupancy factors are strongly correlated with the displacement parameters. We obtained site occupancies of  $occ_{Ba} = 45$  (1)% and  $occ_{Ca} = 55$  (1)% by applying the constraint  $occ_{Ba} + occ_{Ca} = 100\%$ . As the experimental uncertainties are much larger than the numerical error given by the refinement program, the occupancies can be considered to be equal within the experimental limits. Furthermore, this is consistent with the results of the EDX measurements, where we obtained values of (nominal *versus* EDX in at.%) Ba: 10/12 (1) and Ca: 10/10 (1), C: 20/23 (2) and O:60/55 (6). We therefore chose to keep the occupancies fixed to  $occ_{Ba} = occ_{Ca} = 50\%$  in the final refinement. The resulting crystal data are listed in Table 3 and the atomic coordinates are given in Table 4. We cross-checked the results of the Rietveld refine-

## research papers

ment with those of the DFT calculations. Virtual crystal approximation (VCA) calculations reproduced the structure, but as the VCA does not allow for local relaxations around the cations, the lattice parameters were systematically  $\sim 7\%$  too large. The parameters of the DFT ground-state structure of two QRS are, as expected, in good agreement with the experimental data, where the PBE exchange correlation functional is known to lead to a slight overestimation of the lattice parameters.

The total energies of the four polymorphs are very similar, where barytocalcite is more stable by only  $4 \text{ kJ mol}^{-1}$  with respect to paralstonite, though it is more stable by  $19 \text{ kJ mol}^{-1}$  than the new phase. Based on these results, the DFT calculations cannot be used to unambiguously decide whether barytocalcite or paralstonite are stable under ambient conditions.

The density of the three known  $\text{BaCa}(\text{CO}_3)_2$  polymorphs only varies in a small range between  $3.68$  and  $3.71 \text{ g cm}^{-3}$  (Dickens & Bowen, 1971; Effenberger, 1980; Sartori, 1975). The density of the new C2 phase ( $3.67 \text{ g cm}^{-3}$ ) fits perfectly into this range.

### 5.3. Description of the structure

The new monoclinic C2 phase has an exceptionally small unit cell with a volume of  $134.66(3) \text{ \AA}^3$  containing only one formula unit. The structure consists of  $\text{CO}_3$ -group layers with Ba/Ca atoms located between the planes. All of the  $\text{CO}_3$  groups are symmetrically equivalent. All  $\text{CO}_3$  groups are located in the (201) lattice plane (Fig. 9), which causes a small reflection at  $\sim 30^\circ$ . This reflection is also present in previous studies and was misinterpreted as a reflection of  $\text{NaNO}_2$  (Massoni *et al.*, 2013, 2015). Each Ba/Ca atom is octahedrally coordinated by six oxygens and the resulting octahedron is strongly distorted (Fig. 10). In contrast to the barytocalcite

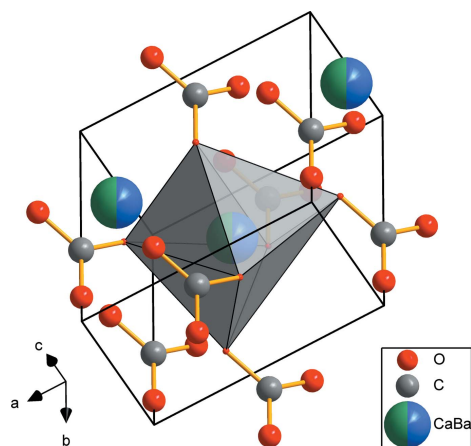


**Figure 10**  
Crystal structure of the new C2 phase. One unit cell is shown, the gray polyhedron shows the distorted octahedral coordination of one Ba/Ca atom.

structure, there are no Ba/Ca– $\text{CO}_3$  chains in the C2 phase. Furthermore, in barytocalcite the Ba atoms are coordinated by 11 oxygen atoms and the Ca atoms by seven oxygen atoms (Dickens & Bowen, 1971). The coordination of the cations in paralstonite also differs from the C2 phase and barytocalcite, as Ba is coordinated by ten oxygen atoms and the Ca by eight oxygen atoms in paralstonite (Effenberger, 1980). The Ba atoms in the carbonate witherite are coordinated by nine oxygen atoms (De Villiers, 1971). In calcite, Ca are coordinated by six oxygen atoms (Markgraf & Reeder, 1985), but the coordination polyhedra are undistorted. In comparison with the C2 phase, where  $\text{CO}_3$  groups are oriented in the (201) lattice plane, in calcite all  $\text{CO}_3$  groups are located in the (001) plane if the hexagonal setting is used. The structure-type of the C2 phase differs from that of the end-member carbonates  $\text{CaCO}_3$  and  $\text{BaCO}_3$  under ambient (Markgraf & Reeder, 1985; De Villiers, 1971) and non-ambient conditions (Townsend *et al.*, 2013; Merlini *et al.*, 2014; Gavryushkin *et al.*, 2017). Furthermore, this structure type does not appear in related double carbonates, *e.g.*  $\text{CaMg}(\text{CO}_3)_2$  (Merlini *et al.*, 2012) or  $\text{BaMg}(\text{CO}_3)_2$  (Pippinger *et al.*, 2014) under non-ambient conditions.

The Rietveld refinement revealed (Ba,Ca)–O interatomic distances in the octahedra between  $2.43$  and  $2.50 \text{ \AA}$ . These averaged values are independent of the actual occupation of a specific atomic position by either Ba or Ca.  $\text{Ba}^{2+}$  in octahedral coordination ( $r_{\text{Ba}} = 1.49 \text{ \AA}$ ) has a significantly larger cation radius than  $\text{Ca}^{2+}$  ( $r_{\text{Ca}} = 1.14 \text{ \AA}$ ) in the same coordination. A structure containing two cations with strongly different radii on the same Wyckoff position may also uptake various cations, *e.g.* some actinides. In a structure with a random distribution of Ba and Ca atoms, this will result in a broad range of (Ba,Ca)–O interatomic distances caused by the differently distorted octahedra. The QRS calculations can be used to extract the structural response to a given composition with a random Ba and Ca distribution (Fig. 11). The interatomic distance distribution for Ba–O and Ca–O shows two maxima, were the Ba–O distance is significantly larger than for Ca–O because of the much larger cation radius. In the

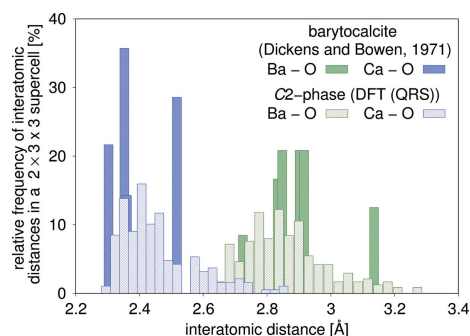


**Figure 11**  
Frequencies of Ba–O (green) and Ca–O (blue) interatomic distances in the new C2 phase from QRS calculations (crosshatched) and in barytocalcite from the work by Dickens & Bowen (1971) (filled).

## research papers

**Table 5**  
Bond distances (Å) and angles (°) of the new C2 phase, barytocalcite and paralstonite.

	C2 phase		Barytocalcite†	Paralstonite‡
	Rietveld	DFT (QRS)		
C—O	≈1.26	1.28–1.32	1.26–1.30	1.28–1.35
O—O	2.18–2.19	2.22–2.26	2.20–2.30	2.22–2.34
Ba—O	2.43–2.50	2.61–3.25	2.73–3.14	2.77–2.84
Ca—O	2.43–2.50	2.27–2.88	2.31–2.52	2.36–2.59
O—C—O	119.8–120.4	119–121	116.6–121.6	120.0

† Dickens & Bowen (1971). ‡ Effenberger (1980).

barytocalcite structure from the work by Dickens & Bowen (1971), the Ba—O and Ca—O distances show a similar distribution but with much less spread. Table 5 shows interatomic distances and angles for the C2 phase obtained from Rietveld refinement in comparison with computational data from QRS and with experimental data for barytocalcite.

#### 5.4. Raman spectroscopy

Experimentally determined Raman spectra for barytocalcite and the C2 phase as well as a theoretical spectrum for barytocalcite are shown in Fig. 12. We assigned the Raman bands in barytocalcite based on the DFT calculations. Following the factor group analysis (DeAngelis *et al.*, 1972), 30 modes can be Raman active ( $\Gamma_{\text{Raman}} = 18A_g + 12B_g$ ) in barytocalcite and 12 modes can be Raman active ( $\Gamma_{\text{Raman}} = 5A + 7B$ ) in the C2 phase. The Raman spectra of the QRS cannot be calculated because the computational effort for DFPT

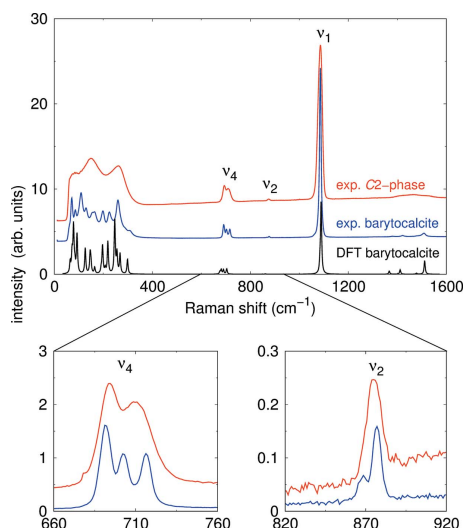


**Figure 12**  
Experimental Raman spectra of the new C2 phase obtained by precipitation compared with experimental spectra and DFT calculations of barytocalcite. The DFT calculated spectrum was scaled by 4%. The region between 660 and 920  $\text{cm}^{-1}$  is magnified for improved clarity for experimental barytocalcite and the C2 phase.

**Table 6**  
Peak positions and FWHM of selected Raman modes of barytocalcite from experiments and DFT-based calculations in comparison with the C2 phase.

Raman mode	Barytocalcite		DFT		C2 phase	
	Experiment		DFT		Experiment	
	Position	FWHM	Position	$\Gamma_{\text{Raman}}^\dagger$	Position	FWHM
$\nu_1$ ( $\text{cm}^{-1}$ )	—	—	1042.9	A	—	—
	1085.7	6.6	1047.5	A	1084.5	13.7
$\nu_2$ ( $\text{cm}^{-1}$ )	868.1	3.3	817.0	A	—	—
	876.8	4.7	828.4	A	875.1	8.7
$\nu_4$ ( $\text{cm}^{-1}$ )	691.7	6.7	652.4	B	694.0	11.5
	691.7	6.7	655.7	A	694.0	11.5
	702.8	7.0	665.3	B	711.1	17.2
	716.4	6.7	676.4	A	711.1	17.2

† DFT-based mode assignments to irreducible representation.

calculations for a structure having 180 symmetrically independent atoms per unit cell is currently too high.

The experimental and theoretical Raman spectra for barytocalcite are in good agreement with each other. There are only some minor deviations between the computational and observed intensities for some low-frequency modes. There is an obvious similarity between the Raman spectra of the new phase and barytocalcite. Although the peak positions are very similar, the Raman bands of the C2 phase have a significantly larger full width at half-maximum (FWHM) (Table 6) which causes severe overlaps for the low-frequency Raman bands.

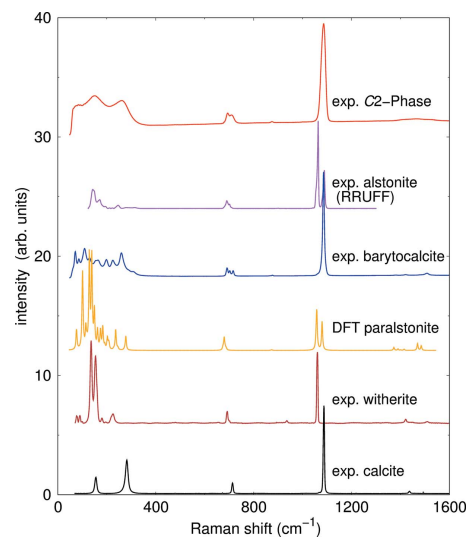


**Figure 13**  
Raman spectra of all known phases in the  $\text{BaCa}(\text{CO}_3)_2$  system. The spectra of calcite and witherite were obtained from the precursor powders and the barytocalcite and paralstonite spectra from DFT calculations. The data from the third polymorph alstonite was taken from the RRUFF database (Lafuente *et al.*, 2015). The spectra of the new C2 phase were obtained from a sample produced by the precipitation synthesis.

The Raman spectra of the C2 phase from the precipitation and HT syntheses are equal.

Perrin *et al.* (2016) observed an increased FWHM of the Raman bands, based on a positional disorder of the CO<sub>3</sub>, in Mg-doped CaCO<sub>3</sub>. The increased FWHM for all observed Raman modes ( $\nu_1$ ,  $\nu_2$ ,  $\nu_4$ ) in our study is therefore consistent with a random distribution of the Ba and Ca atoms, which causes a local distortion around the Ba and Ca environments.

Furthermore, the Raman spectroscopy gave clear evidence for having only one type of symmetrically equivalent CO<sub>3</sub> group in the C2 phase. The Raman mode  $\nu_4$  corresponds to the scissoring mode of the CO<sub>3</sub> group, and in a structure with two symmetrically independent CO<sub>3</sub> groups a triplet is expected, as observed in barytocalcite. The two symmetrically independent CO<sub>3</sub> groups in barytocalcite also lead to two out-of-plane bending modes ( $\nu_2$ ). In comparison, in the C2 phase only one doublet for  $\nu_4$  and a single peak for  $\nu_2$  is present, consistent with the presence of only one symmetrically independent CO<sub>3</sub> group. The symmetrical stretching ( $\nu_1$ ) shows a mode at the same position in barytocalcite and the C2 phase.

We conclude that all known carbonates in the BaCa(CO<sub>3</sub>)<sub>2</sub> system can be distinguished by Raman spectroscopy (Fig. 13). Furthermore, their Raman spectra are distinct from those of the end-member carbonates BaCO<sub>3</sub> and CaCO<sub>3</sub>.

## 6. Conclusions

In summary, we found a fourth polymorph of BaCa(CO<sub>3</sub>)<sub>2</sub>, the 'C2 structure'. It is probable that this compound exists naturally, and that would then constitute a new mineral. We have solved the structure by a combination of DFT calculations and Rietveld refinements of powder diffraction data. The new polymorph crystallizes in the acentric space group C2. Although SHG experiments did not unequivocally confirm the absence of a centre of symmetry, there is no physically reasonable unit cell with C2/m symmetry and one formula unit of BaCa(CO<sub>3</sub>)<sub>2</sub>. Raman spectra are indicative of cation disorder in agreement with the result of the Rietveld refinement, as broad and overlapping Raman peaks at low energies are expected if the structure is characterized by a range of locally distorted cation polyhedra. We demonstrated that the C2 phase can be synthesized following three different synthesis routes (precipitation, HT synthesis and mechanosynthesis). We have also shown that single-phase barytocalcite crystals can be obtained experimentally by hydrothermal synthesis, but not from precipitation or high-temperature synthesis. These findings point towards significant differences in the growth mechanism, reaction rates and thermodynamic stability between barytocalcite and the C2 phase, which is very likely to have a strong influence on their ability to incorporate radioactive ions. It is therefore now of interest to reevaluate the suitability of BaCa(CO<sub>3</sub>)<sub>2</sub> polymorphs as a matrix for the retention of radioactive isotopes, and such a study is currently in progress.

## Funding information

We gratefully acknowledge the funding from the DFG (project Wi1232/44-1).

## References

- Alm, K. F. (1960). *Ark. Mineral. Geol.* **2**, 399–410.
- Altomare, A., Cuocci, C., Giacobozzo, C., Moliterni, A., Rizzi, R., Corriero, N. & Falcicchio, A. (2013). *J. Appl. Cryst.* **46**, 1231–1235.
- Bayarjargal, L., Fruhner, C.-J., Schrod, N. & Winkler, B. (2018). *Phys. Earth Planet. Inter.* **281**, 31–45.
- Bayarjargal, L., Winkler, B., Haussühl, E. & Boehler, R. (2009). *Appl. Phys. Lett.* **95**, 061907.
- Boultif, A. & Louër, D. (2004). *J. Appl. Cryst.* **37**, 724–731.
- Brice, W. R. & Chang, L. L. Y. (1973). *Am. Mineral.* **58**, 979–985.
- Brooks, I. H., Heath, C. A., Kirstein, B. & Roberts, D. G. (1974). *Carbon-14 in the HTGR Fuel Cycle*. San Diego, California: General Atomic Company.
- Burton, B. P. & Van de Walle, A. (2003). *Phys. Chem. Miner.* **30**, 88–97.
- Chang, L. L. Y. (1965). *J. Geol.* **73**, 346–368.
- Chang, L. L. Y. (1971). *Am. Mineral.* **56**, 1660–1673.
- Clark, S. J., Segall, M. D., Pickard, C. J., Hasnip, P. J., Probert, M. I. J., Refson, K. & Payne, M. C. (2005). *Z. Kristallogr.* **220**, 567–570.
- Cossner, B. & Mussnug, F. (1930). *Zentralbl. Mineral. Geol. Palaeontol.* **A1930**, 321.
- Croff, A. G. (1976). *An Evaluation of Options Relative to the Fixation and Disposal of <sup>14</sup>C-Contaminated CO<sub>2</sub> as CaCO<sub>3</sub>*. Oak Ridge, Tennessee: Oak Ridge National Laboratory.
- DeAngelis, B. A., Newnham, R. E. & White, W. B. (1972). *Am. Mineral.* **57**, 255–268.
- De Villiers, J. P. R. (1971). *Am. Mineral.* **56**, 758–767.
- Dickens, B. & Bowen, J. S. (1971). *J. Res. Natl Bur. Stan.* **75A**, 197–203.
- Effenberger, H. (1980). *Neues Jahrb. Mineral. Monatsh.* pp. 353–363.
- Gavryushkin, P. N., Martirosyan, N. S., Inerbaev, T. M., Popov, Z. I., Rashchenko, S. V., Likhacheva, A. Y., Lobanov, S. S., Goncharov, A. F., Prakupenka, V. B. & Litasov, K. D. (2017). *Cryst. Growth Des.* **17**, 6291–6296.
- Grandjean, A. & Leturcq, G. (2005). *J. Nucl. Mater.* **345**, 11–18.
- Hohenberg, P. & Kohn, W. (1964). *Phys. Rev.* **136**, B864–B871.
- Kabekkodu, S. (2010). *Powder Diffraction File Inorganic and Organic Data Book*. Newtown Square, PA USA: International Centre for Diffraction Data.
- Lafuente, B., Downs, R. T., Yang, H. & Stone, N. (2015). *The Power of Databases: the RRUFF Project*, pp. 1–30. Berlin, Germany: Walter de Gruyter GmbH.
- Larson, A. C. & Von Dreele, R. B. (2004). *GSAS*. Los Alamos National Laboratory Report LAUR 86-748. Los Alamos National Laboratory, New Mexico, USA.
- Markgraf, S. A. & Reeder, R. J. (1985). *Am. Mineral.* **70**, 590–600.
- Massoni, N. & Le Gallet, S. (2016). *J. Nucl. Mater.* **476**, 13–19.
- Massoni, N., Le Gallet, S., Hoffmann, S., Launeau, P., Grin, Y. & Bernard, F. (2015). *J. Eur. Ceram. Soc.* **35**, 297–308.
- Massoni, N., Marcou, C., Rosen, J. & Jollivet, P. (2014). *J. Nucl. Mater.* **454**, 230–237.
- Massoni, N., Rosen, J., Chartier, M. & Cozzika, T. (2013). *J. Nucl. Mater.* **441**, 152–158.
- Merlini, M., Crichton, W. A., Chantel, J., Guignard, J. & Poli, S. (2014). *Mineral. Mag.* **78**, 225–233.
- Merlini, M., Crichton, W. A., Hanfland, M., Gemmi, M., Müller, H., Kuppenko, I. & Dubrovinsky, L. (2012). *Proc. Natl Acad. Sci. USA*, **109**, 13509–13514.
- Monkhorst, H. J. & Pack, J. D. (1976). *Phys. Rev. B*, **13**, 5188–5192.
- Perdew, J. P., Burke, K. & Ernzerhof, M. (1996). *Phys. Rev. Lett.* **77**, 3865–3868.

---

## research papers

---

- Perrin, J., Vielzeuf, D., Laporte, D., Ricolleau, A., Rossman, G. R. & Floquet, N. (2016). *Am. Mineral.* **101**, 2525–2538.
- Pippinger, T., Miletich, R., Effenberger, H., Hofer, G., Lotti, P. & Merlini, M. (2014). *Phys. Chem. Miner.* **41**, 737–755.
- Rietveld, H. M. (1969). *J. Appl. Cryst.* **2**, 65–71.
- Roberts, A. C. (1978). *Geol. Surv. Can.* **78-1C**, 49–52.
- Sartori, F. (1975). *Lithos*, **8**, 199–207.
- Terada, J. (1952). *J. Phys. Soc. Jpn.*, **7**, 432–434.
- Terada, J. (1953). *J. Phys. Soc. Jpn.*, **8**, 158–164.
- Toby, B. H. (2001). *J. Appl. Cryst.* **34**, 210–213.
- Townsend, J. P., Chang, Y.-Y., Lou, X., Merino, M., Kirklin, S. J., Doak, J. W., Issa, A., Wolverton, C., Tkachev, S. N., Dera, P. & Jacobsen, S. D. (2013). *Phys. Chem. Miner.* **40**, 447–453.
- Vinograd, V. L., Sluiter, M. H. & Winkler, B. (2009). *Phys. Rev. B*, **79**, 104201.
- Winkler, B., Pickard, C. & Milman, V. (2002). *Chem. Phys. Lett.* **362**, 266–270.
- Wojdyr, M. (2010). *J. Appl. Cryst.* **43**, 1126–1128.
- Zunger, A., Wei, S., Ferreira, L. & Bernard, J. (1990). *Phys. Rev. Lett.* **65**, 353–356.



Contents lists available at ScienceDirect

Journal of Solid State Chemistry

journal homepage: [www.elsevier.com/locate/jssc](http://www.elsevier.com/locate/jssc)Incorporation of Europium into  $(\text{Ba,Ca})_2(\text{CO}_3)_2$ Dominik Spahr<sup>a,\*</sup>, Lkhamsuren Bayarjargal<sup>a</sup>, Victor Vinograd<sup>b</sup>, Martin Etter<sup>c</sup>, Jacek Raddatz<sup>a,d</sup>, Björn Winkler<sup>a</sup><sup>a</sup> Institute of Geosciences, Goethe University, Frankfurt, Germany<sup>b</sup> Institute of Energy and Climate Research (IEK-6), Nuclear Waste Management and Reactor Safety, Forschungszentrum Jülich, Jülich, Germany<sup>c</sup> Deutsches Elektronen Synchrotron (DESY), Hamburg, Germany<sup>d</sup> Frankfurt Isotope and Element Research Center (FIERCE), Goethe University, Frankfurt, Germany

## ARTICLE INFO

## Keywords:

$(\text{Ba,Ca})_2(\text{CO}_3)_2$   
Europium incorporation  
Raman spectroscopy  
X-ray powder diffraction

## ABSTRACT

Synchrotron-based powder diffraction measurements in combination with inductively coupled plasma optical emission spectrometry, Raman and fluorescence spectroscopy show that  $(\text{Ba,Ca})_2(\text{CO}_3)_2$  can incorporate significant amounts (up to 6 mol%) of europium. This solid solution is therefore of potential interest for the solidification of nuclear waste streams involving aqueous nitrate solutions of lanthanides. Europium replaces Ba/Ca on lattice sites and is not incorporated as an interstitial defect. Charge compensation is likely due to the presence of  $\text{OH}^-$  groups as we could exclude a coupled substitution involving  $\text{Na}^+$ . The Eu-containing compound is stable to at least 723 K. We show that the one-phase-field of  $(\text{Ba}_x\text{Ca}_{1-x})\text{CO}_3$  solid solutions at ambient conditions is larger ( $0.36 < x < 0.51$ ) than previously thought. The synthesis routes employed here lead to compounds which have similar molar volumes than those of the naturally occurring  $(\text{Ba,Ca})$ -double carbonates, in noted contrast to another synthetic phase, “balcite”.

## 1. Introduction

Three naturally occurring polymorphs (barytocalcite, paralstonite and alstonite) of the double carbonate  $\text{BaCa}(\text{CO}_3)_2$  have been identified up to now, each having a distinct crystal structure [1–5]. In addition, a synthetic  $\text{BaCa}(\text{CO}_3)_2$  phase called “balcite” was found by Whittaker and Joester (2017) [6], while we independently described a phase with the same composition having  $C2$  space group symmetry [7]. The structural models for the synthetic phases differ as Whittaker and Joester (2017) [6] described “balcite” having  $R3m$  space group symmetry with  $Z = 3$ , where the carbonate groups are in either one of two orientations, which are related by a  $60^\circ$  rotation. In our model, we described the structure having  $C2$  space group symmetry with  $Z = 1$  and an ordered arrangement of the carbonate group. The volume per  $\text{CO}_3$ -group ( $V_{\text{CO}_3}$ ) is significantly larger for “balcite” ( $V_{\text{CO}_3} = 72.88 \text{ \AA}^3$ ) [6] than for the “ $C2$ ” phase ( $68.20(1) \text{ \AA}^3$ ) [7] or for the natural occurring polymorphs barytocalcite ( $66.6(1) \text{ \AA}^3$ ) [1], paralstonite ( $67.0(6) \text{ \AA}^3$ ) [2] or alstonite ( $65.9\text{--}67.4 \text{ \AA}^3$ ) [3–5]. However, a close inspection of the powder diffraction data of the two synthetic phases strongly suggests that in both studies the same phase has been obtained.

The synthesis of “balcite” ( $\text{Ca}_{0.5}\text{Ba}_{0.5}\text{CO}_3$ ) was described as a two-step process [6]. An amorphous and hydrous calcium–barium carbonate precursor ( $\text{Ca}_{1-x}\text{Ba}_x\text{CO}_3 \cdot 1.2\text{H}_2\text{O}$ ) was obtained by precipitation synthesis in cold aqueous solutions and filtered under vacuum. Afterwards the precursor was heated to 383 K to obtain the “balcite” phase [6]. We demonstrated that an anhydrous amorphous Ca/Ba carbonate precursor can be obtained by mechanochemical activation of the end-member carbonates ( $\text{CaCO}_3$ ,  $\text{BaCO}_3$ ) in stoichiometric proportions using a planetary ball mill [7]. The synthetic crystalline  $\text{BaCa}(\text{CO}_3)_2$  phase can be obtained by heating a mechanochemical activated precursor or directly by mechanochemical synthesis using a long milling time [7]. In contrast to Whittaker and Joester (2017) [6] we found that crystalline and single phase  $\text{BaCa}(\text{CO}_3)_2$  can also directly be obtained by precipitation synthesis without further heating using slow precipitation rates at ambient conditions.

In earlier studies Chang (1965) [8] and Chang (1971) [9] described the subsolidus phase relations in the  $\text{CaCO}_3$ – $\text{BaCO}_3$  system as a function of composition, temperature and pressure. They determined the stability of a rhombohedral Ba/Ca-carbonate for a Ba content between 39% and 54% ( $< 673 \text{ K}$ ) and between 37.5% (933 K) and 59% (1023 K)

\* Corresponding author.

E-mail address: [d.spahr@kristall.uni-frankfurt.de](mailto:d.spahr@kristall.uni-frankfurt.de) (D. Spahr).<https://doi.org/10.1016/j.jssc.2021.122759>

Received 14 September 2021; Received in revised form 15 November 2021; Accepted 17 November 2021

Available online 9 December 2021

0022-4596/© 2021 Elsevier Inc. All rights reserved.

for a pressure of 25 kbar. At elevated temperatures (933 K for Ca rich, 1023 K for Ba rich) they reported a disordered rhombohedral Ba/Ca-carbonate. These observations were reproduced by Brice and Chang (1973) [10]. They obtained a disordered calcite-type solid solution with 37.5%–57.5% Ba concentration at 923 K and 5 kbar. The investigations on the  $\text{CaCO}_3$  —  $\text{BaCO}_3$  system were complemented by investigations of Whittaker et al. (2018) [11] who studied the amorphous and hydrous  $\text{Ca}_{1-x}\text{Ba}_x\text{CO}_3 \cdot 1.2\text{H}_2\text{O}$  solid solution. They probed the local environment of the cations for various compositions and studied the crystallization process of the solid solution from the precursor with increasing temperature and observed that the solid solution becomes more ordered with increasing barium content.

Here, we extend the earlier studies of the  $(\text{Ca,Ba})\text{CO}_3$  system and investigate the incorporation of europium, which serves as a proxy for other lanthanides and actinides. One motivation for this study is to contribute to the discussion of spent fuel recycling allowing to reuse major actinides (U, Pu) as fuels for Generation IV fast reactors [12]. Such a recycling is already partially performed within the so-called PUREX (Plutonium and Uranium Reduction Extraction) process, currently implemented in France, Russia and Japan, permitting re-using of fissionable Pu in MOX fuels and U in REU (re-enriched U-oxide) fuels [12–14]. The separation of minor actinides (MA: Np, Am, Cm) from the PUREX- raffinate, which is currently planned for disposal as a vitrified waste, and their subsequent transmutation into short-lived nuclides would permit to significantly reduce the nuclear waste burden on a geological repository. The significant reduction of the heat generation would increase the repository capacity and drastically reduce the time interval required for radiotoxicity to reduce to a safe level [12,15–17]. A recently developed hydrometallurgical process named ALSEP (Actinide Lanthanide Separation) demonstrated a co-extraction of MA with lanthanides from the PUREX raffinate and their subsequent effective separation from each other [18,19]. The potential additional waste stream from an ALSEP-like process will likely be an aqueous nitrate solution of various lanthanides, which would require solidification. Here we hypothesize that  $\text{BaCa}(\text{CO}_3)_2$  could serve as a potential waste form for such a waste stream. Although the amount of REE in natural calcite is below 0.1 mol % [20], the structural flexibility of disordered  $\text{BaCa}(\text{CO}_3)_2$  double carbonate implies that significant amounts of lanthanides may be incorporated. The potential role of  $\text{BaCa}(\text{CO}_3)_2$  for the immobilization of radioactive  $^{14}\text{C}$  has already been investigated in the last decades [21–25], but as there was some misidentification of the phases present [7] these studies probably need to be revisited. Also,  $\text{BaCa}(\text{CO}_3)_2$  could be potentially important within the concept of a direct disposal of spent nuclear fuel in deep geological formations. As, in any geological repository concrete will likely be employed. Over geological time scales, this concrete will decompose and carbonates will be formed. If a waste container fails, barium may be introduced into the surrounding materials and rocks due to the dissolution of spent nuclear fuel.  $^{138}\text{Ba}$  occurs in the spent fuel as the fission product of  $^{235}\text{U}$  and  $^{239}\text{Pu}$ , while  $^{137}\text{Ba}$  is generated due to the decay of  $^{137}\text{Cs}$  [26]. The decay product  $^{137}\text{Ba}$  is a stable isotope. The presence of  $\text{CaCO}_3$ , either in the engineered or in a geological clay barrier, and the Ba from the waste may then lead to the formation of  $\text{BaCa}(\text{CO}_3)_2$  or related phases. These new minerals may then become host phases for radioactive ions present in the nuclear waste.

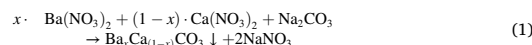
We choose europium as a representative element to study the ability of  $\text{BaCa}(\text{CO}_3)_2$  to incorporate lanthanides. The chemical composition of the samples was determined by inductively coupled plasma optical emission spectrometry (ICP-OES) and the structure was analyzed by synchrotron-based X-ray powder diffraction (HRXPD). These data were complemented by Raman spectroscopy and time-resolved laser fluorescence spectroscopy (TRLFS), and allowed us to demonstrate that a significant amount of a lanthanide dissolved in an aqueous solution may be incorporated in a Ba-Ca double carbonate by precipitation.

## 2. Experimental

### 2.1. Synthesis

#### 2.1.1. Precipitation synthesis

The C2-phase of  $\text{BaCa}(\text{CO}_3)_2$  was synthesized by precipitation synthesis according to Spahr et al. (2019) [7] following the nitrate route to obtain solid solutions with a range of Ba/Ca ratios:



where  $0 \leq x \leq 1$ .

We introduced up to 8% europium ( $x_{\text{Eu}} = 0.08$ ) into the feed solution during the precipitation synthesis to obtain Eu-doped  $\text{Ba}_x\text{Ca}_{(1-x)}\text{CO}_3$  samples by adding  $\text{Eu}(\text{NO}_3)_3 \cdot 6\text{H}_2\text{O}$ . We used analytical grade barium nitrate  $\text{Ba}(\text{NO}_3)_2$  (99.95% purity, chemPUR, Karlsruhe, Germany), calcium nitrate tetrahydrate  $\text{Ca}(\text{NO}_3)_2 \cdot 4\text{H}_2\text{O}$  (99.9% purity, chemPUR, Karlsruhe, Germany), europium nitrate hexahydrate  $\text{Eu}(\text{NO}_3)_3 \cdot 6\text{H}_2\text{O}$  (99.9% purity, Strem chemicals, Cambridge, United Kingdom), and sodium carbonate  $\text{Na}_2\text{CO}_3$  (99.9% purity, Merck KGaA, Darmstadt, Germany) as starting materials. The starting materials were dissolved separately in bidistilled water to obtain solutions with a concentration of  $0.1 \text{ mol l}^{-1}$ . The barium-, calcium- and europium-nitrate solutions were mixed in stoichiometric proportions according to equation (1) and added to the sodium carbonate solution with a drop rate of  $\sim 2 \text{ ml min}^{-1}$  while stirring at ambient temperature. The suspension was filtered under vacuum and the resulting precipitate was washed with distilled water repeatedly. Finally, the resulting powder was dried at 333(1) K in an oven.

The  $\text{CaCO}_3$  polymorph vaterite was obtained by precipitation when we added 50 ml of a  $\text{Ca}(\text{NO}_3)_2$  solution with  $0.2 \text{ mol l}^{-1}$  concentration dropwise to 100 ml ammonium bicarbonate  $(\text{NH}_4)\text{HCO}_3$  solution with  $0.02 \text{ mol l}^{-1}$  concentration.

#### 2.1.2. High-temperature synthesis

The C2-phase of  $\text{BaCa}(\text{CO}_3)_2$  can also be obtained by high-temperature synthesis [7]. We used a stoichiometric mixture of barium carbonate  $\text{BaCO}_3$  (99.95% purity, Alfa Aesar, Karlsruhe, Germany) and calcium carbonate  $\text{CaCO}_3$  (99.95% purity, Merck KGaA, Darmstadt, Germany) as starting materials to obtain  $\text{BaCa}(\text{CO}_3)_2$  solid solutions by high-temperature synthesis (3).



where  $0 \leq x \leq 1$ .

$\text{BaCO}_3$  and  $\text{CaCO}_3$  were ground together in a Fritch Pulverisette 7 premium line planetary micro mill equipped with agate crucibles and 10 mm sized agate balls for mechanical activation. We used a 10:1 ball to sample mass ratio with 500 rpm and ground them for 120 min. The obtained precursor material was pressed to 6 mm sized pellets employing a pressure of 6 kbar. The pellets were sealed into quartz glass ampoules under argon atmosphere. Afterwards the ampoules were heated in a muffle furnace to temperatures between 473(1) K and 823(1) K for 48 h. They were cooled down to ambient temperature by switching off the oven.

### 2.2. Sample characterization

#### 2.2.1. X-ray powder diffraction

The power samples from the precipitation and high-temperature synthesis were characterized by powder X-ray diffraction (XRD) using a PANalytical X'Pert Pro with Bragg-Brentano geometry and a PANalytical PIXcel<sup>3D</sup> detector. The diffractometer was equipped with a Johansson monochromator and a copper X-ray tube. The measurements were performed with  $\text{Cu } K_{\alpha 1}$  radiation and  $1/2^\circ$  fixed divergence slits. Instrument parameters were obtained by measuring a Si-standard of

99.999% purity. The samples from the precipitation synthesis were measured as received without further grinding. The samples from the high-temperature synthesis were ground mechanically in an agate mortar while the samples from the precipitation synthesis were used as received. The powders from both synthesis routes were mounted on an oriented Si single crystal sample holder and measured in a range of  $10^\circ < 2\theta < 80^\circ$  with a scan speed of  $0.09^\circ \text{ min}^{-1}$ . The samples had a typical thickness of  $\sim 0.2 \text{ mm}$  as they were slightly pressed into a trench in the sample holder.

Synchrotron-based powder diffraction was performed at Beamline P02.1 at PETRA II (DESY) in Hamburg [27] using a Perkin Elmer XRD1621 area detector and a wavelength of  $0.2071 \text{ \AA}$  ( $\sim 60 \text{ keV}$ ). The beam size on the sample was  $\sim 1 \text{ (H)} \times 1 \text{ (V)} \text{ mm}^2$ . The samples were measured in capillaries ( $\varnothing = 0.5 \text{ mm}$ ) for 180 s which were rotated around their long axis which was perpendicular to the beam. The detector parameters and the detector to sample distance were calibrated by measuring a  $\text{LaB}_6$  powder standard.

We used the program DIOPTAS [28] to integrate and calibrate the synchrotron diffraction patterns. Rietveld refinements [29] on all powder diffraction data were carried out using the software package GSAS-II [30].

### 2.2.2. Raman spectroscopy and fluorescence measurements

For Raman spectroscopy and fluorescence measurements we used an OXXIUS S.A. LaserBoxx LMX532 laser with a wavelength of  $532.14 \text{ nm}$  and a Princeton Instruments ACTON SpectraPro 2300i spectrograph with a Pixis256E CCD camera. The set-up is described in more detail in Bayarjargal et al. (2018) [31]. Time-resolved laser fluorescence spectroscopy was performed with a Continuum Surelite III-10 Laser and the same spectrograph using a Hamamatsu C6270 photomultiplier tube (see Fruhner et al. (2018) [32]). The samples were placed inside of  $0.5 \text{ mm}$  diameter Quartz glass capillaries and measured in transmission (TRLFS) geometry. Temperature-dependent measurements were carried out using a Oxford Instruments Cryostream with nitrogen in a temperature range between  $300 \text{ K}$  and  $100 \text{ K}$ . Background correction and fitting of the experimental Raman spectra was performed using the software package Fityk [33].

### 2.2.3. Inductively coupled plasma optical emission spectrometry

Solution based element analyses were carried out on an inductively coupled plasma optical emission spectrometer (ICP-OES, Thermo Scientific iCap 6300 Duo at the Institute of Geosciences, FIERCE). For the Ba,

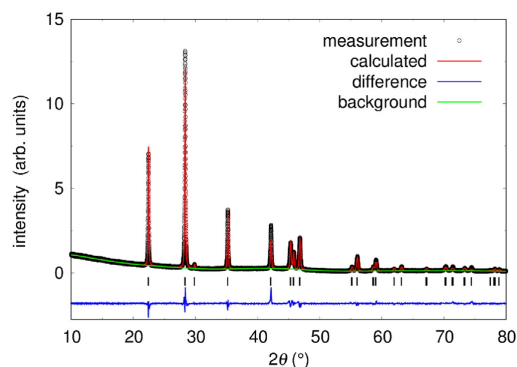


**Fig. 1.** Rietveld refinement of diffraction data obtained with  $\lambda = 1.5406 \text{ \AA}$  for  $\text{BaCa}(\text{CO}_3)_2$  ( $x_{\text{Ba}} = 0.5$ ) in the monoclinic C2 structure with  $Z = 1$  ( $wR = 7.6\%$ ). Reflection positions are indicated by tickmarks and the residuals between measurement and refinement are shown by the blue lines. (For interpretation of the references to colour in this figure legend, the reader is referred to the Web version of this article.)

Ca and Eu measurements  $50 \text{ mg}$  of the  $\text{Ba}_x\text{Ca}_{1-x}\text{CO}_3$  samples and  $150 \text{ mg}$  of the Eu-doped samples were dissolved in  $1.8 \text{ ml}$   $0.045 \text{ M}$   $\text{HNO}_3$  containing  $1 \text{ mg g}^{-1}$  of Yttrium (Y) in order to correct for matrix effects. Overall samples were background corrected, standardized to Y, and drift corrected. Concentrations of the samples were calculated based on standard solutions made from single-element solutions. Precision was calculated based on a standard solution measured after every 10 samples. Based on this, the precision was  $\sim 3\%$  for Ba and Ca and  $1.5\%$  for Eu (1SD).

### 2.2.4. Scanning electron microscopy

Scanning electron microscopy was carried out using a Phenom World ProX desktop SEM. Energy dispersive X-ray spectroscopy (EDX) measurements were performed for a semi-quantitative characterization of the composition using a silicon drift detector. The powders were mounted without coating on aluminum stubs using sticky carbon tape. The samples were measured under low vacuum conditions to reduce charging effects on the sample with an acceleration voltage of  $15 \text{ kV}$ .

## 3. Results and discussion

### 3.1. $\text{BaCO}_3$ , $\text{BaCa}(\text{CO}_3)_2$ and $\text{CaCO}_3$

We successfully synthesized the end-member carbonates witherite ( $\text{BaCO}_3$ ,  $\text{Ba}_x = 1$ ) and calcite ( $\text{CaCO}_3$ ,  $\text{Ba}_x = 0$ ) of the  $\text{Ba}_x\text{Ca}_{1-x}\text{CO}_3$  solid solution by precipitation synthesis. The powder samples are single phase within the experimental uncertainties of  $\sim 3\%$  and are very well crystallized. No increase of the background due to the presence of an amorphous phase was observed in the powder diffraction data. The description of the experimental data by a Rietveld refinement is very satisfactory (Supplementary Information Fig. S1 a & b).

Furthermore, the hexagonal polymorph vaterite ( $\text{CaCO}_3$ ,  $\text{Ba}_x = 0$ ) can also be obtained by precipitation synthesis using slightly different synthesis conditions. Unfortunately, we were unable to obtain single phase samples (Supplementary Information Fig. S1 c). The samples show small peaks which can be assigned to calcite and another peak at  $\sim 39^\circ$  which cannot be identified. The amount of calcite impurity is  $< 3\%$ . The structural parameters obtained from the samples of the end-member carbonates are in good agreement with the established structural models of witherite [34], calcite [35] and vaterite [36].

Fig. 1 shows a Rietveld refinement on the data of a  $\text{Ba}_x\text{Ca}_{1-x}\text{CO}_3$  sample with an equimolar concentration of the Ba and Ca ( $x_{\text{Ba}} \approx 0.5$ ) in space group C2 [7]. No second phase or increased background intensity can be observed within experimental uncertainties. Table 1 lists the structural parameters obtained from the Rietveld refinements and the parameters for “balcrite” ( $x_{\text{Ba}} \approx 0.5$ ) obtained by Whittaker and Joester (2017) [6]. The refined atomic coordinates and isotropic displacement parameters obtained by Rietveld refinement are listed in the Supplementary Information (Table S1). As the  $\text{Ba}^{2+}$  cations ( $r_{\text{Ba}} = 1.49 \text{ \AA}$ ) are significantly larger in octahedral coordination than the Ca cations ( $r_{\text{Ca}} = 1.14 \text{ \AA}$ ) in the same coordination, the normalized volume per  $\text{CO}_3^{2-}$ -group ( $V_{\text{CO}_3}$ ) decreases from  $\sim 76 \text{ \AA}^3$  in  $\text{BaCO}_3$  to  $\sim 62.4 \text{ \AA}^3$  in  $\text{CaCO}_3$  (vaterite) or to  $\sim 61.4 \text{ \AA}^3$  in  $\text{CaCO}_3$  (calcite) with decreasing Ba content. For the C2-phase  $V_{\text{CO}_3}$  is approximately the mean value between  $\text{BaCO}_3$  and  $\text{CaCO}_3$  while  $V_{\text{CO}_3}$  is significantly larger ( $72.88 \text{ \AA}^3$ ) in “balcrite” [6].

### 3.2. $\text{Ba}_x\text{Ca}_{1-x}\text{CO}_3$ solid solution

#### 3.2.1. ICP-OES

We synthesized samples with different  $\text{Ba}_x$  concentration in order to obtain  $\text{Ba}_x\text{Ca}_{1-x}\text{CO}_3$  solid solutions by precipitation and high-temperature synthesis. Our ICP-OES measurements (Fig. 2) show a decrease in the Ba/Ca ratio in the samples obtained by precipitation synthesis in comparison to the nominal  $\text{Ba}_x$  concentration in the feed

**Table 1**

Structural parameters of  $\text{Ba}_x\text{Ca}_{(1-x)}\text{CO}_3$  for  $\text{Ba}_x = 1$  (witherite),  $\text{Ba}_x = 0.5$  (C2-phase) and  $\text{Ba}_x = 0$  (calcite and vaterite) obtained by Rietveld refinement on samples from precipitation synthesis. The structural parameters of “balcrite” [6] are also shown.  $V_{\text{CO}_2}$  describes the unit cell volume per  $\text{CO}_2$ -group.

	witherite	calcite	vaterite	C2-phase	balcrite <sup>a</sup>
chemical formula	$\text{BaCO}_3$	$\text{CaCO}_3$	$\text{CaCO}_3$	$\text{BaCa}(\text{CO}_3)_2$	$\text{BaCa}(\text{CO}_3)_2$
$\text{Ba}_x$	1.0	0.0	0.0	0.51(1)	0.52(2)
Crystal data					
Crystal system	Orthorhombic	Trigonal	Hexagonal	Monoclinic	Trigonal
Space group	<i>Pmca</i>	<i>R3c</i>	<i>P6<sub>3</sub>mmc</i>	<i>C2</i>	<i>R3m</i>
<i>a</i> (Å)	5.3012(7)	4.9907(1)	4.1266(1)	6.659(2)	5.2371
<i>b</i> (Å)	8.917(1)	4.9907(1)	4.1266(1)	5.0932(2)	5.2371
<i>c</i> (Å)	6.4362(9)	17.0671(1)	8.4680(3)	4.1779(9)	9.2053
$\alpha$ (°)	90.0	90.0	90.0	90.0	90.0
$\beta$ (°)	90.0	90.0	90.0	109.12(1)	90.0
$\gamma$ (°)	90.0	120.0	120.0	90.0	120.0
<i>Z</i>	4	6	2	1	3
<i>V</i> (Å <sup>3</sup> )	304.3(1)	368.14(1)	124.88(1)	133.87(1)	218.65
$V_{\text{CO}_2}$ (Å <sup>3</sup> )	76.08(2)	61.37	62.44(1)	68.20(1)	72.88
$\rho$ (g cm <sup>-3</sup> )	4.31	2.71	2.66	3.68	3.39
Refinement					
<i>R</i> (%)	6.5	5.8	6.6	7.0	
<i>wR</i> (%)	8.9	8.4	10.3	7.6	
No. of reflections	108	32	26	51	
No. of parameters	33	22	20	25	
No. of restraints	6	6	6	6	

<sup>a</sup> Whittaker and Joester (2017) [6].

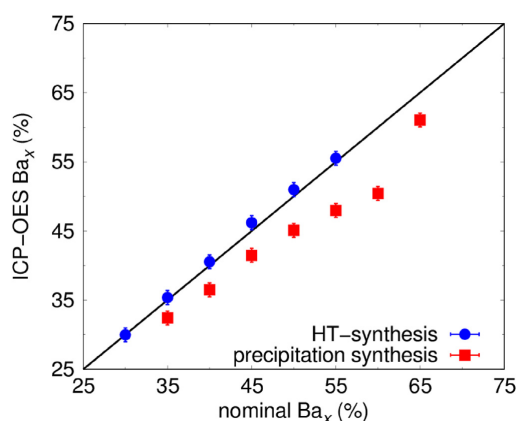


**Fig. 2.** ICP-OES measurements of the  $\text{Ba}_x$  concentration as a function of the nominal  $\text{Ba}_x$  concentration employed in the synthesis of the samples obtained by precipitation and high-temperature synthesis. The straight line is a guide to the eye.

solution, which is in agreement with the observations by Whittaker and Joester (2017) [6]. The Ba/Ca ratio in samples from the high-temperature synthesis do not substantially differ from the stoichiometric ratio of the starting materials within the experimental error limits.

### 3.2.2. X-ray powder diffraction

We varied the Ba concentration during the synthesis until new peaks appear in the X-ray powder diffraction data to determine the composition range in which solid solutions can be formed. The powder diffraction data on the samples from the precipitation synthesis (Fig. 3 a) reveal that the samples with  $\text{Ba}_x$  concentrations between  $\text{Ba}_x = 0.51$  and  $\text{Ba}_x = 0.36$  are single phase within the experimental uncertainties, established to be

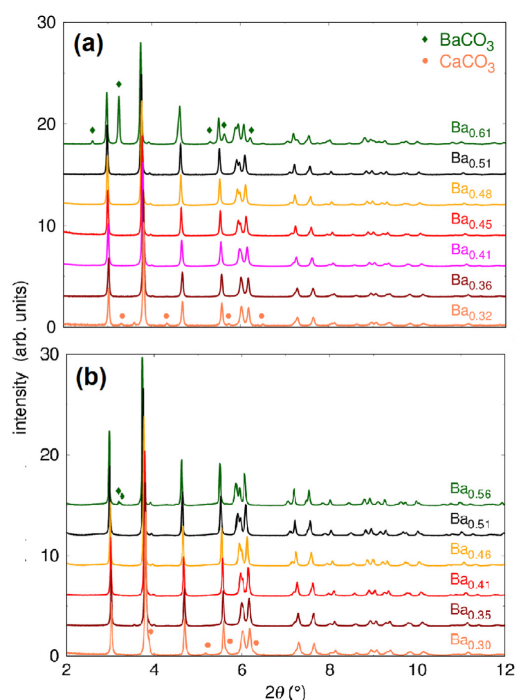


**Fig. 3.** X-ray powder diffraction data of  $\text{Ba}_x\text{Ca}_{(1-x)}\text{CO}_3$  obtained with  $\lambda = 0.2071$  Å from precipitation (a) and high-temperature synthesis (b) for different  $\text{Ba}_x$  concentrations. The reflection appearing in the diffractograms with  $\text{Ba}_x = 0.51$  (◆) belong to  $\text{BaCO}_3$  and the reflections in the diffractograms with  $\text{Ba}_x = 0.35$  (●) belong to  $\text{CaCO}_3$ .

D. Spahr et al.

Journal of Solid State Chemistry 307 (2022) 122759

<3%. No reflections of a second phase or an increased background can be observed. Changing the  $Ba_x$  concentrations to  $Ba_x = 0.61$  or  $Ba_x = 0.32$ , respectively, causes the appearance of new reflections. They belong either to witherite ( $BaCO_3$ ) for the sample with  $Ba_x = 0.61$  or to the hexagonal polymorph of  $CaCO_3$  vaterite for the sample with  $Ba_x = 0.32$  concentration.

Since the C2-phase can also be obtained phase pure by high-temperature synthesis we used this synthesis route to obtain the  $Ba_xCa_{(1-x)}CO_3$  solid solution as well (Fig. 3 b). In the high-temperature synthesis the borders of the phase field match the data from the precipitation synthesis. For  $Ba_x = 0.30$ , first reflections of calcite appear in the powder diffraction data and for  $Ba_x = 0.56$  witherite is present.

The change in the  $Ba_x$  concentration causes a significant shift of the reflection positions in the powder diffraction data. With increasing Ba content, the peak positions shift to lower  $2\theta$ -values. This shift is caused by a noticeable change of the lattice parameters (Supplementary Information Fig. S2). All three lattice parameters  $a$ ,  $b$  and  $c$  increase with increasing  $Ba_x$  concentration and consequently the volume of the unit cell increases. The increase along the  $a$ -axis is approximately twice than that of the other two axes. The unit cell volume changes by  $\sim 3.5\%$  in the composition range where we obtained single phase samples. For the samples with lower and higher  $Ba_x$  concentration, the lattice parameters still shift, but the  $Ba/(Ba + Ca)$  ratio obtained from the ICP-OES measurements had to be corrected by the amount of the second phase. Fig. 4 shows  $V_{CO_3}$  as a function of the  $Ba_x$  concentration and for the three natural occurring polymorphs and “balcrite”. The single phase fields for the  $CaCO_3$  —  $BaCO_3$  solid solution at elevated temperatures and pressures [8] and the “balcrite” phase [6] are also shown.

### 3.3. $Ba_{0.455}Ca_{0.545}CO_3:Eu$

#### 3.3.1. ICP-OES

We used the precipitation synthesis to obtain samples with  $(BaCa)_{(1-x)}CO_3 + Eu_x$  composition. The ICP-OES measurements (Fig. 5 a) show that the  $Ba/Ca$  ratio in the  $Eu$ -doped samples is  $Ba_x \approx 0.455(8)$  which is in good agreement with the  $Ba/Ca$  ratio in the undoped sample having an equimolar  $Ba/Ca$  concentration in the feed-solution ( $Ba_x = 0.45$ ). The  $Ba/Ca$  ratio seems to increase slightly with increasing  $Eu_x$  concentration, but the samples can be described to a very good approximation as  $Ba_{0.455}Ca_{0.545}CO_3:Eu$ .

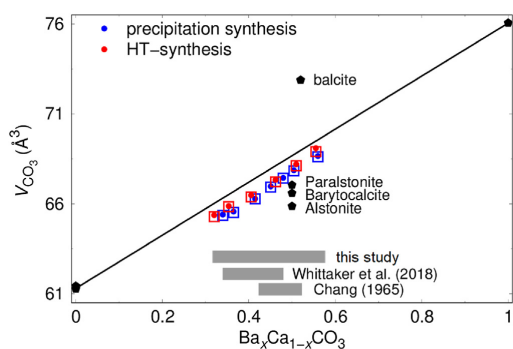


Fig. 4. Unit cell volume per  $CO_3$ -group of the  $Ba_xCa_{(1-x)}CO_3$  solid solution from precipitation and high-temperature synthesis from synchrotron ( $\bullet$ ) and laboratory ( $\square$ ) powder diffraction experiments for single phase samples. The synthetic “balcrite” [6] phase and the three natural occurring polymorphs barytocalcite [1], paralstonite [2] and alstonite [3] are also shown. Error bars representing the uncertainty in  $V_{CO_3}$  and  $Ba_x$  are smaller than the symbol size. Grey boxes indicate the single phase fields for  $CaCO_3$  —  $BaCO_3$  solid solutions according to Whittaker and Joester (2017) [6] and Chang (1965) [8] and the present study.

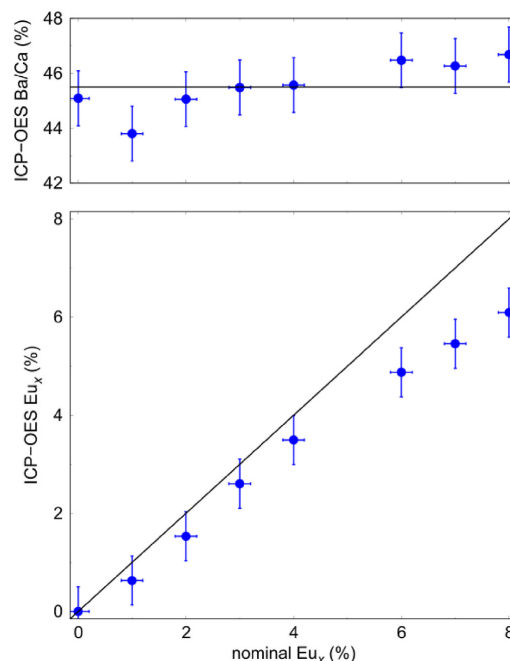


Fig. 5. ICP-OES measurements of the  $Ba/Ca$  ratio (a) and the  $Eu_x$  concentration (b) as a function of the nominal  $Eu_x$  concentration employed in the synthesis in the samples obtained by precipitation synthesis. The straight line in (a) is a linear fit and in (b) a guide to the eye.

The measurements also show an increasing  $Eu_x$  concentration in the resulting precipitant with increasing  $Eu_x$  concentration in the feed solution (Fig. 5 b). The ICP-OES results reveal that we were able to synthesize samples with an  $Eu_x$  concentration up to 6%. The nominal  $Eu_x$  concentration in the feed-solution is slightly higher than  $Eu_x$  in the precipitant and the difference increases with increasing  $Eu_x$  concentration.

#### 3.3.2. X-ray powder diffraction

With increasing europium concentration in the sample up to  $Eu_x = 0.065$  we detected no secondary crystalline phase appearing in the X-ray powder diffraction data since no new peaks occur (Fig. 6). Furthermore, the Rietveld refinements on the sample doped with 6.1% europium still show a very satisfactory fit of the established structural model to the diffraction data (Table 1). We observe an intensity decrease of  $\sim 80\%$  between  $Eu_x = 0.00$  and  $0.061$  for all reflections, while the background intensity is increasing. The reduced signal-to-noise ratio is probably due to a decrease of the crystallinity and an increasing amount of an amorphous phase.

With increasing  $Eu_x$  concentration the reflection positions shift significantly to higher  $2\theta$ -values. Fig. 6 shows in exemplary manner two enlarged peaks for samples with concentration up to  $Eu_x = 0.061$ . The shift of the reflection positions is caused by a noticeable change in the  $a$ ,  $b$ , and  $c$  lattice parameters. The lengths of all three lattice parameters are decreasing with increasing  $Eu_x$  concentration. The unit cell volume of the crystalline phase decreases by  $\sim 1.7\%$  between  $Eu_x = 0$  and  $Eu_x = 0.061$  (Fig. 7). The reduced unit cell volume is consistent with the incorporation of  $Eu$  on the  $Ba/Ca$  position.  $Eu^{3+}$  has a significantly smaller cation radius in octahedral coordination ( $r_{Eu^{3+}} = 0.95 \text{ \AA}$ ) [37] than the radius of a hypothetical “ $Ba_{0.455}Ca_{0.545}$ ” atom ( $r_{Ba_{0.455}Ca_{0.545}} = 1.16 \text{ \AA}$ ) in the same coordination. The expected

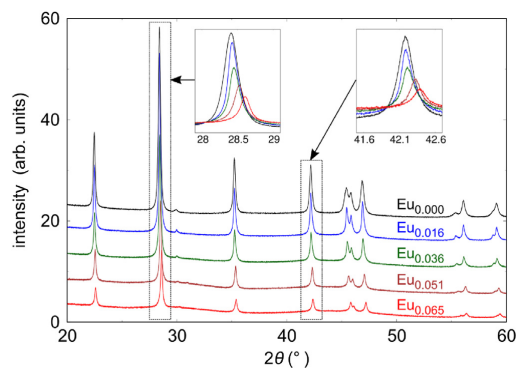


Fig. 6. X-ray powder diffraction data of  $\text{Ba}_{0.455}\text{Ca}_{0.545}\text{CO}_3:\text{Eu}$  obtained with  $\lambda = 1.5406 \text{ \AA}$  from precipitation synthesis for different  $\text{Eu}_x$  concentrations. Two peak positions are shown enlarged.

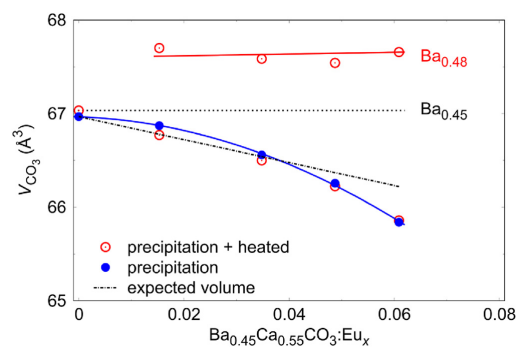


Fig. 7. Unit cell volume per  $\text{CO}_3$  group of  $\text{Ba}_{0.455}\text{Ca}_{0.545}\text{CO}_3:\text{Eu}_x$  for different  $\text{Eu}_x$  concentrations obtained by precipitation synthesis from synchrotron powder diffraction experiments. Open circles (•) represent samples heated to 723 K after the precipitation synthesis. There are two distinct phases in the sample, differing slightly in the Ba and Eu-content. Error bars representing the uncertainty in  $V$  and  $\text{Eu}_x$  are smaller than the symbol size. The dash-dotted line shows the expected volume decrease based on the cation size ratios.

volume decrease per  $\text{CO}_3$ -group for  $\text{Ba}_{0.455}\text{Ca}_{0.545}\text{CO}_3:\text{Eu}$  based on the cation sizes is shown in Fig. 7.

Heating an Eu-doped sample to 723 K leads to the formation of a second crystalline phase in the sample (Fig. 8). The amorphous background due to the precursor of the amorphous phase disappears. The new phase is isostructural but with a slightly increased unit cell volume (Fig. 7). The unit cell volume of the second crystalline phase does not substantially differ between samples with different  $\text{Eu}_x$  concentrations. The unit cell volume of the first crystalline phase is not affected by the heating process. Therefore, we conclude that the Eu-concentration of the phase first formed is not affected by the heating process. The Eu-concentration of the second phase is small and constant. The larger unit cell volume of the second crystalline phase relative to the volume expected for a Ba/Ca ratio of 0.45:0.55 implies a slight enrichment of Ba, thus implying that the amorphous phase was slightly enriched with Ba with respect to the phase formed first. We estimated a  $\text{Ba}_{0.48}$  concentration of the former amorphous phase based on the unit cell volume of the undoped samples (Supplementary Information Fig. S2). That would indicate that the Eu preferentially replaces Ba. Charge compensation requires the presence of  $\text{OH}^-$ -defects, but their effect on the unit cell volume seems to be negligible.

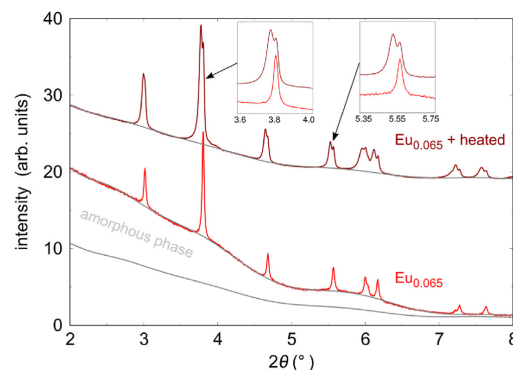


Fig. 8. Synchrotron powder diffraction data obtained with  $\lambda = 0.2071 \text{ \AA}$  of  $\text{Ba}_{0.455}\text{Ca}_{0.545}\text{CO}_3:\text{Eu}$  where  $\text{Eu}_x = 0.061$  as received from precipitation synthesis and from precipitation synthesis with subsequently heating to 723 K. Two peak positions are shown enlarged.

### 3.3.3. Raman spectroscopy

We used Raman spectroscopy to measure the influence of the Eu-incorporation into the structure on the Raman active  $\text{CO}_3$  stretching mode at  $\sim 1080 \text{ cm}^{-1}$  (Fig. 9). The instrumental broadening of our instrument, as determined by measuring a Si standard, is  $1\text{--}2 \text{ cm}^{-1}$ . Hence, significantly larger broadening of Raman peaks is due to sample properties. Raman spectroscopy is sensitive to the local environment, and due to the disordered nature of our samples, a group theoretical analysis was beyond the scope of the present study. Instead, we used two pseudo-Voigt functions to fit the slightly asymmetric peak of the  $\text{CO}_3$  stretching mode in undoped samples obtained from the precipitation synthesis, as this gives a satisfactory description of the scattered intensity. The full widths at half maximum (FWHM) were constrained to be identical. With increasing Eu-concentration we observe an increased asymmetric broadening of the peak and we had to introduce a third pseudo-Voigt function for an accurate description of the  $\text{CO}_3$  stretching mode. The peak center of the first two functions were constrained to the values obtained from the undoped sample ( $1077 \text{ cm}^{-1}$  and  $1088 \text{ cm}^{-1}$ ) and the FWHM of the three functions after the fit ( $\sim 15 \text{ cm}^{-1}$ ) does not substantially differ in comparison to the undoped sample.

After the heat treatment of the Eu-doped sample a new peak at  $1055 \text{ cm}^{-1}$  appears and the first two pseudo-Voigt functions shift  $\sim 2 \text{ cm}^{-1}$  to

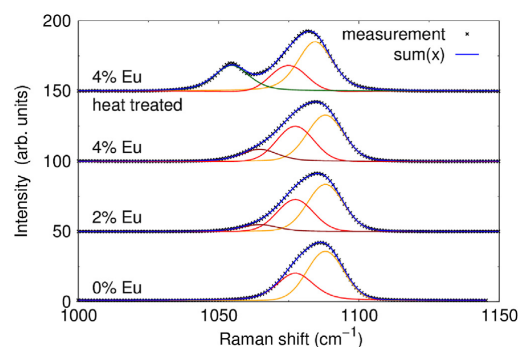


Fig. 9. Raman spectroscopy on the  $\text{CO}_3$  stretching mode in  $\text{Ba}_{0.46}\text{Ca}_{0.54}\text{CO}_3 + \text{Eu}_x$  samples with different  $\text{Eu}_x$  concentrations and heated samples containing two crystalline phases. The experimental data were fitted with two or three pseudo-Voigt functions respectively.

lower wavenumbers (Fig. 9). The FWHM of all functions is constrained to be identical and does not differ from the samples from the precipitation synthesis prior to the heat treatment. The new  $\text{CO}_3$  stretching mode is therefore unambiguously associated with the formation of the second crystalline phase during the heat treatment, and clearly the local environment of the  $\text{CO}_3$ -groups differs slightly for the two phases.

### 3.3.4. Fluorescence measurements

The incorporation of Eu into the  $\text{Ba}_{0.455}\text{Ca}_{0.545}\text{CO}_3$  structure causes a strong fluorescence (Fig. 10). The fluorescence measurements were performed either at ambient temperature or at 100 K. The measurements at low temperatures show a significant improvement of the resolution between the peaks of the different transitions of the  $\text{Eu}_{0.016}$  sample. Samples with different  $\text{Eu}_x$  show only minor differences except an increase in the absolute intensity of the fluorescence signal after precipitation synthesis. In contrast, the heated samples containing two crystalline phases show a significantly different fluorescence signal, as the heat treatment leads to the appearance of new fluorescence peaks. The new peaks are shifted by a few nm with respect to the wave-lengths of the transitions for the untreated samples. This is best observed for the very strong  ${}^5\text{D}_0 \rightarrow {}^7\text{F}_2$  transition. These observations are consistent with our model, namely that heat treatment leads to the formation of two isostructural phases, differing only slightly in the Ba and Eu-content. The amount of Eu in each phase cannot be determined, as a very small amount of Eu is sufficient to obtain a strong fluorescence signal in carbonates (e. g. calcite [38,39]).

We used time-resolved laser fluorescence spectroscopy to determine the lifetime ( $\tau$ ) of the  ${}^5\text{D}_0 \rightarrow {}^7\text{F}_0$  and the  ${}^5\text{D}_0 \rightarrow {}^7\text{F}_2$  transition in  $\text{Eu}_x = 0.061$  precipitated and heat-treated samples (Supplementary Information Fig. S3). Multiple measurements of the lifetime at the same transition wavelength were averaged. The lifetimes do not differ substantially from  $\tau \approx 1$  ms for any of our samples. This leads us to conclude that  $\text{Eu}^{3+}$  is incorporated into very similar environments in both crystalline phases, where the local environment only differs in the concentration of Ba or Ca as nearest neighbors.

## 4. Conclusion

We demonstrated that Ba/Ca-carbonate solid solutions, obtained by either solid-state reactions or by precipitation synthesis, have a wider single-phase field than previously reported [8,11]. The samples obtained by precipitation synthesis show a slightly decreased Ba/Ca ratio in comparison to the nominal  $\text{Ba}_x$  concentration in the feed solution. The

unit cell volume per  $\text{CO}_3^{2-}$ -group increases approximately linearly from the Ca-rich to the Ba-rich phase and is only slightly smaller than the expected below the expected volume of an ideal mixture between the end-member carbonates calcite and witherite. This is in contrast to the “baltite” phase [6], which has a significantly larger unit cell volume in comparison to the ideal mixture. The origin of this discrepancy remains unclear.

We found by ICP-OES that adding europium nitrate during the precipitation synthesis of  $\text{Ba}_{0.455}\text{Ca}_{0.545}\text{CO}_3$  in the feed solution results in an increased Eu-concentration in the samples up to  $\sim 6$  %. The Eu-uptake causes a significant decrease of the unit cell volume with increasing Eu-concentration. This is only expected when the Europium replaces a divalent cation, as any incorporation as an interstitial would very likely lead to an expansion of the lattice. During the precipitation synthesis an amorphous component is formed, which can be crystallized by heating. The second crystalline phase has the same structure as the phase formed first, but slightly different lattice parameters, indicating a slight enrichment of Ba and a low and constant Eu concentration.

This is consistent with the findings of Raman spectroscopy and fluorescence measurements. The fluorescence lifetimes are  $\sim 1$  ms for all samples. This strongly suggests that the Eu is only incorporated into one crystallographic position of Ca/Ba. The measured lifetime indicates a quenching by an OH-group close to the Eu ion [40], similar to observations in calcite [38,39]. In Eu-containing hydrocalcite, the Eu is surrounded by 6  $\text{OH}^-$ -“quencher” [41]. The presence of  $\sim 1$   $\text{OH}^-$ -group for each Eu in  $\text{Ba}_{0.455}\text{Ca}_{0.545}\text{CO}_3\text{:Eu}$  would not only explain the lifetime, but would also provide the mechanism for charge balancing. As we did not observe any sodium in an EDX analysis of our samples, and hence a coupled substitution of  $\text{Eu}^{3+} + \text{Na}^+$  for two divalent cations is very likely negligible in the present case, the incorporation of  $\text{OH}^-$ -groups provides a plausible mechanism. The weakly scattering hydrogen atoms cannot be detected by X-ray diffraction in powder diffraction studies, especially as we have very strongly scattering elements such as Ba and Eu in our sample. While IR-spectroscopy often provides insight into the presence of hydrogen in crystal structures, preliminary FTIR-studies were inconclusive.

In summary, our results unambiguously demonstrate that significant amounts of  $\text{Eu}^{3+}$  ( $\sim 6$  %) can be incorporated into Ba/Ca double carbonate solid solutions. This is by far larger than the amount of rare earth elements (REE) found as trace-elements in naturally occurring carbonates. In naturally occurring carbonates, such as  $\text{CaCO}_3$  or  $\text{MgCa}(\text{CO}_3)_2$ , the highest concentrations of light REE are typically  $<0.2\%$  [42–44]. For europium Stipp et al. (2006) [20] reported that the concentrations in  $\text{CaCO}_3$  obtained by ambient temperature precipitation experiments are in the same order of magnitude than in natural samples ( $<0.1\%$ ). Syntheses at higher temperatures or by other mechanisms [45,46] also did not allow the incorporation of higher concentrations. While a thermodynamic assessment and a determination of the concentration of OH-defects in our samples is still outstanding, the results presented here indicate that Ba/Ca-double carbonates may potentially be useful for the solidification of waste steams containing lanthanides.

### CRedit authorship contribution statement

**Dominik Spahr:** Data curation, Formal analysis, Investigation, Methodology, Validation, Visualization, Writing – original draft, Writing – review & editing. **Lkhamsuren Bayarjargal:** Conceptualization, Data curation, Formal analysis, Investigation, Methodology, Supervision, Validation, Visualization, Writing – original draft, Writing – review & editing. **Victor Vinograd:** Conceptualization, Formal analysis, Funding acquisition, Project administration, Supervision, Writing – original draft, Writing – review & editing. **Martin Etter:** Data curation, Formal analysis, Investigation, Methodology, Resources, Writing – original draft, Writing – review & editing. **Jacek Raddatz:** Data curation, Formal analysis, Investigation, Methodology, Resources, Writing – original draft, Writing

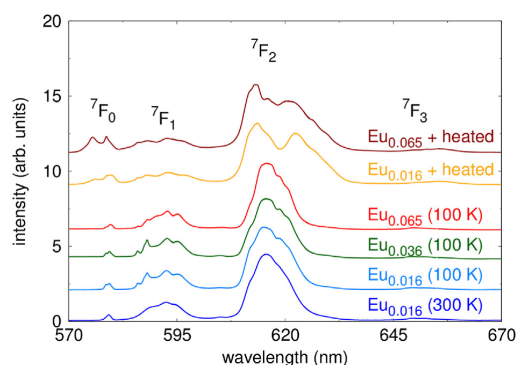


Fig. 10. Fluorescence of  $\text{Ba}_{0.46}\text{Ca}_{0.54}\text{CO}_3 + \text{Eu}_x$  samples with different  $\text{Eu}_x$  concentrations up to  $\text{Eu}_x = 0.065$  and heated samples containing two crystalline phases. Measurements were performed either at 300 K or at 100 K for an improvement of the peak-resolution.

– review & editing, **Björn Winkler**: Conceptualization, Data curation, Formal analysis, Funding acquisition, Investigation, Methodology, Project administration, Resources, Supervision, Validation, Writing – original draft, Writing – review & editing.

#### Declaration of competing interest

The authors declare that they have no known competing financial interests or personal relationships that could have appeared to influence the work reported in this paper.

#### Acknowledgements

We gratefully acknowledge funding from the DFG (project Wi1232 and Ba4020) and the DFG-Research Unit FOR2125/CarboPaT. DS appreciate the support from Rita Luchitskaia. BW is grateful for support by the BIOVIA Science Ambassador program. This is FIERCE contribution No. 84. We acknowledge DESY (Hamburg, Germany), a member of the Helmholtz Association HGF, for the provision of experimental facilities. Parts of this research were carried out at PETRA III, beamline P02.1.

#### Appendix A. Supplementary data

Supplementary data to this article can be found online at <https://doi.org/10.1016/j.jssc.2021.122759>.

#### References

- [1] B. Dickens, J.S. Bowen, The Crystal Structure of BaCa(CO<sub>3</sub>)<sub>2</sub> (barytocalcite), *J. Res. Natl. Bur. Stand. (U.S.)* 75A (1971) 197–203.
- [2] H. Effenberger, The Crystal Structure of the Mineral Paralstonite, BaCa(CO<sub>3</sub>)<sub>2</sub>, *N. Jb. Miner. Mh.*, 1980, pp. 353–363.
- [3] F. Sartori, New data on alstonite, *Lithos* 8 (1975) 199–207.
- [4] L. Bindi, A.C. Roberts, C. Biagioni, The crystal structure of alstonite, BaCa(CO<sub>3</sub>)<sub>2</sub>: an extraordinary example of ‘hidden’ complex twinning in large single crystals, *Mineral. Mag.* 84 (2020) 699–704.
- [5] R. Chulíá-Jordán, D. Santamaría-Perez, J. Ruiz-Fuertes, A. Otero-de-la-Roza, C. Popescu, Crystal Structure of BaCa(CO<sub>3</sub>)<sub>2</sub> Alstonite Carbonate and Its Phase Stability upon Compression, *Earth Space Chem.* 5 (2021) 1130–1139.
- [6] M.L. Whittaker, D. Joester, ACBC to Balcite: Bioinspired Synthesis of a Highly Substituted High-Temperature Phase from an Amorphous Precursor, *Adv. Mater.* 29 (2017) 1606730.
- [7] D. Spahr, L. Bayarjargal, V. Vinograd, R. Luchitskaia, B. Winkler, A new BaCa(CO<sub>3</sub>)<sub>2</sub> polymorph, *Acta Crystallogr. B* 75 (2019) 291–300.
- [8] L.L.Y. Chang, Subsolidus phase relations in the aragonite-type carbonates, *J. Geol.* 73 (1965) 346–368.
- [9] L.L.Y. Chang, Subsolidus phase relations in the systems BaCO<sub>3</sub>-SrCO<sub>3</sub>, SrCO<sub>3</sub>-CaCO<sub>3</sub>, and BaCO<sub>3</sub>-CaCO<sub>3</sub>, *Am. Mineral.* 56 (1971) 1660–1673.
- [10] W.R. Brice, L.L.Y. Chang, Subsolidus phase relations in aragonite-type carbonates. III. The system MgCO<sub>3</sub>-CaCO<sub>3</sub>-BaCO<sub>3</sub>, MgCO<sub>3</sub>-CaCO<sub>3</sub>-SrCO<sub>3</sub> and MgCO<sub>3</sub>-SrCO<sub>3</sub>-BaCO<sub>3</sub>, *Am. Mineral.* 58 (1973) 979–985.
- [11] M.L. Whittaker, W. Sun, K.A. DeRocher, S. Jayaraman, G. Ceder, D. Joester, Structural Basis for Metastability in Amorphous Calcium Barium Carbonate (ACBC), *Adv. Funct. Mater.* 28 (2018) 1704202.
- [12] J. Serp, C. Poinssot, S. Bourg, Assessment of the anticipated environmental footprint of future nuclear energy systems. Evidence of the beneficial effect of extensive recycling, *Energies* 10 (2017) 1445.
- [13] C. Poinssot, S. Bourg, N. Ouvrier, N. Comberoux, C. Rostaing, M. Vargas-Gonzalez, J. Bruno, Assessment of the environmental footprint of nuclear energy systems. Comparison between closed and open fuel cycles, *Energy* 69 (2014) 199–211.
- [14] A.P. Paiva, P. Malik, Recent advances on the chemistry of solvent extraction applied to the reprocessing of spent nuclear fuels and radioactive wastes, *J. Radioanal. Nucl. Chem.* 261 (2004) 485–496.
- [15] P. Baron, S. Cornet, E. Collins, G. DeAngelis, G. Del Cul, et al., A review of separation processes proposed for advanced fuel cycles based on technology readiness level assessments, *Prog. Nucl. Energy* 117 (2019) 103091.
- [16] G. Modolo, A. Geist, M. Migurditchian, Minor actinide separations in the reprocessing of spent nuclear fuels: recent advances in Europe, in: R. Taylor (Ed.), *Reprocessing and Recycling of Spent Nuclear Fuel*, Woodhead Publishing, Oxford, 2015, pp. 245–287.
- [17] A. Geist, J.-M. Adnet, S. Bourg, C. Ekberg, H. Galand, P. Guilbaud, M. Migurditchian, G. Modolo, C. Rhodes, R. Taylor, An overview of solvent extraction processes developed in Europe for advanced nuclear fuel recycling, part 1 — heterogeneous recycling, *Separ. Sci. Technol.* (2020) 1–16.
- [18] A. Gelis, P. Kozak, A. Breshears, M. Brown, C. Launier, E. Campbell, G. Hall, T.G. Levitskaia, V. Hofeltz, G. Lumetta, Closing the nuclear fuel cycle with a simplified minor actinide lanthanide separation process (ALSEP) and additive manufacturing, *Sci. Rep.* 9 (2019) 12842.
- [19] A. Wilden, F. Kref, D. Schneider, Z. Paparigas, G. Modolo, G.J. Lumetta, A. Gelis, J.D. Law, A. Geist, Countercurrent actinide lanthanide separation process (ALSEP) demonstration test with a simulated PUREX raffinate in centrifugal contactors on the laboratory scale, *Appl. Sci.* 10 (2020) 7217.
- [20] S.L.S. Stipp, J.T. Christensen, L.Z. Lakshatnov, J.A. Baker, T.E. Waight, Rare Earth element (REE) incorporation in natural calcite: upper limits for actinide uptake in a secondary phase, *Radiochim. Acta* 94 (2006) 523–528.
- [21] A. Grandjean, G. Leturcq, Natural sintering of carbonate powder for use as a carbon-14 immobilization matrix, *J. Nucl. Mater.* 345 (2005) 11–18.
- [22] N. Massoni, J. Rosen, M. Chartier, T. Cozzika, Study of barytocalcite as a conditioning matrix for carbon 14: comparison of several synthesis routes, *J. Nucl. Mater.* 441 (2013) 199–207.
- [23] N. Massoni, C. Marcou, J. Rosen, M. Chartier, P. Jollivet, The use of barytocalcite for carbon 14 immobilization: one-year leaching behavior, *J. Nucl. Mater.* 454 (2014) 230–237.
- [24] N. Massoni, S. Le Gallet, S. Hoffmann, L. P. Y. Grin, F. Bernard, Sintering of synthetic barytocalcite BaCa(CO<sub>3</sub>)<sub>2</sub>, kutnahorite CaMn(CO<sub>3</sub>)<sub>2</sub> and rhodochrosite MnCO<sub>3</sub> for carbon-14 sequestration, *J. Eur. Ceram. Soc.* 35 (2015) 297–308.
- [25] N. Massoni, S. Le Gallet, Investigation of the sintering of barytocalcite with BaCO<sub>3</sub> as a secondary phase for immobilizing carbon-14, *J. Nucl. Mater.* 476 (2016) 13–19.
- [26] M.-M. Bé, V. Chisté, C. Dulieu, E. Browne, Able of radionuclides (Vol. 3: a = 3 to 244), *Geol. Soc. Spec. Publ.* 443 (2006) 1–8.
- [27] A.-C. Dippel, H.-P. Liermann, J.T. Deltz, P. Walter, H. Schulte-Schrepping, O. Seeck, H. Franz, Beamline P02.1 at PETRA III for high-resolution and high-energy powder diffraction, *J. Synchrotron Radiat.* 22 (2015) 675–687.
- [28] C. Prescher, V.B. Prakapenka, DIOPTAS: a program for reduction of two-dimensional X-ray diffraction data and data exploration, *High Pres. Res.* 35 (2015) 223–230.
- [29] H.M. Rietveld, A profile refinement method for nuclear and magnetic structures, *J. Appl. Crystallogr.* 2 (1969) 65–71.
- [30] B.H. Toby, R.B. Von Dreele, *GSAS-II*: the genesis of a modern open-source all purpose crystallography software package, *J. Appl. Crystallogr.* 46 (2013) 544–546.
- [31] L. Bayarjargal, C.-J. Fruhner, N. Schrodt, B. Winkler, CaCO<sub>3</sub> phase diagram studied with Raman spectroscopy at pressures up to 50 GPa and high temperatures and DFT modeling, *Phys. Earth Planet. In.* 281 (2018) 31–45.
- [32] C.-J. Fruhner, L. Bayarjargal, N. Schrodt, R. Luchitskaia, W. Morgenroth, B. Winkler, Pressure-induced phase transition from calcite to aragonite detected by fluorescence spectroscopy, *Eur. J. Mineral.* 30 (2018) 711–720.
- [33] M. Wojdyr, *Fityk*: a general-purpose peak fitting program, *J. Appl. Crystallogr.* 43 (2010) 1126–1128.
- [34] J.P.R. de Villiers, Crystal structures of aragonite, strontianite, and witherite, *Am. Mineral.* 56 (1971) 758–767.
- [35] S.A. Markgraf, R.J. Reeder, High-temperature structure refinements of calcite and magnesite, *Am. Mineral.* 70 (1985) 590–600.
- [36] S.R. Kamhi, On the structure of vaterite, CaCO<sub>3</sub>, *Acta Crystallogr.* 16 (1963) 770–772.
- [37] R.D. Shannon, Revised effective ionic radii and systematic studies of interatomic distances in halides and chalcogenides, *Acta Crystallogr.* A32 (1976) 751–767.
- [38] M. Marques Fernandes, M. Schmidt, C. Walther, D. Boshach, R. Klenze, Site-selective time-resolved laser fluorescence spectroscopy of Eu<sup>3+</sup> in calcite, *J. Colloid Interface Sci.* 321 (2008) 323–331.
- [39] S.E. Hellebrandt, S. Hofmann, N. Jordan, A. Barkleit, M. Schmidt, Incorporation of Eu(III) into calcite under recrystallization conditions, *Sci. Rep.* 6 (2016) 33137.
- [40] W.D. Horrocks, D.R. Sudnick, Lanthanide ion probes of structure in biology — laser-induced luminescence decay constants provide a direct measure of the number of metal-coordinated water-molecules, *J. Am. Chem. Soc.* 101 (1979) 334–340.
- [41] T. Stumpf, H. Curtius, C. Walther, K. Dardenne, K. Ufer, T. Fanghänel, Incorporation of Eu(III) into hydrotalcite: a TRFMS and EXAFS study, *Environ. Sci. Technol.* 41 (2007) 3186–3191.
- [42] I.M. Kjarsgaard, Rare earth elements in sovitic carbonatites and their mineral phase, *J. Petrol.* 39 (2007) 2105–2121.
- [43] A.R. Chakhmouradian, C. Böhm, A. Demény, E. Reguir, E. Hegner, C.R. A. N.M. Halden, P. Yang, “Kimberlite from Wekusko Lake, Manitoba: actually a diamond-indicator-bearing dolomite carbonatite, *Lithos* 112 (2009) 347–357.
- [44] A.R. Chakhmouradian, E. Reguir, C. Couëslan, P. Yang, Calcite and dolomite in intrusive carbonatites. II. Trace-element variations, *Min. Pet.* 110 (2016) 361–377.
- [45] J. Sysma, A. Meijer, G. Blasse, Spectroscopy of Gd<sup>3+</sup> and Eu<sup>3+</sup> in the calcite structure, *J. Solid State Chem.* 99 (1992) 78–84.
- [46] M. Kang, J. Liu, G. Yin, R. Sun, Preparation and characterization of Eu<sup>3+</sup>-doped CaCO<sub>3</sub> phosphor by microwave synthesis, *Rare Met.* 28 (2009) 439–444.



## Incorporation of rare earth elements into $(\text{Ba}, \text{Ca})_2(\text{CO}_3)_2$

Dominik Spahr<sup>a,\*</sup>, Lkhamsuren Bayarjargal<sup>a</sup>, Victor Vinograd<sup>b</sup>, Rita Luchitskaia<sup>a</sup>, Björn Winkler<sup>a</sup>

<sup>a</sup> Institute of Geosciences, Goethe University, Frankfurt, 61184, Germany

<sup>b</sup> Institute of Energy and Climate Research (IEK-6), Nuclear Waste Management and Reactor Safety, Forschungszentrum Jülich, Jülich, 52428, Germany

### ARTICLE INFO

**Keywords:**  
 $(\text{Ba}, \text{Ca})_2(\text{CO}_3)_2$   
 Rare earth element incorporation  
 Raman spectroscopy  
 X-ray powder diffraction

### ABSTRACT

The structural effects of the incorporation of the rare earth elements (REE) La, Ce, Pr, Nd, Eu, Sm, Gd, Er, Tm, Yb and Y into a synthetic Ba–Ca carbonate have been investigated. We precipitated solutions with a composition  $\text{Ba}_{0.9}\text{Ca}_{1.1}(\text{CO}_3)_2$  doped with REE-nitrates. The precipitate, with few exceptions, consisted of a crystalline solid, slightly depleted in Ba with respect to the expected composition, and an amorphous phase. On heating, the whole sample became crystalline and consisted of a Ba-enriched and a Ba-depleted phase. The phases are isostructural. The lattice parameters are strongly influenced by the incorporation of  $\approx 6\%$  REE. There is a linear dependence of the unit cell volume on the radius of the incorporated REE for those elements with a radius  $< 1.0 \text{ \AA}$ , i.e. Yb, Tm, Er, Y, Gd, Sm, Eu, Nd and Pr, while the unit cell volume of a sample doped with La ( $r(\text{La}) = 1.03 \text{ \AA}$ ) and Ce ( $r(\text{Ce}) = 1.01 \text{ \AA}$ ) is not well described by this dependency. Raman spectroscopy shows that the local environment of the  $\text{CO}_3$ -groups does not differ substantially between the Ba-enriched and the Ba-depleted phase, but changes linearly as a function of the ionic radius of the REE. The present study clearly shows that substantial amounts of REE can be incorporated into the Ba–Ca-carbonate studied here, making it potentially useful as a matrix in nuclear waste treatments involving aqueous nitrate solutions of lanthanides and actinides.

### 1. Introduction

Ba- and Ca-containing double carbonates,  $\text{Ba}_x\text{Ca}_{2-x}(\text{CO}_3)_2$ , and related compounds have been investigated for a long time [1] and are currently studied in several contexts. Here, we investigate the incorporation of rare earth elements into a synthetic  $\text{Ba}_x\text{Ca}_{2-x}(\text{CO}_3)_2$  polymorph, as this polymorph can be obtained by precipitation (amongst other techniques) and is a potential host for actinides and lanthanides separated from waste streams in processes generating aqueous nitrate solutions, such as the Actinide Lanthanide Separation Process (ALSEP) [2,3].

There are, however, still open questions regarding the structures of some  $\text{Ba}_x\text{Ca}_{2-x}(\text{CO}_3)_2$  polymorphs and the subsolidus stabilities, and as this has led to some confusion in the past (see discussion in Spahr, Bayarjargal, Vinograd, Luchitskaia and Winkler [4] regarding the use of barytocalcite as a matrix for  $^{14}\text{C}$ ) it seems worthwhile to summarize the most recent results of structures and properties in this system.

Three polymorphs of  $\text{BaCa}(\text{CO}_3)_2$ , namely barytocalcite, paralstonite and alstonite have been found in nature up to now. The crystal structure of barytocalcite has been solved by Dickens and Bowen [5] and that of

paralstonite by Effenberger [6]. Their structures are undisputed. The barytocalcite structure can be described as a distorted dolomite-type structure in which there is planar ordering of cations into alternating Ba and Ca layers. In contrast, in paralstonite there are dolomite-like Ca–Ba planar ordered layers but the carbonate anions are no longer co-planar between the cation layers. Although large high-quality crystals of alstonite are available, its structure is still discussed controversially. A new structural model based on space group  $P31m$  with a large unit cell volume ( $\approx 1614 \text{ \AA}^3$ ) was recently proposed by Bindi, Roberts and Biagioni [7]. In their study alstonite is described with a layered crystal structure, formed by the alternation of mixed Ba–Ca layers and  $\text{CO}_3$  groups parallel to  $\{0001\}$ . Later Chuliá-Jordán, Santamaria-Perez, Ruiz-Fuertes, Otero-de-la Roza and Popescu [8] suggested that in fact the space group is  $P321$ .

A synthetic fourth polymorph was obtained by Whittaker and Joester [9] by precipitation and, independently, by Spahr et al. [4] by precipitation, high-temperature reaction of the constituent carbonates and by mechanochemical activation. Seknazi, Levy, Polishchuk, Katsman and Pokroy [10] repeated the synthesis by precipitation. Saito, Kagi, Marugata, Komatsu, Enomoto, Maruyama and Kawano [11] synthesized

\* Corresponding author.

E-mail address: [d.spahr@kristall.uni-frankfurt.de](mailto:d.spahr@kristall.uni-frankfurt.de) (D. Spahr).

<https://doi.org/10.1016/j.solidstatesciences.2023.107129>

Received 14 September 2022; Received in revised form 8 February 2023; Accepted 13 February 2023

Available online 10 March 2023

1293-2558/© 2023 Elsevier Masson SAS. All rights reserved.

“Ba-doped calcites” by precipitation combined with a high-pressure treatment. Saito et al. [11] seemed to have been unaware of the earlier work, as they erroneously claimed to have, for the first time, obtained samples where Ba was in excess of Ca. Regrettably, that study doesn’t include any details regarding the structural analysis, and hence will not be considered further here. Whittaker and Joester [9] called this compound “balcite”, a term which we prefer not use as we believe that mineral-like names should be approved by the appropriate commission of the IMA in order to avoid inconsistencies. We will therefore refer to this phase here as the “C2-phase” which has a C-centered, monoclinic structure with a relatively small ( $\approx 134 \text{ \AA}^3$ ) unit cell volume [4].

The powder diffractograms in these studies seem to be very similar. Rietveld refinements of powder diffraction data by Whittaker and Joester [9] were carried out in space group  $R\bar{3}m$ , giving a volume of  $V_{\text{CO}_3} = 72.88 \text{ \AA}^3/\text{CO}_3\text{-group}$ , significantly larger than the corresponding values for the natural polymorphs ( $V_{\text{CO}_3} = 65.8\text{--}67.04 \text{ \AA}^3/\text{CO}_3\text{-group}$ ). In contrast, the Rietveld refinement with a monoclinic unit cell by Spahr, Bayarjargal, Vinograd, Etter, Raddatz and Winkler [12] yielded a value of  $V_{\text{CO}_3} = 68.20(1) \text{ \AA}^3/\text{CO}_3\text{-group}$ . For a structure with composition Ba:Ca  $\approx 1:1$  and space group symmetry  $R\bar{3}m$  Seknazi et al. [10] obtained very different lattice parameters than those given by Whittaker and Joester [9]; ( $a_{\text{Seknazi}} = 5.07986(7) \text{ \AA}$ ,  $a_{\text{Whittaker}} = 5.2371 \text{ \AA}$ ,  $c_{\text{Seknazi}} = 8.9277(1) \text{ \AA}$ ,  $c_{\text{Whittaker}} = 9.2053 \text{ \AA}$ ), but give  $V_{\text{CO}_3}$  values in close agreement to those obtained by Spahr et al. [4,12]. It is worthwhile to note that the lattice parameters of the synthetic phase seem to be independent of the synthesis route, where rather different synthesis routes (mechano-synthesis, high-temperature synthesis and precipitation) have been employed by Spahr et al. [4,12]; so it seems unlikely that the origin of that discrepancy is due to different ordering states.

There is currently no consensus on the best description of the structure of the synthetic compound. The Rietveld refinements by Whittaker and Joester [9] (besides the systematic off-set of the lattice parameters) and by Seknazi et al. [10] seem to describe the diffraction data as well as those by Spahr et al. [4,12]. This is not surprising, as of course the contribution by Ba dominates the structure factor. In any model involving disorder of the oxygen atoms, their contribution to the structure factor becomes even smaller than in those with an ordered arrangement. The model by Spahr et al. [4,12] seems simpler and describes all observations in a consistent fashion, and hence we will use this structural model here. We would also like to note that in the case of precipitation synthesis, synchrotron diffraction doesn’t provide a significant advantage relative to diffraction studies using a sealed-tube x-ray source, as the widths of the diffraction peaks are determined by the sample, not the instrument.

It is worthwhile to note that there has been no report of an experimental synthesis of alstonite. Recently it has been shown that paralstonite can be obtained by heating of alstonite [13]. Spahr et al. [4] seems to have been the first to synthesize barytocalcite, as the purported synthesis of barytocalcite by Massoni, Rosen, Chartier and Cozzika [14] yielded in fact the new synthetic polymorph (see discussion in Spahr et al. [4]). The relative stabilities of the four polymorphs have not been investigated experimentally, e.g. by calorimetry. In fact, while syntheses based on precipitates may lead to the formation of metastable compounds, this is generally not the case for high-temperature reactions. Spahr et al. [4] obtained the C2-phase from a reaction from the carbonates at 823 K without the presence of a fluid, and also by dry mechanochemical activation and via two precipitation routes, while barytocalcite was only obtained hydrothermally.

In an extensive and detailed study, Chang [1] studied the subsolidus behaviour of the  $\text{BaCO}_3\text{--CaCO}_3$  system. Three points are noteworthy. First of all, the boundaries separating phase fields were obtained from in situ high-temperature diffraction studies and we judge them to be reliable. Secondly, due to the limited data analysis capabilities at that time, the structures present at a given temperature and composition were inferred, and are not based on structural refinements. In fact, in the

study of Chang [1] no diffraction data are shown. At that time, the data analysis typically was based on the “X-ray powder data file” [15]. As was discussed by Spahr et al. [4], the entry for  $\text{BaCa}(\text{CO}_3)_2$  in the powder diffraction file in use at the time, which claimed to be “barytocalcite” (I-0770) [15] was, in fact, not for barytocalcite, but rather that of the polymorph rediscovered by Whittaker and Joester [9]. Thirdly, in the interesting range of Ba:Ca = 1:1 there is only very limited data. The main finding of that study, which we think is undisputed, is that in the  $\text{BaCO}_3\text{--CaCO}_3$  system at temperatures  $> 775 \text{ K}$  in the vicinity of compositions with Ba:Ca = 1:1 a Ba–Ca–solid solution with variable composition is the stable phase. Chang [1] termed this the “disordered rhombohedral phase”, but this is not based on any structural refinement. A direct synthesis from the oxide well within the stability field leads to the C2-phase. We therefore conclude that the question concerning the relative stabilities of the Ba–Ca–carbonates at ambient pressure is not unambiguously answered yet.

Complex temperature-induced structural changes have been observed in synthetic  $\text{Ba}_x\text{Ca}_{2-x}(\text{CO}_3)_2$ , but are not fully consistent with each other. Seknazi et al. [10] observed the formation of a Ba-enriched and a Ba-depleted phase from “partially ordered Ba-calcite”, where a sharp (104) reflection of the well-crystallized initial phase degrades into two very broad and weak reflections upon heating by 573 K. Whittaker et al. [13] observed, upon heating precipitated  $\text{BaCa}(\text{CO}_3)_2$  to 873 K, that the widths of the reflections became narrower, i.e. an increase in the crystallinity and a grain coarsening. Whittaker et al. [13] concluded that at temperatures between 423 and 873 K there is an ordering of the Ba and Ca cations. In contrast, Spahr et al. [4] saw no difference in the ordering of the cations when comparing samples obtained from precipitation to those obtained by a direct reaction at high temperatures from milled calcite and witherite.

When precipitating  $\text{Ba}_x\text{Ca}_{2-x}(\text{CO}_3)_2$  from a feed-solution that contained europium, a crystalline and an amorphous phase were formed [12]. Heating to 723 K leads to the formation of two crystalline phases, which are isostructural, but differ slightly in their lattice parameters. This has been interpreted as the formation of a slightly Ba-enriched and a slightly Barium-depleted phase and is the basis for the present study. Irrespective of the gaps in our knowledge concerning the best description of the structure of the C2-phase, it was rather surprising that substantial amounts of europium (up to  $\approx 6\%$ ) could be incorporated into  $\text{Ba}_x\text{Ca}_{2-x}(\text{CO}_3)_2$ , and this evoked the question if other rare earth elements could be incorporated equally well. This question has been studied here, also with the aim to provide more experimental constraints to this challenging system.

## 2. Material and methods

### 2.1. Precipitation synthesis

$\text{BaCa}(\text{CO}_3)_2$  was synthesized by precipitation according to equation (1) following a nitrate route [4]. We found earlier by ICP-OES and EDX measurements [12], that an equimolar Ba–Ca concentration in the feed solution leads to samples with a  $\text{Ba}_{0.9}\text{Ca}_{1.1}(\text{CO}_3)_2$  concentration, while adding europium does not change the Ba–Ca ratio. Here, we introduced 8 at.% of different rare earth elements (La, Ce, Pr, Nd, Eu, Sm, Gd, Er, Tm, Yb) or Yttrium into the feed solution during the precipitation synthesis ( $x_{\text{REE}} = 0.08$ ) to obtain samples with  $\text{Ba}_{0.9}\text{Ca}_{1.1}(\text{CO}_3)_2 + \text{REE}_x$  composition.



A list of the employed starting materials in the precipitation synthesis is shown in Table 1. All chemicals were analytical grade and used as purchased.

The starting materials were dissolved separately in bidistilled water to obtain solutions with a concentration of  $0.1 \text{ mol l}^{-1}$ . The barium- and calcium-nitrate solutions were mixed in stoichiometric proportions

D. Spahr et al.

Solid State Sciences 139 (2023) 107129

**Table 1**  
Starting materials for the precipitation synthesis.

compound	purity (%)	manufacturer
Ba(NO <sub>3</sub> ) <sub>2</sub>	99.95	chemPUR, Karlsruhe, Germany
Ca(NO <sub>3</sub> ) <sub>2</sub> ·4H <sub>2</sub> O	99.9	strem chemicals, Cambridge, United Kingdom
Na <sub>2</sub> CO <sub>3</sub>	99.9	Merck KGaA, Darmstadt, Germany
La(NO <sub>3</sub> ) <sub>3</sub> ·6H <sub>2</sub> O	99.99	Merck KGaA, Darmstadt, Germany
Ce(NO <sub>3</sub> ) <sub>3</sub> ·6H <sub>2</sub> O	99.5	Alfa Aesar, Kandel, Germany
Pr(NO <sub>3</sub> ) <sub>3</sub> ·6H <sub>2</sub> O	99.9	Merck KGaA, Darmstadt, Germany
Nd(NO <sub>3</sub> ) <sub>3</sub> ·6H <sub>2</sub> O	99.9	Merck KGaA, Darmstadt, Germany
Eu(NO <sub>3</sub> ) <sub>3</sub> ·5H <sub>2</sub> O	99.9	Merck KGaA, Darmstadt, Germany
Sm(NO <sub>3</sub> ) <sub>3</sub> ·6H <sub>2</sub> O	99.999	Merck KGaA, Darmstadt, Germany
Gd(NO <sub>3</sub> ) <sub>3</sub> ·6H <sub>2</sub> O	99.9	Merck KGaA, Darmstadt, Germany
Er(NO <sub>3</sub> ) <sub>3</sub> ·5H <sub>2</sub> O	99.9	Merck KGaA, Darmstadt, Germany
Tm(NO <sub>3</sub> ) <sub>3</sub> ·5H <sub>2</sub> O	99.9	Merck KGaA, Darmstadt, Germany
Yb(NO <sub>3</sub> ) <sub>3</sub> ·5H <sub>2</sub> O	99.999	Merck KGaA, Darmstadt, Germany
Y(NO <sub>3</sub> ) <sub>3</sub> ·4H <sub>2</sub> O	99.99	Merck KGaA, Darmstadt, Germany

according to equation (1), while an appropriate amount of the REE-nitrate solution was added to achieve a concentration of 8% in the feed solution. The Ba–Ca/REE nitrate solution was added drop-wise to a sodium carbonate solution ( $\approx 2 \text{ ml min}^{-1}$ ) while stirring at ambient temperature. After the synthesis the resulting suspension was filtered under vacuum. The precipitate was washed with distilled water and the resulting powder was dried at 333(1) K for 12–18 h in a drying oven.

The heat treatment of the powders obtained from the precipitation synthesis was performed at 723 K in a muffle furnace for 12 h. The heating rate was  $\approx 100 \text{ K h}^{-1}$  for all samples and the samples were cooled down to ambient temperature by switching of the oven within 4–5 h.

## 2.2. X-ray powder diffraction

We used a PANalytical X'Pert Pro diffractometer with Bragg–Brentano geometry for X-ray powder diffraction (XRD) to characterize the samples obtained from the precipitation synthesis. The diffractometer was equipped with a PANalytical PIXcel<sup>3D</sup> detector, a copper X-ray tube and a Johansson monochromator. The measurements were performed with Cu K<sub>α1</sub> radiation and variable divergence slits (10 mm irradiation length) to ensure a good signal-to-noise ratio. Instrument parameters were obtained by measuring a Si-standard with 99.999% purity. All powders were measured as received without further grinding, while they were mounted on an oriented Si single crystal sample holder. Le Bail and Rietveld refinements on the powder diffraction data were carried out using the software package GSAS-II [16–18].

## 2.3. Raman spectroscopy

Raman spectroscopy was performed with a custom-built set-up [19]. The set-up consists of an OXXIUS S.A. LaserBoxx LMX532 laser with a wavelength of 532.14 nm and a Princeton Instruments ACTON SpectraPro 2300i spectrograph equipped with a Pixis256E CCD camera. The samples were placed on an aluminum stub. Background correction and fitting of the Raman spectra was performed using the software package Fityk [20].

## 2.4. Scanning electron microscopy

We used a Phenom World ProX desktop SEM for scanning electron microscopy. Images were acquired with a Back-scattered Electron Detector (BSE), while energy dispersive X-ray spectroscopy (EDX) measurements for a semi-quantitative characterization of the composition were performed using a silicon drift detector (SDD). The powder samples were mounted on aluminum stubs using sticky carbon tape without subsequent coating and the samples were measured under low vacuum conditions to reduce charging effects. Images were acquired with an acceleration voltage of 15 kV while EDX was performed with 10 kV.

## 3. Results and discussion

### 3.1. Synthesis

We successfully synthesized well-crystalline Ba–Ca carbonates doped with a variety of trace elements (La, Ce, Pr, Nd, Eu, Sm, Gd, Y, Er, Tm, Yb) by precipitation synthesis followed by a heat treatment. Depending on the added element the powders vary strongly in their color (Fig. 1). While the Pr-doped sample appears brown, Nd-incorporation causes a light blue color, and Er leads to a light rose color. Some elements such as e. g. La, Eu, or Yb do not cause a significant color change.

We used EDX to ensure that the composition of the powder samples was close to the expected composition. We found that all samples have a slightly decreased Ba–Ca ratio corresponding to a Ba<sub>0.9</sub>Ca<sub>1.1</sub>(CO<sub>3</sub>)<sub>2</sub> composition, which is the expected composition for samples with an equimolar Ba–Ca-ratio in the feed solution [4,9]. Furthermore, the EDX measurements clearly show the incorporation of significant amounts of the particular trace elements into the Ba–Ca carbonate during the precipitation. The trace elements are still present after the repeated washing of the samples with distilled water and heating up to 723(1) K. Due to the fine grain size of the powders and the intergrowth of the individual grains we could not determine grain sizes in the SEM.

The concentration of the dopant cannot be determined precisely by EDX, as there are very large relative errors in EDX measurements for low concentrations. However, a combination of the semi-quantitative EDX data with the diffraction and spectroscopy data discussed below implies that there are no significant differences in the incorporation mechanisms of the individual REE. We found earlier that 8% europium in the feed solution results in  $\approx 6\%$  in the solid [4], and hence we expect a similar concentration for the trace elements studied here.

### 3.2. X-ray powder diffraction

Fig. 2 shows selected X-ray powder diffraction data of Ba–Ca carbonates doped with different REE after the precipitation synthesis and before the heating in comparison to the heated sample. Before the heating procedure two phases are present. One is crystalline while the other is very poorly crystalline or amorphous (Fig. 2). As poor crystallinity and small crystallite size both contribute to peak broadening, a grain size growth during the heat treatment could not be quantified from the powder diffraction data. The powder data of the unheated as well as of the heated samples show no unexpected reflections due to impurity phases.

This is in good agreement with the results for the Eu-doped samples we found earlier [4]. Especially for the small cations such as Y and Yb the amorphous phase is dominant and only tiny reflections can be observed. After heating the amorphous phase disappears and two



Fig. 1. Color of Ba–Ca carbonate powder samples, doped with different trace elements (La, Pr, Nd, Eu, Sm, Gd, Y, Er, Tm, Yb) after the precipitation synthesis and the subsequent heat treatment at 723(1) K.

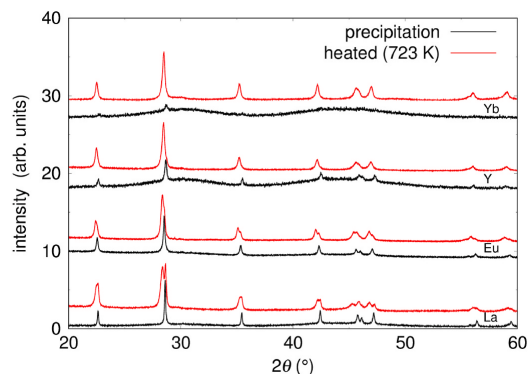


Fig. 2. X-ray powder diffraction data of Ba-Ca carbonates doped with different trace elements (La, Eu, Y, Yb) after the precipitation synthesis and before the heating in comparison to the heated sample (723(1) K).

crystalline phases are present. As the initial set of reflections remains essentially unchanged, it seems that the amorphous precipitate crystallized during the heat treatment, with no exchange between the newly formed crystals and the existing ones. As the diffraction patterns are very similar, but only slightly off-set, we conclude that both phases are isostructural, but differ in the lattice parameter only. Fig. 3 shows an enlargement between 20 and 40° of the X-ray powder diffraction data of Ba-Ca carbonates doped with Nd, Gd and Yb. For Nd and Gd two isostructural phases coexist in about equal proportions, while for the very small Yb ( $r(\text{Yb}) = 0.87 \text{ \AA}$ ) [21] only one phase can be observed (VI-fold coordination is assumed).

This observation can be explained by the coexistence of a Ba-enriched and a Ba-depleted phase. Such a coexistence has been observed earlier by Seknazi et al. [10]; but in that study, the Ba-enriched and the Ba-depleted phase were thought to have different space group symmetries. Also, in the study of Seknazi et al. [10] the coexisting phases have broad and weak reflections, while in our study they are very well crystalline. We have also observed this earlier when incorporating Eu into  $\text{Ba}_{0.9}\text{Ca}_{1.1}(\text{CO}_3)_2$  [12]. We used the X-ray powder diffraction data to determine the unit cell volume of the samples doped with different trace elements after the heating process (Fig. 4 and Table 2).

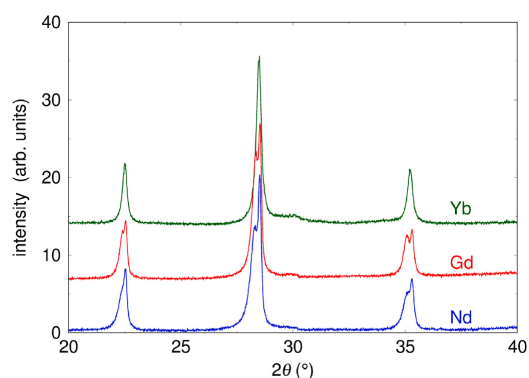


Fig. 3. Enlargement of parts of the X-ray powder diffraction data of Ba-Ca carbonates doped with different trace elements after the heating treatment. Two well-crystalline isostructural phases coexist in about equal proportions in Nd and Gd, while for Yb one phase can be observed.

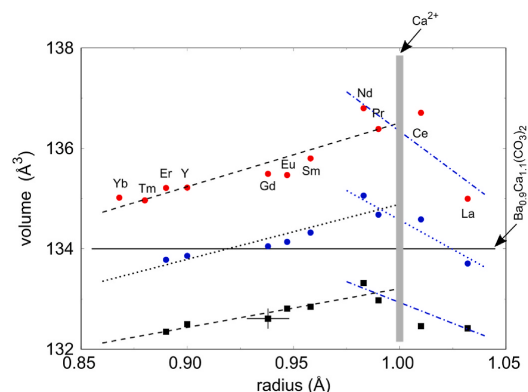


Fig. 4. Unit cell volume of Ba-Ca carbonates doped with different rare earth elements after the precipitation synthesis and the subsequent heating up to 723(1) K. For all elements except Yb and Tm one phase with a larger and one with a smaller volume than those of a sample with  $\text{Ba}_{0.9}\text{Ca}_{1.1}(\text{CO}_3)_2$  ( $\approx 134 \text{ \AA}^3$ ) composition are present. The volume of the phase crystallizing during the heat treatment is significantly larger (red circles). The dashed lines are guides to the eye, showing that for small REE there is a linear dependence of the unit cell volumes on the dopant and the dashed-dotted lines shows the trends for larger REE. The dotted line is a guide to the eye for the average of the unit cell volumes of the Ba-enriched and -depleted phases. The cation radius of  $\text{Ca}^{2+}$  ( $r(\text{Ca}) = 1.0 \text{ \AA}$ , VI-fold coordination) is shown as a grey bar to highlight the relative atomic radii [21]. Representative error bars ( $0.2 \text{ \AA}^3$  for the unit cell volume,  $0.01 \text{ \AA}$  for the ionic radii) are shown for one data point.

Table 2

Selected structural parameters of Ba-Ca carbonates doped with different rare earth elements after the precipitation synthesis and the subsequent heating up to 723(1) K. One phase with a larger (first line) and one with a smaller volume (second line) than those of a sample with  $\text{Ba}_{0.9}\text{Ca}_{1.1}(\text{CO}_3)_2$  ( $\approx 134 \text{ \AA}^3$ ) composition are present except for the Yb doped sample.

trace element	$a$ (Å)	$b$ (Å)	$c$ (Å)	$\beta$ (°)	$V$ (Å <sup>3</sup> )
La	6.655(2)	5.104(1)	4.221(6)	109.65(3)	135.00(4)
	6.616(5)	5.079(1)	4.169(7)	109.0(3)	132.41(8)
Pr	6.679(3)	5.114(3)	4.231(9)	109.31(5)	136.39(8)
	6.636(4)	5.083(4)	4.17(1)	108.89(6)	132.97(8)
Sm	6.692(2)	5.123(1)	4.190(7)	109.01(3)	135.80(6)
	6.623(6)	5.086(5)	4.17(1)	108.97(9)	132.85(5)
Gd	6.683(2)	5.122(1)	4.186(7)	108.97(3)	135.49(6)
	6.624(3)	5.080(3)	4.166(9)	108.92(5)	132.61(5)
Er	6.661(5)	5.118(5)	4.198(9)	109.14(9)	135.21(8)
	6.579(9)	5.120(5)	4.14(1)	108.4(1)	132.4(1)
Yb	6.642(2)	5.111(2)	4.209(9)	109.08(4)	135.02(2)
-	-	-	-	-	-

Fig. 4 shows the unit cell volume of the crystalline phases. The unit cell volume is mainly determined by the concentration of Ba in the solid (Ba-enriched or Ba-depleted) and by the radius of the REE, where we assume very similar REE-concentrations of  $\approx 6\%$  [12] for all compounds. The observed behaviour can consistently be explained by a process where initially a Ba-depleted phase is precipitated, which has a smaller unit cell than expected for a compound with the nominal concentration. Correspondingly, barium is enriched in the amorphous precipitate, which, when crystallizing in the same structure, then consequently has a larger unit cell volume. In fact, an average of the unit cell volumes of the Ba-depleted and the Ba-enriched phases gives a unit cell volume which deviates only in one case (Nd) by more than 0.3% from the value expected from the composition of the solution.

Clearly, the unit cell volume of both phases changes as a function of the cation radius of the dopant. Hence, the dopant has to be present in

D. Spahr et al.

Solid State Sciences 139 (2023) 107129

both phases. The changes as a function of cation radius are, to a good approximation, the same for both the Ba-enriched and the -depleted phases, as the straight lines in Fig. 4 are essentially parallel. This leads to the conclusion that nearly similar amounts of the REE are incorporated in the Ba-enriched and -depleted phases. As the phases are isostructural and differ only very slightly in their composition, this is the expected behaviour.

The present data indicate that the change in the dependence of the unit cell volume on the radius of the dopant at around 1.0 Å. This may be rationalized by noting that in octahedral coordination the ionic radius of  $\text{Ca}^{2+} = 1.0$  Å, while the ionic radius of  $\text{Ba}^{2+} = 1.35$  Å (VI-fold coordination is assumed) [21]. For those REE with radii smaller than that of  $\text{Ca}^{2+}$  we therefore would expect that their incorporation always leads to a decrease in the unit cell volume, while for those with radii larger than  $\text{Ca}^{2+}$  the behaviour depends on whether they predominantly replace  $\text{Ca}^{2+}$  or  $\text{Ba}^{2+}$ .

As was noted by Spahr et al. [12]; sodium concentrations were below the detection limit in the solids, and as TRIFS for the Eu-doped compound has shown [12], charge compensation is achieved by incorporation of hydroxyl groups.

### 3.3. Raman spectroscopy

We performed Raman spectroscopy on Ba–Ca carbonates doped with different trace elements. With a laser wavelength of 532 nm some samples fluoresce extremely strongly, which prevented Raman measurements. Fig. 5 shows selected Raman spectra of Ba–Ca carbonate doped with different REE elements.

We observe no significant difference between the powders doped with different trace elements (La, Nd, Gd, Y, Yb) and an undoped sample with  $\text{Ba}_{0.9}\text{Ca}_{1.1}(\text{CO}_3)_2$  composition, except a slight increase of the full width at half maximum (FWHM) of the bands upon doping. The characteristic and dominant Raman mode of carbonates with trigonal  $\text{CO}_3^{2-}$ -groups is the  $\text{CO}_3$ -stretching mode. For the Ba–Ca carbonate it has a Raman shift of  $\approx 1090$   $\text{cm}^{-1}$ . The Raman shift of the  $\text{CO}_3$ -stretching mode linearly depends on the cation radius of the incorporated REE (Fig. 6) where  $f(r_{\text{cation}}) = a \cdot x + b$  with  $a = -38(2)$   $\text{cm}^{-1} \text{Å}^{-1}$  and  $b = 1123(2)$   $\text{cm}^{-1}$ .

Raman spectroscopy is a local probe, as it is sensitive to the changes in bonding due to the local environment. In the present case, the  $\nu_1$  band is slightly broadened, so there is some variation in the local environment influencing the strength of the C–O bonds, which is what effectively is probed. Nevertheless, the Raman spectra are an independent confirmation of the incorporation of the REE in the C2-phase, as there is no

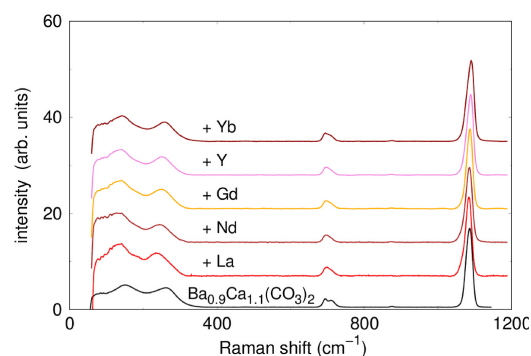


Fig. 5. Raman spectra of Ba–Ca carbonates doped with different trace elements (La, Nd, Gd, Y, Yb) after the precipitation synthesis and the subsequent heating up to 723(1) K in comparison to an undoped sample with  $\text{Ba}_{0.9}\text{Ca}_{1.1}(\text{CO}_3)_2$  composition.

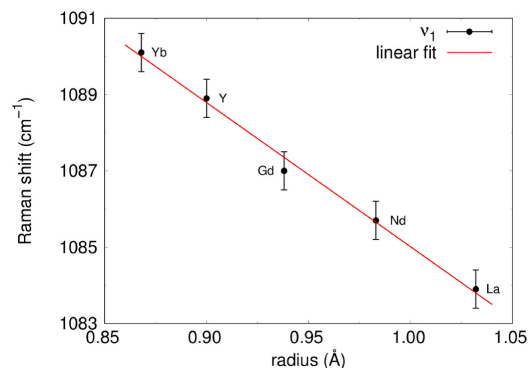


Fig. 6. Peak maximum of the  $\text{CO}_3$ -stretching mode of Ba–Ca carbonates doped with different trace elements (La, Nd, Gd, Y, Yb). The red line is a linear fit to the experimental data.

other explanation for the linear dependence of the Raman shift of the stretching vibration on the radius of the dopant. The Raman spectra also confirm that the environments experienced by the  $\text{CO}_3$ -groups are very similar in the Ba-enriched and the Ba-depleted phase.

### 4. Conclusion

For the on-going discussion on the structure and properties of the synthetic Ba–Ca-carbonate, three topics are of interest, namely (a) the structure of the phase, (b) the relative stability of the phase, and (c) the formation of precursor phases and the incorporation of REE into this structure. We think that the  $\text{Ba}_x\text{Ca}_{2-x}(\text{CO}_3)_2$  phases studied by Whittaker and Joester [9]; Whittaker, Sun, DeRocher, Jayaraman, Ceder and Joester [22]; Whittaker, Su, Duggins, Ceder and Joester [23]; Whittaker et al. [13]; Seknazi et al. [10]; Spahr et al. [4,12]; Saito et al. [11] are all the same. There seems to be a consensus that this phase can have an appreciable variation in stoichiometry.

With respect to the structure of this phase, the present study confirms that the description of the precipitated phase in a monoclinic structure describes the diffraction data well. Only future single crystal diffraction experiments will allow to reliably distinguish between the two structural models currently employed, namely the one used here [4,12] and that of a trigonal structure with variations in the cation and anion order [9,10,13,23].

The relative stability of the phase is also still open to discussion. Whittaker et al. [13] heated a sample with a ratio of Ba:Ca = 1:1 to 873 K. We note that the C2-phase can be formed by direct reaction of the carbonates at high temperatures. In contrast, barytocalcite can only be formed hydrothermally in the laboratory. There have been no reports of the synthesis of alstonite, but paralstonite can be formed by heating alstonite [13]. There is agreement that the free energies of these compounds differ only slightly. We think that it is problematic to refer to Chang [1] as showing that barytocalcite is the stable phase below 800 K, as that study contains no structural data and at that time a data analysis based on the available information in the X-ray powder data file would have led to an erroneous identification of the C2-phase as barytocalcite. This would explain the observation of Whittaker et al. [13] that heating the C2-phase does not lead to the formation of another polymorph. It would also explain why we don't observe barytocalcite by mechano-synthesis and by reaction of the carbonates at ambient pressure. The situation changes if pressure is involved - barytocalcite can be obtained in nice, but small, crystals hydrothermally [4].

The present study has shown that significant amounts of REE can be incorporated into the C2-phase. This is a phase which could be formed

when precipitating aqueous nitrate solutions containing radionuclides. It therefore seems worthwhile to now extend the study to understand the precipitation of solutions containing multiple dopants and tetravalent dopants. A prerequisite for a further quantitative understanding however is more information regarding the structure-property relations. We therefore conclude that now single crystal diffraction studies in conjunction with reliable thermodynamic data are required to advance our understanding of this interesting phase.

#### Author contribution

All authors contributed equally to the design of the study, the experiments, data analysis and manuscript writing.

#### Declaration of competing interest

The authors declare that they have no known competing financial interests or personal relationships that could have appeared to influence the work reported in this paper.

#### Data availability

Data will be made available on request.

#### Acknowledgements

We gratefully acknowledge funding from the DFG (project Wi1232 and Ba4020) and the DFG-Research Unit FOR2125/CarboPaT.

#### References

- [1] L.L.Y. Chang, Subsolidus phase relations in the systems  $\text{BaCO}_3\text{-SrCO}_3$ ,  $\text{SrCO}_3\text{-CaCO}_3$  and  $\text{BaCO}_3\text{-CaCO}_3$ , *J. Geol.* 73 (1965) 346–368, <https://doi.org/10.1086/627065>.
- [2] A. Gelis, P. Kozak, A. Breshears, M. Brown, C. Launier, E. Campbell, G. Hall, T. G. Levitskaia, V. Hoffeltz, G. Lumetta, Closing the nuclear fuel cycle with a simplified minor actinide lanthanide separation process (ALSEP) and additive manufacturing, *Sci. Rep.* 9 (2019), 12842, <https://doi.org/10.1126/science.184.4134.351>.
- [3] A. Wilden, F. Krefit, D. Schneider, Z. Papatrigas, G. Modolo, G.J. Lumetta, A. Gelis, J. D. Law, A. Geist, Countercurrent actinide lanthanide separation process (ALSEP) demonstration test with a simulated PUREX raffinate in centrifugal contactors on the laboratory scale, *Appl. Sci.* 10 (2020) 7217, <https://doi.org/10.3390/app10207217>.
- [4] D. Spahr, L. Bayarjargal, V. Vinograd, R. Luchitskaia, B. Winkler, A new  $\text{BaCa}(\text{CO}_3)_2$  polymorph, *Acta Crystallogr. B* 75 (2019) 291–300, <https://doi.org/10.1107/S2052520619003238>.
- [5] B. Dickens, J.S. Bowen, The crystal structure of  $\text{BaCa}(\text{CO}_3)_2$  (barytocalcite), *J. Res. Natl. Bur. Stand. (U.S.)* 75A (1971) 197–203.
- [6] H. Effenberger, The Crystal Structure of the Mineral Paralstonite,  $\text{BaCa}(\text{CO}_3)_2$ , *N. Jb. Miner. Mh.*, 1980, pp. 353–363.
- [7] L. Bindi, A.C. Roberts, C. Biagioni, The crystal structure of alstonite,  $\text{BaCa}(\text{CO}_3)_2$ : an extraordinary example of ‘hidden’ complex twinning in large single crystals, *Min. Mag.* 84 (2020) 699–704, <https://doi.org/10.1180/mgm.2020.61>.
- [8] R. Chuliá-Jordán, D. Santamaria-Perez, J. Ruiz-Fuertes, A. Otero-de-la Roza, C. Popescu, Crystal structure of  $\text{BaCa}(\text{CO}_3)_2$  alstonite carbonate and its phase stability upon compression, *Earth Space Chem.* 5 (2021) 1130–1139, <https://doi.org/10.1021/acsearthspacechem.1c00032>.
- [9] M.L. Whittaker, D. Joester, ACBC to balcite: bioinspired synthesis of a highly substituted high-temperature phase from an amorphous precursor, *Adv. Mater.* 29 (2017), 1606730, <https://doi.org/10.1002/adma.201606730>.
- [10] E. Seknazi, D. Levy, I. Polishchuk, A. Katsman, B. Pokroy, Experimental and theoretical insights into the bioinspired formation of disordered Ba-calcite, *Adv. Funct. Mater.* 30 (2020), 1805028, <https://doi.org/10.1002/adfm.201805028>.
- [11] A. Saito, H. Kagi, S. Marugata, K. Komatsu, D. Enomoto, K. Maruyama, J. Kawano, Incorporation of incompatible Strontium and Barium Ions into Calcite ( $\text{CaCO}_3$ ) through amorphous calcium carbonate, *Minerals* 10 (2020) 270, <https://doi.org/10.3390/min10030270>.
- [12] D. Spahr, L. Bayarjargal, V. Vinograd, M. Etter, J. Raddatz, B. Winkler, Incorporation of europium into  $(\text{Ba,Ca})_2(\text{CO}_3)_2$ , *J. Solid State Chem.* 307 (2022), 122759, <https://doi.org/10.1016/j.jssc.2021.122759>.
- [13] M.L. Whittaker, E. Pri-gal, A. Schmidt, D. Joester, Superlattice ordering transitions driven by short-range structure in barium calcium carbonates, *Faraday Discuss* 235 (2022) 416–432, <https://doi.org/10.1039/d1fd00086a>.
- [14] N. Massoni, J. Rosen, M. Chartier, T. Cozzika, Study of barytocalcite as a conditioning matrix for carbon 14: comparison of several synthesis routes, *J. Nucl. Mater.* 441 (2013) 199–207, <https://doi.org/10.1016/j.jnucmat.2013.06.003>.
- [15] J.V. Smith (Ed.), X-Ray Powder Data File. Sets 1-5 (Revised), American Society for Testing Materials, 1960.
- [16] A. Le Bail, H. Duroy, J.L. Fourquet, Ab-initio structure determination of  $\text{LiSBWO}_6$  by X-ray powder diffraction, *Mater. Res. Bull.* 23 (1988) 447–452, [https://doi.org/10.1016/0025-5408\(88\)90019-0](https://doi.org/10.1016/0025-5408(88)90019-0).
- [17] H.M. Rietveld, A profile refinement method for nuclear and magnetic structures, *J. Appl. Crystallogr.* 2 (1969) 65–71, <https://doi.org/10.1107/S0021889869006558>.
- [18] B.H. Toby, R.B. Von Dreele, *GSAS-II*: the genesis of a modern open-source all purpose crystallography software package, *J. Appl. Crystallogr.* 46 (2013) 544–546, <https://doi.org/10.1107/S0021889813003531>.
- [19] L. Bayarjargal, C.J. Fruhner, N. Schrodt, B. Winkler,  $\text{CaCO}_3$  phase diagram studied with Raman spectroscopy at pressures up to 50 GPa and high temperatures and DFT modeling, *Phys. Earth Planet. In.* 281 (2018) 31–45, <https://doi.org/10.1016/j.pepi.2018.05.002>.
- [20] M. Wojdyr, *Fityk*: a general-purpose peak fitting program, *J. Appl. Crystallogr.* 43 (2010) 1126–1128, <https://doi.org/10.1107/S0021889810030499>.
- [21] R.D. Shannon, Revised effective ionic radii and systematic studies of interatomic distances in halides and chalcogenides, *Acta Crystallogr. A* 32 (1976) 751–767, <https://doi.org/10.1107/S0567739476001551>.
- [22] M.L. Whittaker, W. Sun, K.A. DeRocher, S. Jayaraman, G. Ceder, D. Joester, Structural basis for metastability in amorphous calcium barium carbonate (ACBC), *Adv. Funct. Mater.* 28 (2018), 1704202, <https://doi.org/10.1002/adfm.201704202>.
- [23] M.L. Whittaker, W. Su, D.O. Duggins, G. Ceder, D. Joester, Dynamic barriers to crystallisation of calcium barium carbonates, *Cryst. Growth Des.* 21 (2021) 4556–4563, <https://doi.org/10.1021/acs.cgd.1c00433>.



# Danksagung

Ich möchte mich bei allen bedanken, die mich in der Zeit während meines Studiums und meiner Promotion unterstützt haben. Im Besonderen:

- Möchte ich mich vor allem bei Björn für die große Unterstützung in den letzten Jahren bedanken. Für die Betreuung während meines kompletten Bachelor- und Masterstudiums und auch in der Zeit der Promotion. Ohne ihn wäre ein erfolgreicher Abschluss meiner Promotion und auch meines Studiums nicht möglich gewesen. Dabei waren sein persönliches Engagement, seine Unterstützung und sein Verständnis für persönliche Probleme ausschlaggebend für die tolle Zusammenarbeit in dieser Zeit.
- Besonderer Dank gilt auch Bayaraa und Eiken. Beide haben mich seit meinem Bachelorstudium extrem unterstützt. Sei es durch die Betreuung von Bachelor- oder Masterarbeit oder im Rahmen meiner Promotion. Auch ohne ihre Unterstützung wäre meine Forschungsarbeit der letzten Jahre so nicht realisierbar gewesen. Durch die Zusammenarbeit mit beiden habe ich nicht nur viel gelernt, sondern mich auch persönlich weiterentwickelt.
- Auch bei all meinen Kollegen bzw. der Arbeitsgruppe Winkler möchte ich mich bedanken. Die gegenseitige Unterstützung in unserer Arbeitsgruppe war ebenfalls ein wichtiger Faktor für das erfolgreiche Arbeiten. Dabei ist die Zusammenarbeit mit Jannes besonders hervorzuheben, für welche ich sehr dankbar bin. Die zahlreichen gemeinsamen Experimente und Messzeiten waren ein wichtiger Bestandteil meiner Forschung. Auch für die großartige Hilfe von Rita möchte ich mich an dieser Stelle noch einmal bedanken.

- Mein Dank gilt auch der Werkstatt unserer Arbeitsgruppe. Durch ihre Hilfe konnten wir nicht nur das CO<sub>2</sub>-Ladesystem für Diamantstempelzellen realisieren, sondern hatten immer tatkräftige technische Unterstützung vor Ort. Sei es falls mal irgendein Gerät nicht mehr funktionierte oder falls auf die Schnelle noch technische Veränderungen nötig waren. Dabei gilt David besonderer Dank, der mit seinem technischen Sachverstand immer ein offenes Ohr für unsere Probleme hatte.
- Dank gilt auch allen meinen Co-Autoren, die durch ihre Unterstützung dazu beigetragen haben diese Forschungen durchzuführen. Hier möchte ich mich besonders bei Victor bedanken, der das zugrundeliegende DFG-Projekt erst möglich gemacht hat.
- Ich möchte mich auch bei meinen Eltern für jegliche Form der Hilfe und Unterstützung bedanken. Sei es durch Korrekturlesen von Berichten im Studium, Manuskripten während der Promotion oder auch inspirierende Diskussionen beim Abendessen. Ohne ihre persönliche Unterstützung hätten Studium und Promotion so nicht funktioniert.
- Auch bei meiner Familie und bei meinen Freunden möchte ich mich für die schönen Zeiten der letzten Jahre bedanken.
- Für die finanzielle Unterstützung meiner Arbeit möchte ich mich bei der Deutschen Forschungsgemeinschaft (DFG), der Johann Wolfgang Goethe-Universität, dem Deutschen Elektronen-Synchrotron (DESY) als Teil der Helmholtz-Gemeinschaft (HGF) und der Hermann-Willkomm-Stiftung bedanken.